Development and Experimental Study of the KOTO Detector System using Three K_L Neutral Decay Modes

Takahiko Masuda

Department of Physics, Graduate School of Science
Kyoto University

February, 2014

Abstract

The KOTO experiment aims at observing the rare CP violation decay of long lived neutral kaons, $K_L \to \pi^0\nu\overline{\nu}$, with the sensitivity of the Standard Model prediction. The detector system of the KOTO experiment was constructed at J-PARC. As we renewed the detector system, it was necessary to understand the detector performance and construct a realistic simulation model which can reproduce experimental data. It was also necessary to build an analysis framework to reconstruct objective events with our detector system.

For this purpose, we measured the K_L beam flux with the measurements of three neutral decay modes: $K_L \to 3\pi^0$, $K_L \to 2\pi^0$, and $K_L \to 2\gamma$. Their kinematics and branching fractions are well known. In addition, initial K_Ls of them are able to be fully reconstructed with our detector system.

This measurement was performed in January 2013. Implementing detailed responses of the detectors to our simulation model, we obtained the realistic simulation model which can reproduce the experimental data. The event reconstruction method was also established. The K_L flux was determined as $(4.182 \pm 0.017_{\text{stat.}} \pm 0.059_{\text{sys.}}) \times 10^7$ K_L per 2×10^{14} proton on target as the weighted average value of the three modes. The results among the three modes were consistent within 2.3 %. The systematic uncertainty, derived from the discrepancy between the experimental data and the simulation data, was 1.4 %.

We established the foundation of the KOTO experiment: a realistic simulation model and an analysis framework. They were evaluated with the measurements of $K_L \to 3\pi^0$, $K_L \to 2\pi^0$, and $K_L \to 2\gamma$. In this thesis, results from these measurements and the obtained performance are described.

Acknowledgements

I would never have completed this thesis without a great deal of help and support from many people. I would like to express my gratitude to them on this occasion.

First of all, I would like to express my sincere appreciation to Prof. Noboru Sasao, for giving me a great opportunity for the research of the kaon physics. He gave me a chance to take the important role in it. I always respect his deep knowledge of physics and inexhaustible inquiring mind. I would like to express heartfelt gratitude to Prof. Tadashi Nomura. His shrewd advice always lead me to the right way which I should go. I would never have reached this successful end without his strong support. My special thanks go to Prof. Hajime Nanjo for his continuous supports and stimulating discussions. He taught me physics and experimental methods from the very rudimentary level. I'm glad to express my cordial gratitude to them here from the bottom of my heart.

I would like to extend my gratitude to all of the KOTO collaborators. I am deeply thankful to Prof. T. Yamanaka, the spokesperson of the KOTO experiment. He taught me various things to perform an experiment. His strong leadership carried this experiment here, and I believe he leads the experiment toward the great success. I would like to extend my appreciation to Prof. T. K. Komatsubara. I learned a lot of things, including attitudes to analyses. I was also helped by him with the strong financial support to build the electronics of the CsI calorimeter. I present my appreciation to Prof. G. Y. Lim and Prof. H. Watanabe for the detector construction and the environment preparation at J-PARC. Without their perfect arrangements, the engineering run could not be performed. I am also grateful to Prof. T. Matsumura, Prof. Y. Tajima, Prof. M. Togawa, and Prof. S. Suzuki for their great work for the detector construction. I would also like to thank Prof. M. Campbell, Prof. J. Comfort, Prof. M. Tecchio, Prof. Y. W. Wah, Mr. M. Bogdan, Dr. J. Ma, Mr. D. McFarland, and Ms. J. Xu for their great work for the complicated DAQ system. My gratitude goes to Dr. H. Morii, Dr. E. Iwai, Dr. T. Shimogawa, Dr. Y. C. Tung, Mr. K. Sato, and Dr. K. Shiomi for giving me invaluable support and advice, and encouragement.

In particular, I would like to thank Dr. Y. Ri, Mr. J. W. Lee, and Mr. Y. Sugiyama. Thanks to their kindness and friendship, the extended stay in Tokai-mura was so enjoyable. My special thanks to Mr. N. Kawasaki, Mr. D. Naito, Mr. Y. Maeda, Mr. S. Banno, Mr. S. Seki, Mr. T. Hineno, and Mr. Y. Takashima for their great contributions to the engineering run. With their hard works, we successfully performed the engineering run. I would like to express my gratitude to Ms. R. Murayama, Mr. H. Yoshimoto, Mr. Y. Nakaya, Ms. Y. Yanagida, Mr. Y. Odani, Mr. G. Takahashi, Ms. M. Sasaki, Mr. H. Yokota, Mr. T. Ota, Mr. T. Toyoda, Ms. M. Isoe, Mr. I. Kamiji, and Mr. K. Nakagiri for their past and future great work for the KOTO experiment.

I am deeply grateful to all the members of the High Energy Physics Group in Kyoto University. Prof. T. Nakaya, Prof. A. K. Ichikawa, Prof. M. Ishino, Prof. A. Minamino, Prof. T. Sumida, Prof. M. Ikeda, Dr. K. Nitta, Dr. C. Bronner, Prof. N. Taniguchi, Prof. K. Hiraide, Prof. Y. Kurimoto,

Dr. Y. Nakajima, Prof. K. Matsuoka, Mr. H. Kawamuko, Mr. S. Gomi, Mr. Y. Kurosawa, Mr. H. Kubo, Mr. T. Usuki, Mr. N. Nagai, Dr. M. Otani, Mr. K. Ieki, Dr. A. Murakami, Mr. T. Kikawa, Mr. K. Suzuki, Mr. S. Takahashi, Mr. K Huang, Mr. T. Hiraki, Ms. S. Hirota, Mr. T. Yamauchi, Mr. K. Goda, Mr. T. Tashiro, Mr. T. Nagasaki, Mr. S. Akiyama, Mr. N. Kamo, Mr. K. Tateishi, Mr. Y. Ishiyama, Mr. T. Kunigo, Mr. M. Jiang, Mr. K. Nakamura, Mr. T. Hayashino, Mr. K. Yoshida. My life in the university have been always happy with them. My special thank goes to the "coffee club" in the laboratory. Unfortunately, this club collapsed into bankruptcy; however, we have "nabe kai". I hope that the kai continues for ever.

At last but not the least, I would like to express my special appreciation to my parents for the infinite supports throughout my life. Finally, I would like to express my sincere thanks to my wife for her understandings and generous supports, and to my daughter for her smiles.

Takahiko Masuda
Kyoto, Japan.
January 2014

Contents

List of Figures

List of Tables

Chapter 1

Introduction

Standard Model (SM) of particle physics, developed in the early 1970s, is based on CPT symmetry which is the combined symmetry of three discrete symmetries:

- Charge conjugation (C) : transforming particle to anti-particle,
- Parity (P) : reflecting the space coordinate from $\vec{x} \to -\vec{x}$,
- Time reversal (T) : inverting the time coordinate from t to $-t$.

Today, we know that C, P, and T symmetries are not good symmetries. In fascinating contrast, while C and P violation in weak interactions are individually maximal, CP is almost conserved. The SM has successfully explained almost all experimental results and well predicted a wide variety of phenomena. There is, however, an important question which SM cannot explain: why does matter dominate this universe and is anti-matter quite rare. Although the asymmetry between matter and anti-matter is explained by CP asymmetry in the SM, the amount of CP violation explained by the SM is not large enough to make the current matter-dominant universe. We thus believe there is a new physics (NP) beyond the SM (BSM), which breaks CP symmetry more; we should examine CP symmetry and search for the NP.

In order to examine the SM, we perform the KOTO experiment which aims at discovering $K_L \to \pi^0\nu\overline{\nu}$ decay events. $K_L \to \pi^0\nu\overline{\nu}$ is one of the most attractive processes to examine the SM. This decay directly breaks CP symmetry. Important virtues of $K_L \to \pi^0\nu\overline{\nu}$ are breaking CP symmetry and its theoretical cleanness. $K_L \to \pi^0\nu\overline{\nu}$ is thus sensitive to BSM which breaks CP symmetry. If the branching fraction of $K_L \to \pi^0\nu\overline{\nu}$ deviates from the SM prediction, it results in the experimental discovery of the evidence of BSM. The KOTO experiment, located at J-PARC (Japan Proton Accelerator Research Complex)[3], started constructing its detector system from the early 2010, and took first data in the early 2013. The main purpose of this thesis is to establish a foundation of the KOTO experiment. The K_L beam yield was measured with the KOTO detector for this purpose.

1.1 Standard Model and CKM Matrix

In the SM, the Lagrangian of the charged current in the weak interaction is given by:

$$\mathcal{L}_{CC} = \frac{-g}{\sqrt{2}} \left[\overline{u_{Li}} \gamma^\mu V_{ij} d_{Lj} W_\mu^+ + \overline{d_{Lj}} \gamma^\mu V_{ij}^* u_{Li} W_\mu^- \right], \tag{1.1}$$

where $i, j = 1, 2, 3$ are generation numbers. u_{Li} are left-handed up-type quarks and d_{Li} are left-handed down-type quarks. $W^{\pm}$ donate the weak bosons. V_{ij} is a element of Cabibbo-Kobayashi-Maskawa (CKM) matrix (V_{CKM})[4] which connects the weak eigenstates (denoted with primes below) and the mass eigenstates:

$$\begin{pmatrix} d' \\ s' \\ b' \end{pmatrix} = \begin{pmatrix} V_{ud} & V_{us} & V_{ub} \\ V_{cd} & V_{cs} & V_{cb} \\ V_{td} & V_{ts} & V_{tb} \end{pmatrix} \begin{pmatrix} d \\ s \\ b \end{pmatrix} = V_{CKM} \begin{pmatrix} d \\ s \\ b \end{pmatrix}. \tag{1.2}$$

Because the CKM matrix is unitary, flavor changing neutral current (FCNC) transitions are forbidden at the tree level and require loop diagrams.

When CP transformation is applied to the Lagrangian, it changes as:

$$\mathcal{L}_{CC} = \frac{-g}{\sqrt{2}} \left[\overline{d_{Lj}} \gamma^{\mu} V_{ij} u_{Li} W_{\mu}^{-} + \overline{u_{Li}} \gamma^{\mu} V_{ij}^{*} d_{Lj} W_{\mu}^{+} \right], \tag{1.3}$$

If V_{ij}^{*} is not same as V_{ij}, the interaction is not invariant under CP transformation. CKM matrix has four free parameters. There are several popular parameterizations of V_{CKM}. One involves three Euler-type angles (θ_{12}, θ_{23}, and θ_{31}) and a complex phase (δ):

$$V_{CKM} = \begin{pmatrix} c_{12}c_{13} & s_{12}c_{13} & s_{13}e^{i\delta} \\ -s_{12}c_{23} - c_{12}s_{23}s_{13}e^{i\delta} & c_{12}c_{23} - s_{12}s_{23}s_{13}e^{i\delta} & s_{23}c_{13} \\ s_{12}c_{23} - c_{12}s_{23}s_{13}e^{i\delta} & -c_{12}c_{23} - s_{12}s_{23}s_{13}e^{i\delta} & c_{23}c_{13} \end{pmatrix}, \tag{1.4}$$

with c_{ij} defined as $\cos\theta_{ij}$ and s_{ij} defined as $\sin\theta_{ij}$. In the Wolfenstein parameterization[5], matrix elements are expanded in powers of $\lambda = |V_{us}| \sim 0.23$:

$$V_{CKM} = \begin{pmatrix} 1 - \frac{1}{2}\lambda^2 - \frac{1}{8}\lambda^4 & \lambda & A\lambda^3(\rho - i\eta) \\ -\lambda + \frac{1}{2}A^2\lambda^5[1 - 2(\rho + i\eta)] & 1 - \frac{1}{2}\lambda^2 - \frac{1}{8}\lambda^4(1 + 4A^2) & A\lambda^2 \\ A\lambda^3\left[1 - (\overline{\rho} + i\overline{\eta})\right] & -A\lambda^2 + \frac{1}{2}A\lambda^4[1 - 2(\rho + i\eta)] & 1 - \frac{1}{2}A^2\lambda^4 \end{pmatrix} + \mathcal{O}(\lambda^6), \tag{1.5}$$

where A, ρ, and η are independent real parameters, $\overline{\rho} = \rho(1 - \lambda^2/2)$ and $\overline{\eta} = \eta(1 - \lambda^2/2)$. This parameterization shows clearly that the off-diagonal elements are small and the diagonal elements are close to unity, which makes a flavor structure. The parameter η represents the complex phase that causes CP violation.

1.2 $K_L \to \pi^0 \nu\overline{\nu}$

We move onto a discussion of the direct CP violating $K_L \to \pi^0 \nu\overline{\nu}$ decay. An important virtue of $K_L \to \pi^0 \nu\overline{\nu}$ is its theoretical cleanness. The theoretical uncertainty of its branching fraction is only 2.5 %[6] as contrasted with the theoretical uncertainty of most other meson decays, especially B system, is as high as 10 %. This is related to the fact that its hadronic matrix elements can be extracted from the leading semileptonic decay, $K^{+} \to \pi^0 e^{+} \nu_e$. Other long-distance contributions and CP conserving contributions are negligibly small[7]. As a consequence of these features, the QCD renormalization scale ambiguities, inherent to perturbative QCD, essentially constitute the only theoretical uncertainties present in the calculation of the branching fraction. The investigation

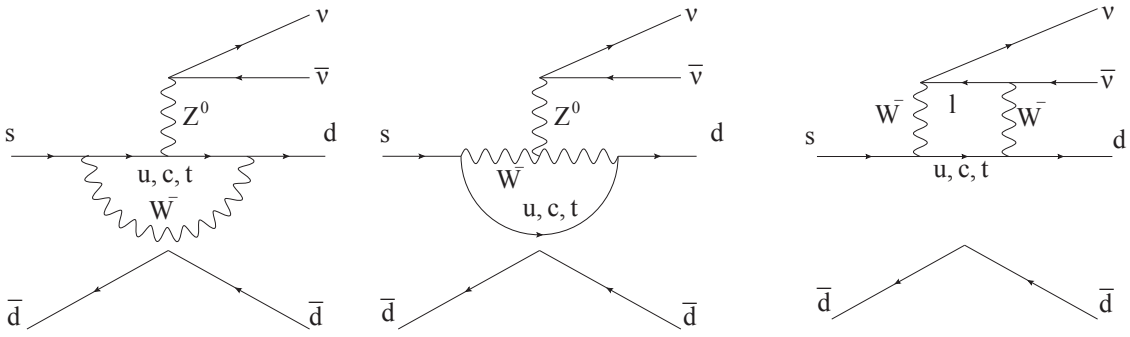

Figure 1.1: Feynman diagrams for $K_L \to \pi^0 \nu\overline{\nu}$.

of $K_L \to \pi^0 \nu\overline{\nu}$ in conjunction with its theoretical cleanliness, allows us to probe to measure η which causes CP violation with good accuracy. In addition, $K_L \to \pi^0 \nu\overline{\nu}$ is quite suppressed in the SM because of the flavor structure of the CKM matrix. It also effective to search especially for NP which breaks the flavor structure.

1.2.1 SM Branching Fraction

The discussion in this section mostly follows the reference[8].

The diagrams of $K_L \to \pi^0 \nu\overline{\nu}$ are shown in Fig. 1.1 and the effective Hamiltonian for $K_L \to \pi^0 \nu\overline{\nu}$ is given as:

$$\mathcal{H}_{eff}(K_L \to \pi^0 \nu\overline{\nu}) = \frac{G_F}{\sqrt{2}} \frac{\alpha}{2\pi \sin^2 \theta_W} V_{ts}^* V_{td} X_t (\overline{s}d)_{V-A} \sum_{l=e,\mu,\tau} (\nu_l \overline{\nu_l})_{V-A} + h.c. \ , \tag{1.6}$$

where G_F is Fermi constant, α is electromagnetic coupling constant, and θ_W is weak mixing angle. X_t is a correction term due to the internal top-quark loop calculated as:

$$X_t = 1.469 \pm 0.017 \pm 0.002, \tag{1.7}$$

where the first error corresponds to the uncertainty of the QCD corrections and the second error corresponds to the uncertainty of the electroweak corrections[6]. To simplify this discussion, we consider one neutrino flavor and define a function as:

$$F = \frac{G_F}{\sqrt{2}} \frac{\alpha}{2\pi \sin^2 \theta_W} V_{ts}^* V_{td} X_t. \tag{1.8}$$

Then the effective hamiltonian (Eq. 1.6) is written as

$$\mathcal{H}_{eff}(K_L \to \pi^0 \nu\overline{\nu}) = F(\overline{s}d)_{V-A} (\nu\overline{\nu})_{V-A} + F^* (\overline{d}s)_{V-A} (\overline{\nu}\nu)_{V-A}, \tag{1.9}$$

and the amplitude for $K_L \to \pi^0 \nu\overline{\nu}$ is given by

$$\begin{aligned} &A(K_L \to \pi^0 \nu\overline{\nu}) = \\ &\frac{1}{\sqrt{2}} \left[F(1+\overline{\varepsilon}) \left\langle \pi^0 \left| (\overline{s}d)_{V-A} \right| K^0 \right\rangle + F^* (1-\overline{\varepsilon}) \left\langle \pi^0 \left| (\overline{d}s)_{V-A} \right| \overline{K^0} \right\rangle \right] (\overline{\nu}\nu)_{V-A}, \end{aligned} \tag{1.10}$$

where we use

$$K_L = \frac{1}{\sqrt{2}}\left[(1+\overline{\varepsilon})K^0 + (1-\overline{\varepsilon})\overline{K^0}\right], \tag{1.11}$$

and ignore $|\overline{\varepsilon}|^2 \ll 1$. Because of

$$CP\left|K^0\right\rangle = -\left|\overline{K^0}\right\rangle, \quad C\left|K^0\right\rangle = \left|\overline{K^0}\right\rangle \tag{1.12}$$

$$\therefore \left\langle \pi^0 \left| (\overline{d}s)_{V-A} \right| \overline{K^0} \right\rangle = -\left\langle \pi^0 \left| (\overline{s}d)_{V-A} \right| K^0 \right\rangle, \tag{1.13}$$

we can rewrite the amplitude as:

$$A(K_L \to \pi^0\nu\overline{\nu}) = \frac{1}{\sqrt{2}}\left[F(1+\overline{\varepsilon}) - F^*(1-\overline{\varepsilon})\right]\left\langle \pi^0 \left| (\overline{s}d)_{V-A} \right| K^0 \right\rangle (\overline{\nu}\nu)_{V-A}. \tag{1.14}$$

The $\overline{\varepsilon}$ can be ignored in comparison with unity, which implies that the indirect CP violation, CP violation in the $K^0 - \overline{K^0}$ mixing, is negligible in this decay. We have

$$F(1+\overline{\varepsilon}) - F^*(1-\overline{\varepsilon}) = \frac{G_F}{\sqrt{2}}\frac{\alpha}{\pi \sin^2\theta_W}\Im(V_{ts}^* V_{td}) \cdot X_t. \tag{1.15}$$

and we get the following relation;

$$A(K_L \to \pi^0\nu\overline{\nu}) = \frac{G_F}{2}\frac{\alpha}{\pi \sin^2\theta_W}\Im(V_{ts}^* V_{td}) \cdot X_t \left\langle \pi^0 \left| (\overline{d}s)_{V-A} \right| \overline{K^0} \right\rangle (\overline{\nu}\nu)_{V-A}. \tag{1.16}$$

This means only top quark contributes to the loop diagram of $K_L \to \pi^0\nu\overline{\nu}$ in Fig. 1.1, which reduces the QCD uncertainty to the level as in Eq. 1.7 being free from the up and charm contributions with more uncertainty.

Next, we consider the amplitude for $K^+ \to \pi^0 e^+ \nu_e$ to reduce the uncertainty of the $K_L \to \pi^0\nu\overline{\nu}$ calculation. The effective hamiltonian and the amplitude for $K^+ \to \pi^0 e^+ \nu_e$ are

$$\mathcal{H}_{eff}(K^+ \to \pi^0 e^+ \nu_e) = \frac{G_F}{\sqrt{2}} V_{us}^* (\overline{s}u)_{V-A} (\overline{\nu_e}e)_{V-A}, \tag{1.17}$$

$$A(K^+ \to \pi^0 e^+ \nu_e) = \frac{G_F}{\sqrt{2}} V_{us}^* \left\langle \pi^0 \left| (\overline{s}u)_{V-A} \right| K^+ \right\rangle (\overline{\nu_e}e)_{V-A}. \tag{1.18}$$

Using isospin symmetry, we have

$$\left\langle \pi^0 \left| (\overline{d}s)_{V-A} \right| \overline{K^0} \right\rangle = \left\langle \pi^0 \left| (\overline{s}u)_{V-A} \right| \overline{K^+} \right\rangle. \tag{1.19}$$

Considering the number of neutrino flavor and taking into account the difference in the lifetimes of K_L and K^+, we have

$$\frac{Br(K_L \to \pi^0\nu\overline{\nu})}{Br(K^+ \to \pi^0 e^+ \nu_e)} = 3\frac{\tau(K_L)}{\tau(K^+)}\frac{\alpha^2}{|V_{us}|^2 2\pi^2 \sin^4\theta_W}[\Im(V_{ts}^* V_{td}) \cdot X_t]^2. \tag{1.20}$$

Using known parameters listed in Tab. 1.1, and applying the isospin breaking corrections, finally we get[6]

$$Br(K_L \to \pi^0\nu\overline{\nu}) = (2.43^{+0.40}_{-0.37} \pm 0.06) \times 10^{-11}. \tag{1.21}$$

The first error is related to the uncertainties in the input parameters. Here main contributions are $A(V_{cb})$: 54 %, $\overline{\eta}$: 39 %. The second error is the contributions of theoretical uncertainties. Thus precise measurement of the $Br(K_L \to \pi^0\nu\overline{\nu})$ determines the value of $\overline{\eta}$.

Table 1.1: Input parameters for the $K_L \to \pi^0 \nu\overline{\nu}$ branching fraction calculation[1]

Input Parameters	Values
Br($K^+ \to \pi^0 e^+ \nu_e$)	0.00507(4)
$\tau(K_L)$	$5.116(21) \times 10^{-8}$
$\tau(K^+)$	$1.2380(21) \times 10^{-8}$
α	1/137.035999679(94)
$\lvert V_{us}\rvert$	0.22534(65)
$\sin\theta_W$	0.23116(13)
X_t	1.469(17)
λ	0.22535 ± 0.00065
A	$0.811^{+0.022}_{-0.012}$
$\overline{\rho}$	$0.131^{+0.026}_{-0.013}$
$\overline{\eta}$	$0.345^{+0.013}_{-0.014}$

1.2.2 Beyond the Standard Model

The discussion in this section mostly follows in reference [9].

In the SM, FCNC transitions in the kaon sector are most suppressed while the effects in $b \to d$ or $b \to s$ transitions are larger, because CKM matrix has the hierarchical structure:

$$\begin{aligned} s \to d : |V_{ts}^* V_{td}| &\sim \lambda^5 \sim 5 \times 10^{-4} \\ \ll \quad b \to d : |V_{tb}^* V_{td}| &\sim \lambda^3 \sim 10^{-2} \\ < \quad b \to s : |V_{tb}^* V_{ts}| &\sim \lambda^2 \sim 4 \times 10^{-2}. \end{aligned} \tag{1.22}$$

The flavor structure of NP, on the other hand, need not have such hierarchies; the largest deviations from the SM predictions are to be expected in kaon sector for such NP. Thus even the measured branching fractions of the $B_s \to \mu^+\mu^-$ and $B^0 \to \mu^+\mu^-$ at LHC were consistent with the SM[10, 11], large NP signatures can still be hoped for in rare kaon decays.

A model independent upper limit for the $Br(K_L \to \pi^0 \nu\overline{\nu})$, called the Grossman-Nir (GN) limit[12], is derived as

$$Br(K_L \to \pi^0 \nu\overline{\nu}) < 4.4 \times Br(K^+ \to \pi^+ \nu\overline{\nu}). \tag{1.23}$$

The correlation between these two modes can be derived from the isospin symmetry. The measured $Br(K^+ \to \pi^+ \nu\overline{\nu})$ is $(1.7 \pm 1.1) \times 10^{-10}$[1]. It yields that the upper limit to the $Br(K_L \to \pi^0 \nu\overline{\nu})$ is 1.2×10^{-9} (68 % C.L.).

Figure 1.2 shows the predicted correlation between the $Br(K_L \to \pi^0 \nu\overline{\nu})$ and the $Br(K^+ \to \pi^+ \nu\overline{\nu})$ in Minimal Flavor Violation (MFV)[13] and major three NP models. MFV does not assume additional CP violation phases, and the flavor mixing can be explained only by the CKM matrix in the SM; thus, the deviation of the branching fraction from the SM prediction is small. In other major NP models shown in Fig. 1.2, on the other hand, can largely deviate the branching fraction. The littlest Higgs model with T-parity (LHT)[14] and the Randall-Sundrum model with custodial protection (RSc)[15] have already started to be probed by LHC. Since they predicted rather small effects in B physics observables recently probed by LHCb, large NP effects in rare K decays are still possible in both scenarios. The SM with a sequential fourth generation (SM4)[16] which assumes a fourth generation of quarks and leptons, is in trouble with LHC data.

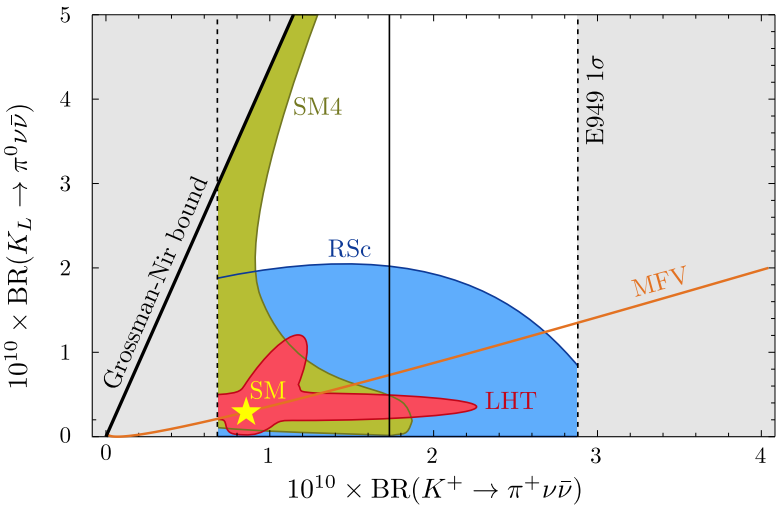

Figure 1.2: Predicted correlation between $Br(K_L \to \pi^0 \nu\overline{\nu})$ and $Br(K^+ \to \pi^+ \nu\overline{\nu})$ in various BSM models. The grey area was ruled out experimentally. The SM prediction point is marked by a star. This figure is quoted from [17]

1.3 History of $K_L \to \pi^0 \nu\overline{\nu}$ search

There were several experiments that searched the $K_L \to \pi^0 \nu\overline{\nu}$ decay, as shown in Fig. 1.3. Due to the small value of $Br(K_L \to \pi^0 \nu\overline{\nu})$, only upper limits were given. The first study was performed by Littenberg. He extracted a limit for the $K_L \to \pi^0 \nu\overline{\nu}$ decay from the data of Cronin and Fitch for the $K_L \to 2\pi^0$ study[18].

The E391a collaboration at KEK performed the first dedicated search for the $K_L \to \pi^0 \nu\overline{\nu}$ decay. Their detector is shown in Fig. 1.4. The detector system consisted of a main electromagnetic calorimeter (shown as "CsI" in Fig. 1.4) and hermetic veto counters. The electromagnetic calorimeter consisted of 576 un-doped CsI crystals whose size was $7.0 \times 7.0 \times 30$ cm^3 (i.e. 16 X_0[1)] long). The calorimeter measured energy and position of a pair of photons from π^0 decays. The upper limit on $Br(K_L \to \pi^0 \nu\overline{\nu})$ was set to be 2.6×10^{-8}[19].

1.4 KOTO Experiment

We prepared a new experiment aiming at a first observation of $K_L \to \pi^0 \nu\overline{\nu}$, named KOTO experiment[20]. The KOTO experiment is a successor experiment to the E391a experiment. This experiment follows the experimental concept that was established by the E391a experiment. While the sensitivity of the E391a experiment was three orders of magnitude far from the SM prediction, the background level was $\mathcal{O}(1)$. For the improvement of the sensitivity, a new dedicated beam line for the KOTO experiment was constructed at J-PARC. The design value of the proton intensity of the Main Ring (MR) accelerator of J-PARC is 100 times higher than that of the KEK-PS. For the background suppression, we updated the main electromagnetic calorimeter and some veto counters in the hermetic veto system. In addition, readout electronics were completely modified. The

[1)] radiation length

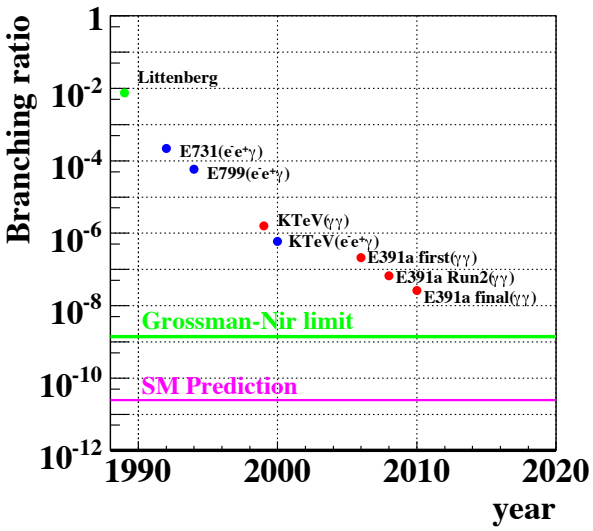

Figure 1.3: History of the $K_L \to \pi^0\nu\overline{\nu}$ search. A green point shows the first study performed by Littenberg. Blue (Red) points in the figure show results of the analysis using a $\pi^0 \to e^+e^-\gamma$ ($\pi^0 \to \gamma\gamma$) decay to identify the K_L decay. A green line shows the GN limit. A pink line shows the prediction in the Standard Model.

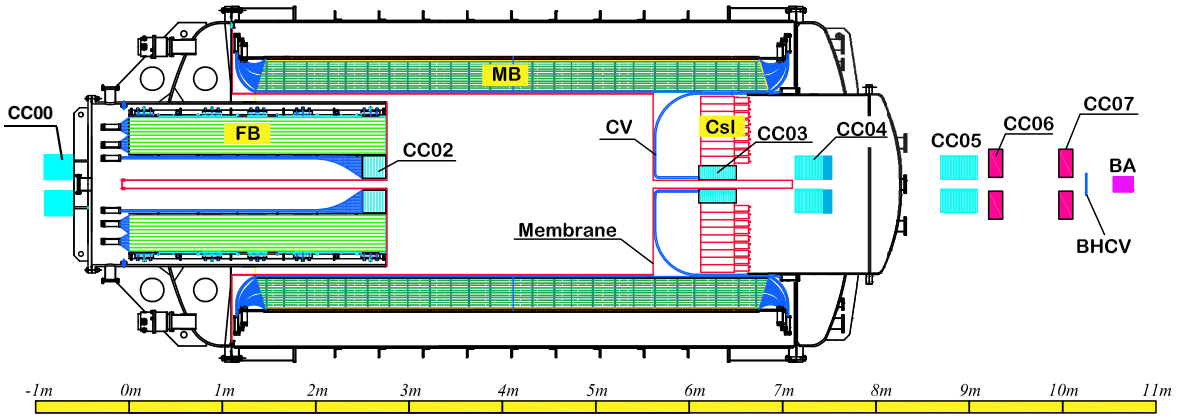

Figure 1.4: Cross-sectional view of the E391a detector. CsI: electromagnetic calorimeter; CV: charge-particle counter; MB and FB: main-barrel and front-barrel photon counters; CC00, CC02-CC07: collar-shaped photon counters; BHCV and BA: beam hole charged-particle and photon counters.

detailed design of the experiment is described in Chap. 2.

1.5 Purpose and Outline of the Thesis

We finished constructing most detectors in the KOTO detector system in December 2012. As the detector system was renewed, it was necessary to understand the actual detector performance and construct a realistic simulation model which reproduce experimental data. Rare decay experiments generally search their objective signals by comparing experimental data and simulated data in which SM process is implemented. The difference between experimental data and simulated data stands for non-SM effects; therefore, the reproducibility of the simulation decides the systematics of the experiment. Especially, the CsI calorimeter is essential. For the $K_L \to \pi^0\nu\overline{\nu}$ search, there is a particular difficulty that all particles in both initial and final states are neutral particles. It means we can neither select specific momentum of K_L by a magnet nor tag the initial K_L by any kind of tracking counters. We have to measure when and where a K_L decay and what a K_L momentum is, by using the main electromagnetic calorimeter information only.

It was also necessary to build an analysis framework to reconstruct objective signals with the detector system. For this purpose, we measured the K_L beam flux with the measurements of three neutral decay modes: $K_L \to 3\pi^0$, $K_L \to 2\pi^0$, and $K_L \to 2\gamma$. Their kinematics and branching fractions are well known. In addition, their initial K_L is able to be fully reconstructed with our detector. These three modes thus are suitable for the evaluation of the event reconstruction method.

The purpose of this thesis is to construct a realistic simulation model and analysis framework with the measurements of the three decay modes. They are foundations of the KOTO experiment as described above. We reconstructed the three modes individually and evaluated the consistency among them, then determined the K_L flux. The comparison between the experimental data and simulated data are discussed.

The outline of this thesis is the following. We first describe the signal detection method and apparatus of the KOTO experiment in Chap. 2. After that we move onto the K_L flux measurement from Chap. 3. In Chap. 3, the situation of the K_L flux measurement is described, including set up and data taking. In Chap. 4, the details of our Monte Carlo simulation are explained. In Chap. 5, the analyses for the three decay modes are described and the K_L flux is determined. In Chap. 6, we discuss obtained detector performance, and a comparison between a previous K_L flux measurement and this flux measurement. We also propose future improvements of the analysis. Finally we conclude this thesis in Chap. 7.

Chapter 2

KOTO Experiment

The KOTO experiment aims at the first observation of the rare CP violating decay, $K_L \to \pi^0\nu\overline{\nu}$. In this chapter, we first explain our detection method for $K_L \to \pi^0\nu\overline{\nu}$ decays and possible background events. Next, we explain the system and apparatus of the KOTO experiment.

2.1 Signal Detection

The final state of the $K_L \to \pi^0\nu\overline{\nu}$ decay is two photons and two neutrinos. As we cannot detect neutrinos because of their small cross section, we are to detect just two photons. Among K_L decay modes, $K_L \to \pi^0\nu\overline{\nu}$ and $K_L \to 2\gamma$ are able to make final state of two photons only. Since two photons from $K_L \to 2\gamma$ fly back-to-back in the K_L rest frame, we can identify $K_L \to \pi^0\nu\overline{\nu}$ decays by requiring that just two photons exist in the final state, and the sum of their momenta is not zero in the K_L rest frame. All other decay modes have more than two particles or contain charged particles in their final states. We can distinguish them from $K_L \to \pi^0\nu\overline{\nu}$ by detecting extra particles.

2.1.1 Signal Reconstruction

Figure 2.1 shows a cross-sectional view of the KOTO detector. The signature of a $K_L \to \pi^0\nu\overline{\nu}$ decay is a pair of photons coming from a π^0 decay without extra particles. An electromagnetic calorimeter (CsI calorimeter) described in Sec. 2.3 measures the energies and positions of the two photons, and hermetic veto counters described in Sec. 2.4 guarantee that there is no extra particle. The decay vertex of the K_L is reconstructed with the assumption that the two photons come from a π^0 decay on the beam axis and the vertices of the K_L and the π^0 are the same[1)]. As two neutrinos carry away momenta, we require the π^0 to have a finite transverse momentum.

Figure 2.2 shows a schematic view of the π^0 reconstruction. If the invariant mass of the two photons is assumed as the nominal π^0 mass (M_{π^0}), the following equation holds:

$$M_{\pi^0}{}^2 = 2E_{\gamma_1}E_{\gamma_2}(1-\cos\theta), \tag{2.1}$$

where E_{γ_1} and E_{γ_2} are the energies of the photons and θ is the angle between the direction of the two photons. Once we measure the energies and hit positions of the two photons in the calorimeter,

[1)] The life time of π^0 is fast (8.4×10^{-17} second) and a π^0 travels shorter than 1 μm. It is negligible short for the apparatus.

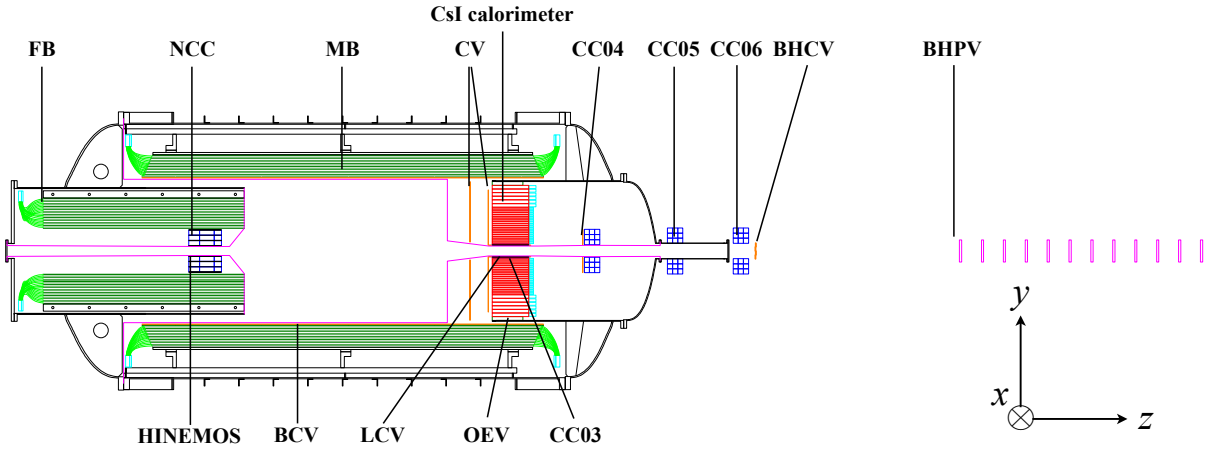

Figure 2.1: Cross-sectional view of the KOTO detector. The K_L beam comes in from the left hand side and decay in flight. The K_L that decays in the central decay region is the target of the analysis. The positive z-axis points in the beam direction, the positive y-axis points up, and the x-axis is defined to satisfy the relation of the right-hand system: $\vec{x} = \vec{y} \times \vec{z}$.

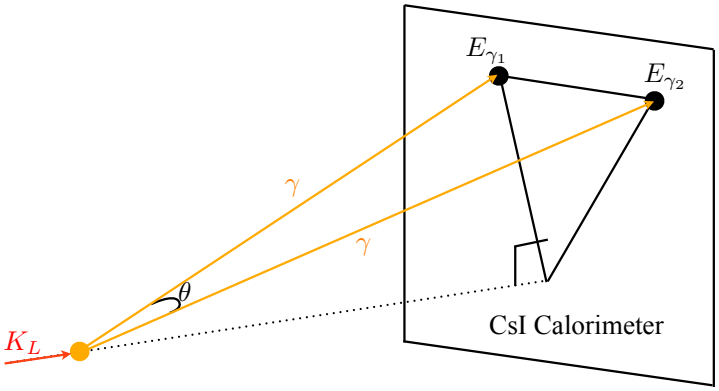

Figure 2.2: Schematic view of the π^0 reconstruction. The right tetragon represents the CsI surface. A K_L, coming from the left side, decays at the solid circle and a pair of photons are generated. The photons fly to the CsI calorimeter, and the calorimeter measures the energies and positions of the photons.

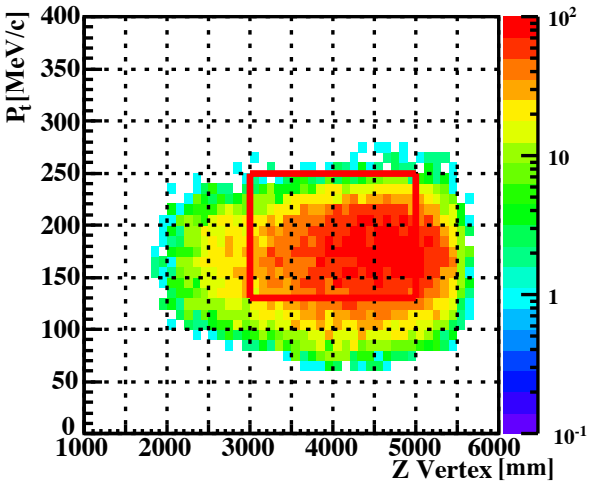

Figure 2.3: Distribution of $K_L \to \pi^0\nu\overline{\nu}$ decays in Z_{vtx}-P_t plane. Default kinematic selections[21] are applied. The box shown in red represents cut values for Z_{vtx} and P_t. The number of entries in the plot is arbitrary.

we can calculate θ. Adding the constraint that the vertex locates on the beam axis and upstream of the CsI surface, we can determine the vertex position as $(0, 0, Z_{vtx})$. More details of the π^0 reconstruction is described in Sec. 5.3.1.

After reconstructing the vertex, the momentum vector of the π^0 is calculated as the sum of two photon momenta. The transverse momentum of the π^0, P_t, is expressed as:

$$P_t = \sqrt{(P_x^{\pi^0})^2 + (P_y^{\pi^0})^2}, \tag{2.2}$$

where $P_x^{\pi^0}$ and $P_y^{\pi^0}$ are x and y components of the π^0 momentum, respectively. The two parameters, Z_{vtx} and P_t, are used for signal and background separation with other kinematic cuts[21]. The distribution of the two parameters of $K_L \to \pi^0\nu\overline{\nu}$ is shown in Fig. 2.3.

2.1.2 Background

In the KOTO experiment, background events are classified into two categories: K_L-decay backgrounds and beam-interaction backgrounds.

K_L decay background

Table 2.1 shows a list of branching fractions of K_L decay modes. All other K_L decays except $K_L \to 2\gamma$ have four or more photons, or contain charged particles in their final states. If some of these particles are identified as two photons and remaining particles are not detected, the decay might be a source of background. Detection efficiency of the hermetic veto counters thus is important to reject the K_L decay background. The $K_L \to 2\gamma$ decay has the same observable final-state particles with the signal decay. It becomes background if we mis-measure its transverse momentum.

beam-interaction background

A single π^0 can be produced by a neutron interaction, $n + A \to \pi^0 + A'$. To prevent neutrons in the beam from interacting with residual gas in the decay region, the decay volume has to be highly evacuated. With an achievable pressure of 10^{-5} Pa, the number of background events due to interactions between neutrons and residual gas is expected to be negligible.

Table 2.1: Branching fractions of K_L decay modes; $K_L \to \pi^0\nu\overline{\nu}$, the major four modes, and relevant two neutral modes are listed. For $K_L \to \pi^0\nu\overline{\nu}$, the SM prediction is shown. For the decay modes including one or more π^0s, the kinematic limits of the π^0 momentum in the K_L rest frame are also indicated. All values are quoted from [1].

Decay Modes	Branching Fraction	Max. momentum [MeV/c]
$K_L \to \pi^0\nu\overline{\nu}$	$(2.4 \pm 0.4) \times 10^{-11}$	231
$K_L \to \pi^{\pm}e^{\mp}\nu$	(40.55 ± 0.11) %	
$K_L \to \pi^{\pm}\mu^{\mp}\nu$	(27.04 ± 0.07) %	
$K_L \to 3\pi^0$	(19.52 ± 0.12) %	139
$K_L \to \pi^+\pi^-\pi^0$	(12.54 ± 0.05) %	133
$K_L \to 2\pi^0$	$(8.64 \pm 0.06) \times 10^{-4}$	209
$K_L \to 2\gamma$	$(5.47 \pm 0.04) \times 10^{-4}$	

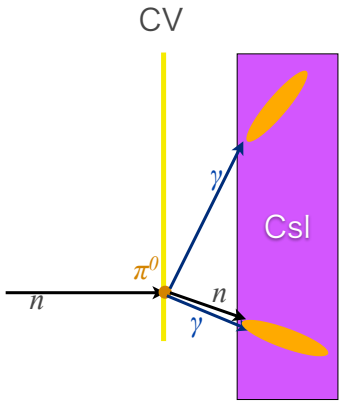

Figure 2.4: Schematic view of the CV-π^0 background. In the bottom cluster, the neutron shower and the photon shower are merged.

Around the beam region, there are accompanied neutrons, which are called "halo neutrons". If a halo neutron interacts with detector materials, it makes π^0 or η which decay into two photons and may fake a signal. An interaction with detector materials, usually, is able to be separated from the signal since the reconstructed vertex locates not in the decay region but at the detector position. However, if the energies of the photons are mis-measured due to leakage of an electromagnetic shower, photo nuclear effect, and additional energy deposition by other particles, the reconstructed vertex may shift into the signal region. This type of background was the main background source in the E391a experiment. An example is shown in Fig. 2.4. In Fig. 2.4 case, halo-neutron hits CV and generates π^0. The two photons from the π^0 enter the CsI calorimeter, and an additional neutron kicked out from the interaction adds the extra energy deposit in one photon. Finally, the reconstructed vertex moves upstream, and this event has possibility to fake a signal. This is called "CV-π^0 background". To reduce these beam-interaction backgrounds, we designed a well collimated K_L beam described in Sec. 2.2.2. Also we improved some of veto counters, especially Neutron Collar Counter (NCC) and Charged Veto (CV) which are described in Sec. 2.4.

Table 2.2: Expected numbers of the signal and backgrounds[2]

	source	value
Signal	$K_L \to \pi^0\nu\overline{\nu}$	2.39 ± 0.03
K_L decays	$K_L \to 2\pi^0$	1.32 ± 0.04
	$K_L \to \pi^+\pi^-\pi^0$	0.11 ± 0.01
	$K_L \to \pi^\pm e^\mp \nu$	0.07 ± 0.04
Halo neutron		0.10 ± 0.05
S/N		1.49

2.1.3 Sensitivity and Signal-to-Noise Ratio

The expected experimental sensitivity and background level of the KOTO experiment are listed in Tab. 2.2. These values were estimated using a Monte-Carlo simulation with the assumption of the full intensity of the J-PARC accelerators and the running time of 3×10^7 seconds. The detailed description can be found in [2]. The expected number of signals is 2.39 and the signal-to-noise ratio is 1.49. The $K_L \to 2\pi^0$ decay is considered to be the main source of backgrounds. The reasons are that the decay mode has only one extra π^0 to veto in the final state, and its branching fraction, 8.65×10^{-4}, is eight orders of magnitude larger than that of the signal mode. The halo neutron background is expected to be less than 5 %.

2.2 Beam Line

A bird's-eye view of the entire facility of J-PARC is shown in Fig. 2.5. We used a new KL beam line constructed in the hadron experimental hall (HD-hall) in J-PARC. In this subsection, the beam components are described. The first half describes the common beam components including J-PARC accelerators. The second half describes the components of the KL beam line after the production target.

2.2.1 Primary Beam Line

The 30 GeV proton beam, accelerated by Main Ring, was extracted to the HD-hall by using a slow extraction technique. A beam extraction in one cycle was called "spill". It had 2 seconds duration every 6 seconds repetition cycle[2)]. The design intensity of the primary beam is 2.0×10^{14} protons per spill and the achieved intensity at the moment of this research was 1.8×10^{13} protons per spill.

The primary proton beam was injected into a production target, called "T1 target", which located in the HD-hall. Generated secondary particles were delivered to our experimental area through a neutral (KL) beam line. The nominal production target was a Ni disk target. The left-most picture of Fig. 2.6 shows the Ni disk target. This nominal Ni disk target was designed for a beam power of 750 kW, but in the early stages of J-PARC, the proton beam power in the HD-hall was less than 100 kW because of the difficulty in reducing the beam loss in the slow extraction devices. Thus several configurations of T1 target were prepared and used to increase the secondary particle yield. The Pt targets, listed in Tab. 2.3, generated twice as many K_L as the Ni target,

[2)] Design values are 0.7 seconds duration every 3.3 seconds repetition cycle.

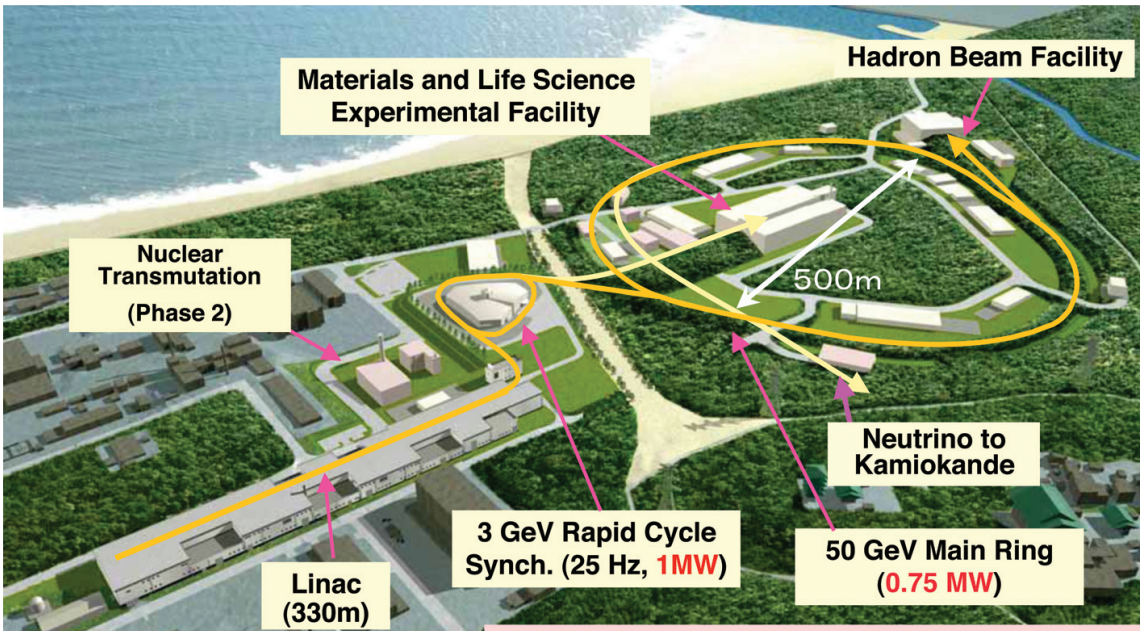

Figure 2.5: Bird's-eye view of the entire facility of J-PARC. This figure is quoted from [22]

mainly owing to its longer nuclear interaction length. At the moment of this research, the final step toward a physics run, the Au target was used, with which similar K_L yield to the Pt target was expected.

2.2.2 KL Beam Line

The beam line connecting from the T1 target to the KOTO detector was the KL beam line. Figure 2.7 shows the schematics of the KL beam line. This beam line was 21-m-long toward 16° direction from the primary proton beam line. The beam was designed in consideration of collecting large amount of K_Ls because of the small branching fraction of the $K_L \to \pi^0\nu\overline{\nu}$ decay. It was also necessary to consider background suppression; a small diameter beam, called "pencil beam", was required. The neutral beam should be well collimated, keeping a sufficient K_L flux which was needed to achieve high sensitivity.

The KL beam line was collimated by a pair of two long collimators: the first collimator was 4-m-long and the second collimator was 5-m-long. They located a distance of 450 mm away from each other. They were made of iron except for their edge regions. The 500-mm-long regions at upstream end of the first collimator and the both ends of the second collimator were made of tungsten. These collimators were designed for suppression of halo neutrons. The resultant solid angle of the collimators was 7.8 μSr, and the size of the beam at the exit of the beam line was determined to be 8.5×8.5 cm^2. Figure 2.8 shows estimated neutron profiles. The halo neutron flux was suppressed by 5 orders of magnitude than the core neutron flux, which corresponded to ten times improvement from the E391a experiment[23]. Figure 2.9 shows experimental data and simulated K_L momentum spectra at the exit of the beam line, which was 21 m downstream from

Table 2.3: Transition of the T1 target. In the column of Target Thickness, total thickness of the target materials and gaps are described separately (the latter in parentheses). This research of this thesis was performed with the Au target listed at the second from the bottom.

Period	Maximal Beam Power	Target Material	Target Thickness	Cooling method
Jan. 2009 -Feb. 2009	1.2 kW	Ni disks w/ gaps	54 (+12) mm	air
Oct. 2009 -Mar. 2010	5 kW	Pt rod Ni block w/ slits	60 mm 54 (+12) mm	air air
Oct. 2010 - Nov. 2010	5 kW	Pt rod Ni block w/ slits	60 mm 54 (+12) mm	air air
Jan. 2012 - Jul. 2012	50 kW	Pt square-bar	60 mm	indirect water cooling
Dec. 2012 - May. 2013	50 kW	Au square-bar w/ slits	64.8 (+1.2) mm	indirect water cooling
Design	750 kW	Ni disks w/ gaps	54 (+12) mm	direct water cooling

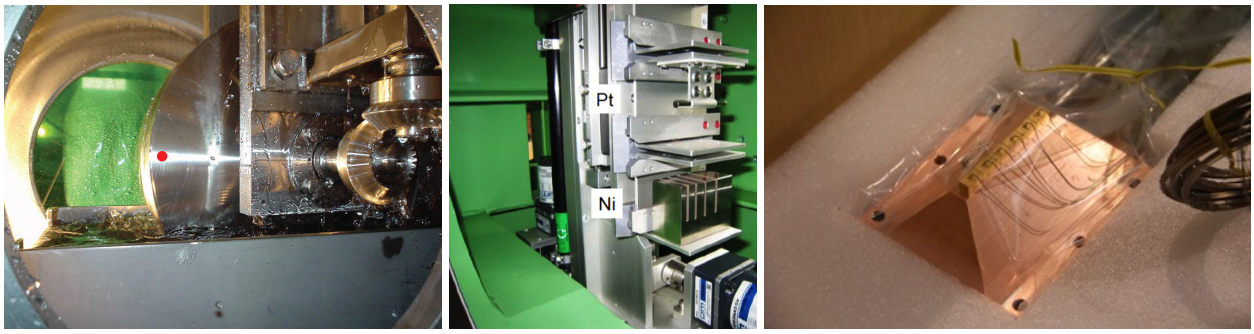

Figure 2.6: Pictures of T1 targets for generations. The left picture shows the nominal rotating Ni disk target soaking the cooling water. The red spot indicates the position of the incident beam. The center picture shows the Pt rod (top) and Ni block (bottom) targets. They were used when the maximal beam power was 5 kW. The right picture shows the Au square-bar target in a plastic bag. This Au target was used in this research.

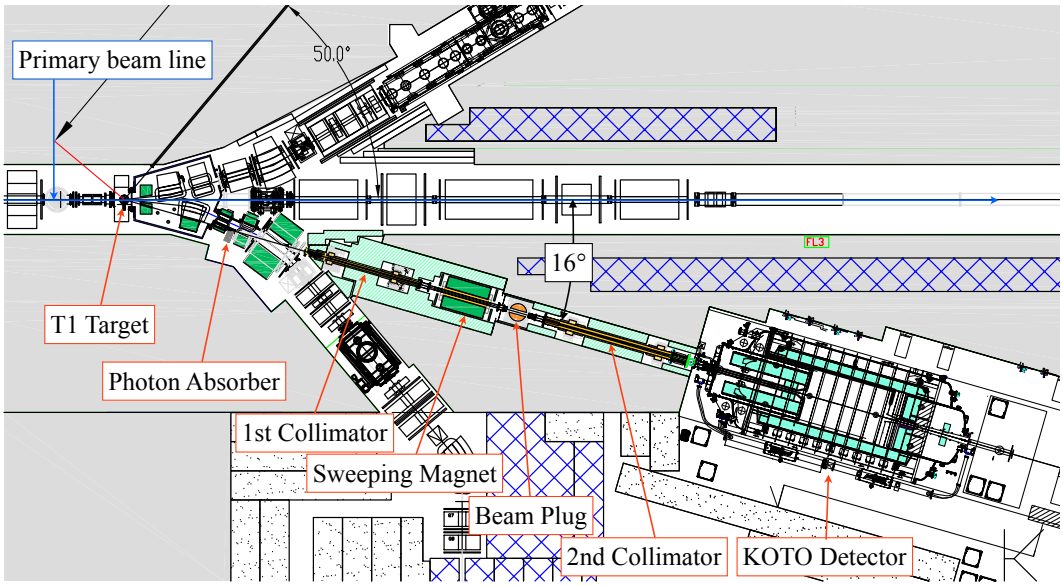

Figure 2.7: Schematics of the KL beam line.

the T1 target. Based on the beam survey performed in February 2010[3)], the number of K_L at the exit of the beam line was 1.94×10^7 per 2×10^{14} protons on target (POT) for the Ni T1 target and 4.19×10^7 per 2×10^{14} POT for the Pt T1 target[24].

2.3 CsI Electromagnetic Calorimeter

The CsI electromagnetic calorimeter was the main detector of the KOTO experiment. It consisted of 2716 undoped CsI crystals, stacked in a cylindrical shape of 2 m diameter and 500 mm (27 X_0) depth along the beam direction. We used crystals of two sizes in cross section: small (25 mm $\times$ 25 mm) and large (50 mm $\times$ 50 mm). As the size of 25 mm was smaller than the Moriere radius of CsI, 35.7 mm[1], we were able to use shower shape information to distinguish good electromagnetic showers from hadronic showers and merged showers which were originated from multiple incident photons. Each crystal was wrapped with a 13 μm thick aluminized mylar. Figure 2.10 shows a front view and a picture of the CsI calorimeter. We stacked 2240 small crystals in the central region and 476 large crystals in the outer region. The CsI crystals were read out by two models of Hamamatsu photomultiplier tubes (PMTs): R5364 for small crystals and R5330 for large crystals, which are summarized in Tab. 2.4. Both CsI crystals and PMTs were previously used in the KTeV experiment[27]. We put a 4.6 mm thick silicone cookie between the crystal and the photocathode of the PMT to improve the light transmission efficiency. We also put an UV transmitting filter to remove the slow component of the scintillation lights[4)].

It was essential for the operation in vacuum to reduce a heat generation. Cooling a heat in vacuum always causes a problem in the first place. In case of the KOTO experiment, the light

[3)] A beam power was 1 to 1.5 kW in this measurement.

[4)] The scintillation light from the CsI contains two components: one is fast (6 ns) and peak light wavelength is 310 nm, and the other is slow (35 ns) and its wavelength is 420 nm[1]. The UV bandpass filter around 310 nm enables us to use only fast component of the scintillation light.

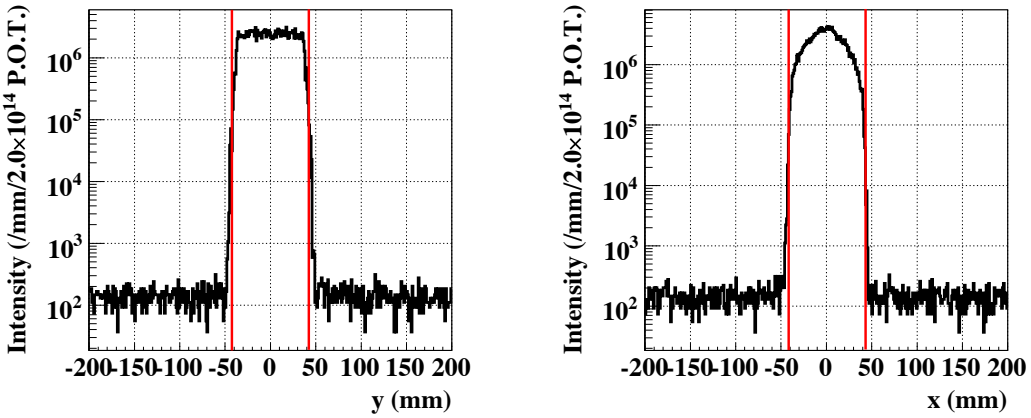

Figure 2.8: Estimated neutron profiles of the KL beam line at the beam exit in the vertical (left) and horizontal planes (right). They were obtained by the beam line simulation. The vertical red lines show 8.5×8.5 cm^2 region.

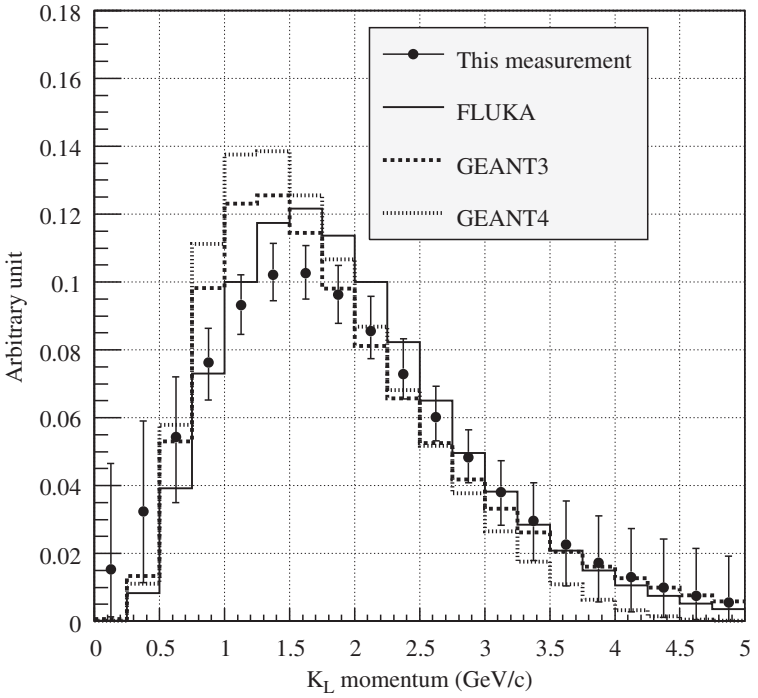

Figure 2.9: K_L momentum spectra at the exit of the beam line. Dots show the experimental data, and histograms show the simulation results obtained with FLUKA[25](solid line), GEANT3[26](dots) and GEANT4(dashed line). All histograms are normalized to be one when integrated. This figure is quoted from [24]

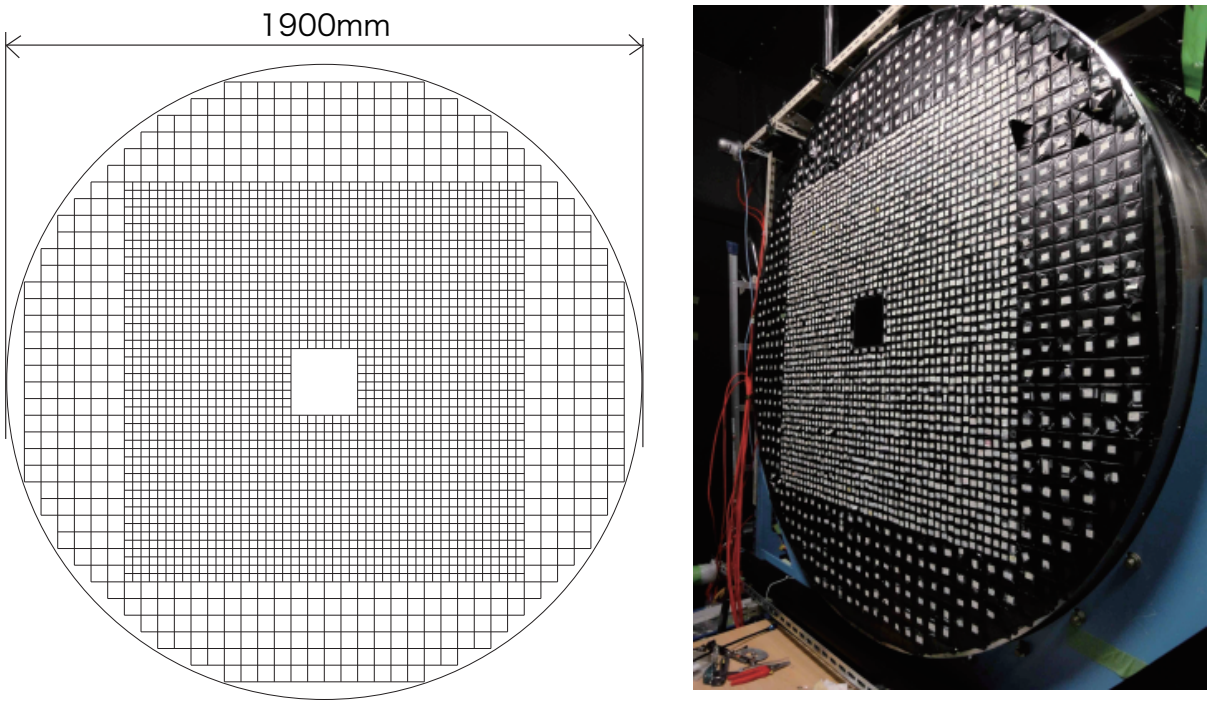

Figure 2.10: Front view (left) and picture (right) of the CsI calorimeter. The central square region is filled with small crystals and outer region is filled with large crystals.

yield of CsI crystals has large temperature dependence of -1.4 %/°C [1]; we had to keep the temperature of the CsI calorimeter around the room temperature. In addition, we confronted the low gain characteristics of the PMTs and the operation itself for thousands of channels in the small space. To realize the CsI calorimeter, we developed original high voltage system. The calorimeter also equipped a gain monitoring system to monitor the gain of whole channels during an operation. It guaranteed the system stability. The latter of this section, we describe the high voltage system and the gain monitoring system in particular.

2.3.1 High Voltage System of the CsI Calorimeter

As the calorimeter was located in vacuum, we had to operate all 2716 PMTs in vacuum. In addition, the low PMT gain was the problem to be solved. We developed the original high voltage system, which consisted of Cockcroft-Walton (CW) bases, preamplifiers, and controllers, to solve these problems. The details of them are described in this subsection.

CW base

A CW base is one type of PMT bases which supplies high voltage to PMTs. It contains a high voltage generating circuit which consists of an oscillator and a ladder of diodes and capacitors[28] (called "CW circuit"). Each step of the ladder provides voltage to a dynode. The most attractive feature is the lack of bleeder current, which results in low power consumption. On the other hand, the internal large-voltage oscillator and switching diodes can be sources of electrical noise.

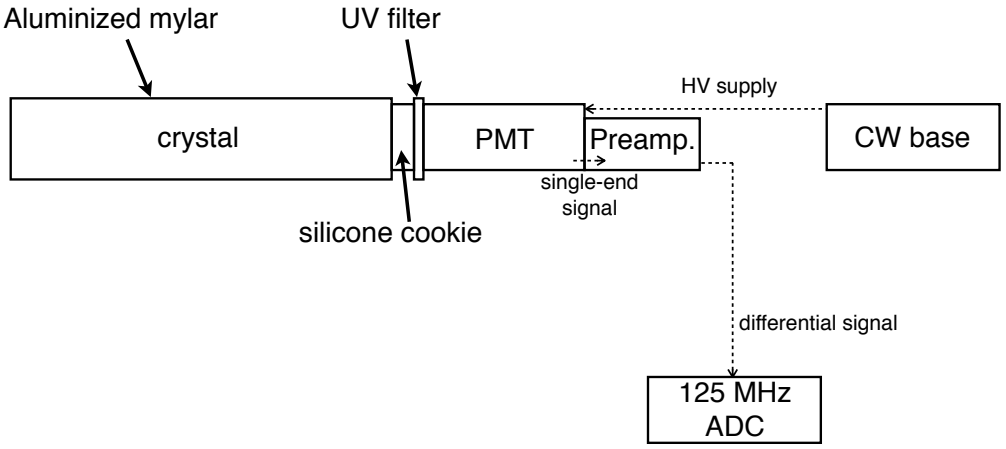

Figure 2.11: Components of the CsI calorimeter.

Table 2.4: Photomultiplier tubes specifications.

item	R5330	R5364
Quantity	476	2240
Photocathode Size	34 mm dia.	15 mm dia.
Photocathode Material	Bialkali	
Window Material	Quartz	
Spectral Response	185–650 nm	
Number of Dynodes	6	5
Voltage Divider Ratio	2:1:2:2:2:2:1	3:2:2:2:2:1
Typical Gain (-1500V)	2×10^4	8×10^3

Table 2.5: KOTO CW base specifications

Parameter	Value	Notes
MODEL No.	HPMC-1.8N-04	for R5364
	HPMC-1.8N-05	for R5330
Drive Voltage	+5 V	
Drive Current	12 mA	for −1500 V
Control Voltage	0 – +1.8 V	
Output Voltage	0 – −1800 V	
Monitor Voltage	0 – +1.8 V	0 – −1800 V
Internal Oscillator	100 V_{p-p}, 150 kHz	square-wave
Cathode Ripple	< 50 mV_{p-p}	−1800 V
Number of Ladders	12	

A picture of the two types of CW bases developed for the small and large CsI crystals is shown in Fig. 2.12. The aluminum rectangular boxes housed the CW circuit while the cylindrical sections contained the PMT socket and a built-in preamplifier described in the next paragraph. These two parts were connected via a shielded flat-cable. The CW base specifications are listed in Tab. 2.5

The schematics of the CW base circuit are shown in Fig. 2.13. As typical of any CW base, it contained an oscillator with a large voltage swing (150 kHz square oscillator with 100 V_{p-p}). To reduce the electrical noise induced by such component, the aluminum boxes enclosing the CW circuit were kept at a distance of 200 mm and 500 mm from their respective preamplifiers and PMTs. In addition, both the preamplifier and the PMT were housed in a metal electrostatic shield. RC filters were placed next to the diode capacitor ladder and inside the PMT socket to reduce the ripple at the output of the CW circuit. Figure 2.14 shows the remaining ripple at the cathode; the amplitude was less than 50 mV_{p-p} for an operation voltage of −1500 V. This corresponded to a gain deviation of less than 0.01 %, given the dependence of the PMT gain (G) from the output voltage(V) of $G \propto V^{0.7-1.2}$. Since the anode was not connected to the CW circuit directly, no observable ripple existed at the anode. The base power consumption was measured to be 60 mW for an output voltage of −1500 V and it increases linearly with the output voltage. The power consumption of the original KTeV base was 700 mW therefore we reduced it by a factor of 10.

Another important characteristic, which should be considered, was the vacuum tolerance. Electrical discharges are common in vacuum. The relation between pressure and discharge voltage is known as Paschenfs law. To prevent the bases from discharging, we filled the aluminum rectangular box containing the CW circuit with a compound resin. The measured maximum voltage before a discharge occurs at a given pressure is shown in Fig. 2.15. For typical CW bases operating of −1300 V under 1 Pa, shown as the black solid point in Fig. 2.15, electrical discharge was not a problem.

The CW bases helped us to operate the CsI calorimeter with the reasonable temperature in this research. It will shown in Sec. 3.2.

Preamplifier

The charge delivered by the PMT was small (∼ 0.5 μA/MeV) and fast (∼ 6 ns decay time). This signal was transferred via a 17-m-long cable and digitized at an ADC module described in Sec. 2.6.1. A preamplifier with the specifications listed in Tab. 2.6 was designed to ensure the

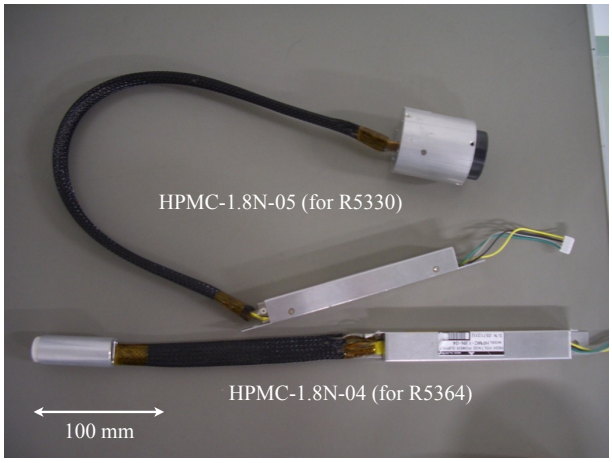

Figure 2.12: Picture of two types of the CW bases developed for the KOTO experiment; the electronics for the base is contained in the rectangular aluminum box, and connected via a shielded flat-cable to a cylindrical aluminum receptacle for the PMT socket and preamplifier.

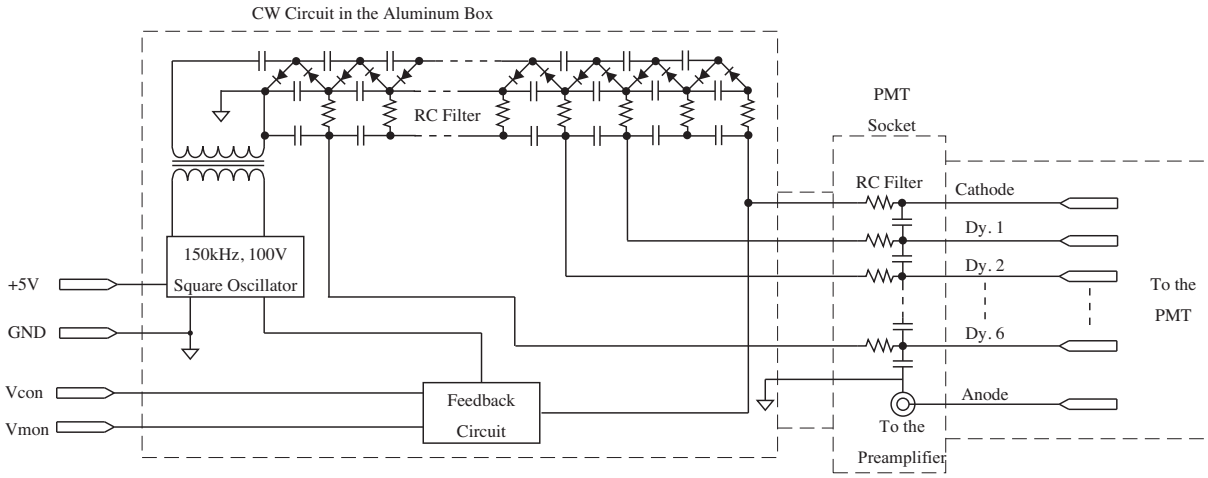

Figure 2.13: Circuit schematics for the HPMC-1.8N-05 base. The schematics for the HPMC-1.8N-04 base are almost the same except for the number of dynode stages and for the RC filter in the PMT socket being dropped. The dashed lines around the components represent the electric shield.

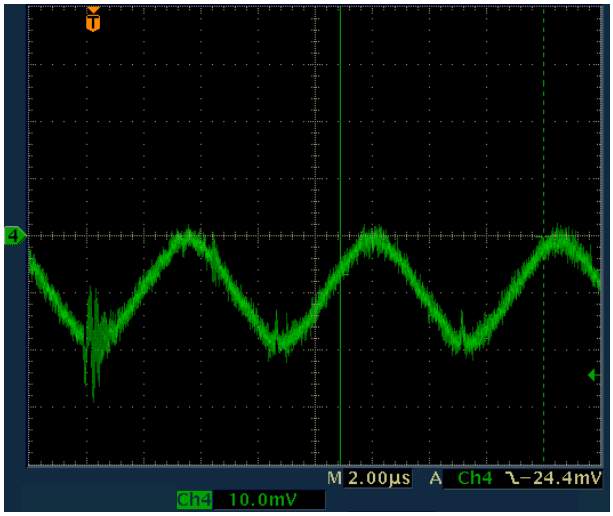

Figure 2.14: Scope capture of the remaining ripple at the cathode output. In this measurement, the cathode is connected to ground via a 510 pF capacitor and a 1 MΩ resistor in series; the voltage drop across the resistor is shown.

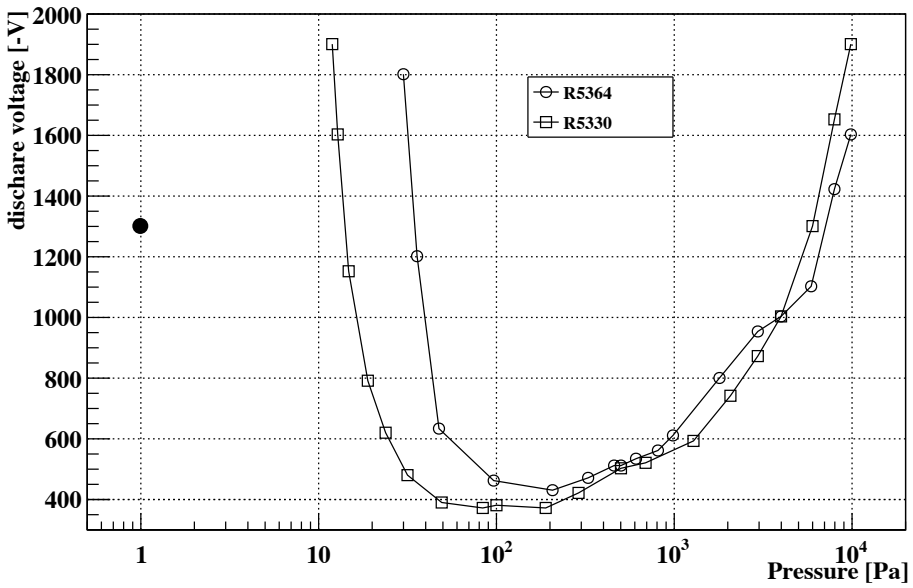

Figure 2.15: Discharge voltage as a function of the pressure for small (open circle) and large (open box) crystal PMTs. The black solid point represents the typical CW bases operating voltage (-1300 V) and pressure inside the vacuum chamber (1 Pa). The maximum operating voltage is -1750 V.

efficient propagation of the signal from the PMT to the ADC module. The required noise level of the preamplifier output was set to be less than 180 μV_{rms} in order to allow the detection of 1 mV (equivalent to 1 MeV) signal from the noise. To accommodate for the individual variability in the PMT gain (standard deviation / mean $\sim$ 30 %) and in the CsI crystals light yield ($\sim$ 20 %), we used three different amplification values, as summarized in Tab. 2.6. Figure 2.16 shows a schematic diagram of the preamplifier. This circuit was mounted on a 17 $\times$ 22 mm^2 printed circuit board (PCB), as shown in Fig. 2.17, and connected to the PMT via a 20-mm-long coaxial cable. Figure 2.18 shows the preamplifier output together with its filtered pulse as simulated with SPICE[29].

To protect the preamplifier against electric discharge, we used three 30 Ω resistors[30] in par-

Table 2.6: Preamplifier specifications. The amplification values are for a 50 Ω input impedance.

Item	Value	Notes
Output	differential	
Dynamic Range	1 mV to 1 V	
Amplification	20	for R5330
	41	for R5364
	67	for low gain R5364
Noise Level	< 180 μV_{rms}	
Decay Time	< 25 ns	faster than the 10-pole filter

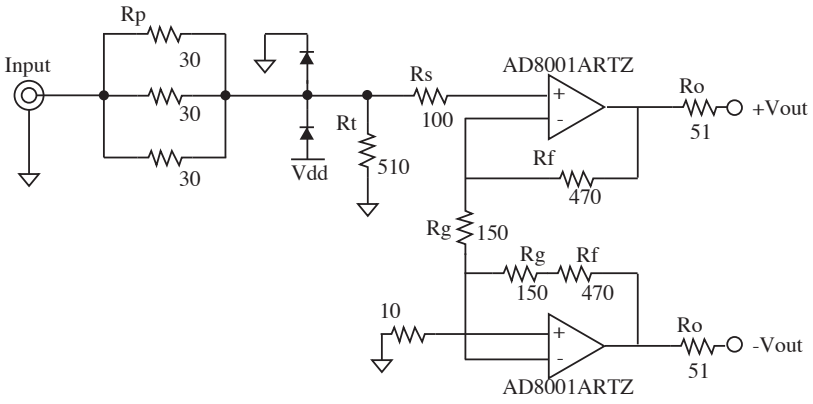

Figure 2.16: Schematics of the preamplifier with a gain of 41. Power supply lines are not drawn.

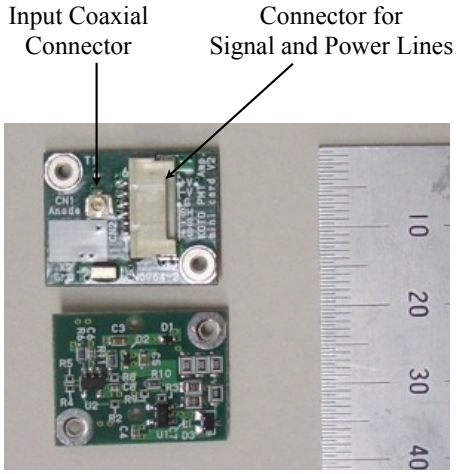

Figure 2.17: Photo of the front (top) and back (bottom) of the preamplifier card. The input signal is carried in via a coaxial connector mounted on the front plane of the card.

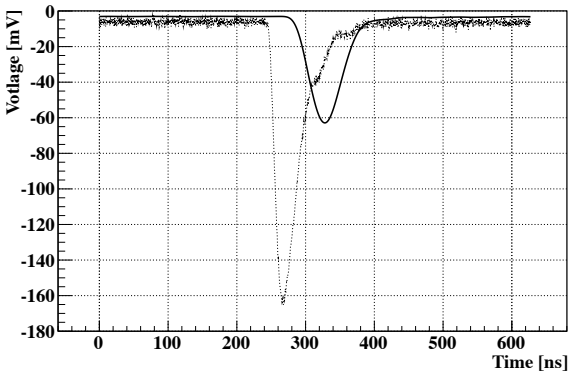

Figure 2.18: Preamplifier output pulse (dotted line) for a cosmic ray going through a CsI crystal overlaid to a SPICE simulation of the ADC board shaped output (solid line).

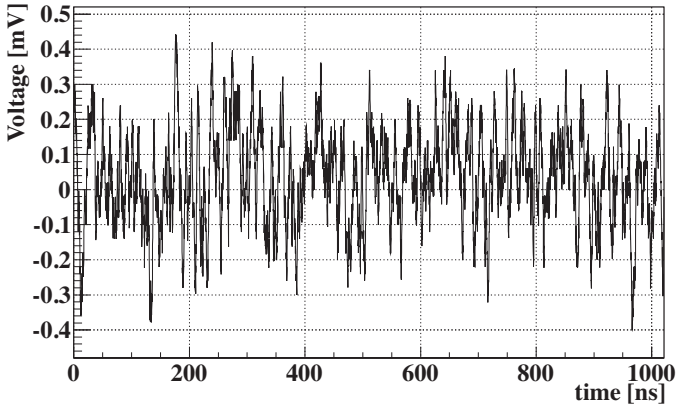

Figure 2.19: Example of the noise at the preamplifier output measured with a digital oscilloscope when the CW base was generating a voltage of −1500 V.

allel as protection resistors, considering a reduction of a burden of the resistors themselves and a redundancy. This keeps the output pulse narrow while realizing the tolerance against discharge. The two following diodes protect the op-amp against overvoltage. The R_s resistor protects the op-amp against overcurrent. This circuitry has successfully survived discharges at voltages as high as 1750 V.

In order to certify the preamplifier together with the CW base, we measured the noise level of all bases at the output of the preamplifiers. In this measurement, the differential signals from the preamplifier were converted to single-ended signals using a converter circuit consisting of two op-amps (LMH6628[31] and ADA4899-1[32])[5)]. Figure 2.19 shows an example of oscilloscope captures for such measurements. Figure 2.20 compares the noise level distributions when the CW bases were turned off and when they output a voltage of −1500 V. The three peaks corresponded to the three values of preamplifier gain. A few percent of the bases had noise levels above the requirement of 180 μV_{rms} if paired to the highest gain preamplifier. In that case they were used in combination with lower gain preamplifiers. This explains the cutoff at 180 μV_{rms} in Fig. 2.20. Finally all bases satisfied the requirement.

High Voltage Controller

To adjust and monitor the high voltage of each PMT channel, we developed the HV control system shown in Fig. 2.21. It consisted of twelve controller modules connected to a PC via a Universal Serial Bus (USB) interface. Each module sent signals and power to sixteen custom made boards, called Back Boards, via 50-pin flat cables. Each Back Board in turn controlled up to sixteen PMTs. The whole system was located inside the vacuum vessel, just behind the calorimeter.

The system was designed to power individual CW bases and preamplifiers. The high voltage of each channel was able to be adjusted and monitored in 1 V step. If a discharge or a malfunctioning condition was detected for a given channel, its power supply was turned off. The temperature of Back Boards, the supply voltages and currents drawn by CW bases and preamplifiers were also read and logged every 1 s to monitor the system stability. A schematic view of the overall system is shown in Fig. 2.22.

The firmware of the controller module instantiated a Human Interface Device (HID) class to communicate with the PC. The HID class is a USB standard classes and supported by almost all operating systems. The software running on the PC was based on a Graphical User Interface (GUI)

[5)] This converter circuit was the same as the input section of the ADC module described in Sec. 2.6.1.

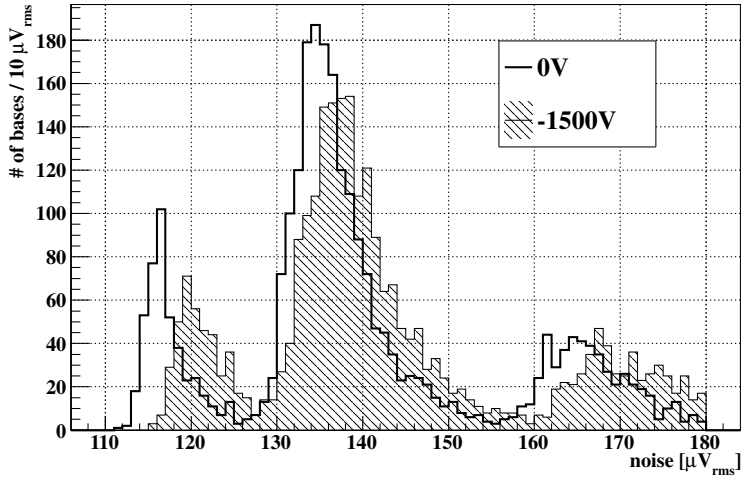

Figure 2.20: Distributions of noise levels at the preamplifier output with the CW bases. The bold histogram shows the noise level distribution when the CW bases were turned off, and the hatched histogram represents the same distribution when the CW base output was set to -1500V. The peaks on the left are for the R5330 PMT, the peaks in the middle are for the R5364 with a gain of 41, and the peaks on the right are for the R5364 PMT with a gain of 67.

written using a Python Tkinter scripts. Figure 2.23 shows a screen shot of the GUI. The supply voltage of each channel was able to be controlled by clicking on the screen. Current and past value of numerous monitoring parameters were also able to be accessed in this way.

2.3.2 Gain Monitoring System

The CsI calorimeter equipped a gain monitoring system using a scintillation light from a liquid dye excited with a pulse laser[6)]. The intensity of the scintillation light was monitored by a PIN photo diode. The scintillation light was distributed to all PMTs with quartz fibers. Schematics of the gain monitoring system is shown in Fig. 2.24. Normalizing the PMT output by the PIN photo-diode output, we were able to monitor the stability of each PMT gain. The wavelength of the secondary light from the liquid dye distributed from 360 nm to 400 nm, and the decay constant was near the CsI scintillation light. To distribute the secondary light to all PMTs uniformly, we used four "bowling balls" shown in Fig. 2.25. Each bowling ball contained a glass case with a diameter of 25 mm which was filled with the liquid dye at its center. More than 700 secondary quartz fibers per ball looked the secondary light emitted from the liquid dye. The secondary quartz fibers fed the secondary light to the downstream surface of the CsI crystals; the light entered the PMT cathode surfaces primarily by reflection from the upstream surface of the crystals.

2.4 Veto Counters

Another important feature of the KOTO experiment was a veto counter system. We use fourteen veto counters as shown in Fig. 2.1. At the moment of this research, the counters which located

[6)] 355 nm Nd-YAG laser.

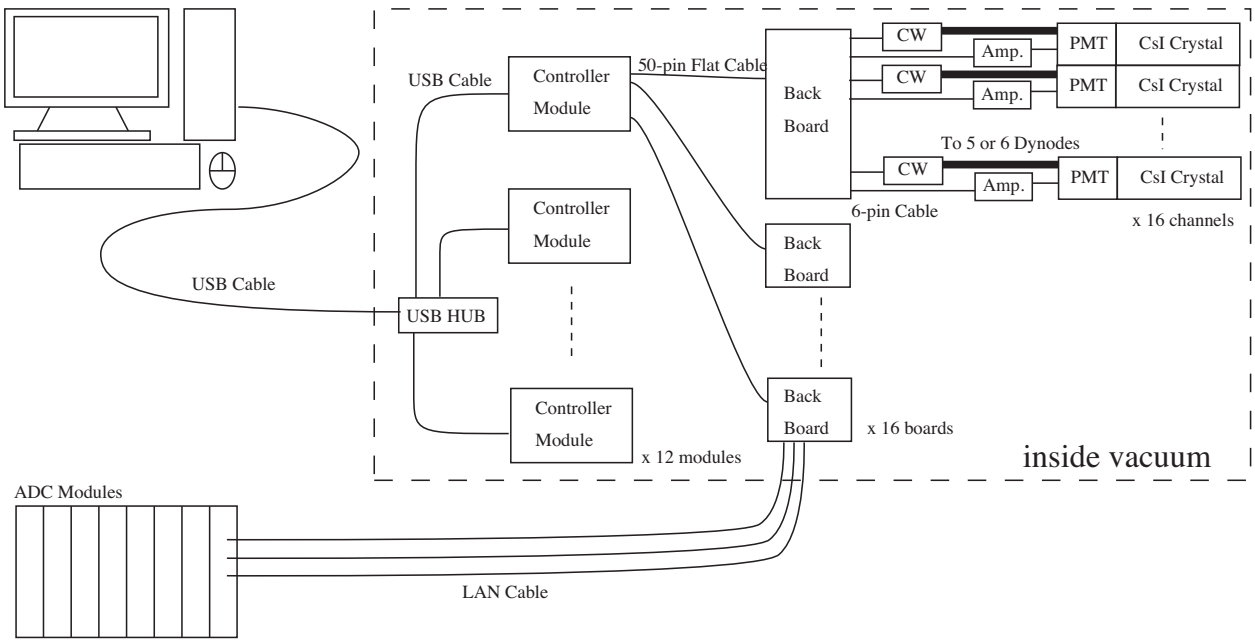

Figure 2.21: Overview of the HV control system. For the analog signals sent by the Back Boards to the ADC modules, we made the unconventional choice of using LAN cables.

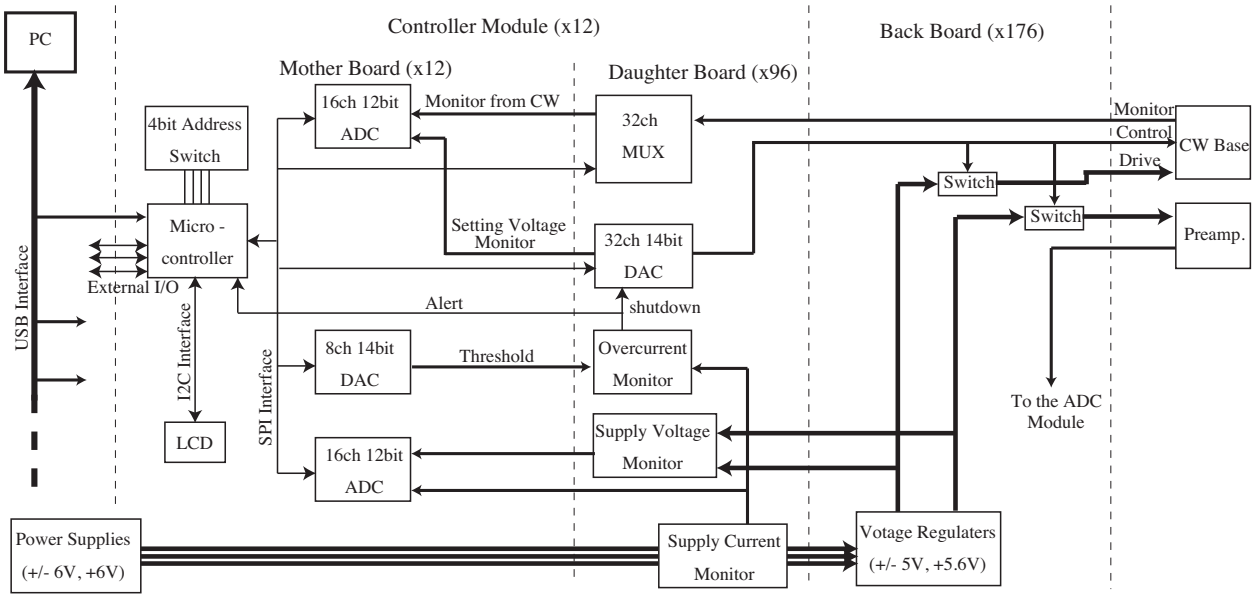

Figure 2.22: Schematic view of the HV control system. Thick(thin) lines indicate analog(digital) signals. The system comprises twelve controller modules. Each module is addressable via a 4-bit address switch. A Liquid-Crystal Display (LCD) is used for debug purposes. Switches mounted on the Back Board are used to turn off power to individual CW bases and preamplifiers.

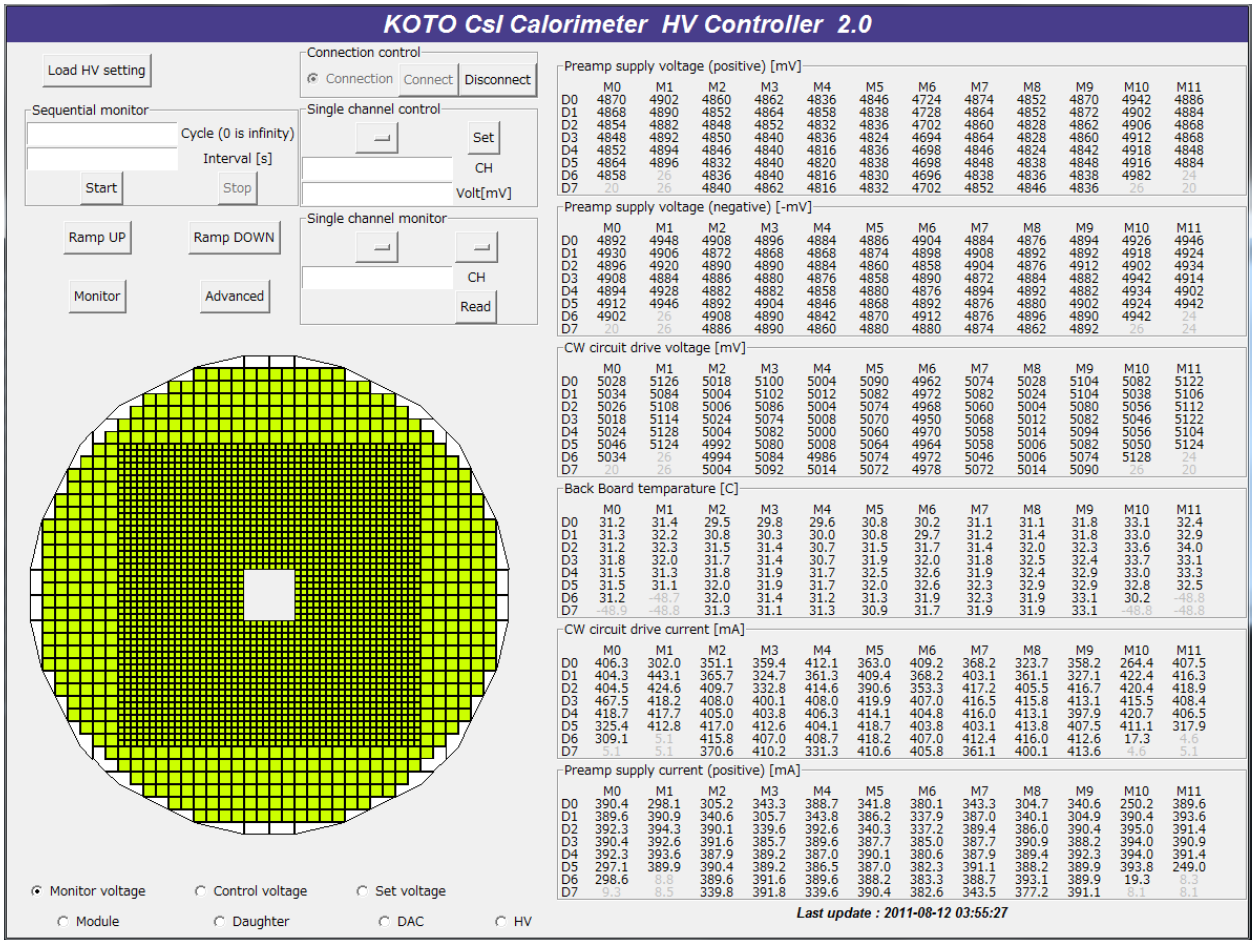

Figure 2.23: Screenshot of the GUI for the HV controller system. The fields at the top left of the screen are for manual controlling and monitoring. The front view of the CsI calorimeter shows the operating status of each individual channel. The numbers to the right show specific monitored values and are usually refreshed every 1 s. The history of a specific value is obtained by clicking on that number.

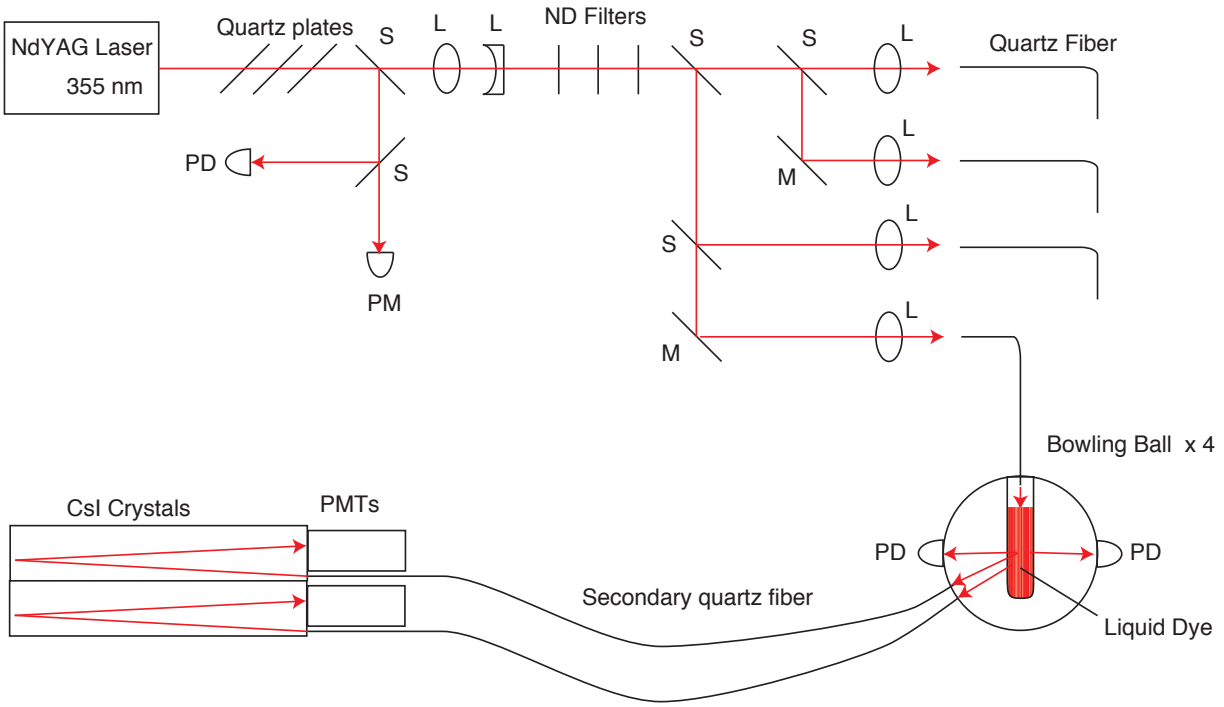

Figure 2.24: Sketch of the gain monitoring system. Nd-YAG laser that emits 355 nm light is used as a primary light source. The laser light excites the liquid dye, and the lights from the dye are distributed to PMTs. Quartz plates are put to reduce the laser intensity; S: splitter; M: mirror; L: focusing lens; PD: photodetector; PM: power meter. We use three ND filters in order to fine-tune the laser intensity.

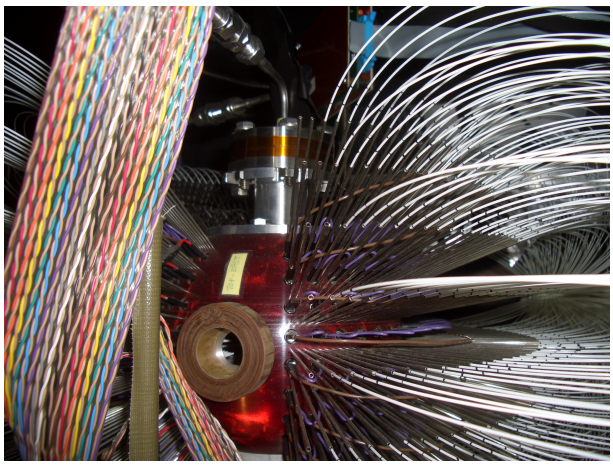

Figure 2.25: Bowling ball for the gain monitoring system. The central red ball contains the liquid dye. Many while thin fibers are secondary quartz fibers.

in the vacuum chamber were installed. This section describes mainly Main Barrel and Charged Veto, which were used in the main analysis of this thesis. The former covered the largest solid angle among our photon veto counters, and the latter detected charged particles hitting on the CsI calorimeter.

2.4.1 Main Barrel

Main Barrel (MB), one of the photon veto counters, surrounds the decay region cylindrically. It was used in the E391a experiment and is used as is without upgrade in an early stage of the experiment. It aims at detecting extra particles from K_L decays in the decay region. The total length along the beam axis was 5.5 m and the inner diameter was 2 m. Figure 2.26 shows a three dimensional drawing of MB. MB consisted of 32 modules, and each module consisted of 45 alternate layers of a plastic scintillator plate and a lead sheet. The inner 15 layers, called "inner module", had lead sheets with the thickness of 1 mm, and the outer 30 layers, called "outer module", had lead sheets with the thickness of 2 mm. In both the inner and outer modules, the thickness of plastic scintillator sheets was 5 mm. The total thickness of the module corresponded to 14 X_0. The cross-sectional view of one module is shown in Fig. 2.27. The scintillation lights originated in the plastic scintillator were absorbed by wavelength shifting fibers (WLSFs) and transferred to two PMTs on the both ends of the module. WLSFs were embedded in and glued to each scintillator plate with the pitch of 10 mm. We used the 1-mm-diameter WLSFs with a multi cladding structure (KURARAY Y-11), and the PMTs with high quantum efficiency for green light (E329-EGP PMT). The typical light yield was 14 photoelectron per MeV (p.e./MeV) at the middle along the module. There were four PMTs equipped for one module; from upstream and downstream ends of inner and outer modules independently[33].

2.4.2 Charged Veto

Charged Veto (CV) is the main charged particle veto counter located in front of the CsI calorimeter. It identifies whether incident particles hitting the CsI calorimeter are charged particles or neutral particles. It consisted of two layers: one was placed 5 cm upstream of the calorimeter, and the other was placed 30 cm upstream of the calorimeter. Each layer consisted of 3-mm-thick and 69-mm-wide plastic scintillators (Saint-Gobain BC404). The front plane consisted of 48 strips and the rear plane consisted of 44 strips; they were aligned as shown in Fig. 2.28. The side edges of all strips had an angle of 30° to the beam direction in order to eliminate the gaps between adjacent strips. Scintillation lights were read with two Multi Pixel Photon Counters (MPPCs, HAMAMATSU S10943-5947(X)) from both ends via WLSFs (KURARAY Y11). Figure 2.30 shows the light yield distribution of front and rear plane of CV[34]. The mean deposit energy from penetrating charged particle was 0.5 MeV, and typical light yield was 19 p.e. per 100 keV. Measured timing resolution for penetrating charged particle was 1.29 ns. The scintillation strips were aligned on a 0.8-mm-thick carbon fiber reinforced plastic (CFRP) plate, which was supported at the edge with an aluminum hexadecagonal ring. The readout electronics were also equipped at the ring. Due to the scintillation strips alignment, one MPPC read scintillation lights traveling a short distance, and the other MPPC read scintillation lights traveling a longer distance. Figure 2.29 is a photo of the construction.

We adopted MPPCs for the photo sensors of CV because of their smallness and high photo detection efficiency; however, the performance of a MPPC was known to be sensitive to temperature. The both gain and photo detection efficiency of a MPPC had temperature dependence of

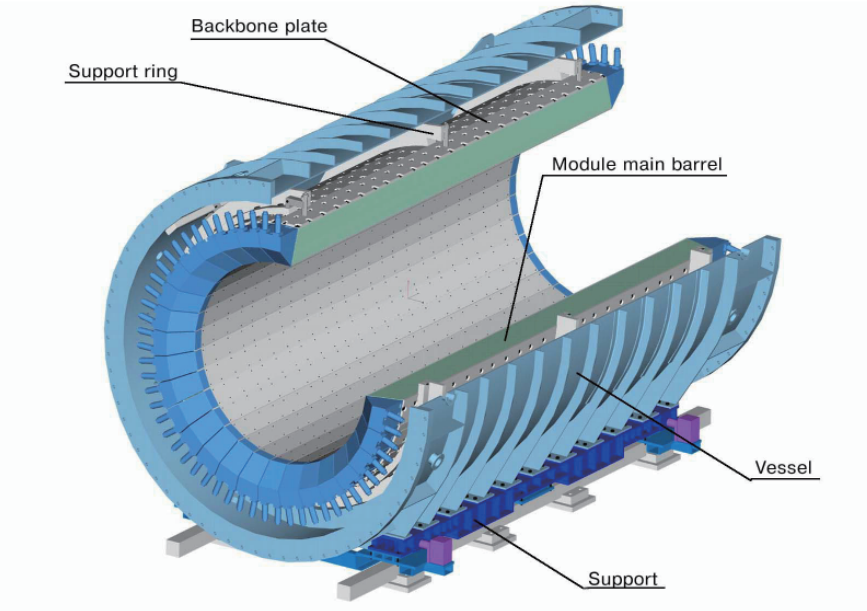

Figure 2.26: Three dimensional drawing of Main Barrel and its support structure. The MB modules are supported by the vacuum vessel.

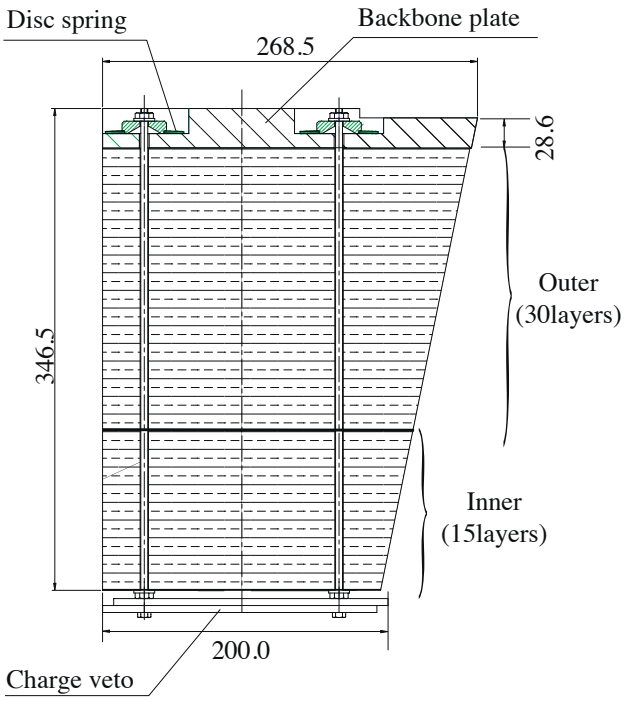

Figure 2.27: Schematic view of a MB module[33].

approximately -5 %/°C. In addition, as the temperature rises, a dark count noise increases, which is made by thermal excitation and has a same pulse shape as one photoelectron signal. We developed a MPPC with a peltier cooling element in order to keep the temperature constant. The peltier transferred heat from the MPPC to the aluminum ring, which equipped water cooling pipes. Monitoring all MPPCs' temperature and controlling the current flow of all peltiers continuously, we achieved small temperature fluctuation of less than 0.1°C. Figure 2.31 shows the feedback circuit for the peltier.

2.4.3 Other Veto Counters

Other Photon Veto Counters

Here, other photon veto counters than MB are described. Front Barrel (FB, [33]) and Neutron Collar Counter (NCC, [35]) suppress K_L decays that occur upstream of the decay volume. FB consisted of sixteen modules that were made of 59 layers of alternating lead and plastic scintillator plates (16 X_0 thick and 2.75 m long). NCC was made of 152 pure CsI crystals and was placed at the entrance of the decay volume, surrounding the neutral beam. NCC was prepared not only to detect photons from K_L decays, but also to measure the flux and energy spectrum of halo neutrons. Outer Edge Veto (OEV) surrounds the calorimeter to fill gaps between the calorimeter and the support structure. It consisted of alternating lead and plastic scintillator plates. CC03 was made of pure CsI crystals and was placed along the beam hole of the CsI calorimeter. CC04-CC06, located downstream of the CsI calorimeter, surround the neutral beam to detect photons passing along the beam. CC04 located inside the vacuum, and CC05 and CC06 located outside the vacuum. Those were made of pure CsI crystals. Beam Hole Photon Veto (BHPV)[36] catches photons inside the beam region. BHPV was placed at the downstream end of the detector system, and started at

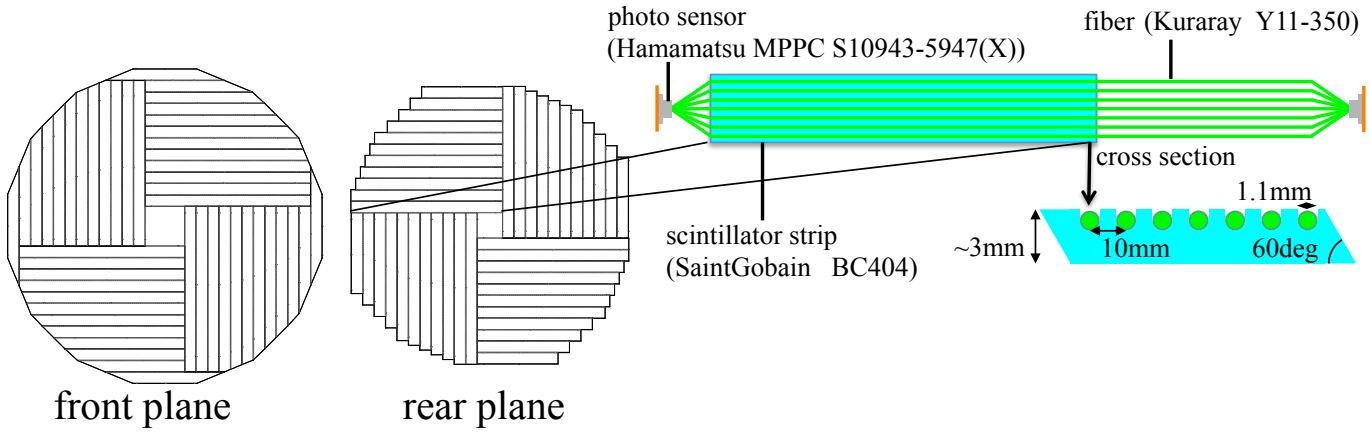

Figure 2.28: Schematic view of CV.

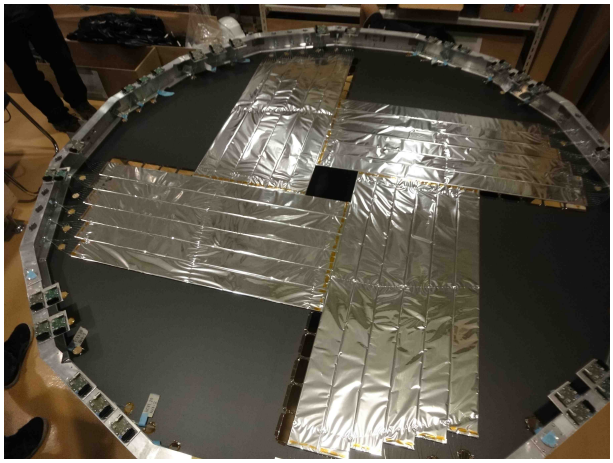

Figure 2.29: Picture of CV construction. Scintillator strips were lapped with the aluminized mylar and put on the black CFRP plate. Aluminum support structure surrounding the scintillators equipped electrical components such as MPPCs and preamplifiers.

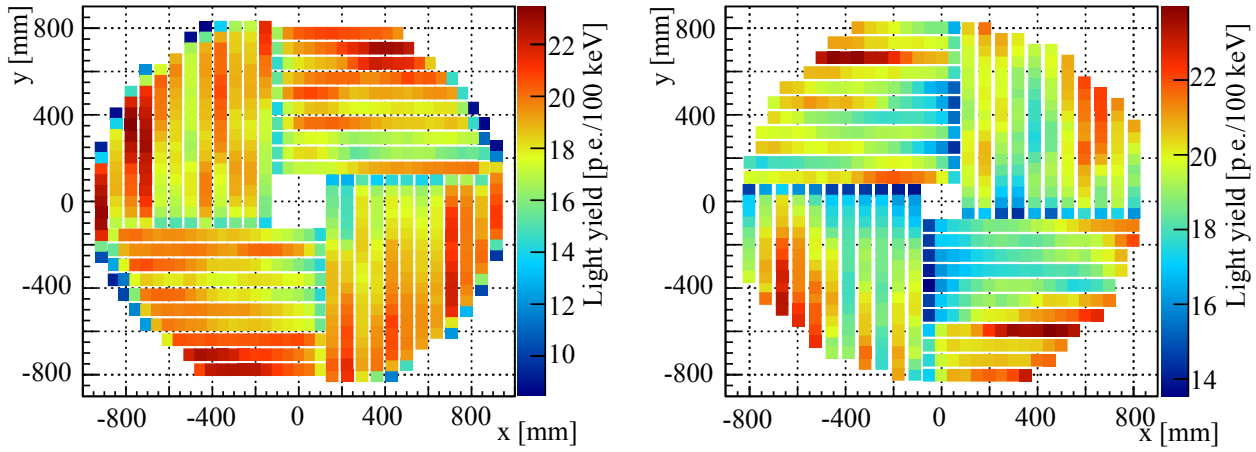

Figure 2.30: Measured light yield distribution of CV as a function of the hit position. Figure on the left shows the front plane and figure on the right shows the rear plane.

5.8 m downstream of the calorimeter. The BHPV consisted of 25 Cerenkov counter modules. Each module was composed of a lead plate, a stack of aerogel tiles, a mirror, a Winston cone, and two PMTs. The lead plate converts photons to pairs of electrons and positrons, and the aerogel tiles emit Cerenkov light with the electrons and positrons. The mirror and the Winston cone guide the Cerenkov light to the PMT. By using Cerenkov light, BHPV is not sensitive to heavy particles in the beam core.

Other Charged Veto Counters

Here, the charged particle veto counters other than CV are summarized. HINEMOS covers the inner surface of NCC, Barrel Charged Veto (BCV) covers the inner surface of MB, and Linear Charged Veto (LCV) covers the inner surface of the CsI calorimeter. Beam Hole Charged Veto (BHCV) is placed inside the beam in front of the BHPV. HINEMOS, BCV, and LCV were made of plastic scintillators and WLSFs read with PMTs. For BHCV, eight plastic scintillators and PMTs were used.

2.5 Other Apparatus

2.5.1 Vacuum System

The decay region should be evacuated to the vacuum level of 10^{-5} Pa to suppress interactions of neutrons in the beam with residual gas, which may generate secondary π^0s and fake a signal. It is, however, difficult to evacuate down to the 10^{-5} Pa level with the detector because of a large amount of out-gassing. To realize this vacuum level, the detector region was separated from the decay region with thin membranes; the detector region is evacuated to the vacuum level of 1 Pa. A vacuum system is shown in Fig. 2.32. The detector region was separated into two regions furthermore: upstream and downstream, because there were some materials in the upstream region emitting an outgas which attacks the silicone cookies used in the CsI calorimeter, which is described in Sec. 4.2.2.

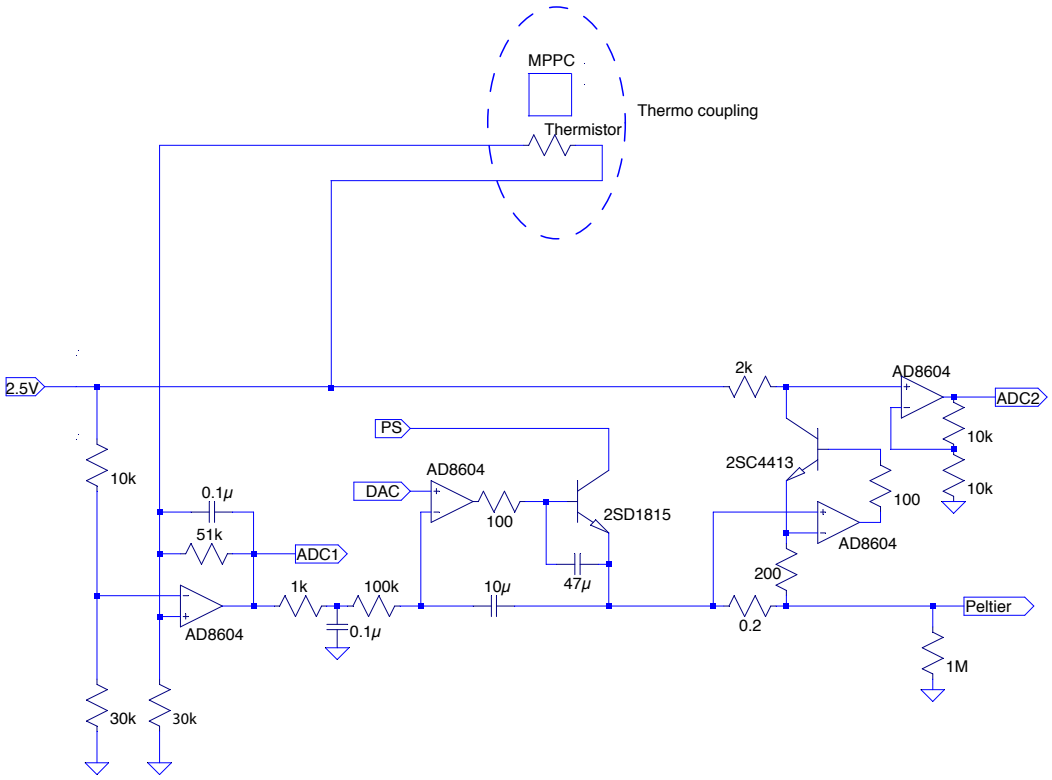

Figure 2.31: Temperature control circuit for CV. A thermistor is located on the same PCB as the MPPC, and all the other components are putted on the control board outside the vacuum chamber. The output of a digital-to-analog converter (DAC) determines the setting temperature for the MPPC, which basically set at 10 °C. PS denotes the power supply for the peltier. The monitored temperature is digitized at the ADC1 and used as a feedback input signal at the second stage which adjusts the current flow fed to the peltier. ADC2 monitors the current flow for the peltier.

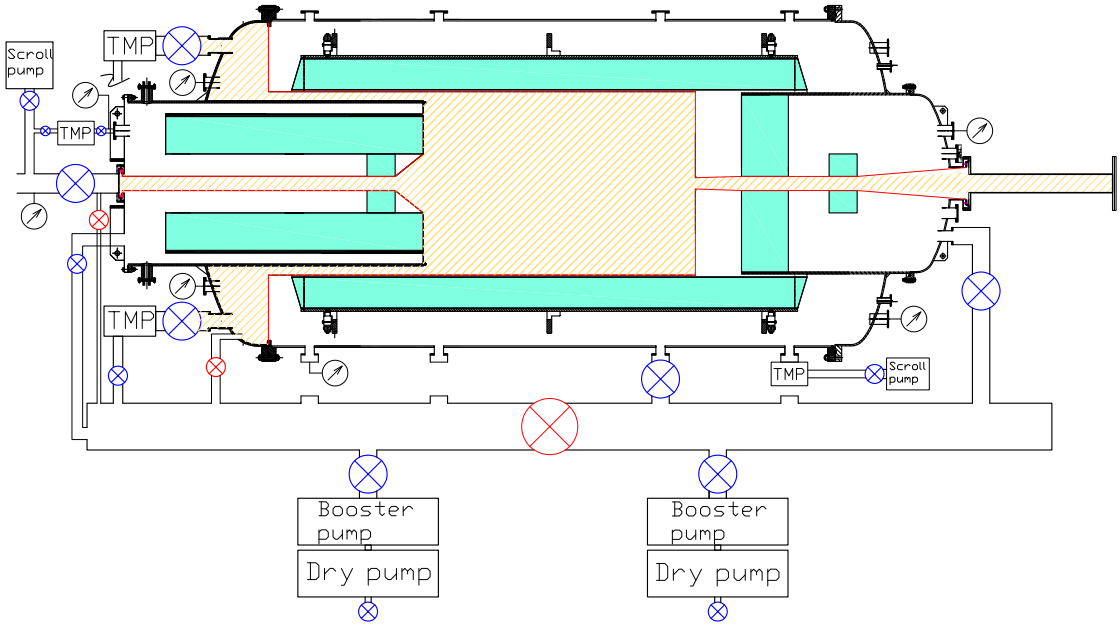

Figure 2.32: Schematics of the vacuum system. The hatched region was the high vacuum region, and the hollow regions including detector materials was the low vacuum region. The red ⊗ marks represent closed bulbs and the blue ⊗ marks represent open bulbs.

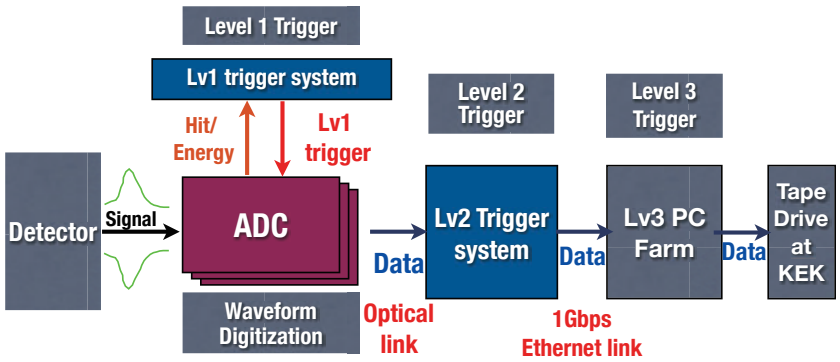

Figure 2.33: Data flow of the DAQ system.

2.5.2 Cooling System

Water cooling system was also installed. This system consisted of water pipes made by copper and chillers. Heat generated at the PMT bases and the preamplifiers inside the vacuum chamber was guided to the cooling pipes with heat conducting materials. Cooling water whose temperature was 10°C flowed in the copper pipes. It transferred the heat to the outside of the vacuum chamber. In the engineering run, the water cooling system was used for the CsI calorimeter, NCC, CV, MB, CC03, and CC04. The temperature monitor system consisted of thermocouples measured the temperature of the CsI upstream and downstream surface, PMTs of each detectors, water cooling pipes, and the vacuum chamber walls.

2.6 Data Acquisition System and Readout

The data acquisition (DAQ) system consisted of two parts: a sampling ADC module and a trigger system. The ADC module digitized analog signals from all detectors; the trigger system determined whether we accept or reject the events, compressed data size, and transferred data to a storage. All analog signals from the detectors were converted to differential signals by preamplifiers or converters, and were transmitted via Category 6 Ethernet cables to the ADC modules. The ADC module digitized differential signals and generated some information processing the digitized data. It transmitted digitized waveforms and processed information (*e.g.* the sum of pulse height) to the trigger system via an optical link. Figure 2.33 shows the data flow of the DAQ system.

2.6.1 ADC Module

We used two types of ADC modules: one type of them was an ADC with 125 MHz sampling rate and 14-bit resolution, and the other type was an ADC with 500 MHz sampling rate and 12-bit resolution. The counters in the beam line (BHCV and BHPV) were read with 500 MHz ADC modules to get through their high counting rate, and other detectors including the CsI calorimeter were read with 125 MHz ADC modules. If we simply read a signal from a CsI crystal with a sampling rate of 125 MHz, we would take only one or two samples on the rising edge and cannot measure the pulse shape precisely. We thus put a low pass filter before digitization to widen and

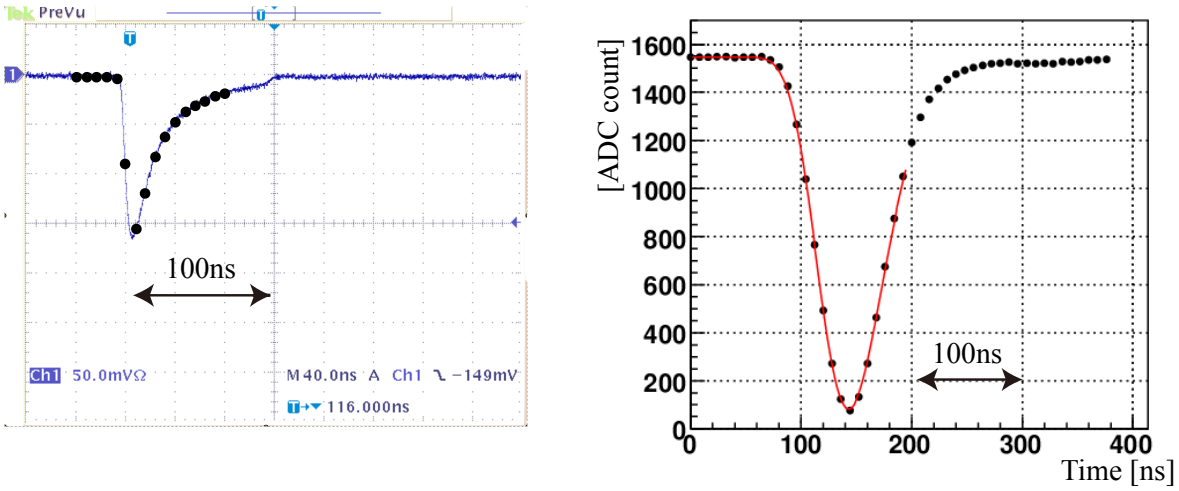

Figure 2.34: Waveforms with and without the low pass filter to show an advantage of the pulse shape widening. Figure on the left shows a signal from a CsI crystal recorded by an oscilloscope. The black dots show an example of a 125 MHz sampling. Figure on the right shows a recorded pulse shape with the filter. The number of samples on the rising edge after the widening is eight or nine, while it is only one before the widening.

shape the pulse to be a gaussian. The full width of half maximum of the widened pulse was approximately 50–60 ns. Figure 2.34 shows waveforms with and without the low pass filter.

Figure 2.35 shows a picture of the 125 MHz ADC module. On the front-panel, there were sixteen analog input channels, a digital I/O to receive a system clock and triggers, and two pairs of optical links to send data to L1 and L2 trigger boards described in the next paragraph. There were 10-pole low pass filters between analog inputs and ADC chips. The digitized waveforms were processed by a Field Programmable Gate Array (FPGA) chip on the board and were temporarily stored in a pipeline buffer in the FPGA to wait for a trigger decision.

2.6.2 Trigger System

The trigger system consisted of three layers: L1, L2, and L3 trigger system. L1 trigger system made trigger decisions with digitized pulse information every cycle of 125 MHz system clock. It gathered energy or hit information recorded by the ADC modules, and calculated total energy information or hit information of each detector. The trigger condition was able to be changed flexibly by changing the firmware of the FPGA on the L1 trigger board. In conceptual design, for example, the L1 trigger system made decision based on the total energy deposit in the CsI calorimeter, CV, MB, and NCC. L1 trigger required the total energy deposit in the CsI calorimeter to be larger than a given threshold, and the total energy deposit of each CV, MB, and NCC to be smaller than certain thresholds.

L2 trigger system processed data event by event. Here, the event was defined as a group of

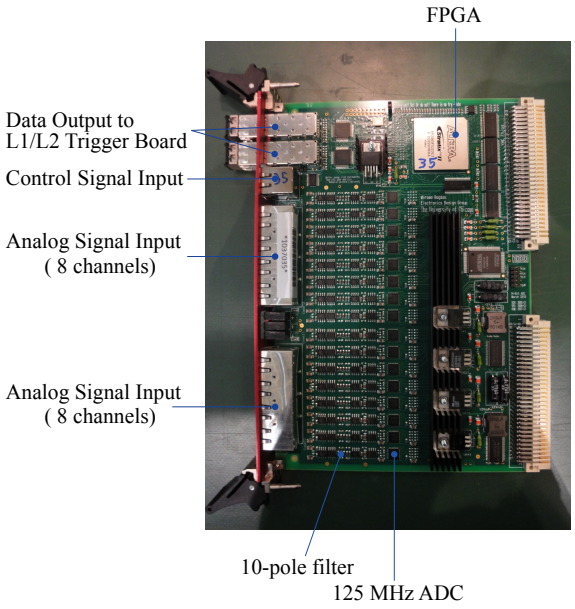

Figure 2.35: Picture of a 125 MHz ADC module. It has sixteen analog input channels. An input differential signal goes to the 10-pole low pass filter, and the output from the filter is digitized by 125 MHz ADC.

waveform data in specific time window, which was 64 samples of the 125 MHz system clock. The L2 trigger logic was also able to be changed flexibly. For example, the L2 trigger system calculated the center of energy deposit (COE) in the CsI calorimeter. The COE made by $K_L \to \pi^0\nu\overline{\nu}$ does not located in the central region in the CsI calorimeter due to the missing energy taken by the two neutrinos. Requiring large COE enabled us to reduce a trigger rate without signal acceptance loss. Each event firing the L2 trigger was stored in buffer memories on the L2 trigger board, and data in the buffer were sent to L3 PC farm via 1 Gbps Ethernet once per spill.

L3 trigger system, which consisted of the PC farm, collected all segments of a single event from all L2 trigger boards and formats a single event data. In conceptual design, L3 trigger system made the trigger based on information by complicated calculation, such as the number of clusters in the CsI calorimeter. L3 trigger system was also able to compress the data size by removing data of channels which had no energy deposit. Processed data was sent from the PC farm located in J-PARC to the storage located in KEK Central Computing System (KEKCC).

Chapter 3

K_L Flux Measurement

We constructed almost all the detector system of the KOTO experiment in December 2012, and performed an engineering run in January 2013 to check the detector operation including the readout system, and peripheral slow control systems. In addition to the commissioning, we had another important purpose in the engineering run. We aimed at measuring the K_L beam flux with our actual detector system and establish the analysis method such as detector calibration, K_L reconstruction, with understanding our detector performance. From this chapter, we describe the K_L flux measurement.

3.1 Measurement Principle

We measured the K_L flux using $K_L \to 3\pi^0$, $K_L \to 2\pi^0$, and $K_L \to 2\gamma$ decays. These decay modes have common event configurations in the final state: all the decay products are photons, and once all of them are detected with the CsI calorimeter, no other particle exists. We were able to get three individual results and make a comparison among them.

$K_L \to 3\pi^0$ and $K_L \to 2\pi^0$ were reconstructed from six and four photons detected in the CsI calorimeter, respectively. In the reconstruction, the number of possible combinations of the two photon pairs is fifteen for $3\pi^0$ and three for $2\pi^0$. The decay vertex position was calculated from the energies and positions of the two photons of each pair by assuming the nominal π^0 mass. To decide on the photon pairing, the variance of the reconstructed vertex positions, named "pairing χ^2_z", was calculated for all possible combinations, and then we selected the pairing with the smallest χ^2_z. $K_L \to 2\gamma$ was reconstructed from two photons by assuming the nominal K_L mass. The details of the reconstructions and selections are described in Chap. 5

In the $K_L \to 3\pi^0$ analysis, we required the number of photons in the CsI calorimeter to be six. Figure 3.1 shows an illustration of a $K_L \to 3\pi^0$ decay in the detector and an example of event displays of $K_L \to 3\pi^0$ candidates. There is no other considerable process that makes six or more photons from K_L decays: it allowed us to use information of only the CsI calorimeter without veto counters to analyze $3\pi^0$ events. In the $K_L \to 2\pi^0$ and $K_L \to 2\gamma$ analyses, on the other hand, we required the number of photons to be four and two, respectively. Figure 3.2 shows event displays of a $2\pi^0$ event and a 2γ event. $K_L \to 3\pi^0$ decays were the main background because four or two photons from them can hit the CsI calorimeter, and the branching fraction of $K_L \to 3\pi^0$ is more than 200 times larger than that of both $K_L \to 2\pi^0$ and $K_L \to 2\gamma$. To suppress the $3\pi^0$ background, we used MB as a photon veto. $K_L \to \pi^+\pi^-\pi^0$ and $K_L \to \pi^\pm e^\mp \nu$ (called "$Ke3$") also

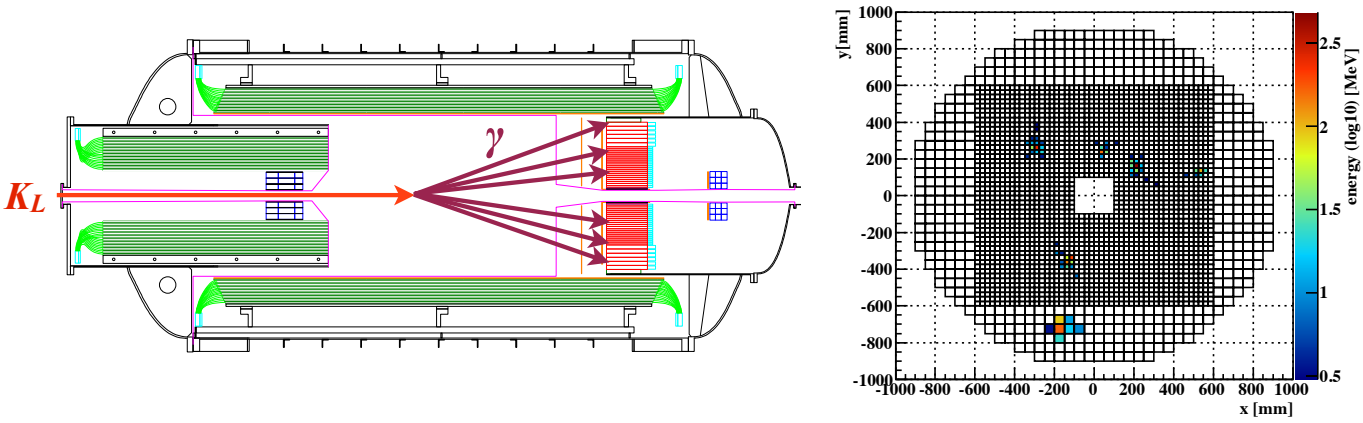

Figure 3.1: Side view (left) and event display (right) of a $K_L \to 3\pi^0$ event.

had to be considered since they were able to create four and two activities in the calorimeter. To suppress these background, we used CV as a charged particle veto. Figure 3.3 shows a side view of a $K_L \to 2\pi^0$ event and Fig. 3.4 shows side views of background events for $K_L \to 2\pi^0$. In the K_L flux measurement, we did not use the other veto counters to reduce the systematic uncertainty due to them, as they were under commissioning in the engineering run period.

3.2 Measurement Conditions

In the engineering run, there were twelve missing and unstable channels in the CsI calorimeter due to unstable connection in the signal lines. We addressed them by masking the corresponding channels both in the experimental and the simulated data.

Figure 3.5 shows the history of the vacuum level of four regions in the vacuum chamber. The decay region was evacuated to a level of 10^{-3} Pa and the detector regions were evacuated at a level of 1 Pa in this period. The achieved pressure levels were worse than the design values, and we considered it had been caused by the remaining moisture in the detector materials, because we achieved the designed vacuum level (10^{-5} Pa) in the following run performed from March to May 2013.

Figure 3.6 shows the history of temperature of several regions. The temperature of all regions was increasing during the run approximately +0.5°C/day. It was due to a increase in temperature of the experimental area itself because of insufficient air conditioning. We thus needed to correct the gain of the CsI calorimeter due to the temperature dependence of the CsI crystals' light yield as described in Sec. 5.2.1.

During K_L flux measurement, the beam power was 15 kW. Spill length was 2 s and the beam repetition cycle was 6 s. The typical proton intensity was 1.8×10^{13} POT per spill.

3.3 Run

The engineering run was performed from 7th January 2013 to 17th January 2013. We took various kind of data set for shakedown and study of the detector and DAQ system. We describe the run

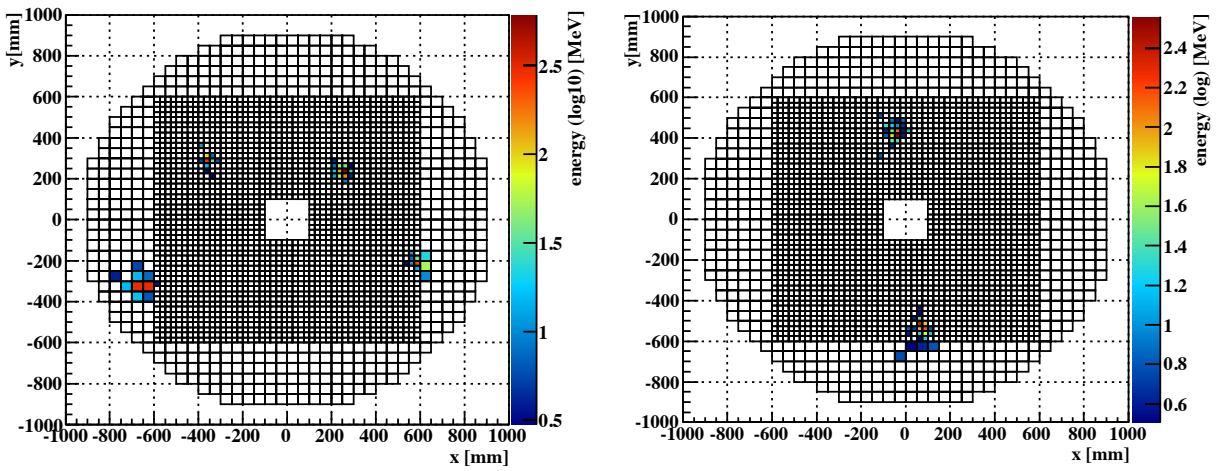

Figure 3.2: Event display of a $K_L \to 2\pi^0$ event (left) and a $K_L \to 2\gamma$ event (right).

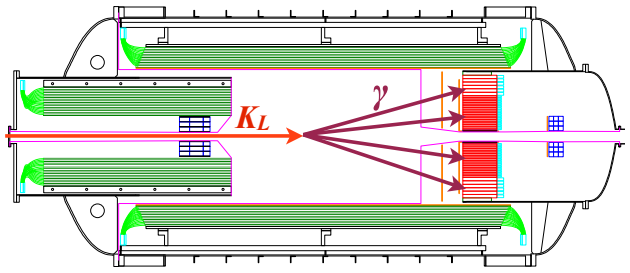

Figure 3.3: Side view of a $K_L \to 2\pi^0$ event.

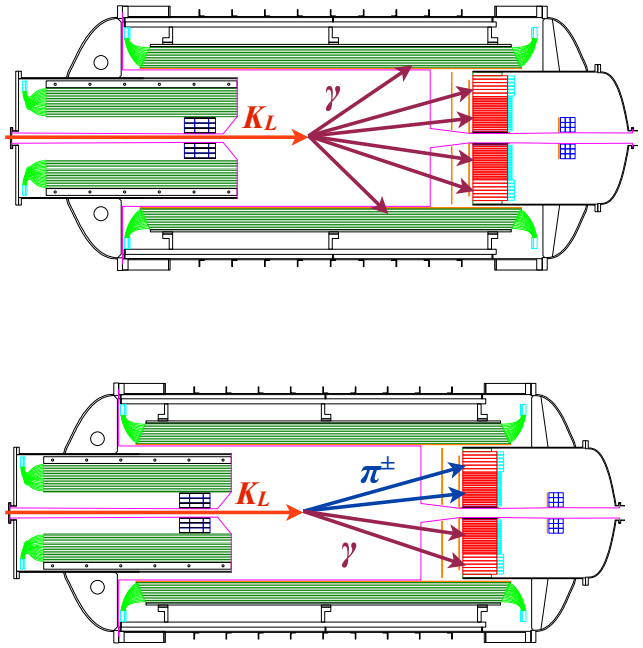

Figure 3.4: Side views of background events for $K_L \to 2\pi^0$ from $K_L \to 3\pi^0$ (top) and $K_L \to \pi^+\pi^-\pi^0$ (bottom).

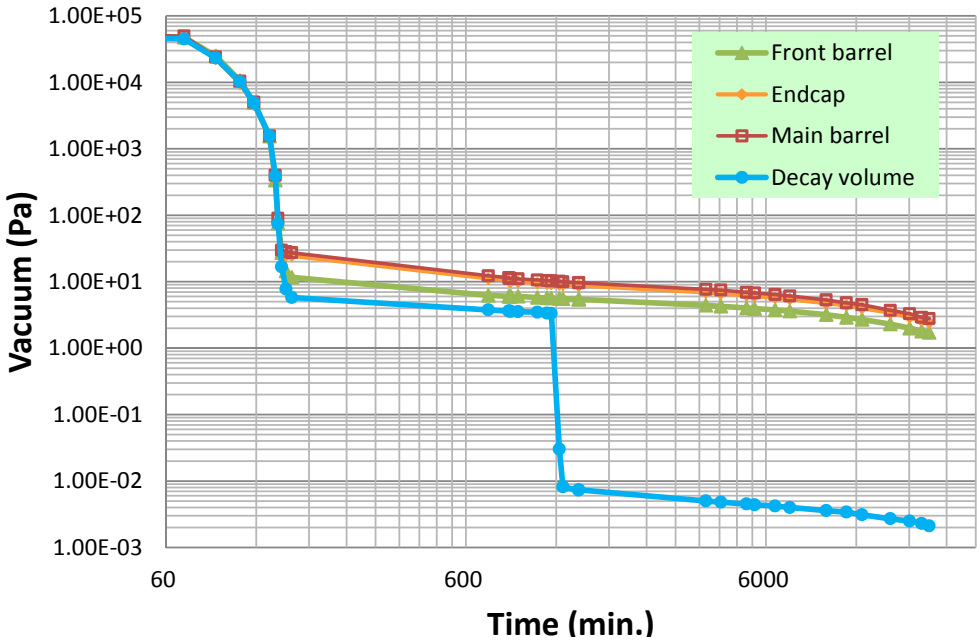

Figure 3.5: Histories of the vacuum level of four sampling points. Green line: around FB; Yellow line: downstream of the CsI calorimeter; Red line: around MB; Blue line: the decay region.

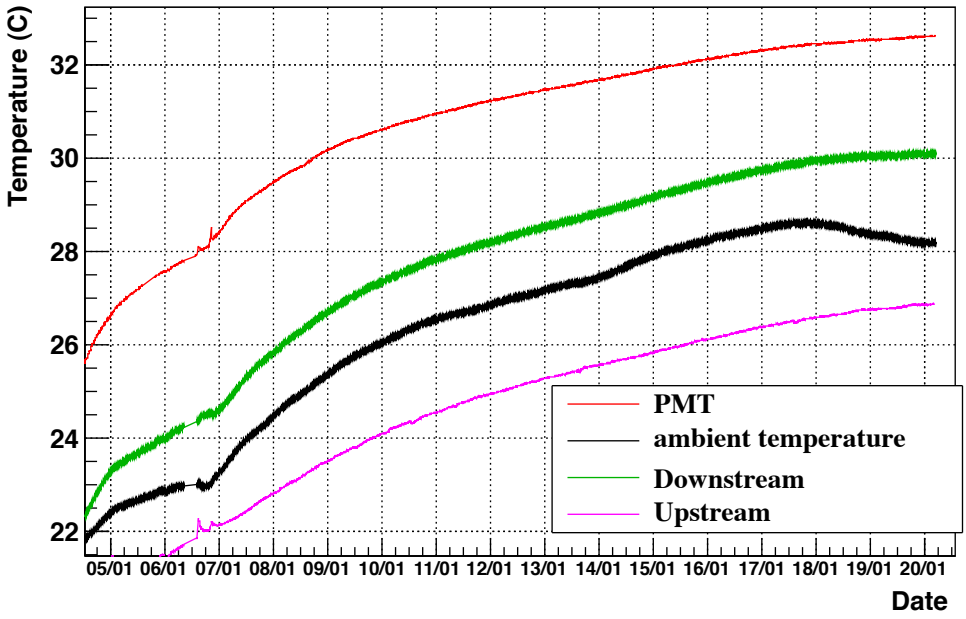

Figure 3.6: Histories of the temperature of four sampling points. Red line: a certain PMT of the CsI calorimeter, Black: the wall of the vacuum chamber, Green: the downstream surface of the CsI calorimeter, Purple: the upstream surface of the CsI calorimeter.

conditions that related to the K_L flux measurement.

3.3.1 K_L Flux Measurement Run

This run aimed at accumulating $K_L \to 3\pi^0$, $K_L \to 2\pi^0$, and $K_L \to 2\gamma$. We mixed five trigger conditions; Half Et as the main trigger, laser trigger, LED trigger, clock trigger, and cosmic-ray trigger, each of which is described below. The last four triggers were called external trigger.

Half Et Trigger

The online trigger required the coincidence between a left (south) half of the CsI calorimeter and the right (north) half of the CsI calorimeter. The L1 trigger system summed up ADC counts of all left half and right half channels clock by clock. They were called "Left Et" and "Right Et", respectively. When Right Et made a peak which was higher than the anteroposterior points and also exceeded a preset threshold, the L1 trigger system checked whether Left Et exceeded the threshold or not. If these conditions were satisfied, the L1 trigger system made a trigger. This trigger mode was called "Half Et".

The objective signals certainly deposited the same energies on two halves of the CsI calorimeter because they had no missing energy. Half Et trigger collected the objective signals effectively. The preset threshold for both halves of the calorimeter was 300 MeV, and the resultant trigger rate was 34 kHz. When we set a simple trigger such that the total deposit energy of the CsI calorimeter was more than 600 MeV, the trigger rate got 63 kHz. This demonstrated the effectiveness of the Half Et trigger.

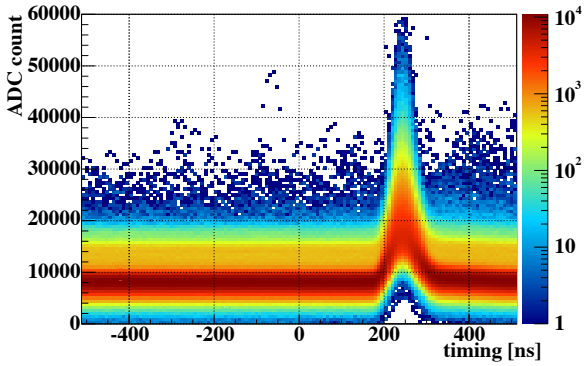

Figure 3.7: Sum of ADC count of all channels of the CsI calorimeter as a function of the trigger time. In this plot, approximately 7×10^4 events are superimposed. The baseline of them fluctuated slowly therefore this baseline of the histogram had vertical width.

External Trigger

Laser trigger :
: The PMT gain of the CsI calorimeter was monitored by the gain monitoring system described in Sec. 2.3.2. The laser flashed with 5 Hz constantly.

LED trigger :
: The MPPC gain of the CV was monitored by an LED monitoring system. Eight blue LEDs were attached on the CV support frame, and their light was fed to each MPPC via a clear fiber. The LEDs flashed with 10 Hz constantly.

Clock trigger :
: We took data with a 10 Hz clock constantly to take pedestal events.

Cosmic ray trigger :
: We placed several trigger counters to detect cosmic rays for FB, MB, and the CsI calorimeter. Coincidence signals of them generated triggers for cosmic ray. The trigger rate was 3–4 Hz.

3.3.2 Accidental Run

This run aimed at recording accidental hits in the detector system. The online trigger logic was same as the Half Et trigger, but the time window was opened 64 clocks (512 ns) or 96 clocks (768 ns) ahead of the time. Figure 3.7 shows the sum of ADC count of all channels of the CsI calorimeter as a function of timing. Signals at 250 ns generated a Half Et trigger and opened the data window, which we used for the analysis, from 0 to 512 ns in usual. In the accidental run, the data window was shifted to the range from -512 ns to 0 ns or -716 ns to -256 ns. There was a micro time-structure of the instantaneous rate of the beam yield, and the rate of accidental activities was affected by the structure. Both analysis data and accidental data contain the same accidental rate because the same trigger condition was used and the time-structure commonly affected. Data taken by this condition were used for the accidental overlay described in Sec. 4.3.

3.3.3 Calibration Run

Cosmic ray run :
: We accumulated cosmic ray signals for calibration purpose while the beam was stopped. The online trigger required that the total energy deposit of each detector exceeded a threshold. We used total energy information of the CsI calorimeter, MB, NCC, and CC04.

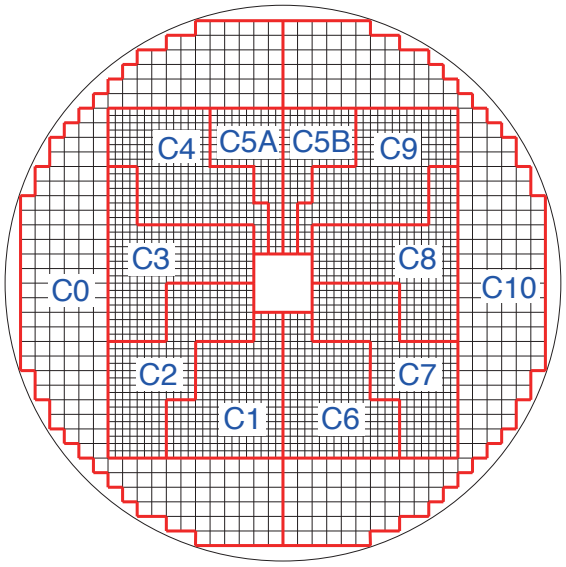

Figure 3.8: Division of the CsI calorimeter for the region counting trigger (front view).

Beam Muon Run :

The KL beam line had a beam plug, made of brass with its thickness of 600 mm, that stopped most of the neutral beam. By closing the plug, we enhanced the portion of muons in the beam. We accumulated penetrating muons from NCC, CV, the CsI calorimeter to CC04 by requiring the coincidence between NCC and CC04. This muon beam was also used for calibration purpose.

Al Target Run :

We performed a special run, called "Al target run", for the calibration of the CsI calorimeter. In the Al target run, an aluminum (Al) target with a thickness of 5 mm and a diameter of 100 mm was inserted in the beam at $z = 2795$ mm. This Al target was hung with a wire at the downstream end of FB[1)]. Using $n + A \to \pi^0 + A'$ reaction, we accumulated π^0 samples whose vertex position was fixed at the Al target position. Figure 3.9 illustrates π^0 production at the Al target. As the trigger condition, we divided the calorimeter into twelve regions as shown in Fig. 3.8, and required the number of regions which had more than 250 MeV energy deposit, to be equal to or more than two. This trigger mode was called "Region Counting". On top of this, we used online veto in order to reduce the trigger rate and accumulate high statistics in short time because the π^0 events with our interest did not have activities in the veto counters.

[1)] The target was normally placed at 74 cm above the beam and moved to the beam core by rolling down the wire in the Al target run.

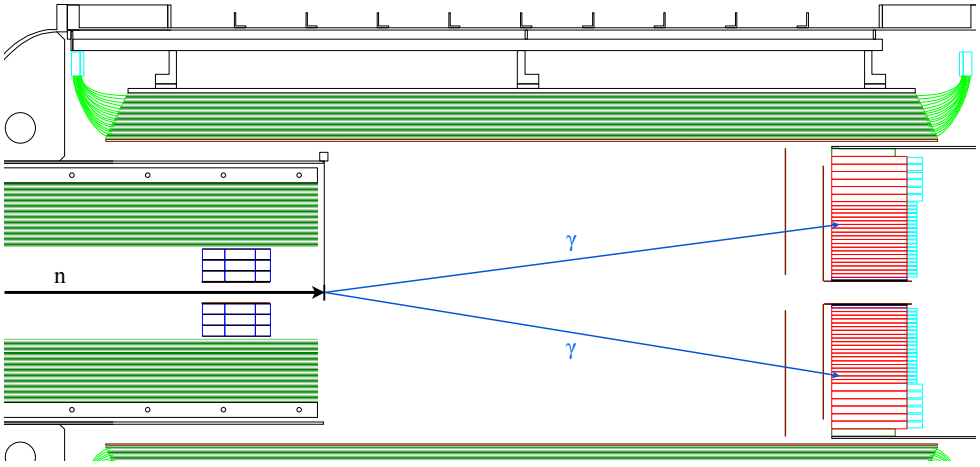

Figure 3.9: Side view of an Al target run event.

Chapter 4

Monte Carlo Simulation

This chapter describes the Monte-Carlo (MC) simulation for the KOTO experiment. The MC simulation is needed to estimate the acceptance of objective signals and to evaluate the contamination of background events from other K_L decays; therefore, the realistic simulation model had to be developed.

For the basement of the MC simulation, we adopted the Geant4 package[37, 38][1)]. Geant4 is a toolkit for the simulation of the passage through matter. It has been designed and constructed physics models which include interactions between particles and materials. They has been commonly used by various particle experiments and continuously varidated their reproducibilities of experimental data. As the interaction between particles and materials is common for all phenomena, we considered that the use of Geant4 was a straightforward approach for the development of our simulation model.

The detector response was inherent for each detector, such as the position dependence of the light yield, photon propagation time in detector materials, electrical noise, and accidental activities. They affected output signals in the real experimental data. We considered these effects should be implemented as realistic as possible to improve its reproducibility.

There were three stages in the simulation processes. As the first stage of the simulation, K_L decay was simulated. K_L beam was generated near the collimator end. Each K_L flied to the downstream, decayed to the preset decay mode, and generated specified secondary particles. In the second stage, the interactions between detector materials and the hit particles were simulated. We used Geant4 to simulate these first two stages. At the final stage, we simulated the detector response in detail.

Information of the energy deposit and the hit timing of each detector were stored with the same format as the experimental data, so that both experimental and simulated data were able to be analyzed by identical analysis programs.

4.1 GEANT4 Simulation

4.1.1 K_L Beam

The first stage of the simulation was to generate a K_L at the beam exit which was 20 m downstream from the T1 target. The following asymmetric Gaussian was used for the momentum distribution

[1)] geant4.9.5.p02

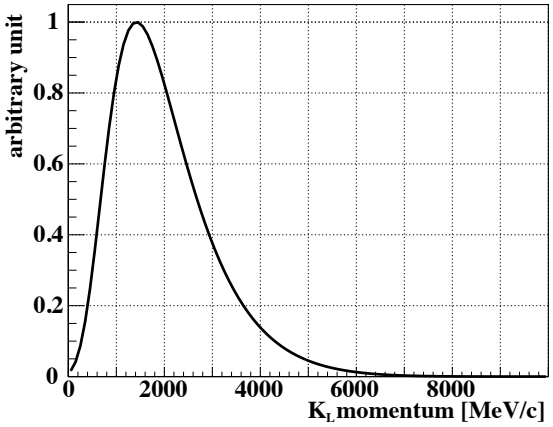

Figure 4.1: K_L momentum distribution expressed by the function of Eq. 4.1.

of generated K_L:

$$\frac{dN}{dp} = N_0 \exp\left[-\frac{(p-\mu)^2}{2\sigma^2}\right], \tag{4.1}$$

$$\sigma = \sigma_0(1-(A+S\times p)(p-\mu)), \tag{4.2}$$

where p is the momentum of K_L, N_0 is an arbitrary normalization factor, μ is the peak of the distribution, σ_0 is the standard deviation of the gaussian shape, and A and S are the offset and the slope that represent characteristics of the asymmetric shape, respectively. The parameters were determined by fitting the measurement with a spectrometer[39]: $\mu = 1.41991$, $\sigma_0 = 0.810237$, $A = -0.301413$, and $S = 0.017092$. Figure 4.1 shows the K_L momentum spectrum in the MC simulation.

Next we simulated the position and direction of the K_L. We first set a primary position at the target, so as to be distributed uniformly in the target image: $x = \pm 9.1$ mm and $y = \pm 1$ mm. This image corresponded to the region in the T1 target where the proton beam hits, seen from the KL beam line. The direction of K_L was selected uniformly. As the narrowest size of the beam hole in the collimators were $x = \pm 7.6$ mm and $y = \pm 12.5$ mm at 7 m downstream from the T1 target, we checked whether the extrapolated K_L position at the narrowest position was inside the collimator or not. If the extrapolated position located in the beam hole, we used this K_L. Schematic views are shown in Fig. 4.2. We finally shifted the x and y positions +4.366 mm and -2.940 mm, respectively, to reflect the real situation.

4.1.2 K_L Decay

The second stage of the simulation was to generate K_L decays. The decay position was calculated by the nominal life time with Lorentz-boost of the K_L. The decay position distributed the exponential curve represented as:

$$f(z) \propto \exp\left(-\frac{z}{\Delta z}\right), \tag{4.3}$$

$$\Delta z = c\tau\beta\gamma = c\tau \times \frac{p}{M_{K_L}}, \tag{4.4}$$

where p and M_{K_L} are the momentum and the nominal mass of K_L, respectively. c is light velocity, τ is the nominal life time of K_L, and β and γ are Lorentz boost factors. After the decay position

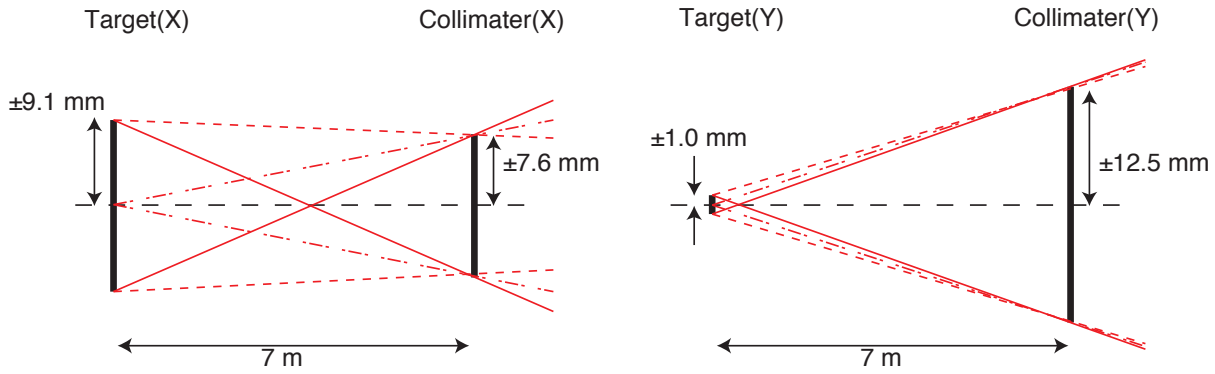

Figure 4.2: Schematic view of the K_L beam direction. The figures on the left and right show the projected view of x and y directions, respectively. Lines connect from the edge and the center of the target to the edge of the narrowest position of the beam hole. The solid lines represent outermost limitations at the detector position.

was determined, each specified decay process was generated. For each decay mode, kinematics of the secondary particles were calculated on the assumption of V-A interaction with the form factor taken from [1].

4.1.3 Interaction in Materials

We simulated the interactions between particles and detector materials with the QGSP_BERT physics list in the Geant4 package. Once a particle was injected into detector materials, interactions between the materials were simulated step by step. The distance between the current step and the next step was determined with a random number weighted on their cross sections implemented in the physics list. This process continued until particle's kinetic energy became zero. We stored the energy deposition, the interaction timing, and the three-dimensional positions for each step. They were called "mtime". These mtime were accumulated for each detector module. The variable, represented as (e_i^{mt}, t_i^{mt}, x_i^{mt}, y_i^{mt}, z_i^{mt}), was stored, where i denotes index of mtime in the module in time domain, e_i^{mt} and t_i^{mt} are energy and time of i-th mtime in the module, respectively. (x_i^{mt}, y_i^{mt}, z_i^{mt}) is three-dimensional positions of i-th mtime in the module.

4.2 Detector Response

In order to improve the reproducibility of the simulation, we considered the detector response. We reprocessed the Geant4 output data to simulate these effects of each detector.

In this section, the definition and calculation methods of the energy deposit and signal timing for each detector module are described. First, the hit timing definition which was common for all detector module is explained. Next the energy deposit definition for each detector is described.

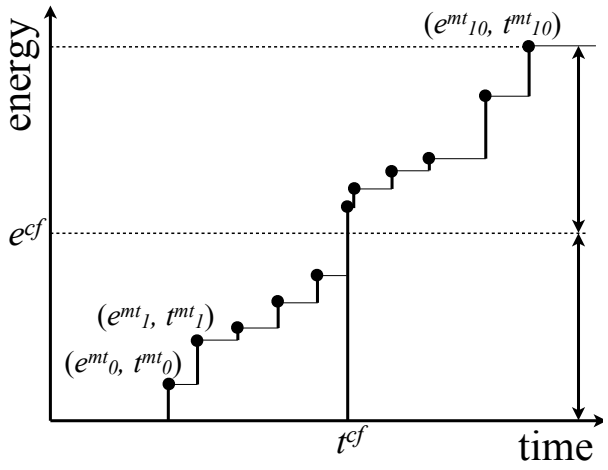

Figure 4.3: Cartoon of the pseudo pulse shape simulation. The eleven black dots represent the mtime array for one module. The horizontal axis, time, shows the each hit time of mtime, and the vertical axis, energy, shows the integrated energy until the specified time. t^{cf} is determined when the integrated energy exceed the e^{cf}.

4.2.1 Signal Timing

We explain the calculation method for the signal timing of each module from the mtime array at first. We used a common method for the CsI calorimeter, MB, and CV. The conceptual cartoon is shown in Fig. 4.3. As we determined the timing of each channel by using the half maximum timing of its pulse shape as describe in Sec. 5.1.1, a hit timing, t^{cf}, was defined as:

$$t^{cf} = t^{mt}_j \quad \text{for} \sum_{i=0}^{j-1} e^{mt}_i < e^{cf} \leq \sum_{i=0}^{j} e^{mt}_i, \tag{4.5}$$

$$e^{cf} = \frac{1}{2}\sum_i e^{mt}_i, \tag{4.6}$$

where e^{cf} is the half maximum of the total energy of the mtime array for one module. t^{cf} was determined when the integrated energy from the initial hit exceeds the e^{cf}.

4.2.2 CsI Calorimeter

We implemented

- the light yield of each crystal,
- the non-uniformity along the depth of the crystal,
- the accuracy of the energy calibration,
- the pedestal fluctuations,
- the light propagation velocity along the depth of the crystal, and
- additional time smearing

for the CsI calorimeter. First four items contribute to the energy resolution of the CsI calorimeter: $\sigma_E/E = a \oplus b/\sqrt{E} \oplus c/E$, where E is energy and $\oplus$ represents addition in quadrature. The light yield affects the stochastic term, b; the non-uniformity and the calibration accuracy affects the

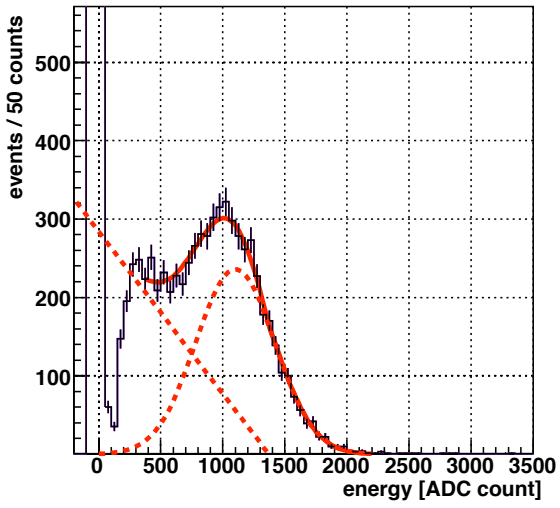

Figure 4.4: ^{137}Cs peak of the ADC distribution. The least squares fit result is shown in red solid line. The fit function consists of the photoelectron peak and the Compton edge shown in red dashed lines.

constant term, a; and the pedestal fluctuation affects the linear term, c. Latter two items and t^{cf} calculation contributes to the timing resolution. The method of the energy calibration and reproducibility of the calibration accuracy are described in Sec. 5.2.

Light Yield and Non-Uniformity

The light yield per energy deposit was different for each crystal. In addition, a non-uniformity of the scintillation light yield per deposit energy along the depth of the crystal existed. The light emitted in the upstream end propagated to the downstream end and was read by the PMT, thus the visible light yield in the upstream region was smaller than the downstream region. To input these effects into our simulation, we checked the relative light yields, as a function of the position for all crystals using 662 keV gamma-ray emitted from a ^{137}Cs radioactive source. Figure 4.4 shows an example of the ADC spectrum for ^{137}Cs signal. We measured such spectrum for each 25 mm step and obtained the uniformity along the crystal depth. Figure 4.5 shows the relative light yield distribution of all crystals. The light yield deviated 20 %. Figure 4.6 shows four examples of the uniformity. In addition, the typical light yield of 12.7 p.e./MeV was measured by using cosmic ray signals for a crystal with the relative light yield of one in Fig. 4.5[40].

There was a silicone cookie between the CsI crystal and the photocathode of the PMT. The silicone cookie was placed in order to increase the transmission efficiency of the scintillation light from the crystal to the PMT. The cookie, however, was found to absorb an outgas from materials, which was opaque to ultraviolet light. In a past vacuum test performed in September 2011, we found such kind of an outgas was evolved from circumjacent cable covers[2)]. This phenomenon decreased the transmission efficiency of the scintillation light to the PMT and decreased the effective light yield of the crystal to the level of 25 %. Figure 4.7 shows some samples of the silicone cookies which were used/not used in the vacuum test, and Fig. 4.8 shows the result of transmission measurement with a spectrograph. The decrease ratio strongly depended on the environments such as evacuation time, vacuum level, temperature and peripheral materials. We mitigated this problem by removing materials that evolved the outgas or by baking the items before use. As the outgas were still evolved during the engineering run, we assumed the reduction of the light yield was approximately

[2)] Most of the cable cover was made of polyvinyl chloride (PCV).

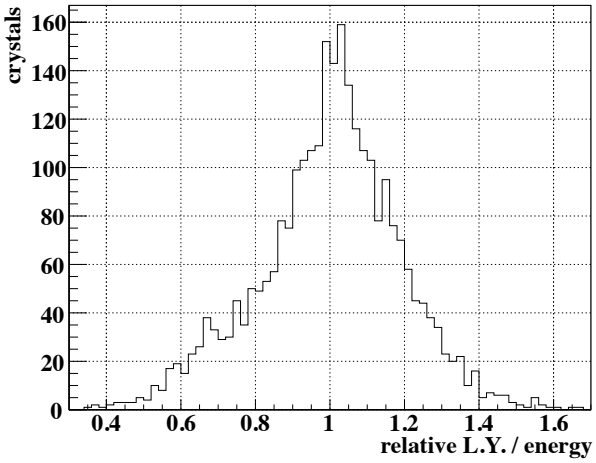

Figure 4.5: Relative light yield distribution of the CsI crystals

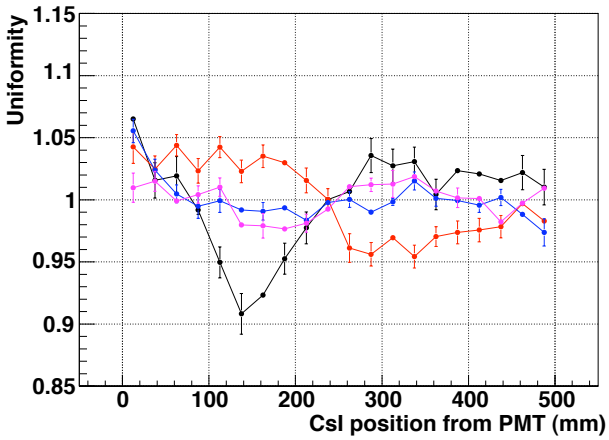

Figure 4.6: Four examples of the uniformity of the CsI light yield as a function of the distance from the PMT.

20–30 %. Finally we set the typical absolute light yield to be 9 p.e./MeV so as to explain the experimental data.

We implemented the effect of light yield as:

$$e_i^{mt'} = e_i^{mt} \frac{Y_{mod}(z_i^{mt})}{\tilde{Y}_{mod}}, \tag{4.7}$$

$$e_{mod} = \text{Poisson}\left[\tilde{Y}_{mod} \sum_i e_i^{mt'}\right] / \tilde{Y}_{mod}, \tag{4.8}$$

where $e_i^{mt'}$ is visible energy at the PMT, $Y_{mod}(z)$ is the absolute light yield at the position of z calculated from the typical absolute light yield and the uniformity, $\tilde{Y}_{mod}$ is the average light yield along z for the module, and Poisson$[x]$ means a generated random integer based on the poisson distribution whose average was x.

Pedestal Fluctuation

Pedestal fluctuation, which mainly came from intrinsic electric noises in the ADC modules, was implemented in the MC simulation to simulate the fluctuation of low energy region. The fluctuation of typically $\sigma \sim 0.45$ MeV was obtained from the experimental data and was implemented into each channel in the MC simulation.

Propagation Velocity

The propagation time of the scintillation light from the position of energy deposit to the photocathode of the PMT was measured by using the cosmic ray events in situ. We used the cosmic ray tracks which were reconstructed by MB, as described in Appendix C, to determine the track position along z axis and the time when the cosmic ray passed the crystal. The velocity, v_p, was 91.0 ± 0.7 mm/ns for the small crystal and 95.9 ± 0.8 mm/ns for the large crystal. The time when the scintillation light generated at the z_i^{mt} arrived at the downstream end of the CsI crystals ($t_i^{mt'}$) was calculated as:

$$t_i^{mt'} = t_i^{mt} + |z_i^{mt} - z_{end}|/v_p, \tag{4.9}$$

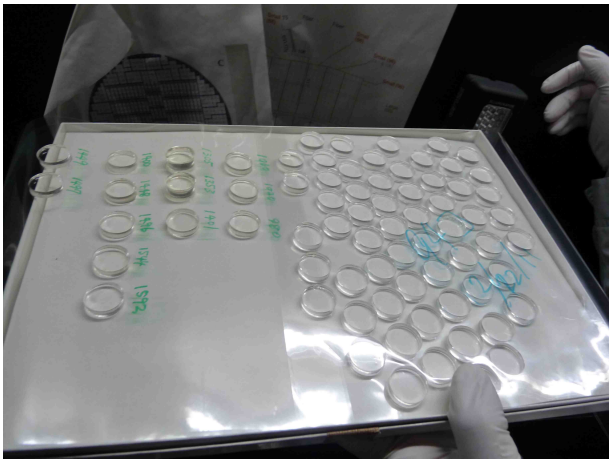

Figure 4.7: Picture of several samples of silicone cookies. Cookies in the right side were new and cookies in the left side were used in the vacuum test.

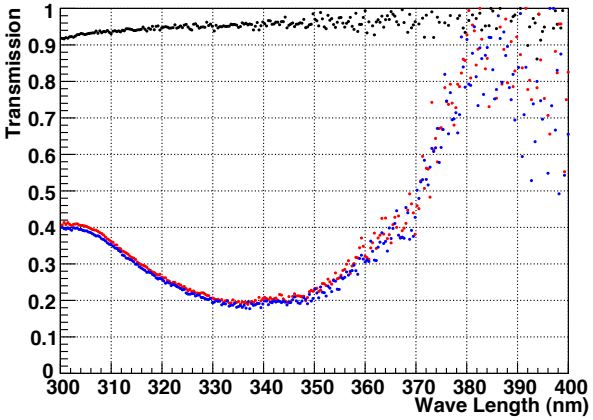

Figure 4.8: Example of the outgas effect on the silicone cookies. The black dots are transmission ratio of a new silicone cookie and red dots and blue dots show that of after a vacuum condition in a test-bench.

where z_{end} is the z position at the downstream surface of the CsI calorimeter.

In case of the CsI calorimeter, the hit time, t^{cf}, was calculated by using the $e_i^{mt'}$ in Eq. 4.8 and $t_i^{mt'}$ instead of e_i^{mt} and t_i^{mt}.

Time Smearing

The timing resolution of a channel depends on the electric noise and the decay time of the scintillation light. We imposed a parametrized fluctuation to approximate these effects. The smearing function we used was $\sigma_t = 10/E \oplus 3.633/\sqrt{E}$, where σ_t is the standard deviation of the additional smearing in the unit of ns, and E is an energy in the unit of MeV in a crystal.

4.2.3 Main Barrel

We implemented

- the attenuation along the module and
- the light propagation velocity along the module

for MB. Using these effects, we separated the hit information for a module to its both upstream and downstream readout channels. The accidental activities, described in later, will be added channel by channel; therefore, the simulated data was also saved for channel by channel.

The length of 5.5 m along the WLSFs caused large position dependence of the light yield per energy and timing delay. These effects were measured with cosmic ray signals after the detector construction finished. We calculated the energy and timing of each module by using information from both ends. This enabled us to correct the fiber attenuation effect and the delay. In the analysis, signals were recorded for each channel, and we calculated the hit timing, hit position, and deposit energy of the module by using upstream and downstream channels of the module. This method was used in the analysis of both experimental data and the MC simulation. They were

calculated as:

$$t_{mod} = \frac{t_u + t_d}{2}, \tag{4.10}$$

$$z_{mod} = \frac{t_u - t_d}{2} \times v_{prop}, \tag{4.11}$$

$$e_{mod} = \frac{e_u}{\exp\left[-z_{mod}/(\Lambda + \alpha z_{mod})\right]} + \frac{e_d}{\exp\left[z_{mod}/(\Lambda - \alpha z_{mod})\right]}, \tag{4.12}$$

where t_{mod} is the hit time of a module, z_{mod} is the hit position along z axis (the center of the MB module is the origin.), v_{prop} is the propagation velocity of light along the WLSF, and e_{mod} is the deposit energy of the module. t_u (t_d) is the hit time of the upstream (downstream) channel, they were calibrated to satisfy Eqs. 4.10 and 4.11. e_u (e_d) is the visible energy of the upstream (downstream) channel. Λ and α represent the attenuation effect. In this case, the attenuation curve for each side we used was:

$$\exp\left[\frac{-z_{mod}}{\Lambda + \alpha z_{mod}}\right] \qquad \text{for the upstream readout, and} \tag{4.13}$$

$$\exp\left[\frac{z_{mod}}{\Lambda - \alpha z_{mod}}\right] \qquad \text{for the downstream readout.} \tag{4.14}$$

The attenuation curves of one module are shown in Fig. 4.9, and the parameters are listed in Tab. 4.1. This fiber effect was implemented into our MC simulation as:

$$e_{ui}^{mt'} = \frac{e_i^{mt}}{2} \exp\left[\frac{-\tilde{z}_i^{mt}}{\Lambda + \alpha \tilde{z}_i^{mt}}\right], \tag{4.15}$$

$$e_{di}^{mt'} = \frac{e_i^{mt}}{2} \exp\left[\frac{\tilde{z}_i^{mt}}{\Lambda - \alpha \tilde{z}_i^{mt}}\right], \tag{4.16}$$

$$e_u = \sum_i e_{ui}^{mt'}, \tag{4.17}$$

$$e_d = \sum_i e_{di}^{mt'}, \tag{4.18}$$

$$t_{ui}^{mt'} = t_i^{mt} + \frac{\tilde{z}_i^{mt}}{v_{prop}}, \tag{4.19}$$

$$t_{di}^{mt'} = t_i^{mt} - \frac{\tilde{z}_i^{mt}}{v_{prop}}, \tag{4.20}$$

where $e_{ui}^{mt'}$ ($e_{di}^{mt'}$) and $t_{ui}^{mt'}$ ($t_{di}^{mt'}$) are visible energy and time when the scintillation light generated at the $\tilde{z}_i^{mt}$ arrives at the upstream (downstream) end, and $\tilde{z}_i^{mt}$ is the z position of the mtime on a system of coordinates with its origin at the center of the MB. In case of MB, the hit time of upstream (downstream) channel was calculated by using the $e_{ui}^{mt'}$ ($e_{di}^{mt'}$) and $t_{ui}^{mt'}$ ($t_{di}^{mt'}$) instead of e_i^{mt} and t_i^{mt}.

4.2.4 Charged Veto

We implemented

- the position dependence of the light yield along the strip,

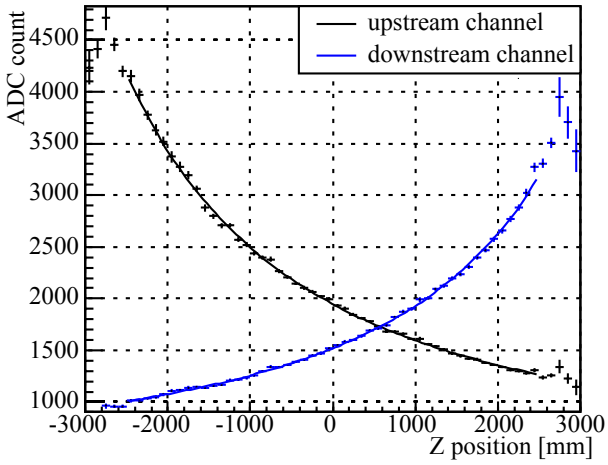

Figure 4.9: Attenuation curve of a MB module taken by cosmic ray events. The horizontal axis shows the penetrated position of the cosmic ray and the vertical axis shows the peak value for the energy deposit by penetrating cosmic rays at the position. The black dots are the data of the upstream readout and the blue dots are that of the downstream readout. These data points were fitted by Eqs. 4.13 and 4.14, respectively.

Table 4.1: Parameters for the MB position dependence

Parameter	Value
v_{prop}	168.1 mm/ns
Λ	4923 mm
α	0.495

· timing resolution

for CV.

A CV module also equipped two readouts at both ends, as is the case with MB. The definitions of energy and hit timing of each strip in both experimental and simulated data were:

$$e_{mod} = e_s + e_l, \tag{4.21}$$
$$t_{mod} = (t_s + t_l)/2, \tag{4.22}$$

where e_{mod} is the deposit energy of a module, t_{mod} is the hit time of a module, e_s (e_l) is the visible energy of the short (long) side channel, and t_s (t_l) is the hit time of the short (long) side channel. The position dependence of the light yield and the timing resolution were measured in advance as described in Sec. 2.4.2. These effects were implemented into our MC simulation as:

$$e_s = e_l = \text{Poisson}\left[\sum_i e_i^{mt} Y_{mod}(x_i^{mt}, y_i^{mt})\right] / 2\tilde{Y}_{mod}, \tag{4.23}$$
$$t_s = t_l = t^{cf} + \text{Gaussian}[0, \sqrt{2}\sigma_t], \tag{4.24}$$

where $\tilde{Y}_{mod}$ is the average light yield for the module, $Y_{mod}(x, y)$ is the light yield at the position of (x, y), and σ_t is the timing resolution of a module. Poisson$[x]$ means a generated random integer based on the poisson distribution whose average is x, and Gaussian$[x, y]$ means a generated random number based on the gaussian distribution whose average is x and standard deviation is y.

Table 4.2: MC Preparation

Mode	Br.	Generated K_L	Equivalent K_L
$K_L \to 3\pi^0$	0.1952	1×10^9	5.123×10^9
$K_L \to 2\pi^0$	8.64×10^{-4}	1×10^7	1.157×10^{10}
$K_L \to 2\gamma$	5.47×10^{-4}	1×10^7	1.828×10^{10}
$K_L \to \pi^\pm e^\mp \nu$	0.4055	5×10^8	1.233×10^9
$K_L \to \pi^\pm \mu^\mp \nu$	0.2704	5×10^8	1.849×10^9
$K_L \to \pi^+\pi^-\pi^0$	0.1254	5×10^8	3.987×10^9
$K_L \to \pi^+\pi^-$	1.967×10^{-3}	1×10^7	5.084×10^9
Other than K_L	6.31×10^{15} POT equivalent		

4.3 Accidental Overlay

In our MC simulation, only one K_L decay was treated in one event. But in the real detector, there were accidental activities which came from other processes that happened at the same time, such as other K_L decays, interactions of beam particles. These accidental activities caused additional energy deposition in the detector and screwed up timing information. Therefore they had to be added to the simulation. We overlaid the experimental data collected in the accidental run, described in Sec. 3.3.2, on the simulated events which satisfied the online trigger condition. The energy deposition was added together channel by channel. For timing information, the hit time of either the simulated hit or the overlaid hit was chosen for each channel by selecting the one with larger energy.

This accidental overlay automatically reflected the pedestal fluctuation including the electric noise because the real experimental data was used. For the accidental data of the CsI calorimeter, we did not store the information of channels with energy lower than 1 MeV to reduce the data size. Therefore, we applied the simulated pedestal fluctuation, described in Sec. 4.2.2, only for channels whose information was not stored.

4.4 MC Preparation

Simulated data was generated for each decay mode separately. The preparations of the MC simulations are listed in Tab. 4.2. In the case of $K_L \to 3\pi^0$, for example, a K_L was generated 10^9 times, and the equivalent K_L number, which was the quotient of the generated K_L and its branching fraction, was 5.123×10^9. In addition to the K_L decays, we prepared neutron and photon simulation. As a generator for them, outputs from a beam line simulation[23] was used.

Chapter 5

Analysis of the K_L Flux Measurement

This chapter is dedicated to the description of the analysis of the K_L flux measurement. In order to reconstruct objective signals, we built an analysis framework, including the photon definition method, the calibration method, and the K_L reconstruction method. The details of them are described through the reconstruction of the three decay modes: $K_L \to 3\pi^0$, $K_L \to 2\pi^0$, and $K_L \to 2\gamma$. A event selection and result of each mode are shown independently. We then combined the results of three modes and determined the K_L flux. The obtained reproducibilities of the MC simulation are explained with the resultant distributions of them. Finally we discuss systematic uncertainty and show the result of the K_L flux with the error estimation.

5.1 Photon Definition in the CsI Calorimeter

Here, we explain the definition method of energy, hit position, and hit timing of a photon in the CsI calorimeter.

5.1.1 Energy and Timing Definition of a Crystal

At the first stage of the analysis, we extracted energy and timing information for each channel from the recorded data digitized with 125 MHz ADC. Figure 5.1 shows an example of the recorded pulse shape. Voltage data of 64 sampling points were stored in one event for each channel.

The base line (B) was defined as the average of the first ten samples in each pulse as: $B = \sum_{i=0}^{9} d_i/10$, where i represents the index of sampling points from 0 to 63, and d_i is ADC count of the i-th point. We summed ADC count of all 64 samples and subtracted the base line contributions as: $I = \sum_{i=0}^{63}(d_i - B)$. This calculated value was called "integrated ADC" (I), and it corresponded to the energy of the channel.

With respect to the timing, we used a constant fraction method. It means that the timing of the pulse was defined at the half maximum in the rising slope, as illustrated in Fig. 5.1. Firstly, we searched the highest point in 64 samples and defined the half maximum value of the pulse considering the base line. We then searched a pair of adjacent data points, from the highest sample, whose interpolated line crossed the half maximum in the rising direction. The crossing point between them was defined as the constant fraction time. This search was processed in the direction of leftward from the highest point.

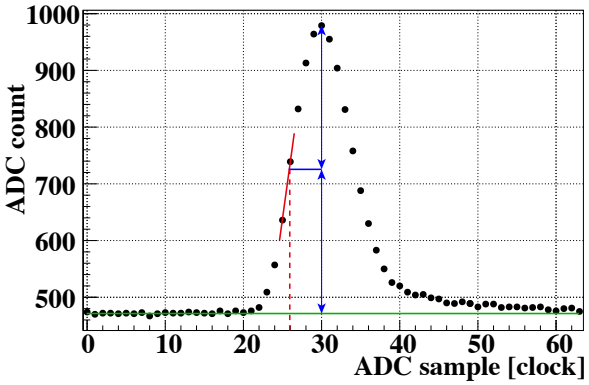

Figure 5.1: Energy and timing definition based on the pulse shape. The base line of this pulse was shown as a green horizontal line approximately 480. Two blue vertical arrows show the half of the pulse height. The red dashed line shows the time definition of this pulse, called constant fraction time.

5.1.2 Clustering

An electromagnetic shower in the calorimeter made by an incident photon developed in accordance with the Moliere radius, and deposited energies on multiple crystals. A group of these activities, called "cluster", was constructed in order to define the energy, hit position, and hit timing of the incident photon. First, we picked CsI crystals with their energy deposit of more than 3 MeV within 150-ns-wide time window. Such crystals were called "cluster seeds". We grouped cluster seeds to construct clusters. The definition of a cluster was a group of cluster seeds which exist within 71 mm from the closest seed in the cluster as shown in Fig. 5.2.

Once this process finished, we calculated the energy deposit, the center position, and the timing of each cluster as:

$$e_{\text{cluster}} = \sum_{i=1}^{n} e_i, \tag{5.1}$$

$$x_{\text{cluster}} = \frac{\sum_{i=1}^{n} x_i e_i}{\sum_{i=1}^{n} e_i}, \tag{5.2}$$

$$y_{\text{cluster}} = \frac{\sum_{i=1}^{n} y_i e_i}{\sum_{i=1}^{n} e_i}, \text{ and} \tag{5.3}$$

$$t_{\text{cluster}} = \sum_{i=1}^{n} \frac{t_i/\sigma_t^2}{1/\sigma_t^2}, \tag{5.4}$$

where e_{cluster}, x_{cluster}, y_{cluster}, and t_{cluster} are the energy deposit, x position, y position, and the timing of a cluster, respectively. n denotes the number of crystals in the cluster. e_i, x_i, y_i, and t_i are the deposit energy, x position, y position, and hit time of i-th crystal, respectively. σ_t is the timing resolution of a crystal measured by a past beam test[40] as: $\sigma_t = 5/e_i \oplus 3.63/\sqrt{e_i} \oplus 0.13$ in the unit of ns for σ_t and MeV for e_i. There could be accidental hits in the cluster at this stage because we only used the loose timing selection of 150-ns-width. We thus removed accidental hits in the next step. Figure 5.3 shows the difference between the timing of a cluster and the hit time of each constitutive crystal as a function of the deposit energy of the crystal. The two red lines represent $\pm 5\sigma$ limits of each energy bin. If the hit time of crystals existed in outside $\pm 5\sigma$, we calculated the time difference normalized by the standard deviation as $|t_i - t_{cluster}|/\sigma$ for each crystals, and removed the crystal, whose hit time was most distant, from the cluster seeds. Removing one crystal from the cluster seeds, we reprocessed grouping again from the first step and iterated until the hit time of all constitutive crystals were inside the $\pm 5\sigma$ limits.

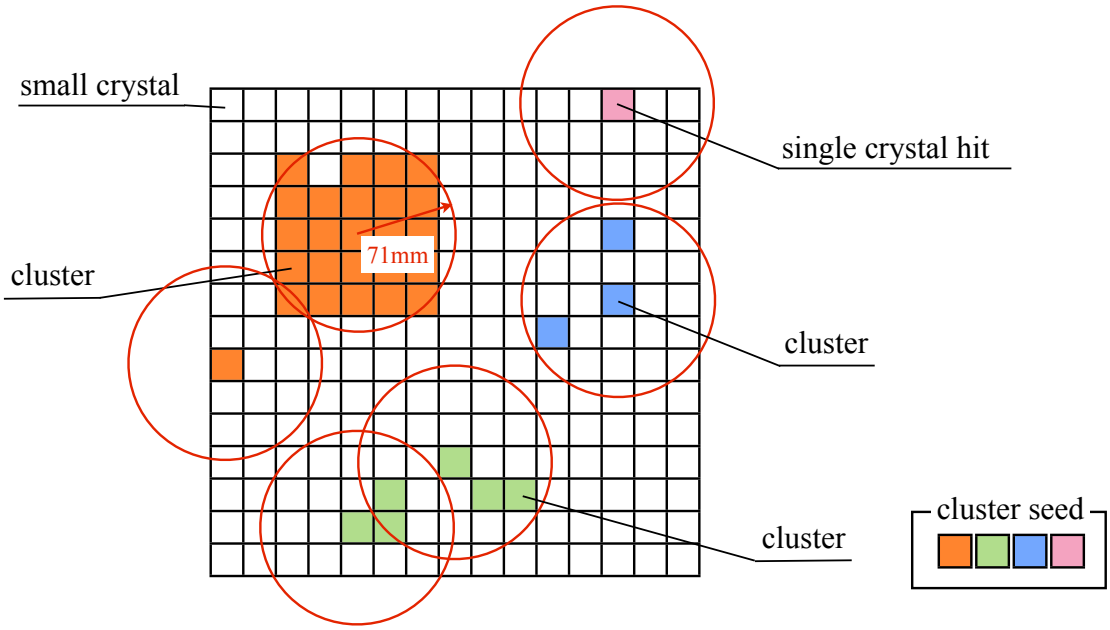

Figure 5.2: Example of the grouping of cluster seeds. The colored boxes represents cluster seeds, and each color shows each cluster. The red circles with 71 mm-radius show the grouping regions. The clusters whose center belongs the same red circle are grouping in the same cluster. There are three clusters and one single crystal hit in this figure.

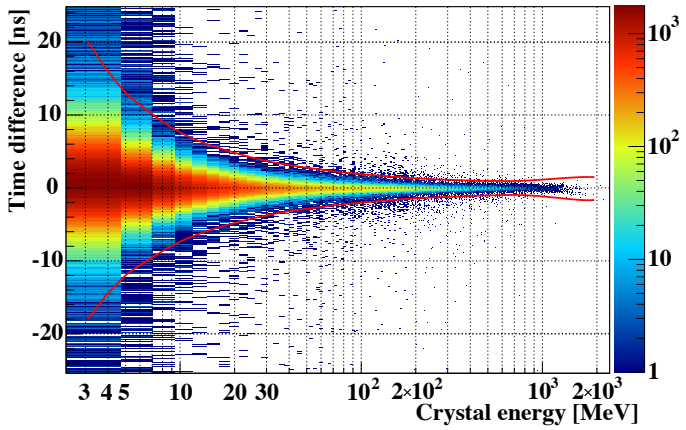

Figure 5.3: Timing cut in the clustering. The vertical axis shows the difference between the timing of a cluster and the hit time of each constitutive crystal and the horizontal axis shows the deposit energy of the crystal. Color represents the number of events in arbitrary unit.

Clusters that had energy deposit of more than 20 MeV were called "photon cluster", and were used for the reconstruction. Other clusters were not counted as photons. Remaining crystals that had energy deposits and did not belong to any cluster were treated as single crystal hits. They were considered as extra activities in the CsI calorimeter and used to veto the events. The calculated deposit energy of a photon cluster was usually lower than the incident photon energy due to shower leakage and the finite threshold (3 MeV) for seeds to be summed up. We corrected the deposit energy of photon clusters with a correction map prepared by a MC simulation.

5.1.3 Energy and Position Corrections due to Incident Angle

The center of energy ($x_{cluster}$, $y_{cluster}$) calculated with Eqs. 5.2 and 5.3 was shifted from the actual incident position of the photon due to its finite incident angle against the surface of the CsI calorimeter. Figure 5.4 illustrates a cartoon of the position shift. P_{inc} is the actual incident position at the CsI surface in the radial direction, P_{coe} is the position of the center of energy in the radial direction, θ is the angle between the beam axis and the line connecting the vertex and P_{inc}, and L_s is the distance from P_{inc} and the center of energy. In general, P_{coe} located outer than P_{inc} due to the direction of the electromagnetic shower development. We needed to correct this shift.

After reconstructing the vertex (described in Sec. 5.3.1), we were able to calculated the incident angle of the photons to the surface of the CsI calorimeter. The incident position, P_{inc}, can be derived as:

$$L_s/X_0 = p_0 + p_1 \ln(E\ [\mathrm{GeV}]), \tag{5.5}$$

$$P_{inc} = P_{coe} - L_s \sin\theta, \tag{5.6}$$

where $X_0 = 18.5$ mm[1] is the radiation length of CsI and E is the energy of the incident photon. Parameters, p_0 and p_1, represent the shower length; they were estimated as $p_0 = 6.490$ and $p_1 = 0.993$ with a MC simulation. Using the new P_{inc}, we re-corrected its energy with the correction map again.

5.2 Calibrations and Corrections

We explain the calibration method and corrections for the CsI calorimeter in this section. The descriptions for the veto counters are in App. A.

5.2.1 Energy Calibration and Corrections

Non-linearity Correction

It was found that a non-linearity in measured energy was caused by the readout electronics. We corrected the non-linearity using data from test-bench measurements. Typical CsI pulse shape from the PMT was recorded with an oscilloscope. A function generator generated this pulse shape, and fed it into the preamplifier. The output pulse from the preamplifier was read by the 125 MHz ADC module. Figure 5.5 shows the ratios of the observed charge to the height of the function generator output as a function of the observed pulse height.

Temperature Correction

Temperature dependence of the CsI output was measured with beam muon runs described in

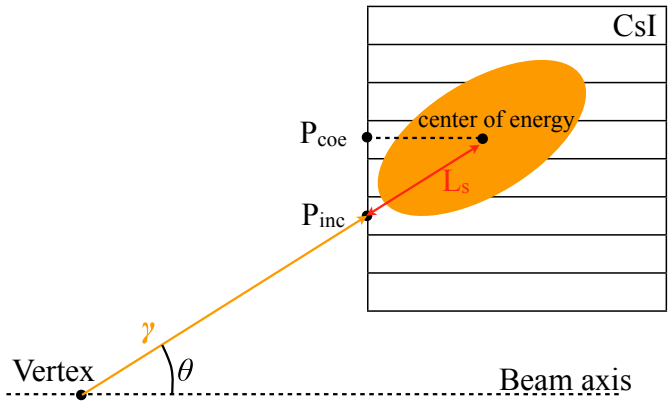

Figure 5.4: Cartoon of the cluster position correction. The photon flying from the vertex entered the CsI calorimeter, and its electromagnetic shower development in the direction as shown in orange circle. The incident position (P_{inc}) and the position of center of energy (P_{coe}) is deviated due to the finite incident angle θ.

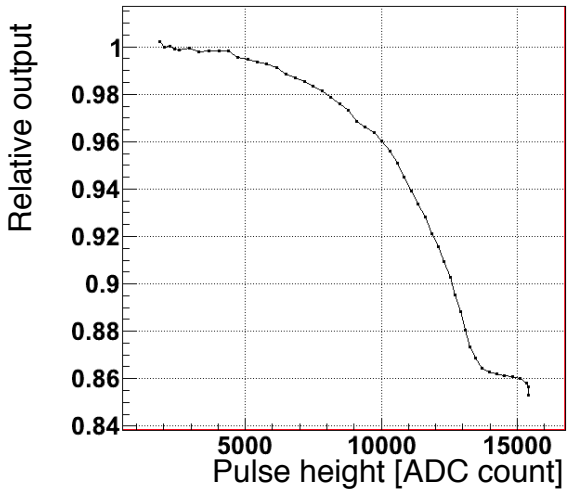

Figure 5.5: Linearity as a function of the output pulse height. The relative output was the ratio of the observed charge to the height of the function generator output.

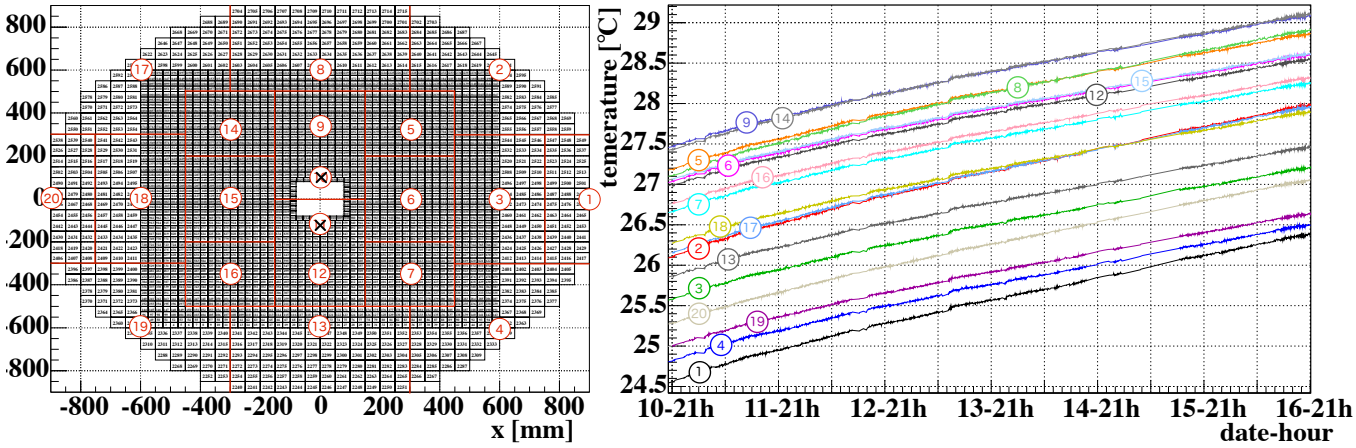

Figure 5.6: Temperature monitor positions on the CsI surface (left) and the temperature history for each monitor (right). The denoted numbers correspond to each other in these two figures. The two monitors marked by × were not working during the run. Each crystals in each region surrounded by red lines were corrected based on each monitor, respectively.

Sec. 3.3.3. Figure 5.6 shows the positions of the temperature monitors (thermocouples) at the upstream surface of the CsI calorimeter. Measured temperatures during the beam time are also shown in the right of Fig. 5.6. Top two figure of Fig. 5.7 show the MIP peak values as a function of the temperature in two regions. Clear correlation between the deposit energy of MIP and the temperature existed. We assumed this relation as exponential slope as $MP = \exp(p_0 + p_1 T)$, where MP is the peak value of MIP, T is the temperature, and p_0 and p_1 are fit parameters. p_1 was the resultant correction factor. Figure 5.8 shows the temperature correction factors of all regions. The average correction factor was -2.46 ± 0.04 %/℃. This factor was larger than the temperature dependence of the CsI crystal light yield[1]. It was able to be explained by the outgas described in Sec. 4.2.2 qualitatively. Bottom two figures of Fig. 5.7 show the corrected MIP peak values as a function of the temperature in each region. These were stable within ±1 % level.

Unstable Channel Correction

We found that output of several channels were unstable during the run period. Figure 5.9 shows an example of unstable channels. It shows the ratio between PMT outputs, when the laser flushed, of an unstable channel and its adjacent channel as a function of RunID which was an identification number of a DAQ run. The period of one run was usually three minutes. The PMT response for the laser signal of the channel changed at the degree of ±7 % during the run period. We corrected this fluctuation in every ten runs. There were thirty unstable channels, and we prepared the correction factors. We suspected that it was caused by a bad electrical contact between a PMT and a PMT base.

Cosmic Ray Calibration

We used three energy calibration methods. The initial energy calibration for the CsI calorimeter was done by using cosmic rays. Figure 5.10 shows an event display of a cosmic ray. We only required two OEV, which surrounded the edge of the CsI calorimeter, had activities to select

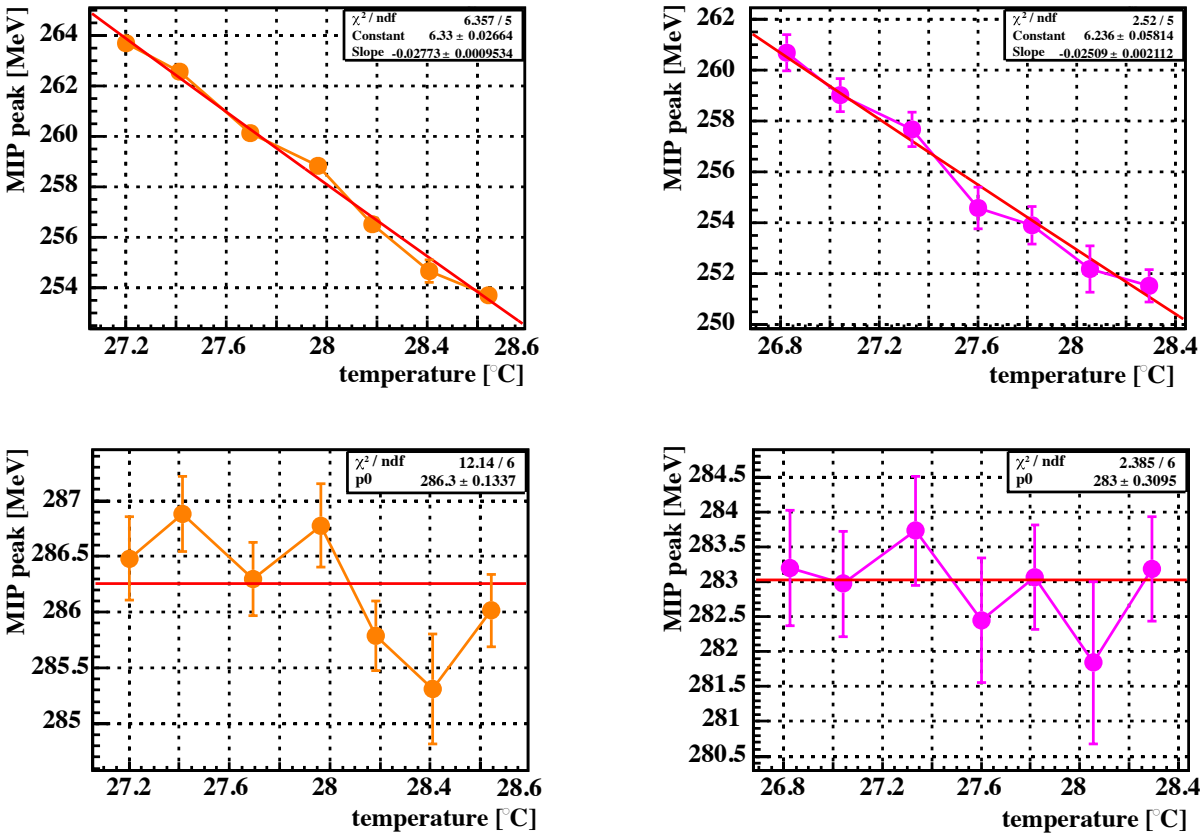

Figure 5.7: Examples of the MIP peak value as a function of the temperature in two regions. Top two figures show the MIP peaks before the temperature correction. They are fitted by exponential curves. Bottom two figures show those after the temperature correction. They are fitted by constant.

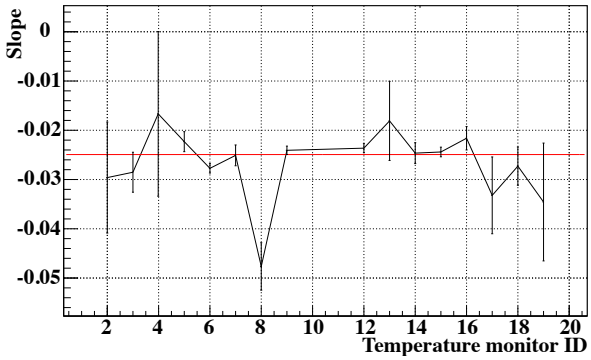

Figure 5.8: Temperature correction factors for all regions. They were fitted by a constant. Horizontal axis shows the index of temperature sensor shown in Fig. 5.6

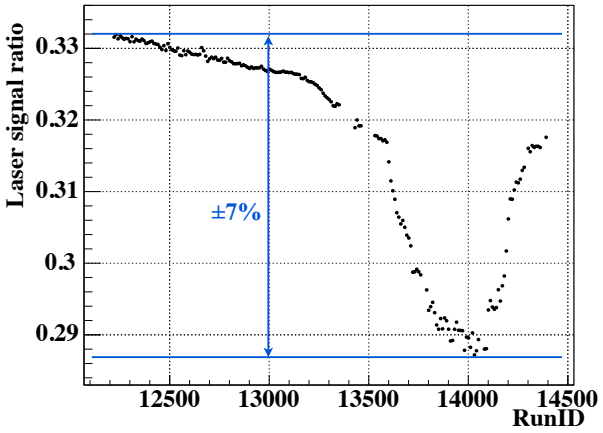

Figure 5.9: Example of the unstable channels. This plot shows the PMT output for the laser pulse from crystal ID 150 divided by that from ID 151 as a function of RunID. The main K_L flux measurement was performed from RunID 13669 to 13770.

cosmic rays. We used a Hough transform method, which identified crystals on a straight line, and removed accidental hits out of the line. After that we determined the track angle with a least square method. To measure the energy deposit in a unit path length, we selected crystals whose both up and down crystals had activities and correcting the path length based on the track angle. The peak in the normalized output was fitted by a Landau function. The calibration factor to convert the integrated ADC to the energy deposit was calculated by assuming the energy deposit in the CsI per a unit path length to be 5.6 MeV/cm[1]. Since the trajectory fitting was made in the two-dimensional plane along the CsI surface, the path length calculation had uncertainty in the direction along the beam line. As the diameter of the CsI calorimeter is 2 m and the depth is 500 mm, the uncertainty of the path length was a few percent. This calibration was used as initial calibration factors for the $K_L \to 3\pi^0$ calibration and the Al target calibration described in the following paragraphs.

$K_L \to 3\pi^0$ Calibration

There was uncertainty in the path-length in the cosmic ray calibration. In addition, the method did not take into account the non-uniformity in the CsI crystals. We could not determine the position along the beam direction where cosmic ray penetrated. These uncertainty made wider distributions in the energy deposit normalized by the path length. We therefore used a method using the $K_L \to 3\pi^0$ decay in order to improve the calibration. The details of the $K_L \to 3\pi^0$ reconstruction is described in Sec. 5.3.

In this calibration process, we used the events having six photon hits in the CsI. We measured the energy and position of six photons with their errors. Assuming (v_x, v_y, v_z) as the decay vertex of K_L, the $3\pi^0$ events have six kinematic constraints expressed as:

$$M(6\gamma) = M(K_L) \quad : \ K_L \text{ mass constraint;} \tag{5.7}$$

$$M(2\gamma) = M(\pi^0) \quad : \ \pi^0 \text{ mass constraint} \times 3 \text{ combinations;} \tag{5.8}$$

$$\sum_{i=1}^{6} x_i E_i = \frac{Z_{\rm csi} - Z_{\rm target}}{v_z - Z_{\rm target}} v_x \sum_{i=1}^{6} E_i \quad : \text{ center of energy } (x); \tag{5.9}$$

$$\sum_{i=1}^{6} y_i E_i = \frac{Z_{\rm csi} - Z_{\rm target}}{v_z - Z_{\rm target}} v_y \sum_{i=1}^{6} E_i \quad : \text{ center of energy } (y); \tag{5.10}$$

where (x_i, y_i) is the hit position of the i-th photon on the CsI surface and E_i is the deposit energy of

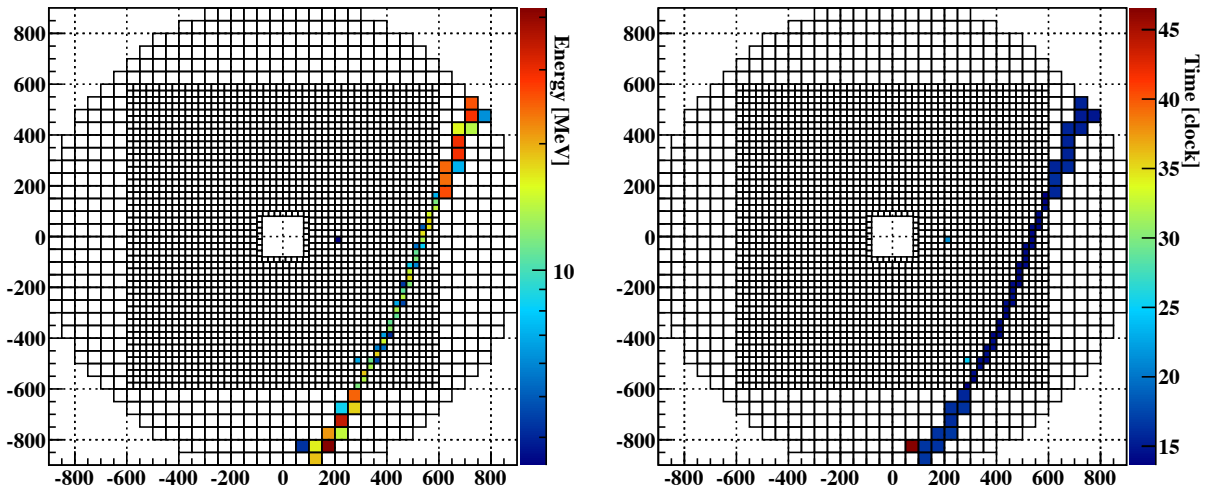

Figure 5.10: CsI event display with a cosmic ray track. The left figure shows the energy distribution in the calorimeter and the right figure shows the hit timing for each channels. The unit of time is clock (1 clock = 8 ns). There were several low energy accidental activities at the off timing.

i-th photon. We set an energy of one photon free in addition to the K_L vertex positions (v_x, v_y, v_z). Adjusting the vertex position, we determined the calibration factor for the photon energy by a method of Lagrange multipliers based on the above constraints. The obtained calibration factor was applied only on the crystal with the largest energy deposit in a cluster. In one $K_L \to 3\pi^0$ event, we determined the calibration factor for each photon individually. We thus got one calibration factor for six crystals in one event. After processing all the $K_L \to 3\pi^0$ event samples, the calibration factor for each crystal was averaged. By using the resultant factors, we iterated this process. The details of the photon selection criteria used in this calibration process are listed in App. D

To reproduce the calibration accuracy, we simulated this calibration process and applied the obtained mis-calibration factors to our MC simulation. Shower leakage caused a mis-calibration, especially in the outermost and innermost region of the CsI calorimeter. The missing channels also caused the same effect. The MC simulation included these effects, too. Before the beginning of the first iteration in the MC simulation, we smeared the calibration factor of each crystal of 5 %. The reconstructed invariant mass width of 6γ as a function of the number of iteration in the experimental data and the MC simulation are shown in Fig. 5.11. The resultant mass width was 3.512 ± 0.005 MeV/c^2 for the experimental data and 3.521 ± 0.005 MeV/c^2 for the MC simulation after the calibration. These values were consistent within 0.3 %. The change of the calibration factors from those by the cosmic ray calibration distributed $\sigma \sim 3$ %. In the $K_L \to 3\pi^0$ calibration, the latitude of the vertex position, which determined θ in Eq. 2.1, correlated the reconstructed energy; therefore, the absolute value of the calibration factor was not able to be decided. To determine the overall scale factor for the calibration factors, we performed the Al target calibration described in the next paragraph.

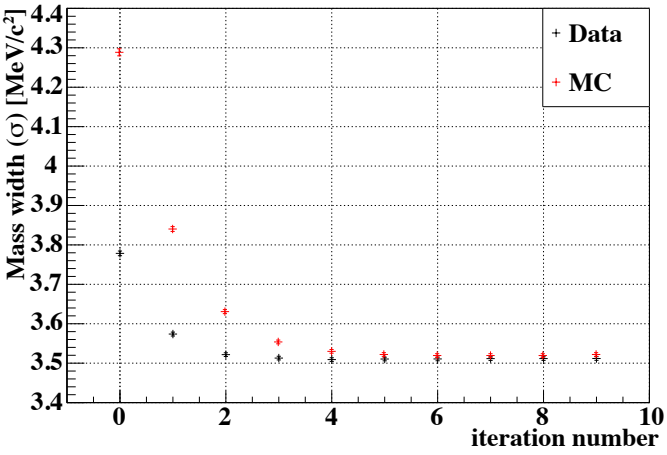

Figure 5.11: Mass peak change as a function of the number of iteration of the $K_L \to 3\pi^0$ calibration. The black points show the read data, and the red points show the MC simulation. Vertical axis is reconstructed $3\pi^0$ mass width fitted by gaussian function. Horizontal axis is the index of iterations.

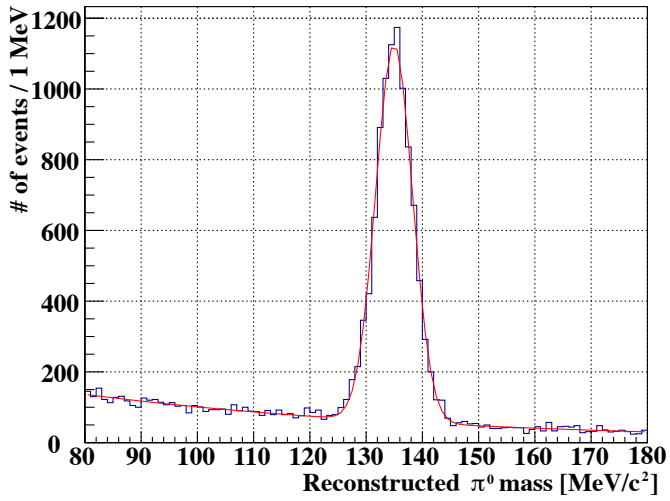

Figure 5.12: π^0 mass peak obtained by the Al target run. The distribution was fitted by a gaussian peak on an exponential slope. The red line indicates the resultant curve.

Al Target Calibration

As we mentioned in Sec. 3.3.3, we inserted the Al target in the beam at $z = 2795$ mm to generate π^0 by interactions with neutrons. Fixing the vertex position, we got the following relation between the reconstructed mass and measured deposit energies of a pair of photons as:

$$C^2 = \frac{(M_{\pi^0})^2}{2E_{\gamma 1}E_{\gamma_2}(1-\cos\theta)}, \tag{5.11}$$

where C is the overall scale factor for the calibration factor. The change from the cosmic ray calibration was 1.06. Figure 5.12 shows the reconstructed π^0 mass peak from the Al target after the calibration. The resultant π^0 mass peak value of 134.98 ± 0.04 MeV was consistent with the nominal mass by definition.

5.2.2 Timing Calibration and Correction

Timing Calibration

We calibrated the timing offset of individual crystal by using cosmic rays. We calculated the time

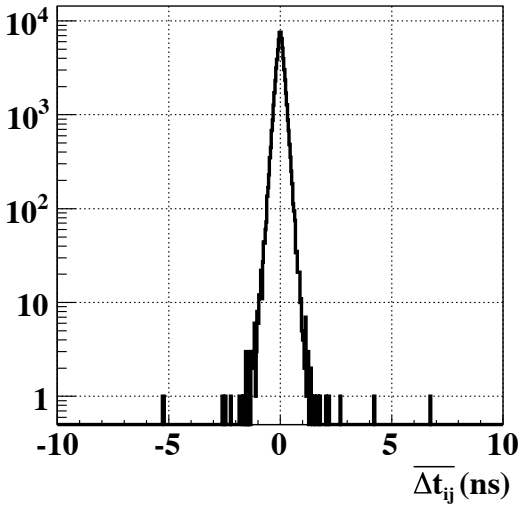

Figure 5.13: CsI timing calibration result. Horizontal axis shows the mean value of the hit timing difference of each pair of crystals after the calibration. The standard deviation of the histogram was 0.2 ns.

difference between two crystals in a track correcting by the time of flight (TOF) as:

$$\Delta t_{ij} = t_i - t_j - L_{ij}/c \qquad \text{for } i < j, \tag{5.12}$$

where i and j are the IDs of crystals, t_i is a hit timing of crystal i, L_{ij} is the distance between crystals i and j in x-y plane, and c is the light velocity. In this calculation, we assumed the cosmic ray flied downward with a velocity of c and was perpendicular to the z axis. We calculated all pairs in a track. After surveying all cosmic ray events, we calculated the mean ($\overline{\Delta t_{ij}}$) and its error ($\sigma_{\Delta t_{ij}}$) for all (i, j) pairs by fitting with a gaussian function. $\overline{\Delta t_{ij}}$ should be zero if the timing offset did not exist. Deviation from zero corresponds to the difference of offsets of the two crystals, $o_i - o_j$. We calculated the offset of each channel by using least square method. The χ^2 definition was:

$$\chi^2 = \sum_{i,j}^{i<j} \left[\frac{\overline{\Delta t_{ij}} - o_i + o_j}{\sigma_{\Delta t_{ij}}} \right]^2, \tag{5.13}$$

where o_i is offset of i-th crystal. Offset values of 2716 crystals were treated as parameters. Figure 5.13 shows the result of the calibration. The resultant width of $\overline{\Delta t_{ij}}$ distribution was 0.2 ns.

Timing Correction

We found the correlation between timing and energy. Figure 5.14 shows that a difference between the timing of a cluster and the timing of a crystal that is included in the cluster correlated with the deposit energy of the crystal. The timing of cluster was calculated with Eq. 5.4. We considered the correlation came from the fact that the pulse shape slightly depends on its height. We made correction on the timing with a quadratic function as:

$$\Delta t = A_1(e - 400) + A_2(e^2 - 400^2) \quad \text{for } e > 400 \text{ MeV}, \tag{5.14}$$

where Δt is a correction value for each crystal in the unit of ns, e is a deposit energy for each crystal in the unit of MeV. Because the time of a cluster was calculated with the time of constitutive crystals, we determined the correlation curve, shown in Fig. 5.14, iteratively. The resultant coefficients were $A_1 = -1.325 \times 10^{-3}$, and $A_2 = 1.592 \times 10^{-6}$. To confirm this correction, we checked two

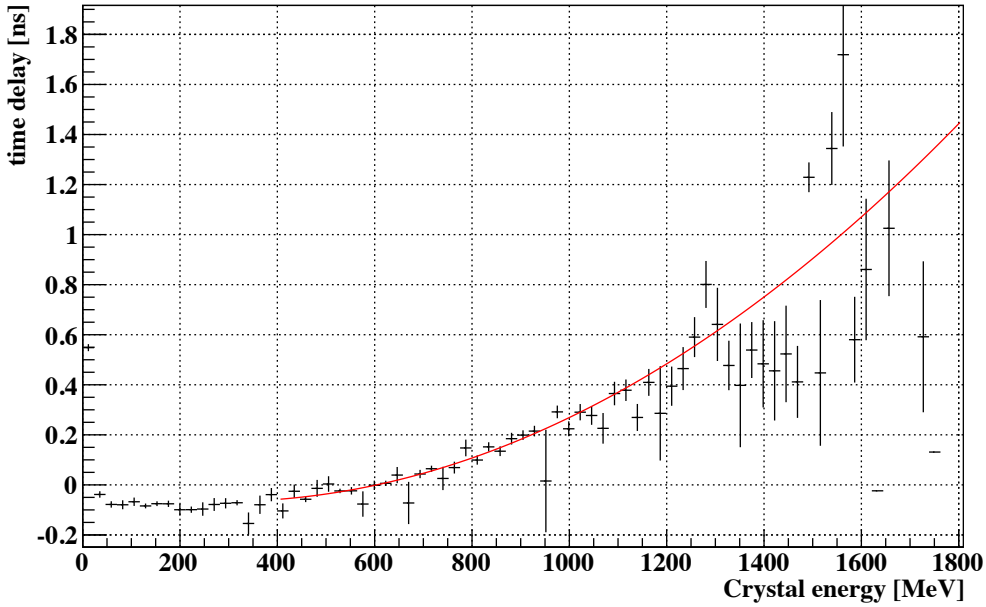

Figure 5.14: Time-Energy correlation curve at the first iteration obtained by the Al target run. The vertical axis shows the difference between a timing of a photon and a timing of a crystal which is included in the photon and the horizontal axis shows the energy of the crystal. The red solid curve is the parametrized quadratic function.

photon events in the π^0 peak ($\pm 1\sigma$, Fig. 5.12) obtained in the Al target run. We checked the time difference between the two photons, of which one had energy of 275 ± 50 MeV. Figure 5.15 shows the result of this correction as a function of the energy of the opposite photon. The correlation in the high energy region was vanished.

5.3 Event Reconstruction

As described in Sec. 3.1, in the analysis of $K_L \to 3\pi^0$, $K_L \to 2\pi^0$, and $K_L \to 2\gamma$ decay, we counted the number of photons in the CsI calorimeter and measured the energies and positions of these photons to reconstruct the vertex and the invariant mass of the initial K_L. We explain how to do that with the CsI calorimeter as the event reconstruction.

In any analysis mode, at the first step of the event reconstruction process, we counted the number of photon clusters, in order to categorize events. We required six or more photon clusters for $K_L \to 3\pi^0$, four or more photon clusters for $K_L \to 2\pi^0$, and two or more photon clusters for $K_L \to 2\gamma$. If there were more photon clusters in the time window, we selected, for the next step, six (or four or two) photon clusters whose mutual timings were closest. The vertex and the invariant mass reconstruction process of all modes were almost same as each other except for the number of photons.

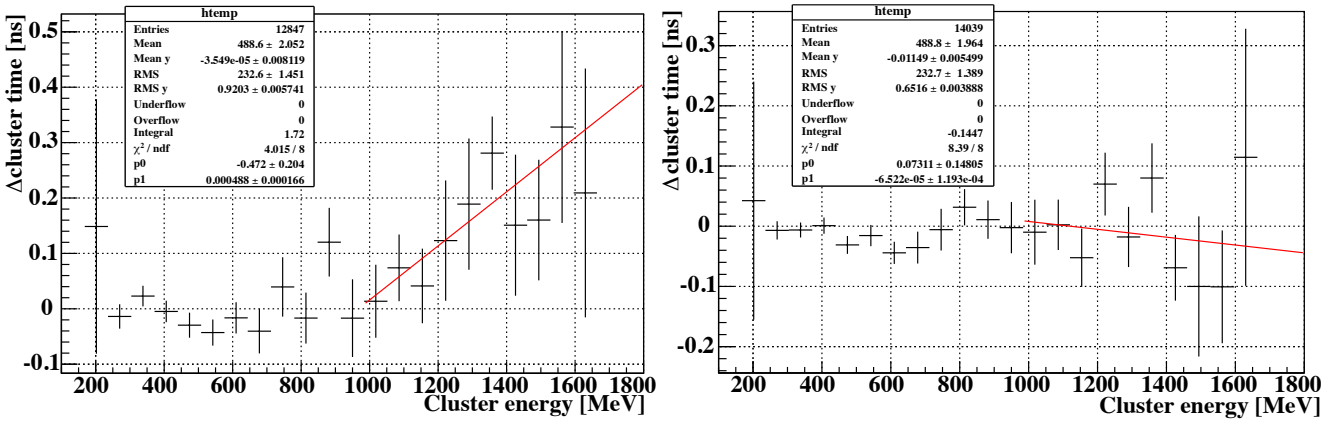

Figure 5.15: Effect of the time correction evaluated by the data in the Al target run. With (left) and without (right) the timing correction. The vertical axis shows the time difference between two photons and the horizontal axis shows the energy of one of two photons that the energy of the other photon is 275 ± 50 MeV. The red lines show fit results by a function of $p0 + p1E$ more than 1000 MeV region, where E is cluster energy.

5.3.1 Vertex Reconstruction

We moved to reconstruct the vertex of π^0 for $K_L \to 3\pi^0$ and $K_L \to 2\pi^0$ with a pair of photon clusters. For $K_L \to 2\gamma$, we reconstructed the K_L vertex in a similar manner. In the π^0 (K_L) reconstruction, we assumed that two photons came from a π^0 (K_L) decay and their invariant mass was equal to the π^0 (K_L) mass. Also, the decay vertex was assumed to be on the beam axis, *i.e.* $(0, 0, Z_{vtx})$. In cases of $K_L \to 3\pi^0$ and $K_L \to 2\pi^0$, the x and y position of the vertex (X_{vtx}, Y_{vtx}) were also calculated. We then calculated the time when the K_L decayed, and finally obtained full position and timing information of the vertex, $(X_{vtx}, Y_{vtx}, Z_{vtx}, T_{vtx})$, after the vertex reconstruction. The vertex reconstruction was processed as follows.

Z_{vtx} reconstruction

Figure 5.16 shows a cartoon of the π^0 reconstruction. The following geometrical relations hold:

$$r_{12}{}^2 = d_1{}^2 + d_2{}^2 - 2d_1 d_2 \cos\theta, \tag{5.15}$$

$$d_1 = \sqrt{r_1{}^2 + (dz)^2}, \tag{5.16}$$

$$d_2 = \sqrt{r_2{}^2 + (dz)^2}, \tag{5.17}$$

where r_{12} is the distance between the hit positions of the two photons, θ is the angle between the momenta of the two photons, d_1 and d_2 are the distances between the decay vertex and the hit positions, and r_1 and r_2 are the distances of the hit positions from the z-axis. On the other hand, the invariant mass of the two photons relates on E_{γ_1}, E_{γ_2}, and θ as described in Eq. 2.1. Using Eq. 2.1 and Eqs. 5.15-5.17, we calculated dz to each pair of photons. The error, σ_{vtx}, was calculated from the energy and position resolutions for each photon, by propagating through these equations. In case of the $K_L \to 2\gamma$ reconstruction, we just replaced the constraint of the invariant mass from M_{π^0} to M_{K_L}.

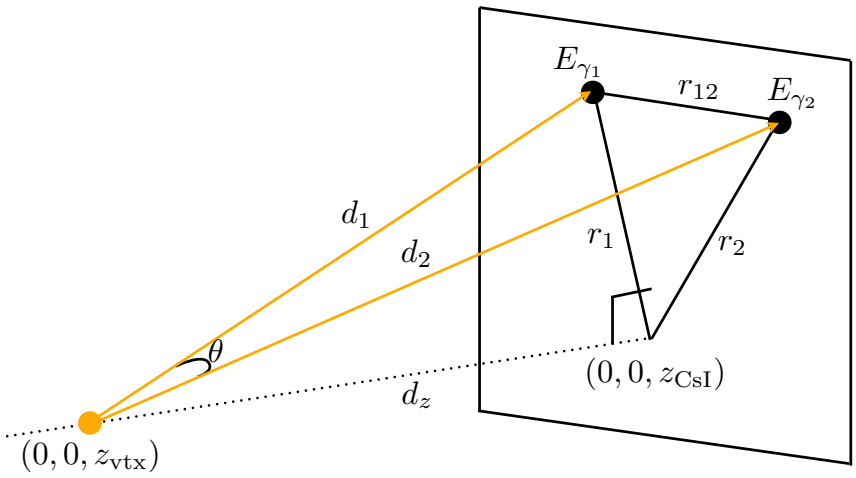

Figure 5.16: Cartoon of the π^0 reconstruction.

For the $K_L \to 3\pi^0$ and $K_L \to 2\pi^0$ modes, K_L was reconstructed from the six and four photons in the CsI calorimeter, respectively. The number of possible combinations of pairs of photons was $({}_6C_4 \times {}_4C_2 \times {}_2C_2)/3! = 15$ for $3\pi^0$ and $({}_4C_2 \times {}_2C_2)/2! = 3$ for $2\pi^0$. The decay vertex (Z_{vtx}) and the error of the vertex (σ_{vtx}) were calculated for all possible π^0 combinations. To find the best combination of the pairs of photons, we defined the variance named "pairing χ_z^2" as:

$$\chi_z^2 = \sum_{i=1}^{n} \frac{(Z_i - \bar{Z})^2}{\sigma_i^2}, \tag{5.18}$$

$$\bar{Z} = \frac{\sum_{i=1}^{n} Z_i/\sigma_i^2}{\sum_{i=1}^{n} 1/\sigma_i^2}, \tag{5.19}$$

where n is the number of π^0: 3 for $K_L \to 3\pi^0$ and 2 for $K_L \to 2\pi^0$. Z_i is the vertex position of i-th π^0, and σ_i is the error of it. We selected the photon pairing with the smallest χ_z^2, and assigned $\bar{Z}$ to the K_L vertex.

X_{vtx} and Y_{vtx} reconstruction for $K_L \to 3\pi^0$ and $K_L \to 2\pi^0$

The vertex reconstruction with the assumption that π^0 decayed on the beam axis was over-constrained condition for the $K_L \to 3\pi^0$ and $K_L \to 2\pi^0$; therefore, we determined the x and y positions of the vertex. We calculated the vertex position in x-y plane at the interpolated position between the T1 target and the center of energy on the CsI surface. Assuming the T1 target

as a point source, the following equations hold:

$$X_{vtx} = X_{coe}\frac{Z_{vtx}-Z_{target}}{Z_{csi}-Z_{target}}, \quad (5.20)$$

$$Y_{vtx} = Y_{coe}\frac{Z_{vtx}-Z_{target}}{Z_{csi}-Z_{target}}, \quad (5.21)$$

$$X_{coe} = \frac{\sum_{i=1}^{n} x_i E_i}{\sum_{i=1}^{n} E_i}, \quad (5.22)$$

$$Y_{coe} = \frac{\sum_{i=1}^{n} y_i E_i}{\sum_{i=1}^{n} E_i}, \quad (5.23)$$

where n is the number of photons: 6 for $K_L \to 3\pi^0$ and 4 for $K_L \to 2\pi^0$, x_i and y_i are the hit positions of i-th photon at the CsI surface, E_i is the energy of i-th photon, X_{coe} and Y_{coe} are the center of energy at the CsI surface, $(X_{vtx}, Y_{vtx}, Z_{vtx})$ is the three-dimensional position of the vertex and Z_{vtx} is same as $\bar{Z}$ in Eq. 5.19. $Z_{target} = -21507$ mm is the z position of the T1 target, and $Z_{csi} = 6148$ mm is the z position at the front surface of the CsI calorimeter.

In case of $K_L \to 2\gamma$, we just used $(0, 0, Z_{vtx})$ for the vertex position.

T_{vtx} reconstruction

Once we determined the vertex position, we calculated the time when the initial K_L had decayed (vertex time, T_{vtx}). For each photon, we calculated the flight length from the vertex to the hit position on the CsI surface and subtracted the flying time from the cluster hit timing as follows.

$$d_i = \sqrt{(x_i - X_{vtx})^2 + (y_i - Y_{vtx})^2 + (Z_{csi} - Z_{vtx})^2}, \quad (5.24)$$

$$T_i = t_i - d_i/c, \quad (5.25)$$

where d_i is the distance from the vertex to the hit position on the CsI surface of the i-th photon, T_i is the calculated time when the i-th photon was at the vertex, and c is light velocity. We defined the vertex time as the weighted mean of each photon timing at the vertex as:

$$T_{vtx} = \frac{\sum_{i=1}^{n} T_i/\sigma_i^2}{\sum_{i=1}^{n} 1/\sigma_i^2}, \quad (5.26)$$

where $\sigma_i = 3.8/\sqrt{E_i} \oplus 0.19$ is the timing resolution of a cluster in unit of ns as a function of E_i, which was obtained from the $K_L \to 3\pi^0$ result in advance.

5.3.2 Mass and Momentum Reconstruction

In the analysis of $K_L \to 3\pi^0$ and $K_L \to 2\pi^0$ decays, we just assumed the nominal π^0 invariant mass. We thus finally reconstructed the K_L mass. We re-calculated the four-momentum of each π^0 assuming the reconstructed vertex position of $(X_{vtx},\ Y_{vtx},\ Z_{vtx})$ without the π^0 mass constraint. The invariant mass of the reconstructed π^0 fluctuated from the nominal π^0 mass due to the resolution. Finally, we got the four-momentum of the initial K_L by summing all four-momenta of π^0s. In case of $K_L \to 2\gamma$, the four-momentum of K_L was calculated by assuming the reconstructed vertex position.

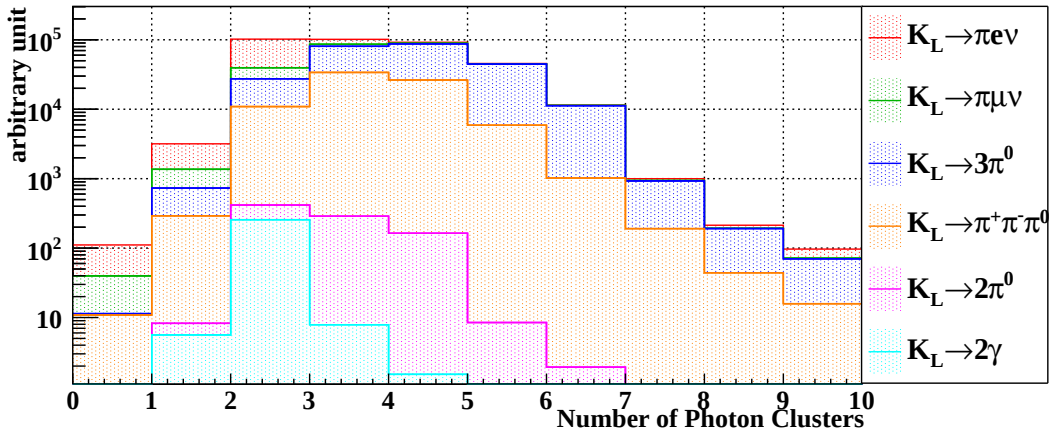

Figure 5.17: Resultant distribution of the number of photon clusters with the requirement of Half Et $>$ 350 MeV in the MC simulation. Objective normalization modes and the main four decay modes are drawn. The histograms are stacked in order.

5.4 Event Selection

Once reconstructions finished, we moved onto the event selection to purify the signal mode. In case of $K_L \to 3\pi^0$, only by selecting events that contained just six photon clusters in the CsI calorimeter, we achieved 10 % background contamination level. For the $K_L \to 2\pi^0$ and $K_L \to 2\gamma$ modes, on the other hand, when we require the number of photon clusters was four or two, signal to background ratios were only 0.18 % for $K_L \to 2\pi^0$ and 0.25 % for $K_L \to 2\gamma$, as shown in Fig. 5.17.

Kinematic cuts were applied to discriminate signal events from background events by using information of photons in the CsI calorimeter. Veto counters' activities were used for vetoing the events in which extra activities existed. We describe the selection flows for each mode in this section.

5.4.1 Primary Event Selection and Veto

At the first process of the event selection, we required several conditions as a primary event selection to compare distributions in the experimental data and the MC simulation. The main purpose of the primary event selection was the definition of the time window for the coincidence of photons and the definition of the fiducial region in the CsI calorimeter. The uncertainty of the online trigger condition was also to be removed here. We also applied veto cut to enhance the signal to noise ratio. The criteria of the primary selection are listed as follows.

Δ Vertex Time :

As all photons were generated at the same point and the same time, the difference between T_i in Eq. 5.25 and T_{vtx} in Eq. 5.26 should be small. We required $|T_i - T_{vtx}| < 3$ ns for all photons. This selection guaranteed all photons were generated at the same time.

Half Et :

"Half Et", which applied the requirement on the energies in both left and right banks of the CsI calorimeter, was used in the online trigger, as described in Sec. 3.3.1. Since the gain and timing adjustments were not perfect in the stage of data taking, the effective energy threshold

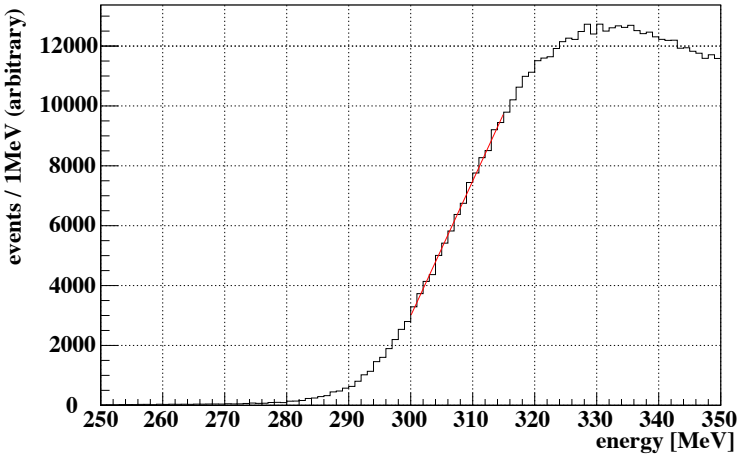

Figure 5.18: Lower Half Et distribution with no selection. The straight line shown in red is the result of linear fit. The half maximum is located at 307.5 MeV.

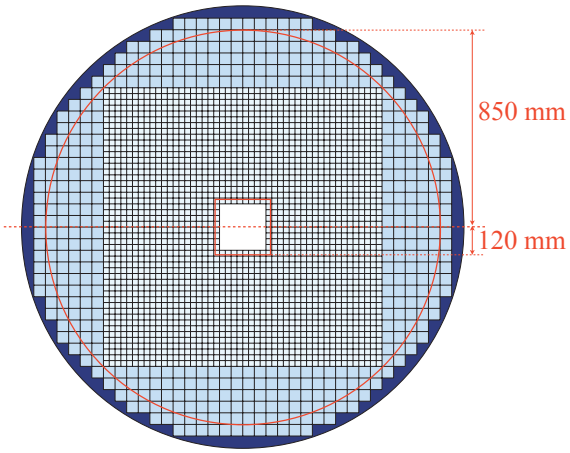

Figure 5.19: Front view of the CsI calorimeter with the limitation lines of the photon hit positions. The central red square shows the innermost limitation and the outer red circle shows the outermost limitation. If any photons hit inside the central square or outside the outer circle, the event was rejected.

was smeared. In the analysis, we calculated the lower Half Et as sum of any activities within the same 150-ns-wide time window as cluster seeds in each left and right half of the CsI calorimeter. Figure 5.18 shows the lower Half Et distribution in the experimental data with no selection. It shows the online threshold was set around 307.5 MeV. To remove the online threshold uncertainty, we set the offline threshold of the Half Et at 350 MeV.

Innermost Photon Hit Position :

We required that the hit position of the innermost photon in the CsI calorimeter should be outside the 240 $\times$ 240 mm^2 square area at the center. This selection removed photons with shower leakage into the beam hole. The limitation is shown in Fig. 5.19 with the limitation of the outermost photon hit position described in the next.

Outermost Photon Hit Position :

We required that the outermost photon in the CsI calorimeter should be within 850 mm from the center of the CsI calorimeter. This was to remove photons with shower leakage out of the calorimeter.

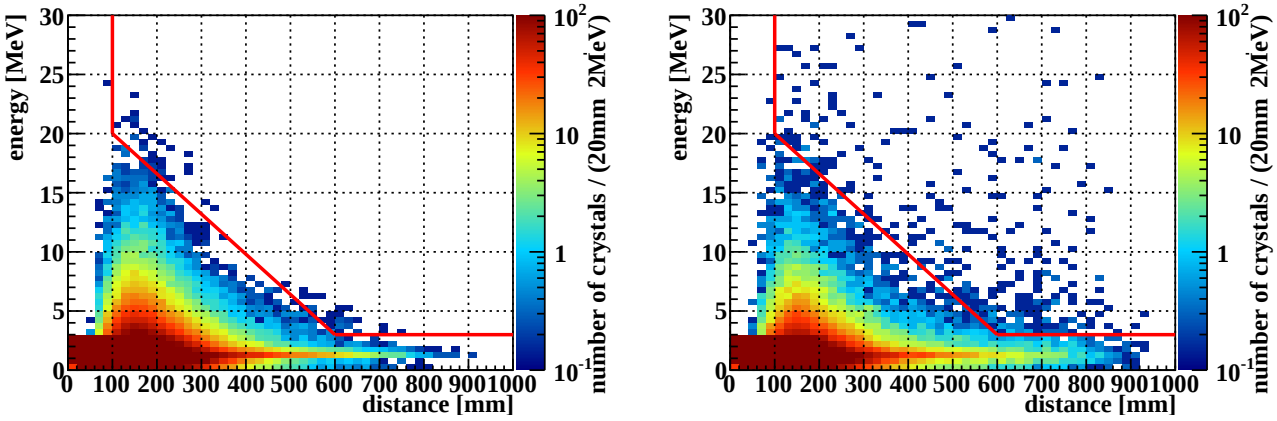

Figure 5.20: Energy deposition in a single hit crystal versus the distance from the nearest photon cluster. The red lines show the energy threshold as a function of the distance. The left figure shows the $K_L \to 2\pi^0$ MC simulation with all selections for $K_L \to 2\pi^0$ except the CsI veto, and the right figure shows the $K_L \to 3\pi^0$ MC simulation with same selections as a background mode for the $K_L \to 2\pi^0$ mode. The number of events in these distributions were normalized based on their branching fractions.

Extra Cluster Veto :

In addition to its main role of measuring the energies and positions of photons, the CsI calorimeter also served as a veto counter for extra photons. We used the closest photon clusters in the time domain for the event reconstruction described in Sec. 5.3. When one or more extra clusters exist in the event time, we vetoed this event. We set the time window of this veto to be ± 10 ns.

CsI Veto :

Cluster seeds not included in any clusters, *i.e.* "single crystal hits", were also vetoed. However, a photon occasionally created single crystal hits near its genuine cluster due to fluctuations in the electromagnetic process, and thus this veto could cause acceptance loss for signal candidates. To avoid this loss, the veto energy threshold for a single crystal hit (E_{thre}) was determined as a function of the distance from the closest cluster, d, as shown in Fig. 5.20:

$$E_{thre} = 23.4 - 0.034d \text{ MeV} \quad \text{for } 100 < d < 600 \text{ mm}, \tag{5.27}$$

$$E_{thre} = 3 \text{ MeV} \quad \text{for } d > 600 \text{ mm}. \tag{5.28}$$

Activities within $d < 100$ mm region were not vetoed. The time window of this veto was set to be ± 10 ns. In case of $K_L \to 3\pi^0$, this and below two veto sets were not used.

CV Veto :

The main role of CV was to veto the $K_L \to \pi^+\pi^-\pi^0$ background for the $K_L \to 2\pi^0$ mode and the $K_L \to \pi^\pm e^\mp \nu$ background for the $K_L \to 2\gamma$ mode. The energy threshold was set to 0.4 MeV and the time window was set to ± 10 ns for each module.

MB Veto :

The main role of MB was to veto the $K_L \to 3\pi^0$ background for the $K_L \to 2\pi^0$ and the $K_L \to 2\gamma$ modes. The energy threshold was set to 5 MeV and the time window was set to -26–$+34$ ns for each inner module. We did not use the outer modules because the outer

modules had many accidental activities of total 1.8 MHz which was mainly caused by particles coming from the primary beam line in this engineering run period[1)].

5.4.2 $K_L \to 3\pi^0$ Selection

With the primary event selection, 96 % of the six cluster events were made by $K_L \to 3\pi^0$ decays. The following selections were applied to enhance the purity of the $K_L \to 3\pi^0$ events. In case of $K_L \to 3\pi^0$, small amount of $K_L \to 3\pi^0$ events were contained in the accidental data. They were added to the MC simulation; therefore, a negligible amount of $K_L \to 3\pi^0$ events contaminated in MC simulations of other modes. Figure 5.21 shows distributions of all parameters which are used for the following selection. In each figure, primary selection is applied. In addition, the previous selections before itself are also applied, *e.g.* the primary selection and the selections of Z_{vtx} and ΔK_L mass are applied to the distribution in Fig. 5.21(c). In case of $K_L \to 3\pi^0$, the dominant background mode was $K_L \to \pi^+\pi^-\pi^0$.

Z_{vtx} :
: The background events, dominated by $K_L \to \pi^+\pi^-\pi^0$, tended to locate downstream region because deposit energies were smaller and the Z_{vtx} moved downstream. As NCC, located at $z = 1990$–2435 mm, limited the acceptance, the upstream region of NCC was excluded from the decay region. We required Z_{vtx} to be in the range of $2000 < Z_{vtx} < 5400$ mm.

ΔK_L Mass :
: The reconstructed K_L mass spectrum is shown in Fig. 5.21(b). There was a peak at the nominal K_L mass: 497.614 MeV/c^2[1]. The tail component was consisted of the other BG modes and also the $K_L \to 3\pi^0$ events whose photon pairing are missed. We selected the peak region ± 15 MeV/c^2.

Photon Energy :
: The energies of photons tend to be small in the background events. Figure 5.21(c) shows the distribution of the minimum energies among six photons. We required the energy to be larger than 50 MeV.

$\Delta\pi^0$ Mass :
: We re-calculated the invariant mass of π^0 with the reconstructed K_L vertex position, which was the weighted mean of three vertices of the π^0s reconstructed by assuming the nominal π^0 mass, as described in Section 5.3.2. The reconstructed π^0 mass therefore fluctuated from the nominal π^0 mass. The fluctuation reflected vertices consistency among three π^0s. We required the deviation of the reconstructed mass from the nominal π^0 mass was less than 10 MeV/c^2. This selection guaranteed the reconstructed K_L vertex was close to the π^0 vertex.

Cluster Distance :
: We required the distance between any two photon clusters to be more than 150 mm. This selection was imposed to avoid the uncertainty of the mis-identification of two photons as one.

Figure 5.22 shows the event reduction and the purity of signal modes in the remaining events as a function of event selection process from the primary event selection. The event reduction was

[1)] The primary beam line downstream of the T1 target toward the beam dump runs next to the KOTO detector separated with thick concrete and iron shields. There was a path where particles could enter the KOTO detector across the shields with scattering. It increased the accidental activity of the outer modules of MB.

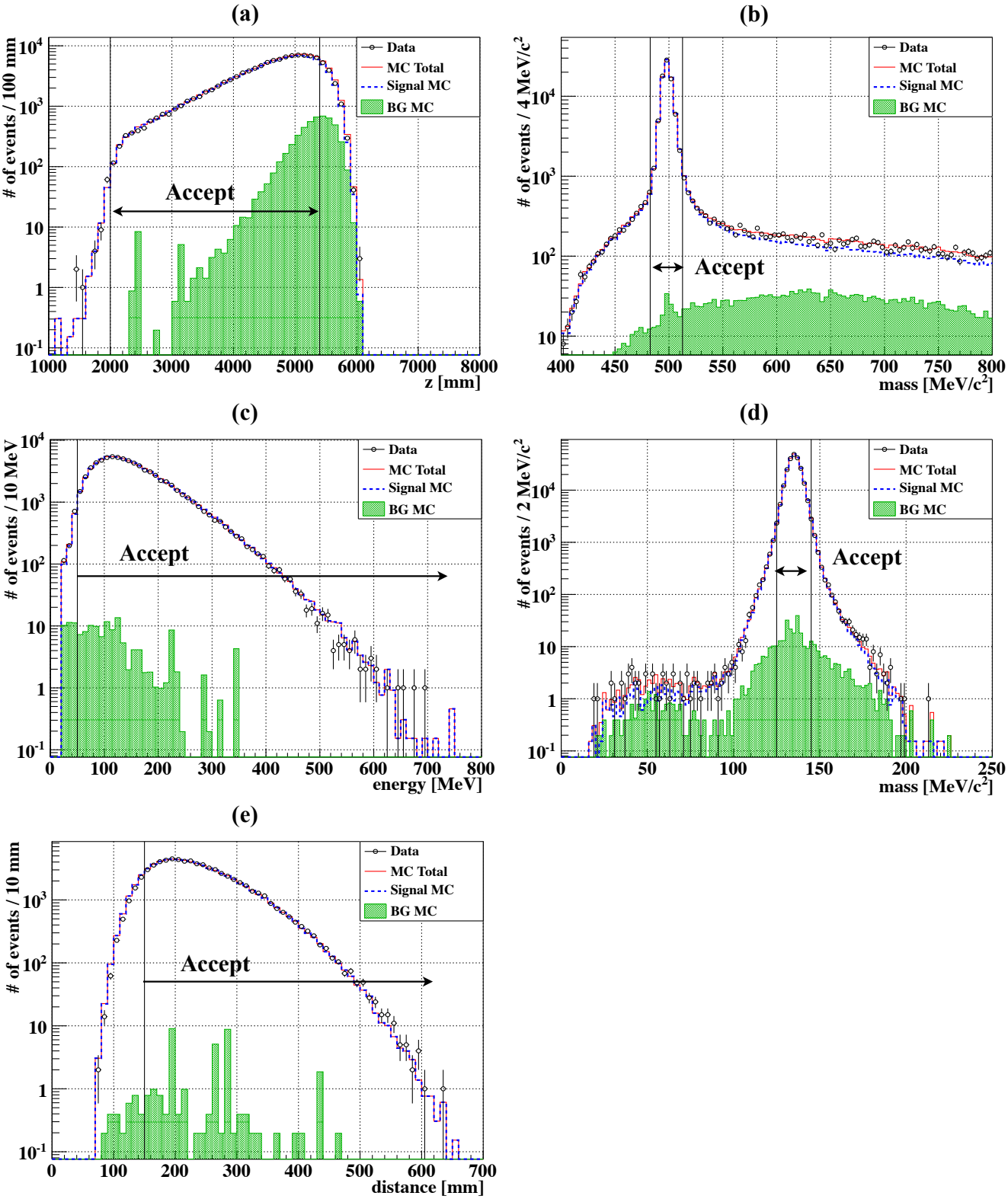

Figure 5.21: Distributions of the $K_L \to 3\pi^0$ event selection. (a) Reconstructed K_L vertex z position; (b) Reconstructed K_L mass; (c) Minimum energy among six photons; (d) Reconstructed three π^0s' mass at the K_L vertex position; (e) Shortest distance among all pairs of photons. In each figure, the open circles show the experimental data; the red solid line shows the sum of all MC simulations; the blue dashed line shows the $K_L \to 3\pi^0$ MC simulation; the green histogram shows other MC simulations for BG. All histograms of MC simulations are normalized by using the final result.

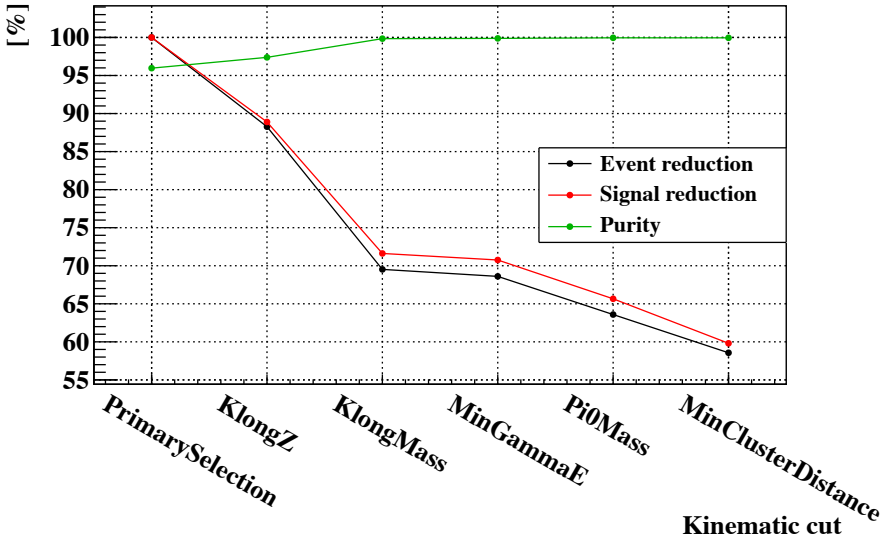

Figure 5.22: $K_L \to 3\pi^0$ event selection flow. Reduction is defined by normalizing to the number of events after the primary event selection. The black dots show the total event reduction in the experimental data, the red dots show the signal reduction in the MC simulation, and the green dots show the fraction of the number of simulated signal events in all MC simulation events.

defined as the fraction of the number of events after the primary event selection in the experimental data. The purity was defined as the fraction of the number of signal simulation events in all simulation events. After the event selection, the purity exceeded 99.9 %. The reconstructed K_L momentum spectra of experimental data and MC simulation, shown in Fig. 5.23, were consistent.

5.4.3 $K_L \to 2\pi^0$ Selection

The purity with the primary event selection was 1 % in the case of $K_L \to 2\pi^0$. We enhanced it by applying the following event selections. Figures 5.24 and 5.25 show the parameters for the following selections as in the case of $K_L \to 3\pi^0$. In case of $K_L \to 2\pi^0$, the dominant background mode was

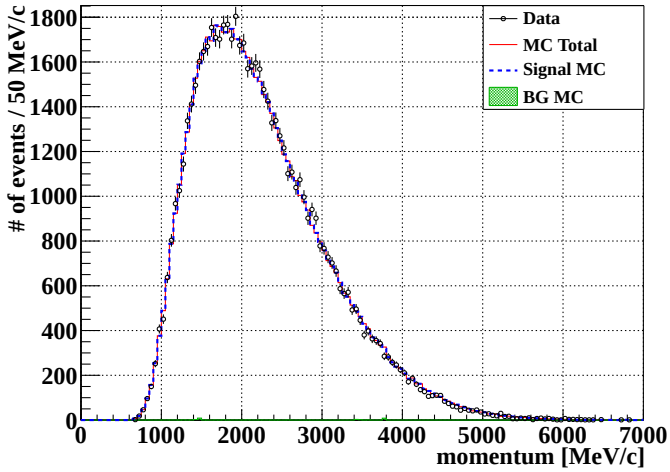

Figure 5.23: Reconstructed K_L momentum spectrum with the $K_L \to 3\pi^0$ selection. The meanings of the histogram here are the same as in Fig. 5.21.

$K_L \to 3\pi^0$.

Z_{vtx} :
Z_{vtx} was limited in the same condition of the $K_L \to 3\pi^0$ selection to determine the same fiducial region for the two modes.

ΔK_L Mass :
The reconstructed K_L mass selection was applied with the same limitation as the $K_L \to 3\pi^0$ selection. The BG, which dominated by $K_L \to 3\pi^0$, did not peak at the K_L nominal mass. The signal purity was enhanced from 1 % to 25 %.

Photon Energy :
The photon energy selection was applied with the same criteria as the $K_L \to 3\pi^0$ selection.

$\Delta\pi^0$ Mass :
We required the deviation of the reconstructed mass from the nominal π^0 mass was less than 6 MeV/c^2 as shown in Fig. 5.24(d).

Cluster Distance :
The same cluster distance selection was applied on the $K_L \to 2\pi^0$ analysis as in the case of $K_L \to 3\pi^0$ selection.

Center of Energy :
The center of energy of all photons at the CsI surface, calculated by Eqs. 5.22 and 5.23, should locate inside the beam shape. This selection was used to reject events with missing energies. We required the both x and y of the center of energy position to be within ± 60 mm.

Shape χ^2 :
The shape χ^2 was an index of goodness of the cluster shape. It separated a normal cluster made of one photon from a fused cluster made of multiple photons. The shape χ^2 was defined as:

$$\text{shape } \chi^2 = \sum_i \left(\frac{E_i^{obs} - E_i^{ref}}{\sigma_i^{ref}} \right)^2 , \tag{5.29}$$

where $E^{obs(ref)}$ denotes observed (expected) energy deposit in each crystal, and σ^{ref} is the standard deviation of the expected energy deposit. E^{ref} and σ^{ref} were derived from the MC simulation for various photon energies, incident polar angles, and azimuthal angles[39]. The reference, whose energy and incident angle were closest to the photon, was selected event by event to calculate shape χ^2. The shape χ^2 was required to be less than 5.

The purity was improved to 89 % with the signal efficiency of 61 % from the primary selection. The main contribution was from the K_L mass cut as shown in Fig. 5.26. Reconstructed K_L momentum spectrum is shown in Fig. 5.27. It was also well reproduced by the MC simulation.

5.4.4 $K_L \to 2\gamma$ Selection

The purity with the primary event selection was 7.4 %. The following selections were applied to purify the signal events. The distributions of the parameters for the selections are shown in Fig. 5.28. In case of $K_L \to 2\gamma$, the dominant background mode was $K_L \to 3\pi^0$, too.

Outermost Photon Hit Position :
We added a requirement to the hit position of the outermost photon in the CsI calorimeter. Photons from BG decays, which were mainly $K_L \to 3\pi^0$, tended to decay near the

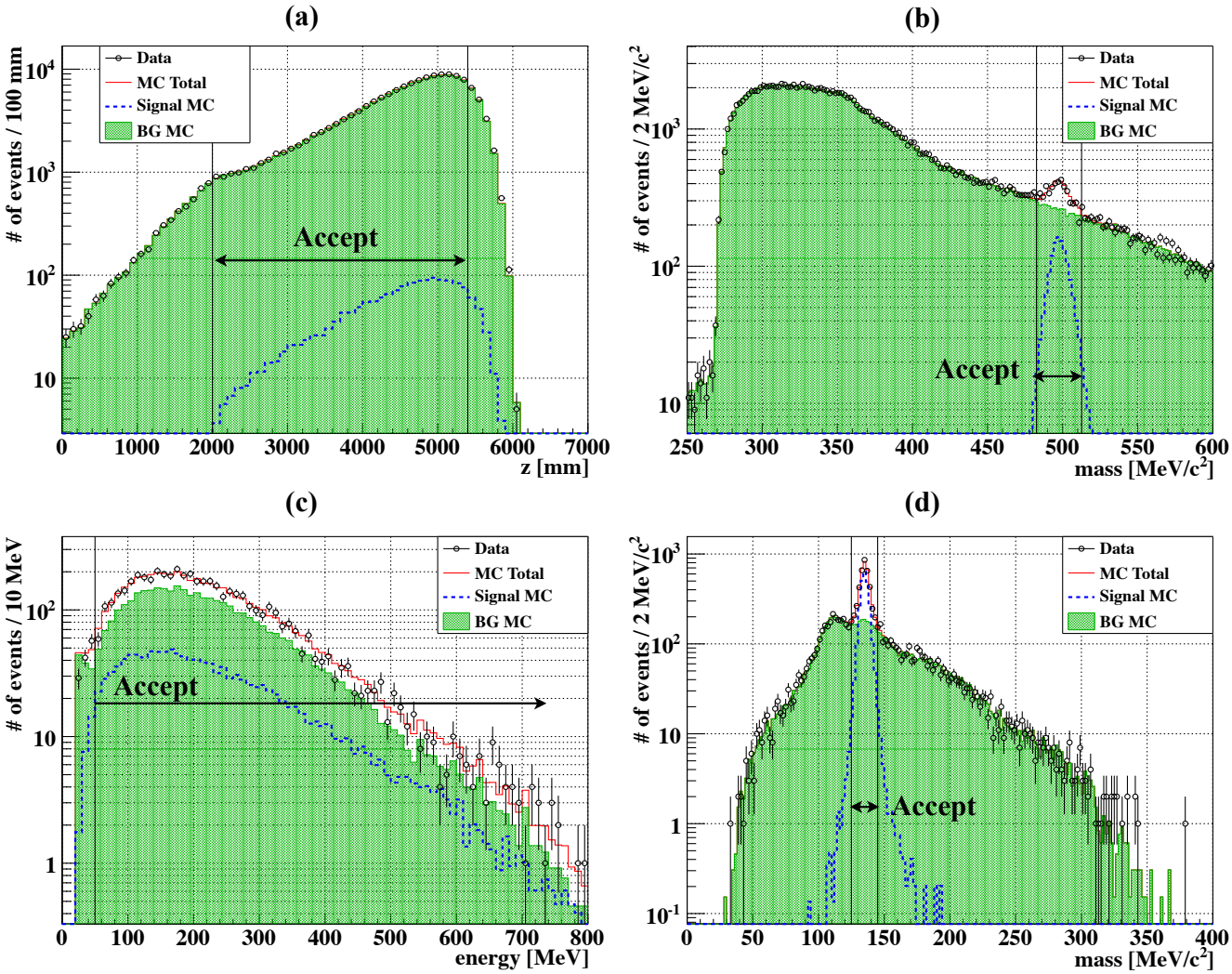

Figure 5.24: Distributions of the $K_L \to 2\pi^0$ event selection. (a) Reconstructed K_L vertex z position; (b) Reconstructed K_L mass; (c) Minimum energy among four photons; (d) Reconstructed two π^0s' mass at the K_L vertex position. In each figure, the blue dashed line shows the $K_L \to 2\pi^0$ MC simulation. The meanings of the other histograms here are the same as in Fig. 5.21.

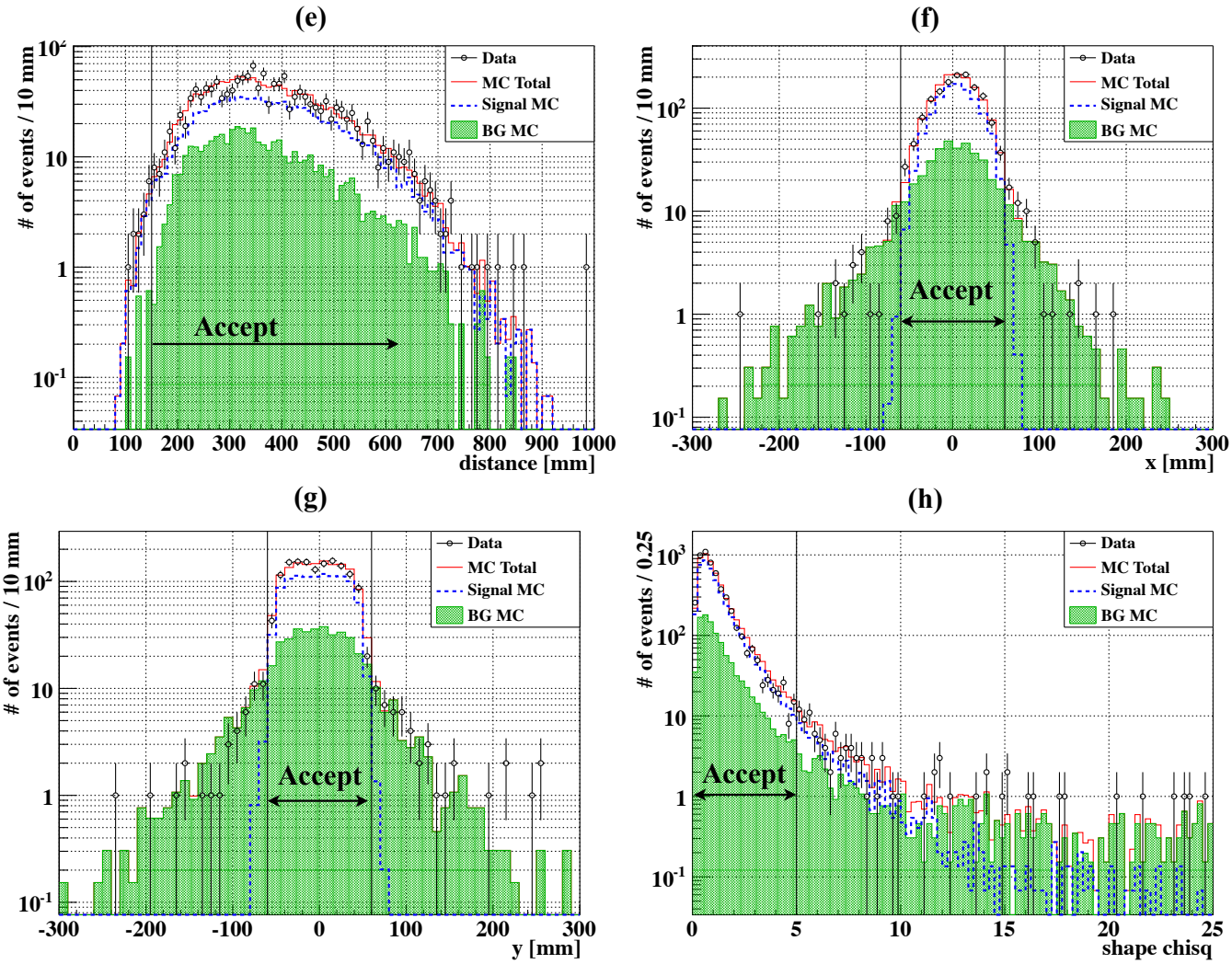

Figure 5.25: Distributions of the $K_L \to 2\pi^0$ event selection (continued). (e) Shortest distance among all pair of photons; (f) x position of the center of energy; (g) y position of the center of energy; (h) Shape χ^2 of four photons.

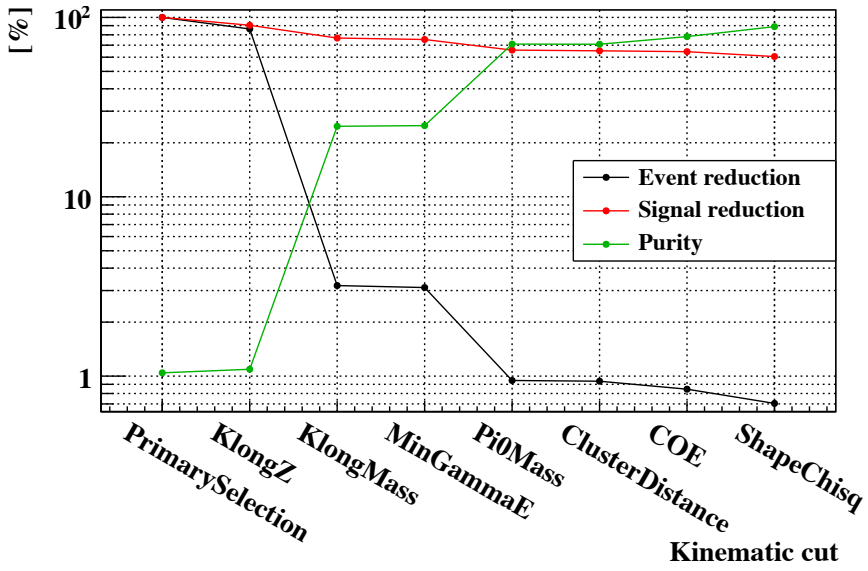

Figure 5.26: $K_L \to 2\pi^0$ event selection flow. The meanings of the plots here are the same as in Fig. 5.22

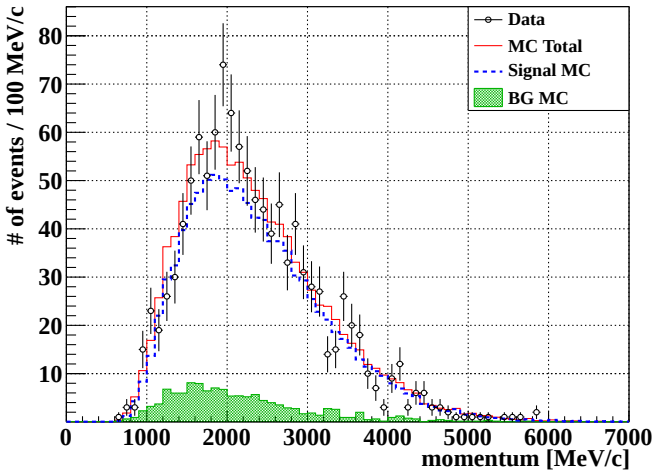

Figure 5.27: Reconstructed K_L momentum spectrum with the $K_L \to 2\pi^0$ selection. The meanings of the histograms here are the same as in Fig. 5.24.

Table 5.1: Event selections for the $K_L \to 3\pi^0$ mode

Kinematic Cut	Min.	Max.
Δ Vertex Time		3 ns
Δ K_L Mass	-15 MeV/c^2	15 MeV/c^2
Half Et	350 MeV	
$\Delta\pi^0$ Mass		10 MeV/c^2
Photon Energy	50 MeV	
Innermost Photon Hit Position	120 mm (square)	
Outermost Photon Hit Position		850 mm (radial)
Cluster Distance	150 mm	
Z_{vtx}	2000 mm	5400 mm
Veto	Energy Threshold	Time Window
Extra Cluster	-	-10 ns – $+10$ ns

CsI calorimeter in order to inject only two photons into the CsI calorimeter. As shown in Fig. 5.28(a), even an outer photon enters the central region of the CsI calorimeter for the BG decays. We required the radial hit position of the outermost photon to be outer than 450 mm.

Z_{vtx} :

Z_{vtx} was used for the event selection as in the case of the other modes. In case of $K_L \to 2\gamma$, photons from BG decays had lower energies, and their invariant mass was required not π^0 but K_L; thus, the reconstructed Z_{vtx} located downstream as shown in Fig. 5.28(b). We required Z_{vtx} to be in the range of $2000 < Z_{vtx} < 5000$ mm.

K_L Transverse Momentum :

To guarantee that there were no other particle which carried away finite transverse momentum, the reconstructed transverse momentum of K_L was required to be zero. In fact, the beam broadening in x-y plane and the resolutions of the CsI calorimeter caused finite transverse momentum even $K_L \to 2\gamma$. We required the transverse momentum to be less than 50 MeV/c.

Shape χ^2 :

The shape χ^2 was used for the event selection to remove fused clusters. The criteria of 5 is same as in the case of $K_L \to 2\pi^0$.

Figure 5.29 shows the cut flow for the $K_L \to 2\gamma$ selection. The purity was improved to 90 % with the signal efficiency of 43 % from the primary event selection. The reconstructed K_L momentum shown in Fig. 5.30 was also well reproduced as in the cases of $K_L \to 3\pi^0$ and $K_L \to 2\pi^0$.

5.4.5 Selection Summary

The event selections for each mode including the primary event selection are summarized in Tabs. 5.1-5.3.

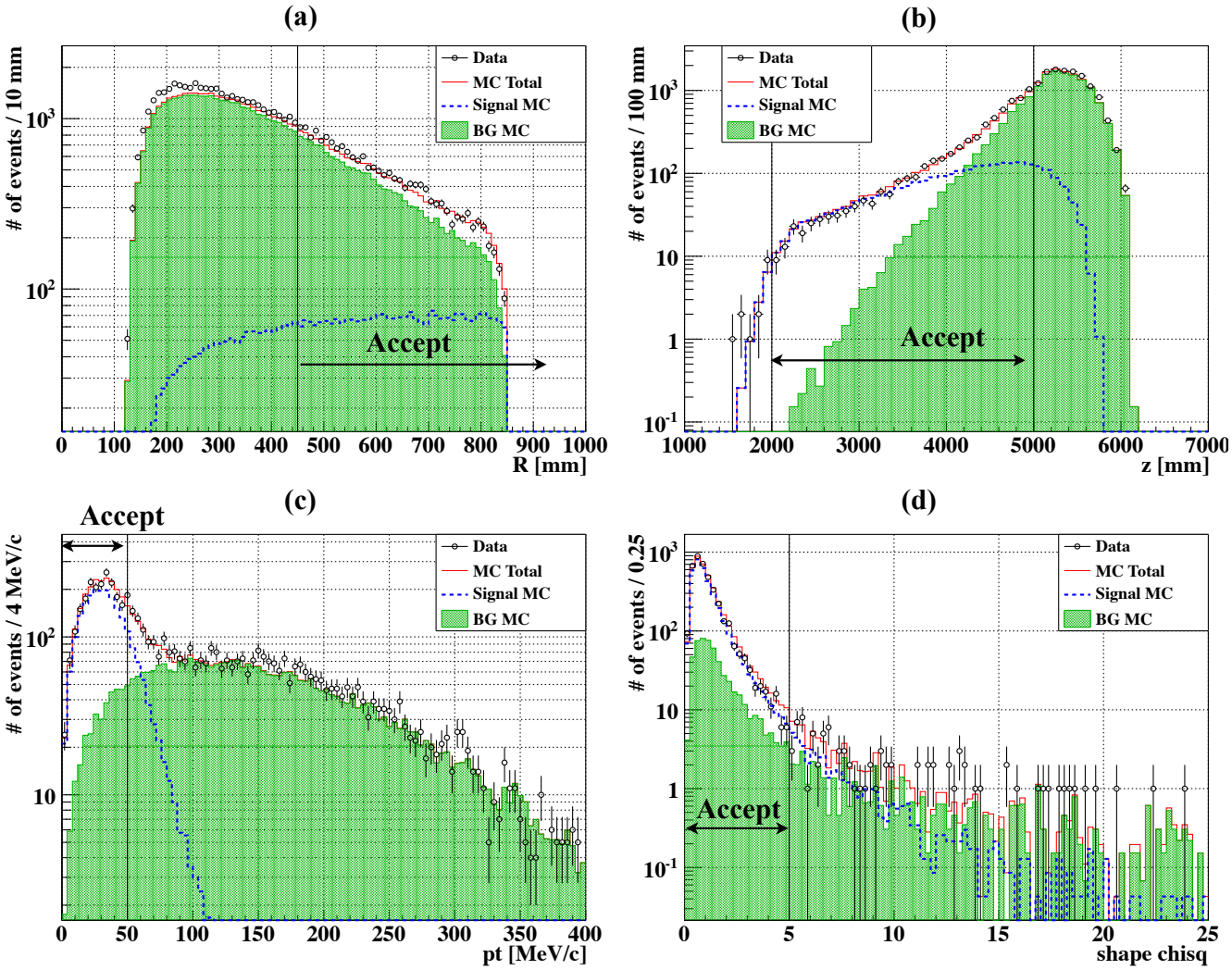

Figure 5.28: Distribution of the $K_L \to 2\gamma$ event selection. (a) Outermost photon hit position (radial); (b) Reconstructed K_L vertex z position; (c) Reconstructed K_L transverse momentum; (d) Shape χ^2 of two photons. In each figure, the blue dashed line shows the $K_L \to 2\gamma$ MC simulation. The meanings of the histograms here are the same as in Fig. 5.21.

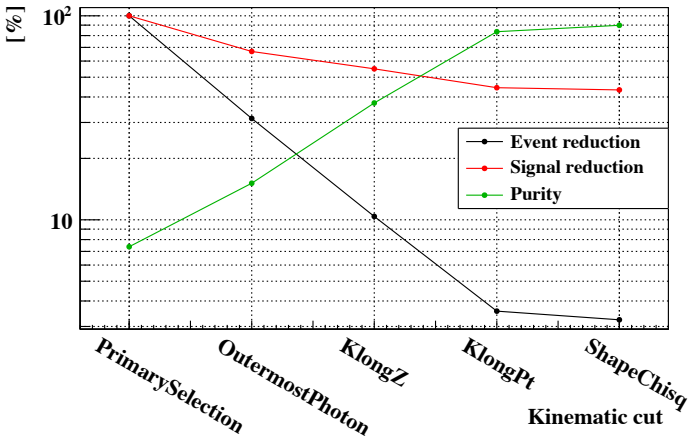

Figure 5.29: $K_L \to 2\gamma$ event selection flow. The meanings of the plots here are the same as in Fig. 5.22

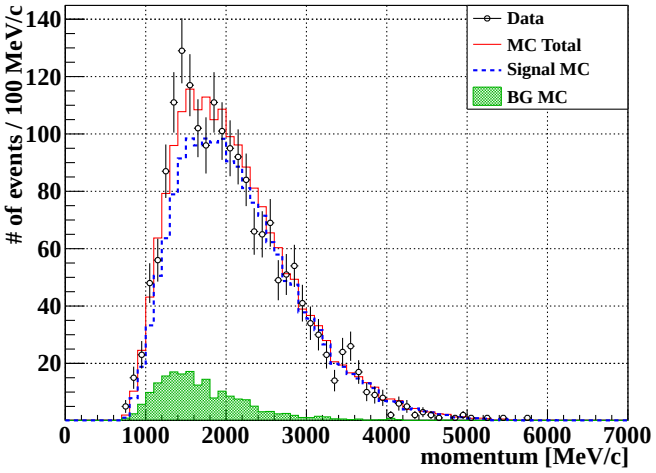

Figure 5.30: Reconstructed $K_L \to 2\gamma$ momentum spectrum. The meanings of the histograms here are the same as in Fig. 5.28.

Table 5.2: Event selections for the $K_L \to 2\pi^0$ mode

Kinematic Cut	Min.	Max.
Δ Vertex Time		3 ns
Δ K_L Mass	-15 MeV/c^2	15 MeV/c^2
Half Et	350 MeV	
$\Delta\pi^0$ Mass		6 MeV/c^2
Photon Energy	50 MeV	
Innermost Photon Hit Position	120 mm (square)	
Outermost Photon Hit Position		850 mm (radial)
Cluster Distance	150 mm	
Z_{vtx}	2000 mm	5400 mm
Shape χ^2		5
Center of Energy		60 mm (square)
Veto	**Energy Threshold**	**Time Window**
Extra Cluster	-	-10 ns – $+10$ ns
CsI Crystal	3–20 MeV	-10 ns – $+10$ ns
CV	0.4 MeV	-10 ns – $+10$ ns
MB Inner	5 MeV	-26 ns – $+34$ ns

Table 5.3: Event selections for the $K_L \to 2\gamma$ mode

Kinematic Cut	Min.	Max.
Δ vertex time		3 ns
Half Et	350 MeV	
Transverse momentum		50 MeV/c
Innermost photon hit position	120 mm (square)	
Outermost photon hit position	450 mm (radial)	850 mm (radial)
Z_{vtx}	2000 mm	5000 mm
Shape χ^2		5
Veto	**Energy Threshold**	**Time Window**
Extra Cluster	-	-10 ns – $+10$ ns
CsI Crystal	3–20 MeV	-10 ns – $+10$ ns
CV	0.4 MeV	-10 ns – $+10$ ns
MB Inner	5 MeV	-26 ns – $+34$ ns

Table 5.4: Number of reconstructed events after applying all selections for the $K_L \to 3\pi^0$. Only the most dominant decay mode with respect to the background is listed because this dominant mode was already negligibly small. The error of the acceptance is the statistical error of the MC simulation.

Data	Rec_{data}		
inclusive	65315		
MC	A_{mode}	$A_{mode} \times Br.$	Fraction (%)
$K_L \to 3\pi^0$ (Signal)	$(4.269 \pm 0.007) \times 10^{-4}$	$(8.332 \pm 0.013) \times 10^{-5}$	99.95
$K_L \to \pi^+\pi^-\pi^0$	$(1.74 \pm 0.19) \times 10^{-7}$	$(2.18 \pm 0.23) \times 10^{-8}$	0.03
A_{total}		$(8.336 \pm 0.013) \times 10^{-5}$	

5.5 Comparison of the Three Modes

The acceptances of the three signal modes were estimated by the MC simulation. The acceptance of each mode (A_{mode}) was calculated as:

$$A_{mode} = \frac{Rec_{mode}}{Gen_{mode}}, \tag{5.30}$$

where Rec_{mode} is the number of reconstructed events after applying all selections, and Gen_{mode} is the number of generated K_L with this decay mode at the beam exit. The total acceptance which includes all decay modes inclusively was calculated with the weight of their branching fractions listed in Tab. 4.2 as:

$$A_{total} = \sum_{mode} A_{mode} \times Br.(mode). \tag{5.31}$$

5.5.1 $K_L \to 3\pi^0$

The number of reconstructed events and acceptances are listed in Tab. 5.4. In case of $K_L \to 3\pi^0$ analysis, the background contamination was less than 0.1 %. This value was small enough to be neglected because it was smaller than both statistical error (0.39 %) uncertainty of its branching fraction (0.61 %)[1]. We thus simply estimated the number of K_L at the beam exit in the accumulated data ($Y(3\pi^0)$) as:

$$Y(3\pi^0) = \frac{Rec_{data}}{A_{total}} = (7.835 \pm 0.033) \times 10^8. \tag{5.32}$$

5.5.2 $K_L \to 2\pi^0$

In case of $K_L \to 2\pi^0$, the background contamination was larger than 10 %. We thus estimated the number of K_L at the beam exit inclusively and exclusively. For the inclusive estimation of the K_L yield, it was calculated using the number of remained events in the experimental data and the total acceptance estimated with the MC simulations including the background contamination. For the exclusive estimation of the K_L yield, on the other hand, we extracted the $2\pi^0$ fraction in the reconstructed events by subtracting the background contamination. We used the reconstructed

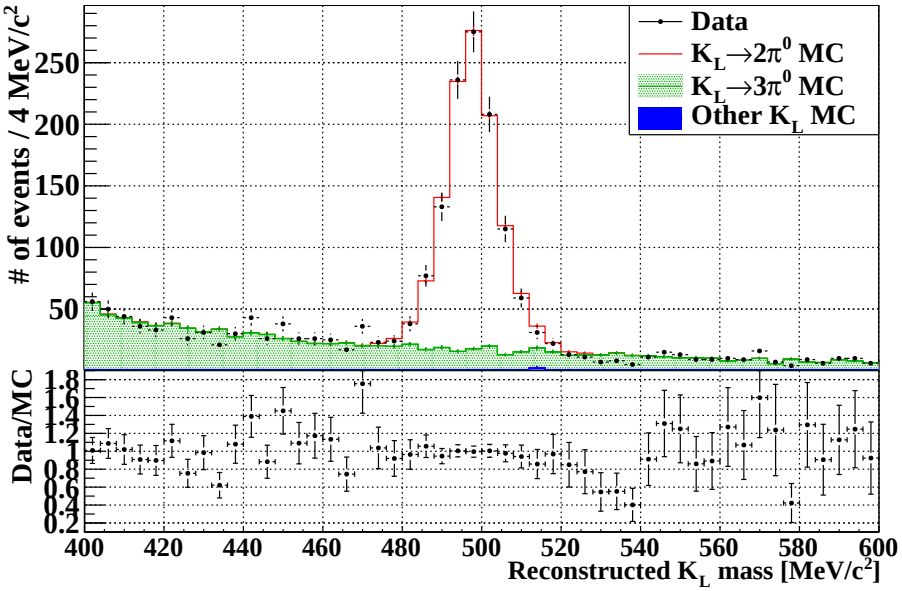

Figure 5.31: Reconstructed K_L mass spectrum with the $K_L \to 2\pi^0$ selection. Black dots show the experimental data, red hollowed histogram shows $K_L \to 2\pi^0$ MC simulation, green hatched histogram shows $K_L \to 3\pi^0$ MC simulation, and blue histogram shows the other MC simulation. The MC histograms are normalized by the $K_L \to 3\pi^0$ result, and they are stacked in order.

mass distribution shown in Fig. 5.31 to estimate the background contamination. We adjusted the scale factors for the signal MC simulation and the background MC simulation to match the data and the MC simulation by minimizing χ^2 defined as:

$$\chi^2 = \sum_{i=1}^{N} \frac{(d_i - \alpha s_i - \beta b_i)^2}{(\sigma_{d_i})^2 + (\alpha\sigma_{s_i})^2 + (\beta\sigma_{b_i})^2}, \tag{5.33}$$

where N is the number of bins, $d_i \pm \sigma_{d_i}$ is the number of events in the i-th bin of the experimental data and its statistical error, $s_i \pm \sigma_{s_i}$ is those of the signal MC simulation normalized by the $K_L \to 3\pi^0$ result, $b_i \pm \sigma_{b_i}$ is those of the background MC simulation, and α and β are the scale factors for the signal MC simulation and the background MC simulation, respectively. α and β are the free parameters. We divided the reconstructed mass distributions from 400 MeV/c^2 to 600 MeV/c^2 evenly into 50 parts (Fig. 5.31). Minimizing the χ^2, we obtained $\alpha = 0.993 \pm 0.034$ and $\beta = 0.956 \pm 0.036$ with $\chi^2/\mathrm{ndf} = 1.11$. As the number of background was 126.5 ± 4.4 when we used the K_L yield obtained from the $K_L \to 3\pi^0$ result, the scaled number of background was 120.8 ± 6.2. Therefore, the number of signals in the experimental data was 1008.2 after the background subtraction.

The number of reconstructed events and acceptances are summarized in Tab. 5.5. The inclusive K_L yield ($Y_{inc}(2\pi^0)$) and the exclusive K_L yield ($Y_{exc}(2\pi^0)$) were determined as:

$$Y_{inc}(2\pi^0) = \frac{Rec_{data}(\text{inclusive})}{A_{total}} = (7.81 \pm 0.24) \times 10^8, \tag{5.34}$$

$$Y_{exc}(2\pi^0) = \frac{Rec_{data}(\text{exclusive})}{A_{2\pi^0}} = (7.85 \pm 0.27) \times 10^8. \tag{5.35}$$

Table 5.5: Number of reconstructed events after applying all selections for $K_L \to 2\pi^0$. We listed the background modes with their contamination of more than 0.1 %.

Data	Rec_{data}		
inclusive	1129		
exclusive	1008.2 ± 34.2		
Mode	A_{mode}	$A_{mode} \times Br.$	Fraction (%)
$K_L \to 2\pi^0$ (Signal)	$(1.487 \pm 0.012) \times 10^{-3}$	$(1.284 \pm 0.011) \times 10^{-6}$	88.8
$K_L \to 3\pi^0$	$(8.23 \pm 0.29) \times 10^{-7}$	$(1.606 \pm 0.056) \times 10^{-7}$	11.1
A_{total}		$(1.446 \pm 0.012) \times 10^{-6}$	

They were consistent with each other. The acceptance of the backgrounds was also well simulated.

5.5.3 $K_L \to 2\gamma$

In case of $K_L \to 2\gamma$, the background contamination was larger than 10 %. We used the same methods as $K_L \to 2\pi^0$ and determined the K_L yield inclusively and exclusively. We used reconstructed transverse momentum spectra to calculate the χ^2 for this mode. We divided the reconstructed transverse momentum distributions from 0 MeV/c to 200 MeV/c evenly into 80 parts as shown in Fig. 5.32. Minimizing the χ^2, we obtained $\alpha = 0.973 \pm 0.025$ and $\beta = 1.023 \pm 0.031$ with $\chi^2/\mathrm{ndf} = 0.86$. As the number of background was 196.4 ± 5.6 when we assume the $K_L \to 3\pi^0$ result, the fitted number of background was 200.9 ± 8.4. The resultant number of signals in the experimental data was 1689.1 after the background subtraction.

The number of reconstructed events and acceptances are summarized in Tab. 5.6. The inclusive K_L yield ($Y_{inc}(2\gamma)$) and the exclusive K_L yield ($Y_{exc}(2\gamma)$) were determined as:

$$Y_{inc}(2\gamma) = \frac{Rec_{data}(\text{inclusive})}{A_{total}} = (7.69 \pm 0.18) \times 10^8, \tag{5.36}$$

$$Y_{exc}(2\gamma) = \frac{Rec_{data}(\text{exclusive})}{A_{2\gamma}} = (7.65 \pm 0.20) \times 10^8. \tag{5.37}$$

They were consistent with each other, too. The acceptance of the backgrounds was also well simulated.

5.5.4 Three Mode Combined

The obtained K_L yield in the accumulated data for each mode summarized in Tab. 5.7. We used exclusive K_L yields for the $K_L \to 2\pi^0$ and the $K_L \to 2\gamma$ analyses here because they were determined by only acceptance of each signal mode. We were thus able to ignore effects from uncertainties of the background acceptance. Each result was consistent within the statistical error. The average of the obtained K_L yield in the accumulated data was determined as $(7.831 \pm 0.032) \times 10^8$. In the next section, we calculated the absolute K_L yield per POT.

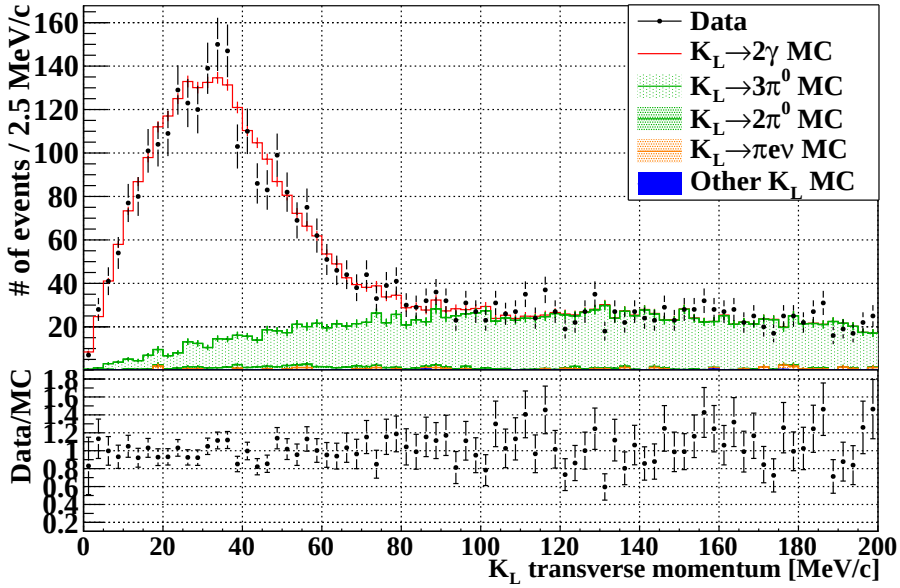

Figure 5.32: Reconstructed K_L transverse momentum spectrum with the $K_L \to 2\gamma$ selection. The black dots show the experimental data, the red hollowed histogram shows $K_L \to 2\gamma$ MC simulation, the green light hatched histogram shows $K_L \to 3\pi^0$ MC simulation, the green dark hatched histogram shows $K_L \to 2\pi^0$ MC simulation, orange hatched histogram shows $Ke3$ MC simulation, and the blue histogram shows the other MC simulations. The MC histograms are normalized by the $K_L \to 3\pi^0$ result, and they are stacked in order.

Table 5.6: Number of reconstructed events after applying all selections for $K_L \to 2\gamma$. We listed the background modes with their contamination of more than 0.1 %.

Data	Rec_{data}		
inclusive	1890		
exclusive	1689.1 ± 44.3		
Mode	A_{mode}	$A_{mode} \times Br.$	Fraction (%)
$K_L \to 2\gamma$ (Signal)	$(4.035 \pm 0.020) \times 10^{-3}$	$(2.207 \pm 0.011) \times 10^{-6}$	89.8
$K_L \to 3\pi^0$	$(1.133 \pm 0.034) \times 10^{-6}$	$(2.212 \pm 0.066) \times 10^{-7}$	9.0
$K_L \to 2\pi^0$	$(2.58 \pm 0.16) \times 10^{-5}$	$(2.23 \pm 0.14) \times 10^{-8}$	0.9
$K_L \to \pi^{\pm} e^{\mp} \nu$	$(1.4 \pm 0.4) \times 10^{-8}$	$(5.68 \pm 2.15) \times 10^{-9}$	0.2
A_{total}		$(2.46 \pm 0.01) \times 10^{-6}$	

Table 5.7: K_L yield obtained by $K_L \to 3\pi^0$, $K_L \to 2\pi^0$, and $K_L \to 2\gamma$. Combined result is also shown.

Mode	K_L Yield ($\times 10^8$)	Relative yield
$K_L \to 3\pi^0$	7.835 ± 0.033	1.001 ± 0.004
$K_L \to 2\pi^0$	7.85 ± 0.27	1.002 ± 0.034
$K_L \to 2\gamma$	7.65 ± 0.20	0.977 ± 0.026
Average	7.831 ± 0.032	1.000 ± 0.004

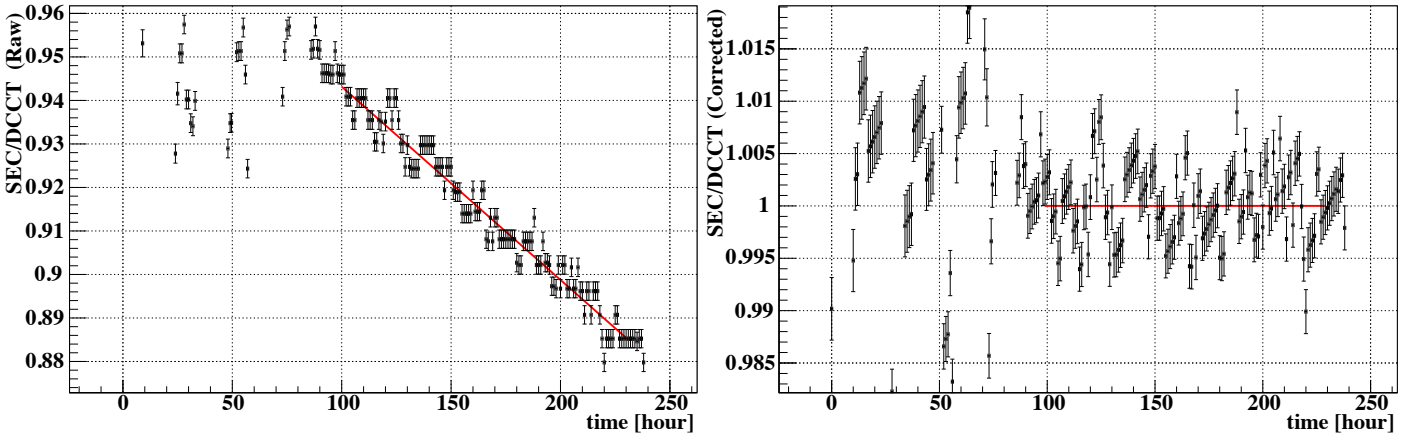

Figure 5.33: SEC/DCCT time change. The figure on the left is raw ratio between SEC count and DCCT and the figure on the right is corrected one. The error bars show the quantization errors. Large deviations in the first half were due to accelerator tuning.

5.6 K_L Flux

In this section, the absolute K_L flux is calculated by using beam intensity information. We counted the scaler counts from a secondary emission chamber (SEC) in the proton extraction line of the MR, which was used to monitor the POT value in each spill. The SEC scaler count was proportional to the proton intensity. The nominal proportionality constant of 2.59×10^9 POT/SEC was provided by the accelerator group. They found, however, that the output from SEC had been decreasing inversely proportional to running time by comparing the SEC count with the measured intensity by a current transformer in the MR, called MR-DCCT. We thus corrected the SEC count based on the running time as shown in Fig. 5.33. The total POT during the measurement (N_{POT}) was determined as $(3.355 \pm 0.013) \times 10^{16}$.

Our DAQ was able to count the trigger with dead time of only 4 clock (32 ns) after a trigger was made. It caused a loss of trigger efficiency. As an loss ratio of triggers depended on the instantaneous trigger rate, we used "Duty Factor (DF)"[41] to estimate the trigger loss during a spill. DF was defined as:

$$DF = \frac{\left[\int_0^T I(t)dt\right]^2}{\int_0^T dt \int_0^T I^2(t)dt}, \tag{5.38}$$

where $I(t)$ is spill intensity and T is spill length. If beam were perfectly flat, DF would be 1. DF and T were provided from the accelerator group in every ten spills. The instantaneous number of triggers was proportional to the instantaneous beam intensity; we defined the number of triggers in the period of dt as $aI(t)dt$. In addition, assuming the ratio of trigger loss was small enough, we approximated that an instantaneous trigger loss ratio depends on the beam intensity; we defined the trigger loss ratio as $bI(t)$. a and b are constant. Our trigger efficiency (ε_{DAQ}) was represented

as 1 minus a fraction of integrated trigger loss in the total trigger:

$$\varepsilon_{DAQ} = 1 - \frac{\int_0^T bI(t)\cdot aI(t)dt}{\int_0^T aI(t)dt} = 1 - \frac{\int_0^T bI^2(t)dt}{\bar{I}T}, \tag{5.39}$$

$$\bar{I} = \frac{\int_0^T I(t)dt}{T}, \tag{5.40}$$

where $\bar{I}$ is an average of beam intensity. If beam were flat, the efficiency would be simply written as:

$$\bar{\varepsilon}_{DAQ} = 1 - b\bar{I}, \tag{5.41}$$

where $\bar{\varepsilon}_{DAQ}$ is a trigger efficiency in case of DF=1. And $b\bar{I}$ can be simply derived by using the number of triggers in a spill without trigger loss (R), spill length (T), and dead time (D) as:

$$b\bar{I} = \frac{R\cdot D}{T}. \tag{5.42}$$

Using Eqs. 5.38-5.42, we got:

$$\frac{1-\varepsilon_{DAQ}}{1-\bar{\varepsilon}_{DAQ}} = \frac{\int_0^T bI^2(t)dt}{b\bar{I}^2T} \tag{5.43}$$

$$= \frac{1}{DF}, \tag{5.44}$$

$$\therefore \varepsilon_{DAQ} = 1 - \frac{R\cdot D}{T\cdot DF}. \tag{5.45}$$

The observed number of triggers in a spill (R_{obs}) was already affected the efficiency as: $R_{obs} = \varepsilon_{DAQ}R$. The efficiency can be rewritten as:

$$\varepsilon_{DAQ}(1-\varepsilon_{DAQ}) = \frac{R_{obs}\cdot D}{T\cdot DF}. \tag{5.46}$$

The capability of the L2 buffer, however, limited the number of processable events in a spill to 7600 events, and several communication errors caused loss of few events. We simply calculated the fraction of the processed events in whole triggered events as the ratio between the number of correctly stored events (N_{event}) divided by the number of triggers (N_{trig}). Finally we obtained:

$$\frac{\text{Number of } K_L}{2\times10^{14}\text{ POT}} = \text{accumulated } K_L \times \frac{N_{trig}}{\varepsilon_{DAQ}N_{event}} \times \frac{(2\times10^{14})}{N_{POT}} \tag{5.47}$$

$$= (4.188\pm0.017)\times10^{7}. \tag{5.48}$$

It was stable during the run period as shown in Fig. 5.34. All parameters used in the calculation are listed in Tab. 5.8.

5.7 Distributions with All the Other Selection

In this subsection, we show and explain each distribution of the parameters used for the event selection. The consistency between the experimental data and the MC simulation for each parameter is an essential topic of this research. Here we show the distribution of each parameter with all event selections were applied except itself.

Table 5.8: Breakdown list of the normalization

Parameter	Value
Average Number of Triggers in a Spill (R_{obs})	68.48 k
Spill Length (T)	1.999 s
Dead Time (D)	32 ns
Duty Factor (DF)	0.4483
Trigger Efficiency (ε_{DAQ})	99.76 %
Number of Triggers (N_{trig})	1.254×10^8
Number of Stored Events (N_{event})	1.401×10^7
Number of POT (N_{POT})	3.355×10^{16}

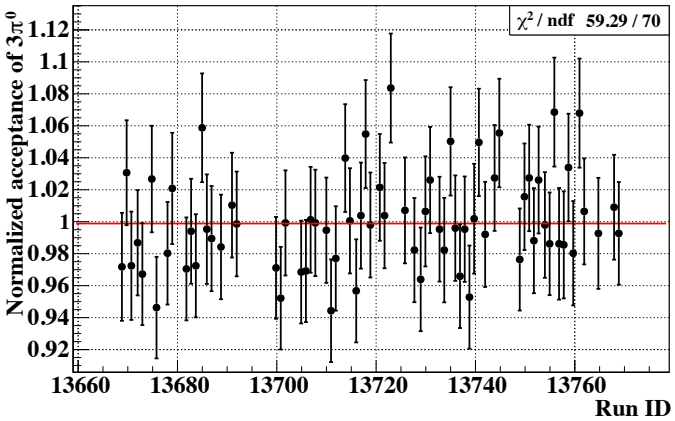

Figure 5.34: Stability of the $K_L \to 3\pi^0$ acceptance. The horizontal axis shows the Run ID. The vertical axis shows the number of reconstructed $3\pi^0$ per proton on target normalized by the resultant value in Eq. 5.48. Each solid points denote the number of $3\pi^0$ in each run. The result of the least squares fit is represented as the red horizontal line.

5.7.1 $K_L \to 3\pi^0$

Figures 5.35 and 5.36 show each distribution of the parameter used for the event selection. Each distribution is described with referring to each figure in the following paragraph.

Figure 5.35(a) represents the maximum of $|T_i - T_{vtx}|$ among six photons (Eq. 5.26). The plateau region above 3 ns was caused by accidental activities. The threshold of 3 ns avoids the discrepancy of the peak region. Figure 5.35(b) is the reconstructed K_L mass distribution. The mass width of the experimental data was reproduced by the MC simulation. The tail regions, made of mis-pairing events, were also reproduced by the MC simulation. As we required three π^0s were able to be reconstructed, the tail started from 405 MeV/c^2 ($3 \times M_{\pi^0}$). Figure 5.35(c) shows the lower Half Et of the CsI calorimeter. The data dropped sharply below 350 MeV because this parameter was used in the online trigger. Figure 5.35(f) shows the hit position of the innermost photon. We selected larger value between x and y position for each photon, and picked the smallest value among those six values as:

$$\text{innermost hit position} = \min\{\max\{x_1, y_1\}, \max\{x_2, y_2\}, \cdots, \max\{x_n, y_n\}\}, \tag{5.49}$$

where n denotes the number of photons: six for the $K_L \to 3\pi^0$ mode[2)], and x_i (y_i) is x (y) position of the i-th photon. Figure 5.36(g) shows the radial hit position of the outermost photon. Fluctuations of calibration factors of the outermost crystals especially large due to the small statistics in the $K_L \to 3\pi^0$ calibration. It caused the deviation of the acceptance of the outermost region, the 850 mm fiducial cut let us avoid this fluctuation. Figure 5.36(h) shows the minimum distance among all pairs of photons. The experimental data did not agree with the MC simulation in the nearside. It was considered that the drop of the experimental data was caused by the following mechanism. The number of crystals of simulated clusters was approximately 4 % smaller than the experimental data as shown in Fig. 5.37. As the clustering process did not use a kind of energy distribution, such as local maxima in x-y plane so far, the cluster size directly affected the distance of clusters; two near clusters fused easily if the cluster size was large. Figure 5.36(j) shows the hit timing distribution of seventh cluster if it existed. The center peak was made by shower fluctuation: one photon made two clusters. The plateau tails consisted of accidental activities.

5.7.2 $K_L \to 2\pi^0$

Figures 5.38-5.40 show each distribution of the parameters for the $K_L \to 2\pi^0$ selection. The contribution of the $K_L \to 3\pi^0$ BG was dominant for this mode, its distributions are drawn separately. As is the case in $K_L \to 3\pi^0$, each distribution is described with referring to each figure in the following paragraph.

Figure 5.38(b) represents the reconstructed mass distribution. A clear peak existed at the nominal K_L mass on the background slope which consisted of the $K_L \to 3\pi^0$ events. The background distribution started from $2 \times M(\pi^0) = 270$ MeV/c^2 because we required two pions were able to be reconstructed. The edge at 360 MeV/c^2 corresponded to the mass difference between K_L and π^0. The slope starting from 360 MeV/c^2 mainly consisted of mis-pairing events whose reconstructed vertex positions located more downstream than the true vertex. Figure 5.38(d) shows the maximum deviation of the reconstructed mass of two π^0 at the K_L vertex position. As the background $K_L \to 3\pi^0$ events were mis-paring events and the reconstructed π^0 vertex randomly distributed, the distribution of $K_L \to 3\pi^0$ was wider than $K_L \to 2\pi^0$. Figures 5.39(k) and 5.39(l) show the x

[2)] In cases of $K_L \to 2\pi^0$ and $K_L \to 2\gamma$, n is four and two, respectively.

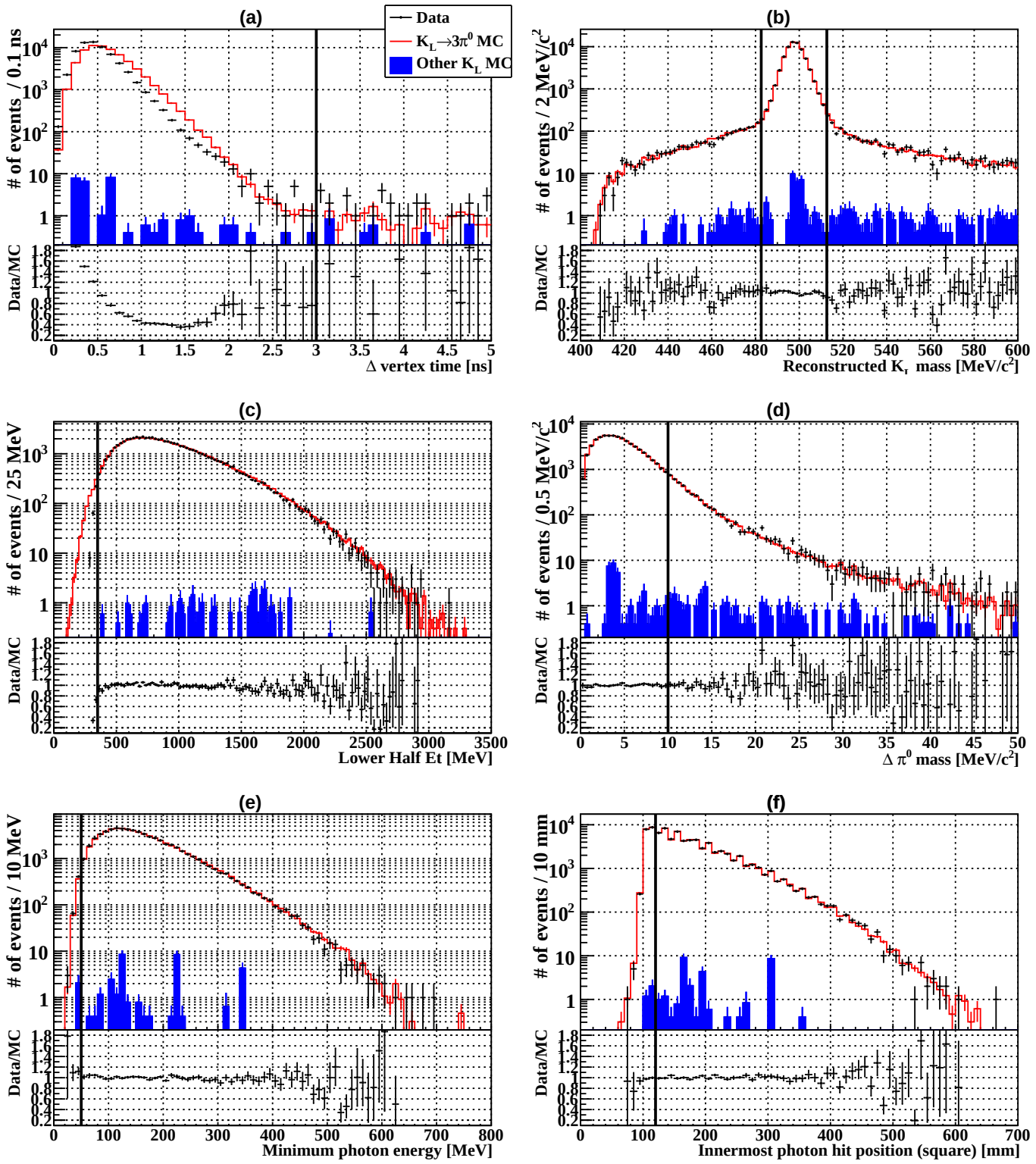

Figure 5.35: The parameter distributions of each selection for the $K_L \to 3\pi^0$ mode. (a) Δ vertex time, (b) Reconstructed K_L mass, (c) Lower Half Et, (d) $\Delta\pi^0$ mass, (e) Minimum photon energy, (f) Hit position (square) of the innermost photon. In each figure, the black solid points represent the experimental data, the red hollow histogram is the $K_L \to 3\pi^0$ MC simulation, and the histogram shown in solid blue is the other K_L MC simulation. All MC distributions are normalized by the result of the K_L flux measurement. The histograms of MC simulations are stacked in order. The lower graph of each distribution shows the ratio between the experimental data and the MC simulation. Solid vertical bars in each distribution represent the threshold of each selection.

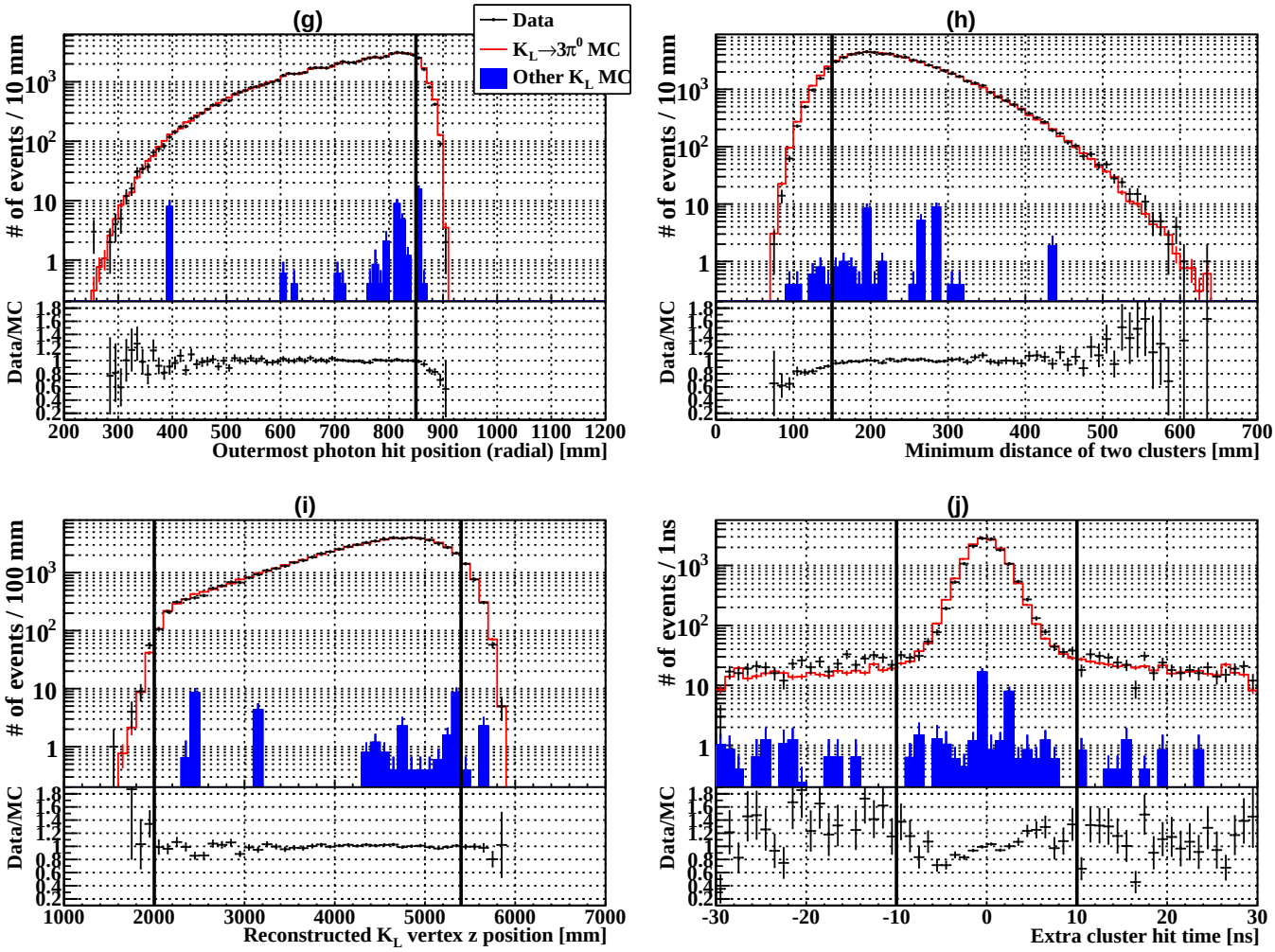

Figure 5.36: The parameter distributions of each selection for the $K_L \to 3\pi^0$ mode (continued). (g) Hit position (radial) of the outermost photon, (h) Minimum distance of all pair of photons, (i) Z position of the reconstructed K_L vertex, (j) Hit time distribution of the seventh cluster.

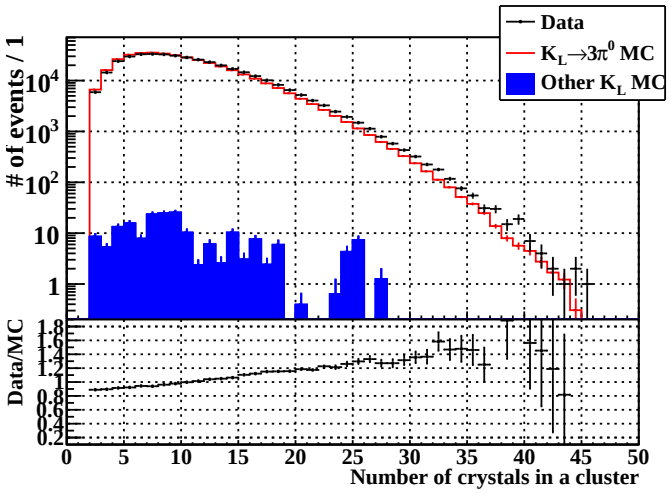

Figure 5.37: Cluster size discrepancy between the experimental data and the MC simulation with the $K_L \to 3\pi^0$ selection. The average size of one cluster in the experimental data was 4.4 % larger than the MC simulation. The meanings of the plots here are the same as in Fig. 5.35.

and y position of the center of energy of four photons at the CsI front surface, respectively. The $K_L \to 3\pi^0$ backgrounds had missing energy and was wider than $K_L \to 2\pi^0$. Figures 5.40(o) and 5.39(p) show maximum deposit energy among the CV modules and hit timing of CV modules having deposit energy above the veto threshold, respectively. The solid blue histogram was dominated by $K_L \to \pi^+\pi^-\pi^0$, but most dominant components come from $K_L \to 2\pi^0$ itself. It was caused by the following process. A photon from $K_L \to 2\pi^0$ primary entered the CsI calorimeter and generated the electromagnetic showers. A part of particles in the shower escaped upstream from the calorimeter and deposit additional secondary activities in the veto counters. This was called "Backsplash". Figures 5.40(q) and 5.40(r) show maximum deposit energy among the MB inner modules and hit timing of MB inner modules having deposit energy above the veto threshold, respectively. The high energy region above the energy threshold was dominated by extra photons directly coming from $K_L \to 3\pi^0$ decay, and the low energy region below the threshold was dominated by the back splash from $K_L \to 2\pi^0$. The plateau region on either side of the central peak in the timing distribution was made by accidental activities.

5.7.3 $K_L \to 2\gamma$

Figures 5.41-5.43 show each distribution of the parameters for the $K_L \to 2\gamma$. The contribution of the three dominant BG modes, $K_L \to 3\pi^0$, $K_L \to 2\pi^0$, and $Ke3$, are drawn separately. As is the case in $K_L \to 3\pi^0$ and $K_L \to 2\pi^0$, each distribution is described with referring to each figure in the following paragraph.

Figure 5.41(b) represents the lower Half Et distribution. In the low energy region below the threshold, the discrepancy between the experimental data and the MC simulation existed. It was due to the following reason. Two photons from $K_L \to 2\gamma$ can hit same half region in the CsI calorimeter. In such case, the Half Et of the other side, where no photon entered, was too small to make online triggers. The MC spectrum thus distributed both low and high energy region. Figure 5.41(c) shows the reconstructed transverse momentum. Ideally, $K_L \to 2\gamma$ does not have any transverse momentum, but the beam broadening in x-y plane and the resolutions of the CsI calorimeter causes finite transverse momentum. These effect was well reproduced and the width of the transverse momentum were agreed. Figure 5.41(d) is the hit position of the innermost photon. In case of $K_L \to 2\gamma$, even the innermost photon hit on the large crystals locating outer than

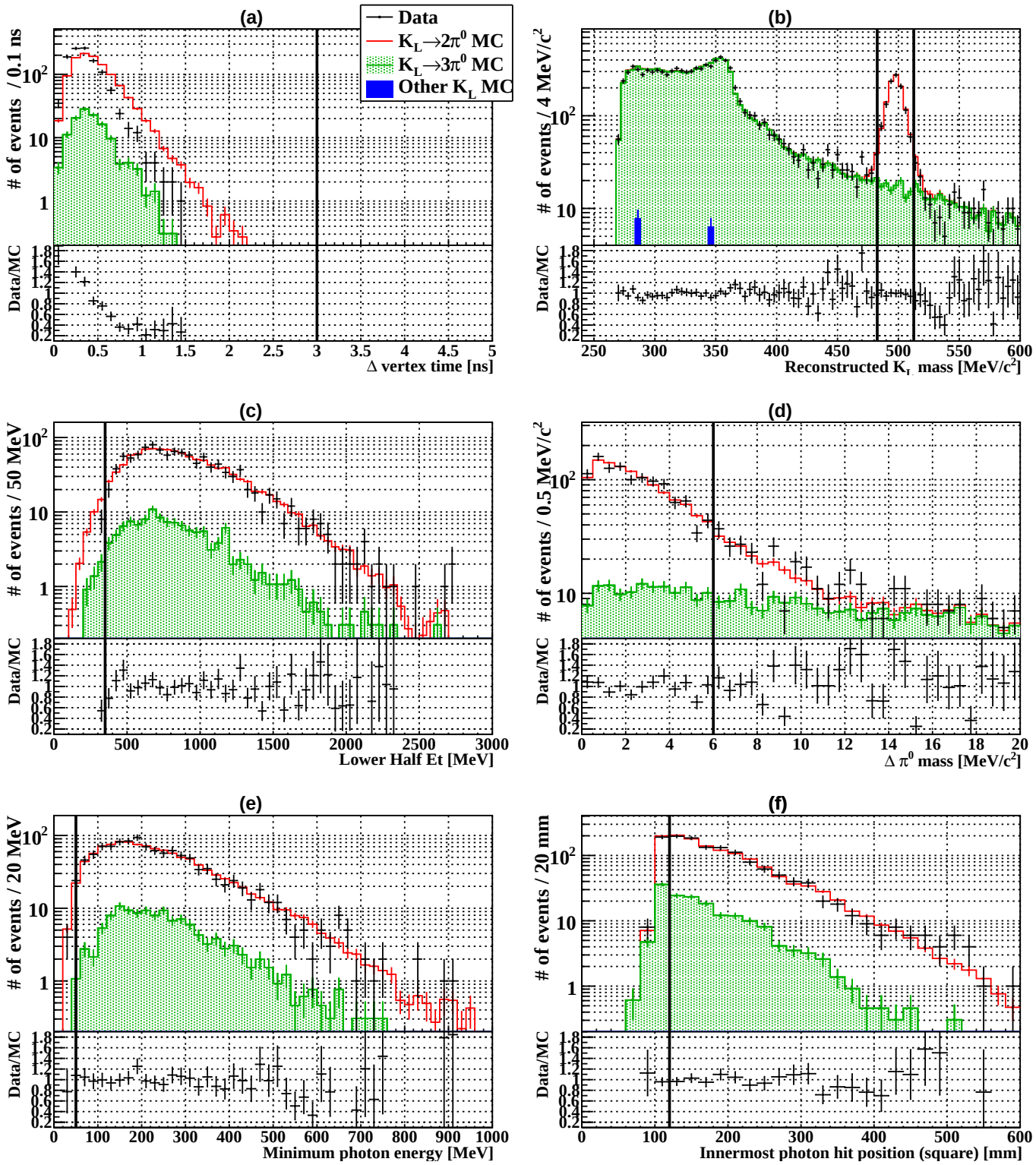

Figure 5.38: Parameter distributions of each selection for the $K_L \to 2\pi^0$ mode. (a) Δ vertex time, (b) Reconstructed K_L mass, (c) Lower Half Et, (d) $\Delta\pi^0$ mass, (e) Minimum photon energy, (f) Hit position (square) of the innermost photon. In each figure, the red hollow histogram is the $K_L \to 2\pi^0$ MC simulation and the green hatched histogram is $K_L \to 3\pi^0$ MC simulation. The meanings of the other plots and their normalization conditions are the same as in Fig. 5.35.

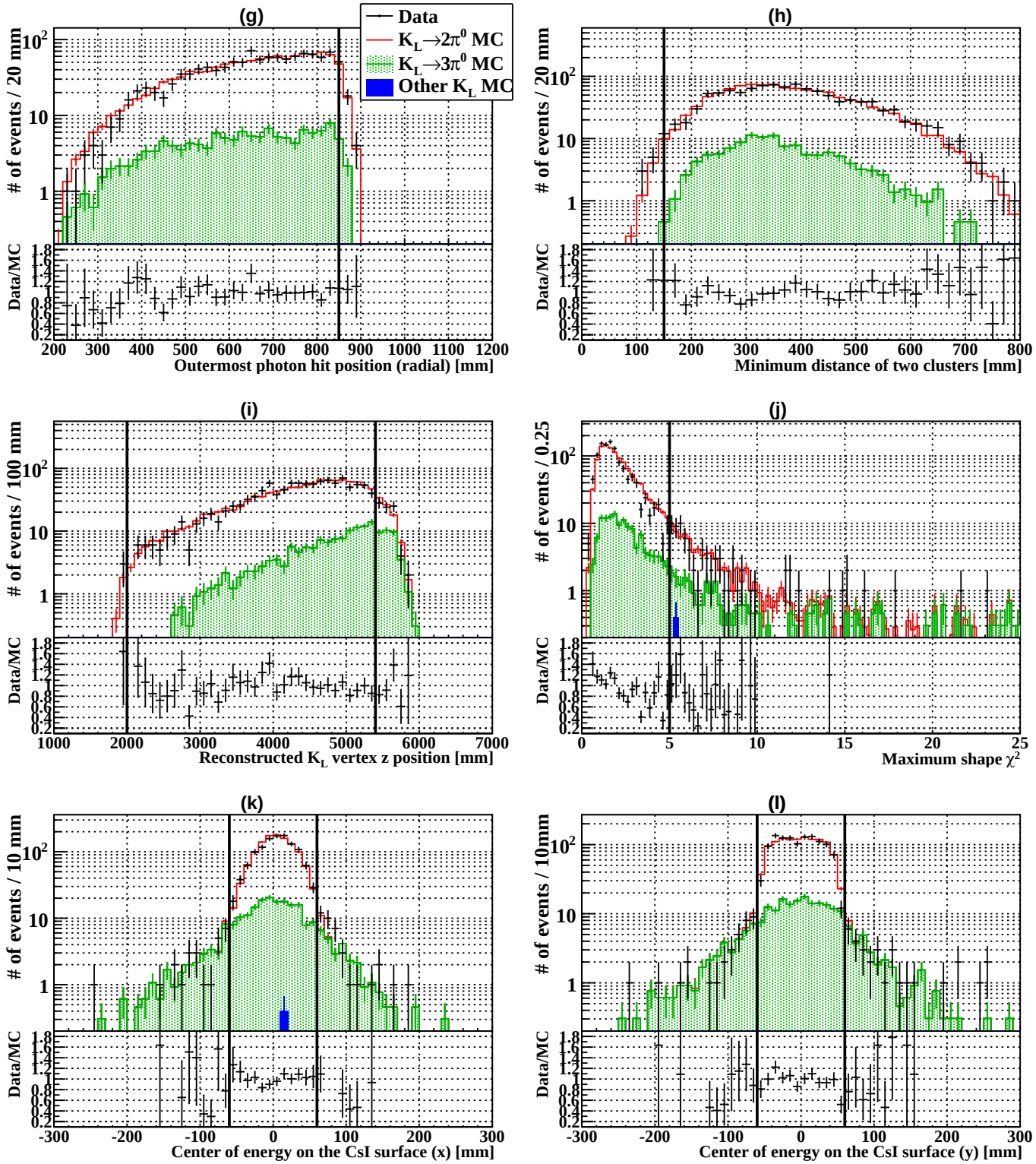

Figure 5.39: Parameter distributions of each selection for the $K_L \to 2\pi^0$ mode (continued). (g) Hit position (radial) of the outermost photon, (h) Minimum distance among all pair of photons, (i) Z position of the reconstructed K_L vertex, (j) Maximum shape χ^2 among four photons, (k) x position of the center of energy, (l) y position of the center of energy.

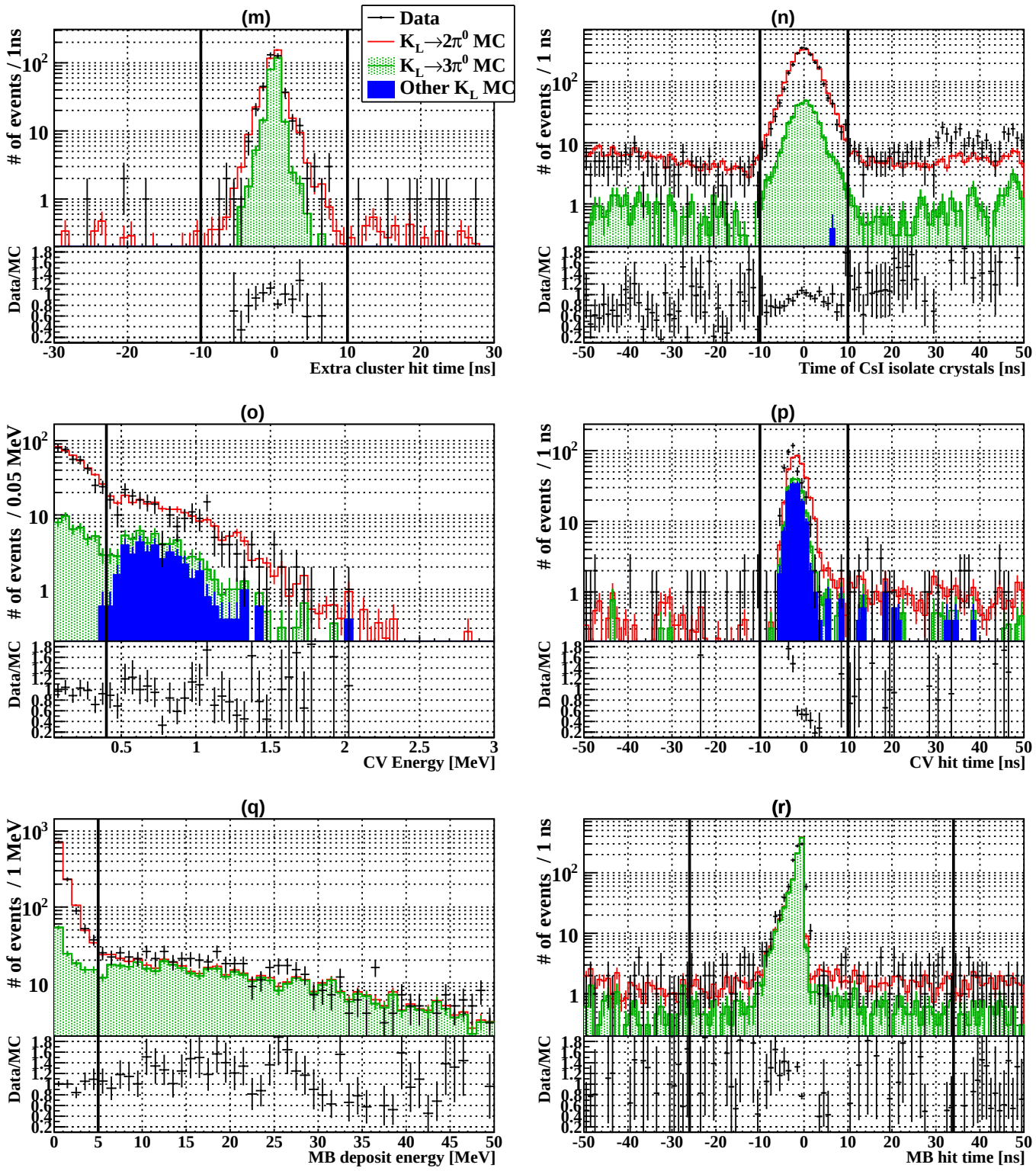

Figure 5.40: Parameter distributions of each selection for the $K_L \to 2\pi^0$ mode (continued). (m) Hit time distribution of the fifth cluster, (n) Hit time distribution of the single hit crystals, (o) Maximum energy among the CV modules, (p) Hit time distribution of the CV modules having deposit energy above 0.4 MeV, (q) Maximum energy among the MB inner modules, (r) Hit time distribution of the MB inner modules having deposit energy above 5 MeV.

600 mm. Figure 5.41(e) shows the radial hit position of the outermost photon. For this mode, we required that it should be outside the 450 mm from the center of the CsI calorimeter as described in Sec. 5.4.4. Figure 5.42(j) shows the maximum deposit energy among the CV modules. There were discrepancy between the experimental data and the $Ke3$ MC simulation above the threshold. It was caused by the fact that the reproducibility of the interaction between charged pions and CsI crystals was poor. It did not affect the spectrum below the threshold region which was dominated by the neutral decay modes. This effect is discussed in details in Sec. 5.8. Figure 5.42(l) shows the maximum energy deposit among the MB inner modules. The high energy region was dominated by extra photons directly coming from $K_L \to 3\pi^0$ decays and the low energy region below the threshold was dominated by the backsplash from $K_L \to 2\gamma$ as in the case of $K_L \to 2\pi^0$.

5.8 Discussion on the Systematic Uncertainties

At the end of this chapter, we focus to systematic uncertainties of the signal acceptance and the normalization. The following paragraphs describe sources and estimation methods of each systematic uncertainty.

Uncertainty Due to the CsI Calorimeter

We estimated the uncertainty due to the CsI calorimeter reproducibility by using the effectiveness of the event selection. The effectiveness in the experimental data slightly differed from that of the MC simulation. We considered the difference to be a source of systematic uncertainty.

The uncertainty of the effectiveness was defined as follows:

$$PA^i_{\text{data(MC)}} = \frac{N_{\text{data(MC)}}(\text{all selections applied})}{N_{\text{data(MC)}}(\text{all selections without } i\text{-th selection applied})}, \tag{5.50}$$

$$FD^i = \frac{PA^i_{\text{data}} - PA^i_{\text{MC}}}{PA^i_{\text{data}}}, \tag{5.51}$$

$$\sigma_{\text{effectiveness}} = \left(\sum_i (FD^i)^2\right)^{1/2}, \tag{5.52}$$

where i is the index of the selection, N is the number of remaining events after the selections specified in the parentheses. PA^i, called "Partial Acceptance", denotes the acceptance value of the i-th selection. FD^i, called "Fractional Difference", is a deviation between the partial acceptance of i-th selection of the experimental data and the MC simulation. The systematic uncertainty due to the effectiveness was evaluated by summing in quadrature.

Figure 5.44 shows the partial acceptance (Top) and the fractional difference (Bottom) for all CsI selections of the $K_L \to 3\pi^0$ analysis. The total uncertainty was 1.38 % and the largest contribution came from the cluster distance selection. Figures 5.45 and 5.46 show the same plots of the $K_L \to 2\pi^0$ and the $K_L \to 2\gamma$, respectively. For $K_L \to 2\pi^0$ and $K_L \to 2\gamma$, the deviations from zero of the fractional differences of all parameters were statistically insignificant. Here, we adopted their center values, although the statistical fluctuations largely contributed for $K_L \to 2\pi^0$ and $K_L \to 2\gamma$. Table 5.9 shows the summary of the uncertainty of this category.

Uncertainty Due to the Veto Counters

The systematic uncertainty of the signal acceptance due to the veto counters, Main Barrel and

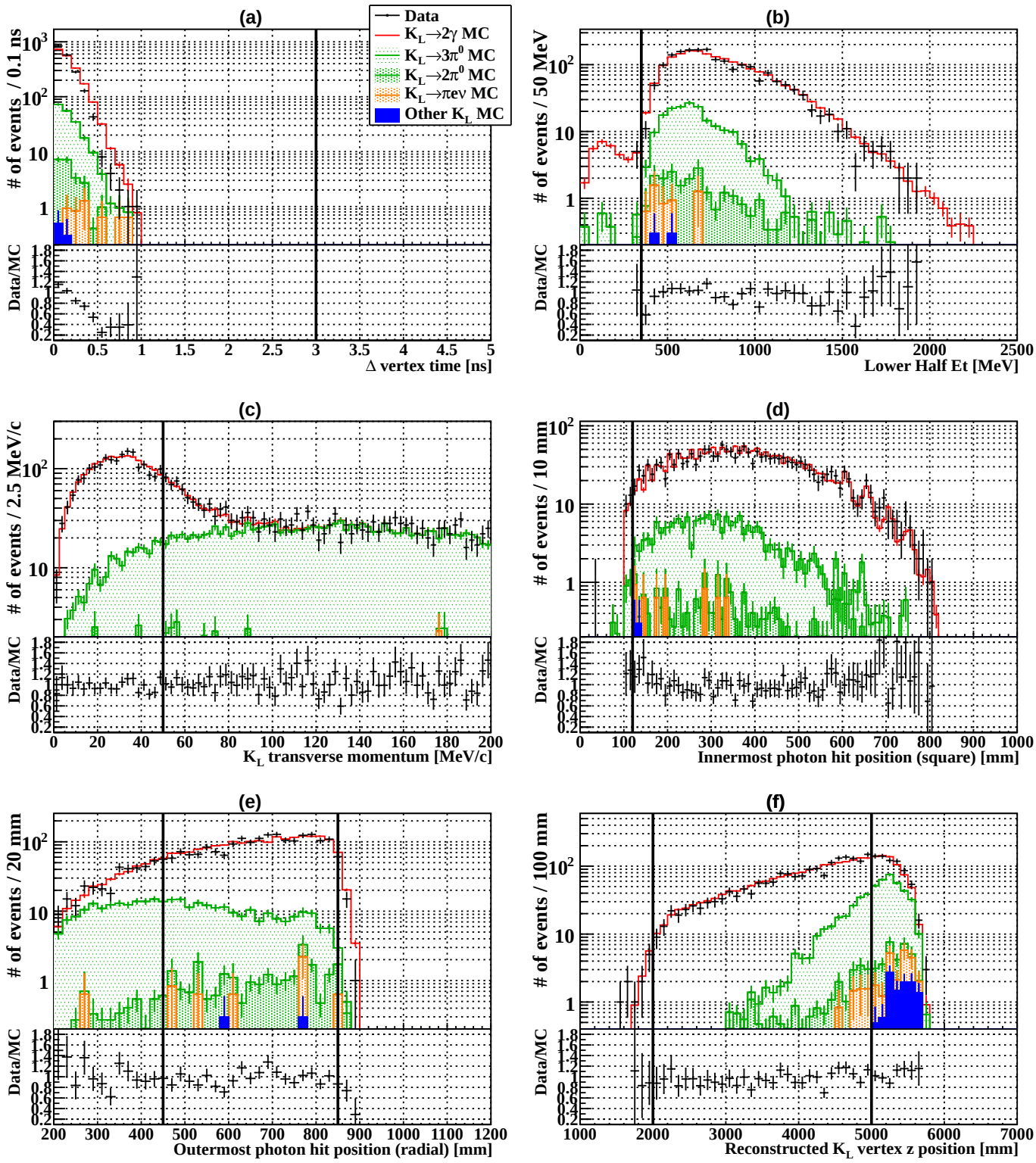

Figure 5.41: Parameter distributions of each selection for the $K_L \to 2\gamma$ mode. (a) Δ vertex time, (b) Lower Half Et, (c) Reconstructed transverse momentum, (d) Hit position (square) of the innermost photon. (e) Hit position (radial) of the outermost photon, (f) Z position of the reconstructed K_L vertex. In each figure, the red hollow histogram is the $K_L \to 2\gamma$ MC simulation, the green light hatched histogram is $K_L \to 3\pi^0$ MC simulation, and the green dark hatched histogram is $K_L \to 2\pi^0$ MC simulation, and the orange hatched histogram is $Ke3$ MC simulation.The meanings of the other plots and their normalization conditions are the same as in Fig. 5.35.

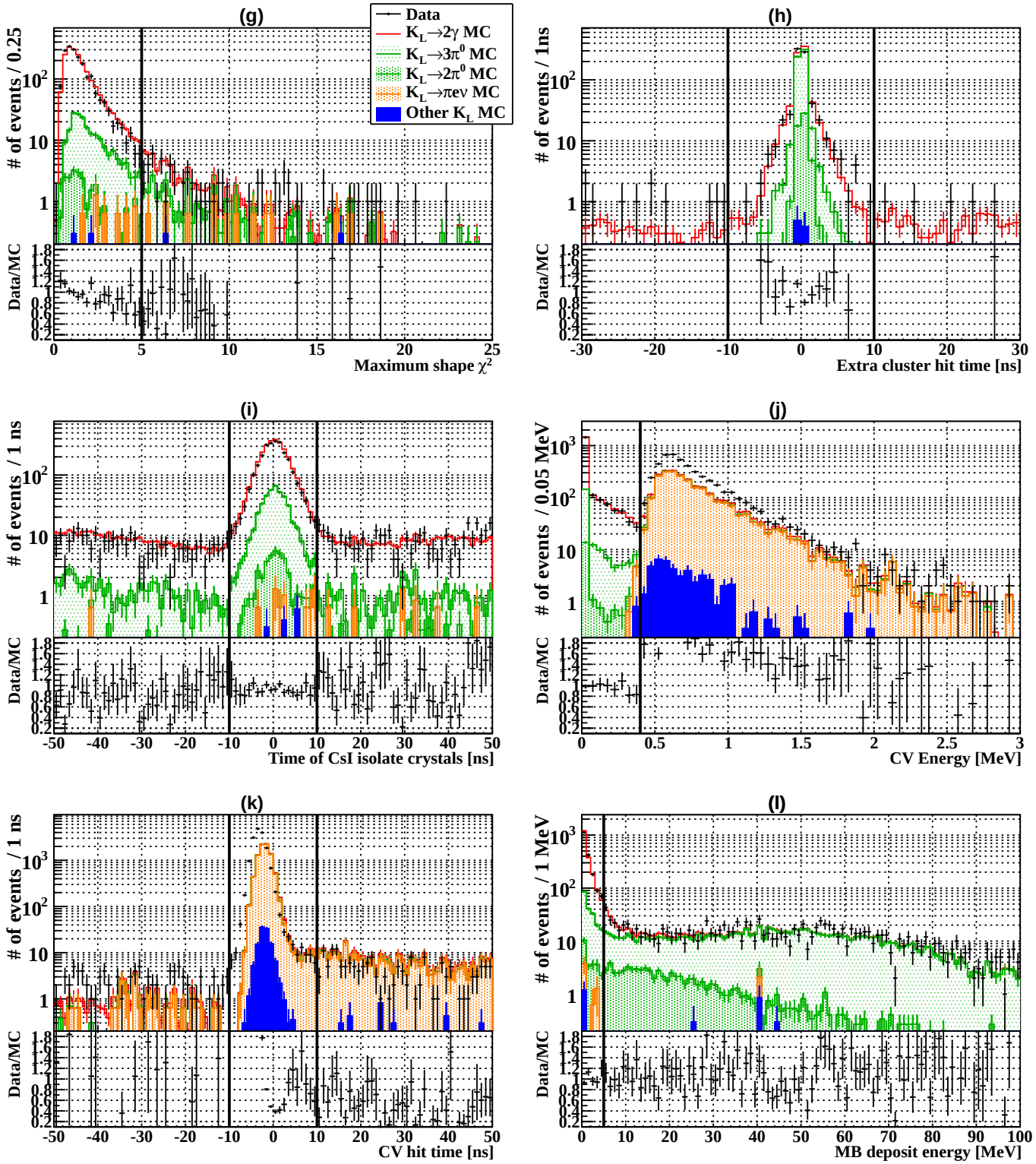

Figure 5.42: Parameter distributions of each selection for the $K_L \to 2\gamma$ mode (continued). (g) Maximum shape χ^2 between two photons, (h) Hit time distribution of the third cluster, (i) Hit time distribution of the single hit crystals, (j) Maximum energy among the CV modules, (k) Hit time distribution of the CV modules having deposit energy above 0.4 MeV, (l) Maximum energy among the MB inner modules.

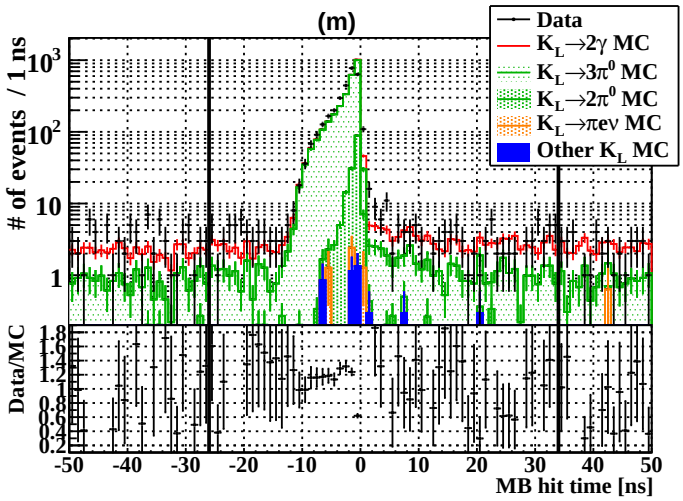

Figure 5.43: Parameter distributions of each selection for the $K_L \to 2\gamma$ mode (continued). (m) Hit time distribution of the MB inner modules having deposit energy above 5 MeV.

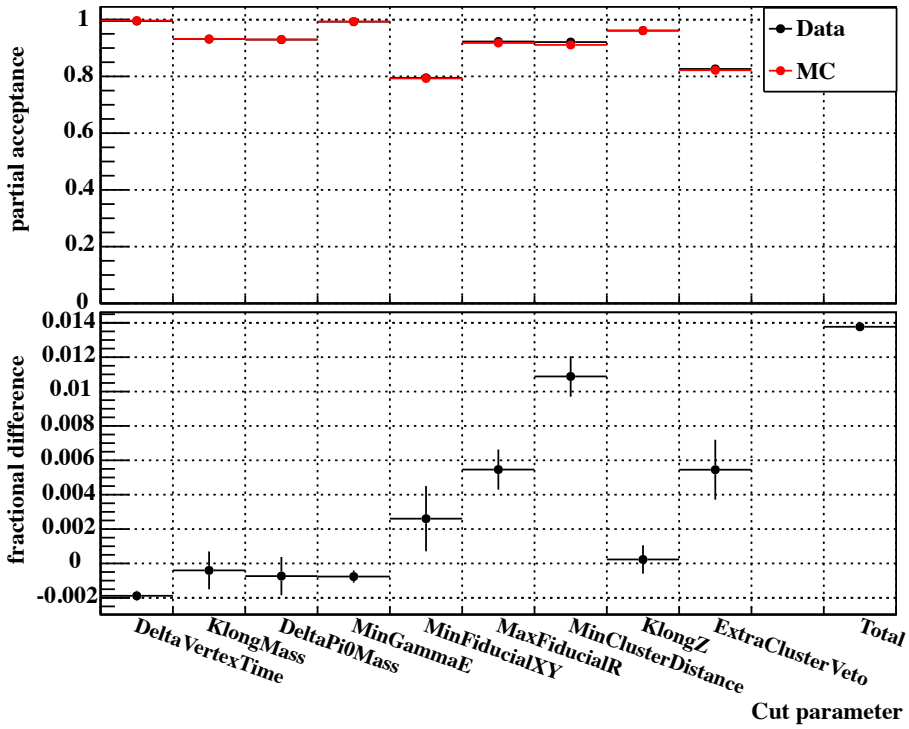

Figure 5.44: Partial acceptance (top) and Cut effectiveness (bottom) of $K_L \to 3\pi^0$.

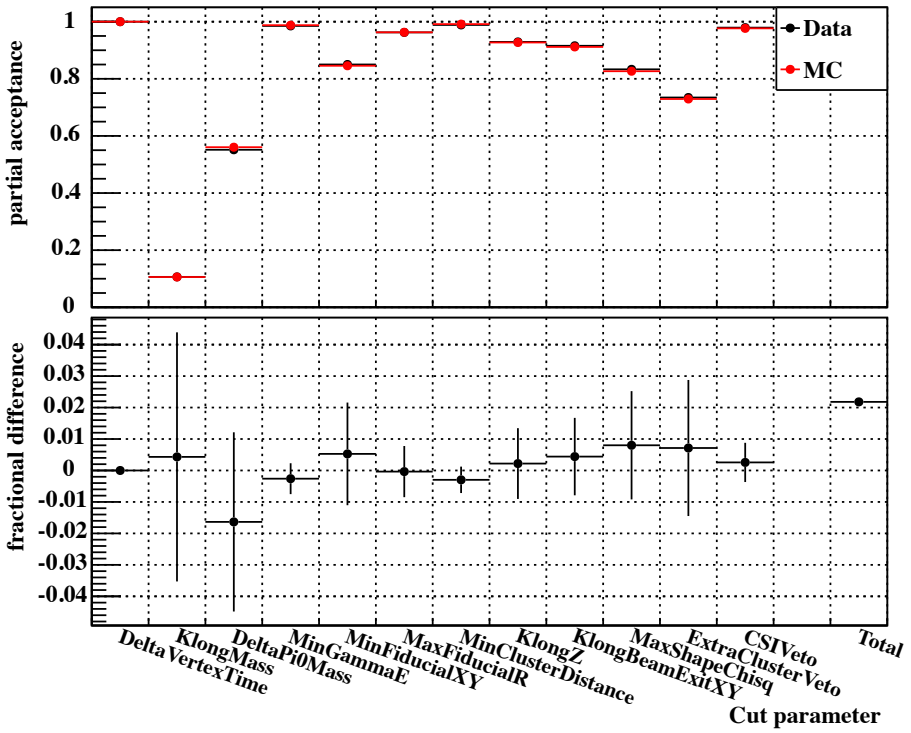

Figure 5.45: Partial acceptance (top) and Cut effectiveness (bottom) of $K_L \to 2\pi^0$.

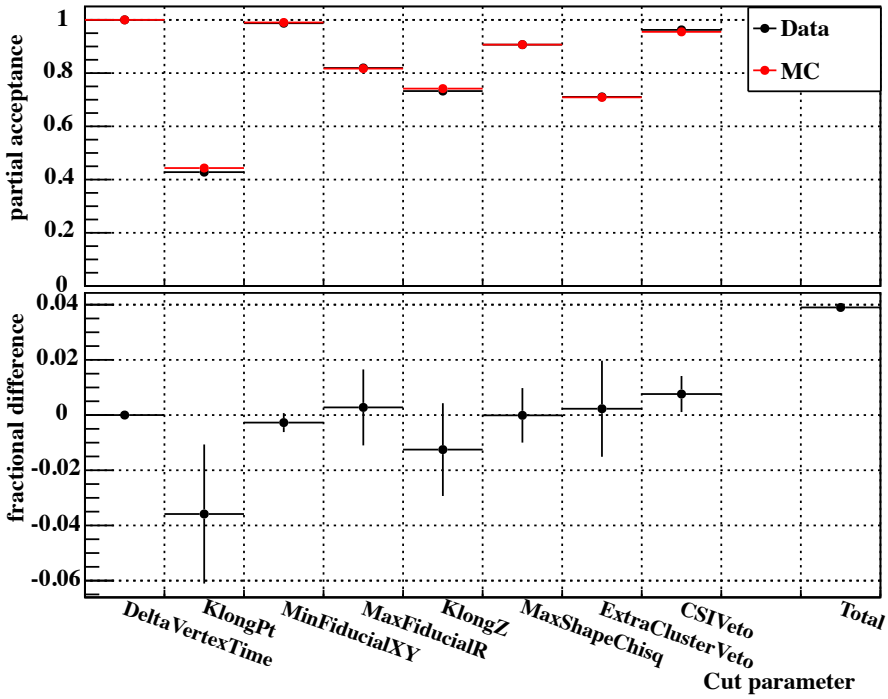

Figure 5.46: Partial acceptance (top) and Cut effectiveness (bottom) of $K_L \to 2\gamma$.

Table 5.9: Uncertainty due to the effectiveness of the CsI selections of each decay mode.

Mode	Value
$K_L \to 3\pi^0$	1.4 %
$K_L \to 2\pi^0$	2.2 %
$K_L \to 2\gamma$	3.9 %

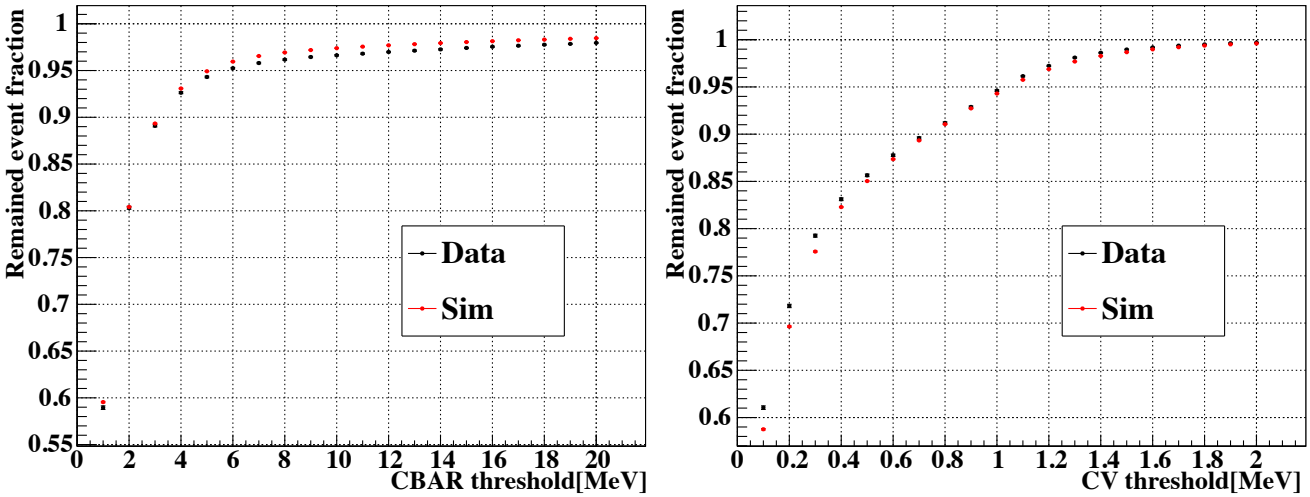

Figure 5.47: Remained events fraction of the $3\pi^0$ as a function of MB energy threshold (left) and CV energy threshold (right). The horizontal axes show the veto energy threshold for MB and CV, and the vertical axes show the remained event fractions. Fractions were normalized by the number of event without MB and CV veto. In both figures, the black dots represents the experimental data and red dots represents the MC simulation.

Charged Veto, consisted of two sources: uncertainty of the accidental loss and the backsplash loss (Sec. 5.7). In terms of such veto effects, $K_L \to 2\pi^0$ and $K_L \to 2\gamma$ had the same configuration of the final state as for $K_L \to 3\pi^0$; multiple photons were in the CsI calorimeter and veto counters had nothing. When we additionally applied the same veto cuts to the $K_L \to 3\pi^0$ analysis, the three modes shared the same physics process of the photon interaction with the CsI calorimeter for the backsplash loss, and also shared the same accidental activities and cut conditions for the accidental loss. Therefore the uncertainty due to the veto counters was commonly evaluated with the deviation between the experimental data and the MC simulations for the signal loss of the $K_L \to 3\pi^0$ with the veto. Figure 5.47 shows the remained event fractions of $K_L \to 3\pi^0$ as a function of MB veto energy threshold (left) and CV veto energy threshold (right). The value of each fraction at the actual veto threshold and the deviation between the experimental data and the MC simulation are listed in Tab. 5.10. These deviations were counted as systematic uncertainties of the $K_L \to 2\pi^0$ and the $K_L \to 2\gamma$ modes.

Uncertainty Due to the Online Threshold

The Half Et was required to be larger than 350 MeV in the offline analysis to eliminate the online

Table 5.10: Signal loss fractions due to the veto counters

Counter	Veto threshold	Data (α)	MC (β)	Deviation ($\lvert\alpha-\beta\rvert/\alpha$)
Main Barrel	5 MeV	0.9431±0.0009	0.9492±0.0003	0.65 %
Charged Veto	0.4 MeV	0.8311±0.0015	0.8228±0.0006	1.00 %

Table 5.11: Number of events change due to the Half Et threshold. The values of MC simulation are normalized by th $K_L \to 3\pi^0$ result.

Mode	Data/MC	350 MeV thre.	307.5 MeV thre.	Increase Ratio	Deviation
$K_L \to 3\pi^0$	Data	65315	65593	+0.43 %	0.24 %
	MC	65315	65751	+0.67 %	
$K_L \to 2\pi^0$	Data	1129	1137	+0.71 %	0.41 %
	MC	1132	1145	+1.15 %	
$K_L \to 2\gamma$	Data	1890	1895	+0.26 %	0.04 %
	MC	1925	1929	+0.23 %	

trigger effect. We estimated the uncertainty due to the online trigger effect by changing the offline threshold from 350 MeV to the same value as the online threshold of 307.5 MeV (Fig. 5.18), and comparing the number of events with all selections. The number of events in case of 350 MeV threshold and 307.5 MeV threshold are listed in Tab. 5.11. The values of the MC simulation were normalized by the $K_L \to 3\pi^0$ acceptance. In this table, the increase ratio is the ratio between the number of events in each threshold minus 1. The deviations for each mode was calculated and was included in the systematic uncertainty.

Uncertainty Due to Other Sources

Branching fraction :

The branching fractions of the three neutral decay modes have uncertainty, and they should be considered. The uncertainty of each branching fraction were quoted from the reference[1] and listed in Tab. 5.12.

POT/SEC :

As we mentioned in Sec. 5.6, we used a proportionality constant to calculate the number of POT from the number of SEC counts. The proportionality constant of 2.59×10^9 has a rounding error of 0.39 %. This error was included in the systematic uncertainty.

Uncertainty in Total

Systematic uncertainties are summarized in Tab. 5.12. The largest uncertainty came from the CsI calorimeter and other uncertainties are smaller than statistical errors for each mode. Finally we got $(4.182 \pm 0.017_{\text{stat.}} \pm 0.059_{\text{sys.}}) \times 10^7$ K_L per 2×10^{14} proton on target as the weighted average value among three modes. Figure 5.48 shows the resultant K_L flux.

Table 5.12: Summary of the systematic uncertainty

Source		$K_L \to 3\pi^0$	$K_L \to 2\pi^0$	$K_L \to 2\gamma$
Mode Dependent	CsI Calorimeter	1.4 %	2.2 %	3.9 %
	Main Barrel	-	1.00 %	1.00 %
	Charged Veto	-	0.65 %	0.65 %
	Online Threshold	0.24 %	0.41 %	0.04 %
	Branching Fraction [1]	0.61 %	0.69 %	0.73 %
Mode Independent	POT/SEC		0.39 %	
Total		1.6 %	2.6 %	4.2 %

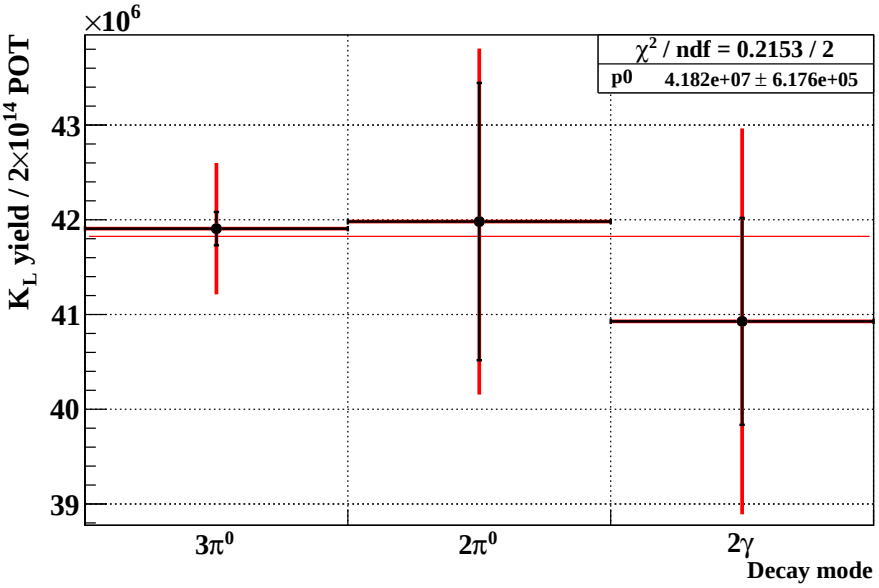

Figure 5.48: Three mode combined result. Vertical axis shows the estimated number of K_L per 2×10^{14} POT. Black bars are statistical errors and red bars are total errors. Horizontal red line shows the weighted average value among three modes.

Chapter 6

Discussion

The obtained distributions of various observables of $K_L \to 3\pi^0$, $K_L \to 2\pi^0$, and $K_L \to 2\gamma$ showed good agreement with MC simulations, and the resultant K_L yields from the analyses of the three modes were consistent with each other. As a consequence, the essential techniques, such as the detector calibration methods, the event reconstruction method, and the reproducibilities of the MC simulation, were successfully established. In addition, our measurement derived the more precise K_L yield than the beam survey which was a previous $K_L \to \pi^+\pi^-\pi^0$ measurement. It guaranteed that we can normalize the K_L yield in this level in the future run of the KOTO experiment. In this section, we discuss the obtained performance of the simulation model in this research. We also estimate the expectation of the signal sensitivity for the KOTO experiment using the simulation model. Finally we discuss several improvements from the previous $K_L \to \pi^+\pi^-\pi^0$ measurement, and potential rooms for the improvements for the future analysis.

6.1 Reproducibility of the MC simulation

The consistent results among the three decay modes were obtained with a discrepancy of 2.3 %. This consistency was owing to the reproducibilities of the MC simulation because we used the MC simulation to evaluate the acceptance of these modes. We succeeded in obtaining this result with no special fine-tuning, but with the implementation of the detailed detector response.

At the first of the discussion, we survey degrees of consistency between the experimental data and the MC simulation.

6.1.1 Reproducibilities of the CsI Calorimeter

The reproducibilities of the CsI calorimeter are essential characteristics for the experiment. When we analyze the main target, $K_L \to \pi^0\nu\overline{\nu}$, the reliability of the event reconstruction is only guaranteed by the reproducibilities of the resolutions of the CsI calorimeter. It is a key for the evaluation of the event selection of $K_L \to \pi^0\nu\overline{\nu}$. The following discussion is relevant to the resolutions of the CsI calorimeter.

Mass Resolution

Figure 6.1 shows the reconstructed K_L mass distribution obtained in the $K_L \to 3\pi^0$ analysis. We gauged the width with a sum of two individual gaussian functions (double gaussian) and adopted the width of one gaussian with larger area. The resultant K_L mass widths were 4.043 ± 0.016 MeV/c^2

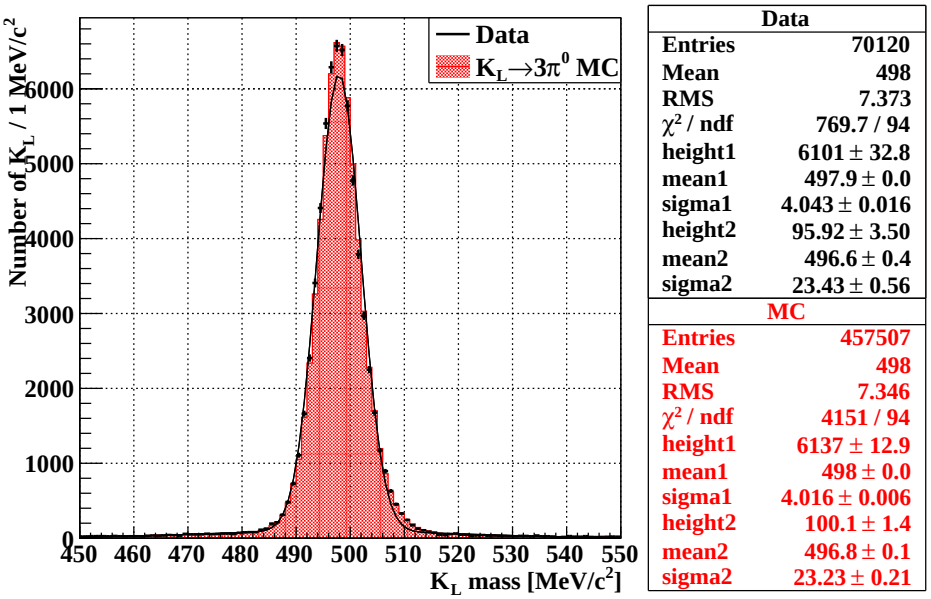

Data	
Entries	70120
Mean	498
RMS	7.373
χ^2 / ndf	769.7 / 94
height1	6101 ± 32.8
mean1	497.9 ± 0.0
sigma1	4.043 ± 0.016
height2	95.92 ± 3.50
mean2	496.6 ± 0.4
sigma2	23.43 ± 0.56
MC	
Entries	457507
Mean	498
RMS	7.346
χ^2 / ndf	4151 / 94
height1	6137 ± 12.9
mean1	498 ± 0.0
sigma1	4.016 ± 0.006
height2	100.1 ± 1.4
mean2	496.8 ± 0.1
sigma2	23.23 ± 0.21

Figure 6.1: Reconstructed K_L mass peak with the $K_L \to 3\pi^0$ selection. The histogram shown in cross bar is the experimental data, the curve is the fitting result with the double gaussian to the experimental data, and the red hatched histogram is the $K_L \to 3\pi^0$ simulation. The right tables show resultant parameters with the double gaussian fitting.

for the experimental data and 4.016 ± 0.003 MeV/c^2 for the MC simulation. They were consistent with each other within 1 %.

Vertex Resolution

As we explained in Sec. 5.3.2, the K_L vertex was calculated as the weighted average of the vertices of three π^0s in the $K_L \to 3\pi^0$ analysis. Thanks to the short life time of π^0, the real vertices of K_L and three π^0s locate at the same position within 1 μm. The distance between reconstructed K_L vertex and π^0 vertex ($\Delta z_{K\pi}$) was thus purely determined by the resolution of the CsI calorimeter[1)]. We gauged these width with a double gaussian. The resultant widths of larger gaussians were 40.97 ± 0.46 mm for the experimental data and 41.45 ± 0.18 mm for the MC simulation. Those of smaller gaussians were 64.77 ± 0.69 mm for the experimental data and 65.35 ± 0.31 mm for the MC simulation. They were also consistent at the level of 1 %.

Energy and Position Resolution

In the designed stage of the experiment, we used parameterized energy resolution and position resolution of the CsI calorimeter for the study of experimental sensitivity. They were $\sigma_E/E = 2\ \%/\sqrt{E} \oplus 1\ \%$ for energy resolution, and σ_x [mm] $= 5/\sqrt{E}$ for position resolution, where E is the photon energy in the unit of GeV. We thus needed to verify the actual performance. As the MC simulation reproduced the experimental data by introducing the detector response, the resolutions, which were evaluated in the simulation, were able to be deemed the real resolutions. We derived the energy resolution and the position resolution of the CsI calorimeter from the MC simulation

[1)] Although the x-y distributions of the K_L beam also contributed the $\Delta z_{K\pi}$, the quantity was only 1.4 %.

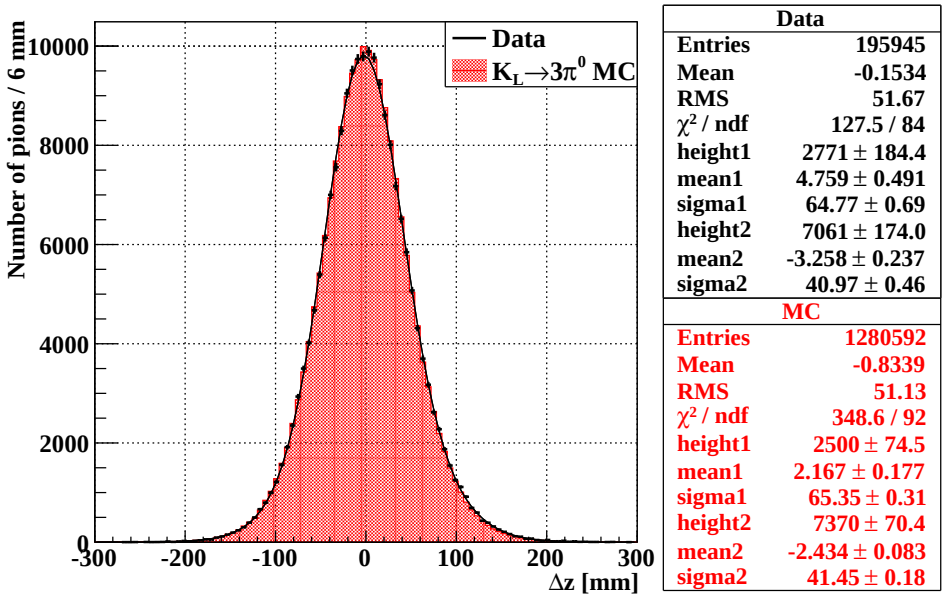

Figure 6.2: Reconstructed distance between the K_L vertex and each of three π^0 vertices. The plots and right table are the same as in Fig. 6.1.

by comparing the reconstructed energy and hit positions of photons to the incident true energy and hit positions of photons as a function of the incident true energy of photons, respectively. The resultant resolutions shown in Fig. 6.3:

$$\frac{\sigma_E}{E} = \frac{(1.934 \pm 0.003)\ \%}{\sqrt{E}} \oplus (0.595 \pm 0.018)\ \%, \tag{6.1}$$

$$\sigma_x\ [\mathrm{mm}] = \frac{3.663 \pm 0.004}{\sqrt{E}} \oplus (2.148 \pm 0.015), \tag{6.2}$$

where E is an energy in the unit of GeV. The errors here are statistical contributions only.

We were able to establish the response of the CsI calorimeter at a level of 1 % from the mass and vertex resolution, and obtained better resolutions than the past expectations for the photon energy range of our experiment.

6.1.2 Reproducibilities of the Accidental Activity

For the consistency among the three modes, accidental overlay should be mentioned. We applied MB and CV veto to the other two modes, while we did not use their information in the $K_L \to 3\pi^0$ analysis. Accidental activities caused the acceptance loss of the $K_L \to 2\pi^0$ and $K_L \to 2\gamma$ modes, and thus affected the consistency between $K_L \to 3\pi^0$, $K_L \to 2\pi^0$, and $K_L \to 2\gamma$. Figures 6.4(a) and (b) show the acceptance loss of $K_L \to 3\pi^0$ in case we applied MB and CV veto conditions, respectively. If accidental activities were not overlaid, there was ∼4.4 % discrepancy between the experimental data and the MC simulation in the loss fraction when we applied MB veto with 5 MeV threshold. The accidental overlay method helped us to reduce it to 1.0 %. The raw energy spectra of MB for reconstructed $K_L \to 3\pi^0$ events, shown in Fig. 6.5, represent the reproducibility in wide energy region. The source of the accidental activities is discussed in Sec. 6.2.3. The CV, on

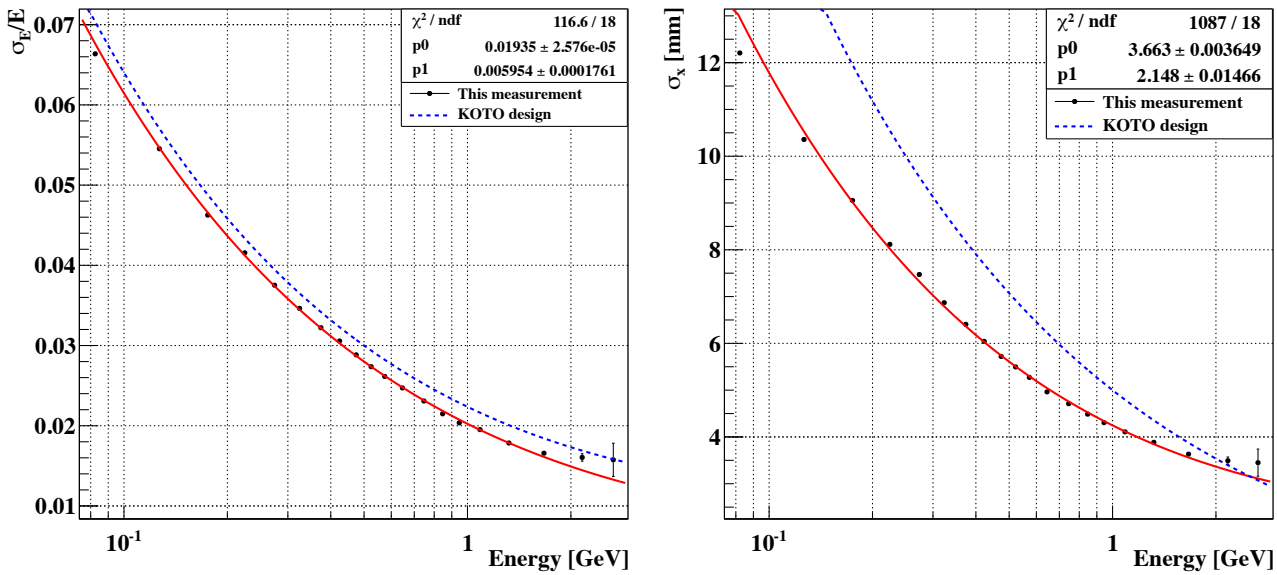

Figure 6.3: Energy resolution (left) and position resolution (right) of the CsI calorimeter. The dots are the obtained resolution as a function of the incident true energy of a photon. The red curves show the resultant function represented as Eqs. 6.1 and 6.2, and the dashed blue curves show the parametrized function used in the design of the experiment.

the other hand, did not have such a large amount of accidental activities; there was no difference between the loss with the accidental overlay and that without the accidental overlay. Figure 6.6 shows the three mode comparison with and without the accidental overlay. If the accidental overlay was not applied, the discrepancy among the three modes became more than 7.3 %, in contrast with the discrepancy of 2.3 % with the overlay. We can conclude the method of the accidental overlay worked well.

6.2 Re-evaluation of the Sensitivity of the $K_L \to \pi^0\nu\overline{\nu}$ Search

The performance of the CsI calorimeter directly affects the experimental sensitivity, which is determined by the number of K_L and the signal acceptance of $K_L \to \pi^0\nu\overline{\nu}$. We had estimated the experimental sensitivity based on the simulation with the parametrized energy and position resolutions as described in Sec. 6.1.1; thus, we revaluated the sensitivity using the realistic simulation model obtained in this research.

The sensitivity of a rare decay experiment is represented by "Single-Event Sensitivity" (SES), which is expressed in our case as:

$$\mathrm{SES} = \frac{1}{N_{K_L} \times A_{sig}}, \tag{6.3}$$

where N_{K_L} is the integrated number of K_Ls at the exit of the beam line during the experiment, and A_{sig} is the acceptance of $K_L \to \pi^0\nu\overline{\nu}$ signals. The expected number of observed events (N_{obs})

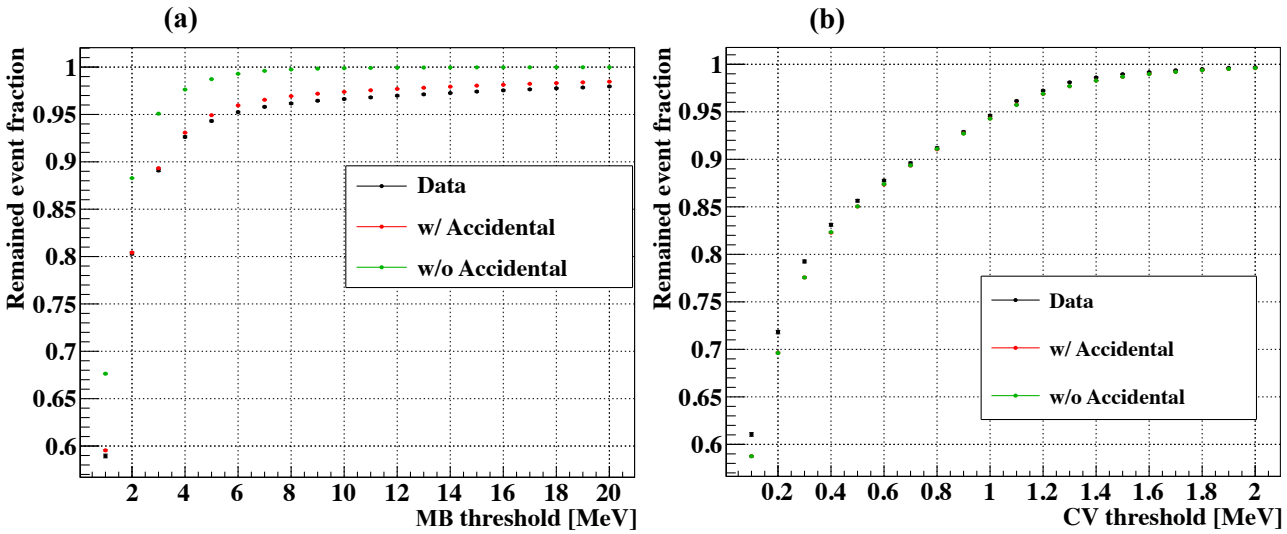

Figure 6.4: Comparison between $K_L \to 3\pi^0$ loss fraction with and without accidental overlay. (a) the loss fraction as a function of the MB inner veto threshold. (b) the loss fraction as a function of the CV veto threshold. Vertical axes show the remained $3\pi^0$ fraction normalized by the number of $3\pi^0$ without veto. Black dots show the experimental data, red dots show the MC simulation with accidental overlay, and green dots show the MC simulation without accidental overlay. In case of CV, red points are almost overlaid by green points.

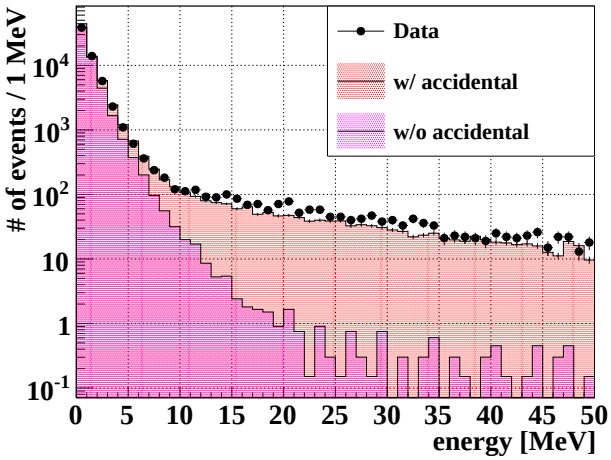

Figure 6.5: Comparison between the energy spectrum of the MB inner modules with and without the accidental overlay. The black dots show the experimental data, the red hatched histogram shows the simulated spectrum with accidental overlay, and the pink hatched histogram shows the simulated spectrum without accidental overlay. The event selections of $K_L \to 3\pi^0$ were applied. The simulated histograms are normalized by the result of the K_L flux measurement.

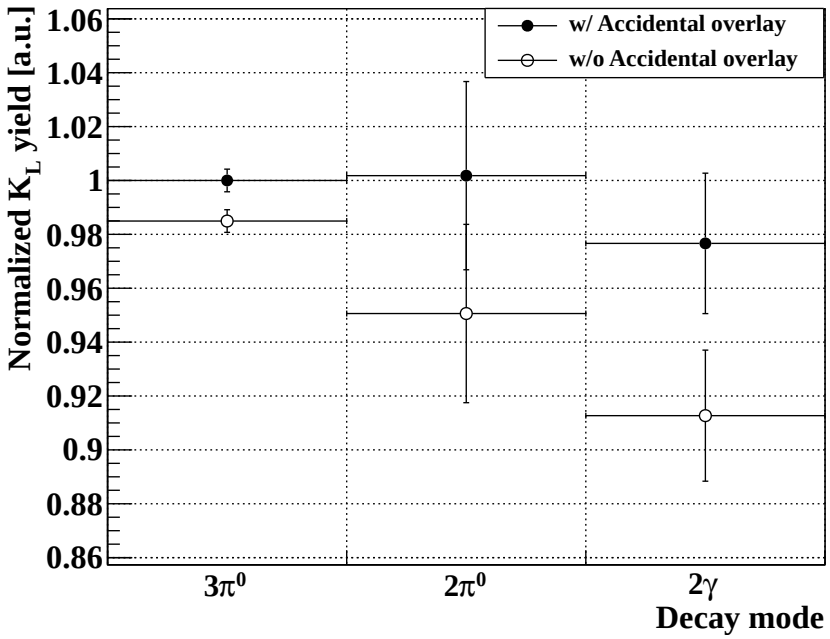

Figure 6.6: Comparison among the three modes with and without accidental overlay. Vertical axis shows the K_L yields normalized by the $K_L \to 3\pi^0$ result. Solid circles show the resultant yields when accidental activities were overlaid, and open circles show the results when accidental activities were not overlaid. The error bars show statistical errors only.

is calculated as:

$$N_{obs} = \frac{\mathrm{Br}(K_L \to \pi^0\nu\overline{\nu})}{\mathrm{SES}}. \tag{6.4}$$

6.2.1 Signal Acceptance

The signal acceptance (A_{sig}) can be divided into the three factors: the decay probability, the geometrical acceptance, and the efficiency of event selections in the analysis. Their definitions and estimated values are described below.

Decay Probability

The decay probability is defined as the probability that a K_L reaching the beam exit will decay in the fiducial region ($3000 < Z_{vtx} < 5000$ mm). The decay probability as a function of the momentum of K_L is shown in Fig. 6.7, and the weighted average over the K_L momentum spectrum (Fig. 4.1) was 3.7 %.

Geometrical Acceptance

The geometrical acceptance is defined as the probability that both photons from a π^0 in the decay region hit the CsI calorimeter. When the x-y positions of a photon at the CsI upstream surface (z=6148 mm) locates outside the 200 mm $\times$ 200 mm square area centered at the CsI calorimeter and also locates within 900 mm from the center of the CsI calorimeter, the photon is considered to

hit. The K_L momentum dependence is shown in Fig. 6.7, and the weighted average over the K_L momentum spectrum was 27 %.

Efficiency of Event Selections

In order to identify $K_L \to \pi^0\nu\overline{\nu}$ decays, the following event selections are applied. The total efficiency of all event selections as a function of the K_L momentum is shown in Fig. 6.7, and the weighted average over the K_L momentum was 21 %.

Photon Energy :
: It is required that there are two photons in the CsI calorimeter with their energies greater than 0.1 GeV and less than 2 GeV. This selection rejects most of accidental hits.

CsI Fiducial :
: The incident positions of photons on the CsI calorimeter should be outside the 300 mm $\times$ 300 mm square area centered at the CsI calorimeter and within 850 mm from the center of the beam. This is to ensure that showers are well contained in the calorimeter, and energies and positions of photons are properly reconstructed.

Z_{vtx} :
: The reconstructed vertex position is required to locate between 3000 mm and 5000 mm.

Transverse Momentum :
: The reconstructed π^0 is required to have transverse momentum between 0.13 GeV/c and 0.25 GeV/c. This cut rejects backgrounds from $K_L \to \pi^+\pi^-\pi^0$ and $K_L \to 2\gamma$ decays.

Collinearity Angle :
: The collinearity angle is defined as the projected angle between two photons' momenta in the CsI calorimeter plane. The collinearity angle is required to be less than 150 degree to reject $K_L \to 2\gamma$ background events.

Cluster Distance :
: The distance between two photons at the front surface of the CsI calorimeter is required to be more than 300 mm.

Total Energy :
: The sum of energies of two photons should be greater than 500 MeV.

Energy-Angle Correlation :
: There is a correlation between the energy (E) and the polar angle (θ) of a photon that comes from a π^0 decay in the $K_L \to \pi^0\nu\overline{\nu}$ signals and enters into the CsI calorimeter. The reconstructed energy and angle of each photon should satisfy kinematics that is consistent with the correlation as: $E \cdot \theta > 2.5$ GeV·degree.

Energy Ratio :
: The ratio between the lower and the higher energy of two photons is required to be greater than 0.2 to reject odd-paring events for $K_L \to 2\pi^0$ decays, which have two photons from different π^0 decays in the calorimeter.

P_t/P_z-Z_{vtx} Correlation :
: The π^0 kinematics is further restricted in the P_t/P_z-Z_{vtx} plane (where P_z is a reconstructed longitudinal momentum of π^0) in order to reduce backgrounds that come from $\eta \to 2\gamma$ productions by halo neutrons in the CV.

Shape χ^2 :
: The definition of the shape χ^2 is same as Eq. 5.29. The criteria is χ^2 <2.5 for the $K_L \to \pi^0\nu\overline{\nu}$ analysis.

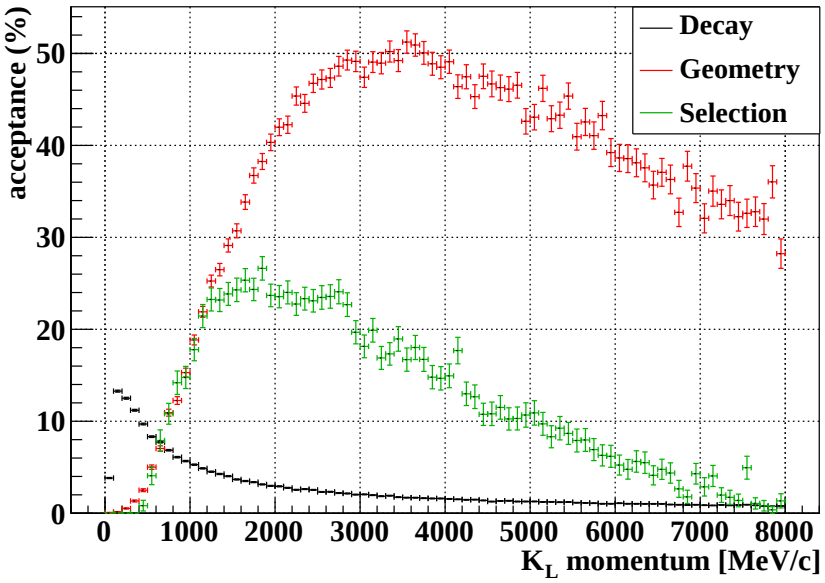

Figure 6.7: $K_L \to \pi^0\nu\overline{\nu}$ acceptance curves of the decay probability (black), the geometrical acceptance (red), and the efficiency of event selections (green). The horizontal axis shows the momentum of K_L, and the vertical axis shows the acceptance of each factor.

Signal Acceptance

The net signal acceptance which was obtained as the product of the above three factors was 0.22 %. Its K_L momentum dependence is shown in Fig. 6.8.

6.2.2 Single Event Sensitivity

In order to estimate the SES, we assumed the K_L yield as 1.94×10^7 K_L per 2×10^{14} POT, which was the resultant value of the beam survey with the Ni target[2)]. For the integrated POT during the experimental period, we adopted the design values: 2×10^{14} POT per spill, 1 spill per 3.3 seconds, and the running time of 3×10^7 seconds. The resultant SES was 2.7×10^{-12}. The parameters for the SES calculation are summarized in Tab. 6.1. In the proposal of the KOTO experiment[21], the SES was 4.0×10^{-12}. We obtained 1.5 times better sensitivity from the proposal using the actual K_L yield and the realistic simulation model of the CsI calorimeter. With the SM prediction of $Br(K_L \to \pi^0\nu\overline{\nu}) = 2.43 \times 10^{-11}$, we expect to observe 9.0 events.

The SES is worsen due to the acceptance loss which includes the accidental loss and the backsplash loss. The estimation of the acceptance loss depends on the experimental condition, such as the instantaneous time structure of the beam power and the noise level of veto counters. If we assume the loss to be 50 %, as we estimated in the proposal, the SES is 5.4×10^{-12} and observation of 4.5 SM events are expected.

6.2.3 Acceptance Loss

In this subsection, we revisit the estimation of the acceptance loss for the $K_L \to \pi^0\nu\overline{\nu}$ search with the realistic simulation model.

[2)] because the Au target in this research can not be used with the design power of the J-PARC accelerator.

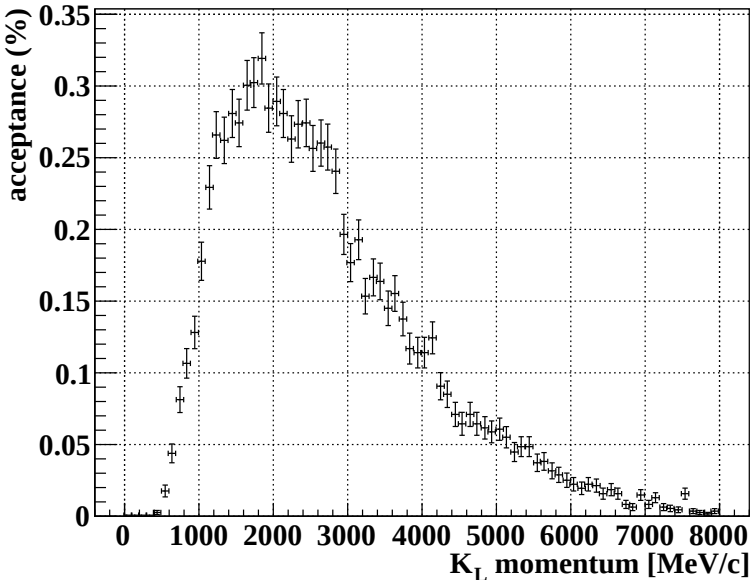

Figure 6.8: Total $K_L \to \pi^0 \nu\overline{\nu}$ signal acceptance as a function of the K_L momentum.

Table 6.1: Breakdown list of the single event sensitivity.

	value
K_L flux (Ni target) / 2×10^{14} POT	1.94×10^7
Integrated POT	1.8×10^{21}
Decay Probability	3.7 %
Geometrical Acceptance	27 %
Event Selection Efficiency	21 %
Single Event Sensitivity	2.7×10^{-12}

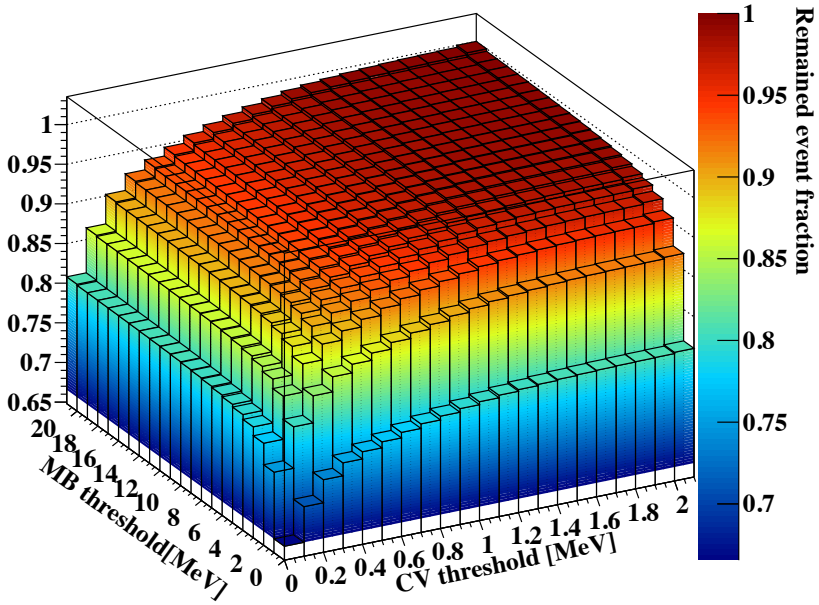

Figure 6.9: $K_L \to \pi^0\nu\overline{\nu}$ backsplash loss due to MB and CV. The bottom left and right axes show the veto energy threshold of MB and CV, respectively. The vertical axis and color show the fraction of the number of remained $K_L \to \pi^0\nu\overline{\nu}$ events from the case without MB Veto and CV Veto. The bins above 2 MeV in CV threshold (the right-most bins) show the fraction without CV veto, and the bins above 20 MeV in MB threshold (the back-most bins) show the fraction without MB veto.

Backsplash Loss

We evaluated the backsplash loss due to MB and CV using the MC simulation. The reproducibility of them was studied in Sec. 5.8 by comparing the acceptance loss of $K_L \to 3\pi^0$. Figure 6.9 shows the backsplash loss for $K_L \to \pi^0\nu\overline{\nu}$ events. The backsplash loss was 33 % when the MB veto energy threshold of 1 MeV and the CV veto energy threshold of 0.1 MeV, while the previous value was 39 %. It is independent of the beam intensity.

Accidental Loss

The accidental loss is the other contribution of signal loss. It depends on the beam intensity. This time, we estimated the accidental loss using the accidental overlay method. When the accidental data taken in the engineering run was overlaid in the $K_L \to \pi^0\nu\overline{\nu}$ MC simulation, the resultant signal loss due to MB and CV was found to 55 %. Figure 6.10 shows the signal loss for $K_L \to \pi^0\nu\overline{\nu}$ events. As the backsplash loss was 33 %, the accidental loss was to be $1-(1-0.55)/(1-0.33) = 33$ %.

Using the MC simulation, the accidental loss due to particles in the K_L beam and daughter particles from K_L decays was only 1.5 % with the assumption of the corresponding beam power. That indicates particles in the K_L beam were not the main source of the accidental loss. The main source was found to be scattered particles from the primary beam line. As shown in Fig. 2.7, there are several equipments in the primary beam line after the T1 target. Parts of scattered and generated particles at the target hit them and generated further secondary particles. Part of them, mostly neutrons, penetrated the concrete and iron shields and came to the KOTO detector. They were the main source of the accidental loss. When the accidental loss is simply scaled by the beam

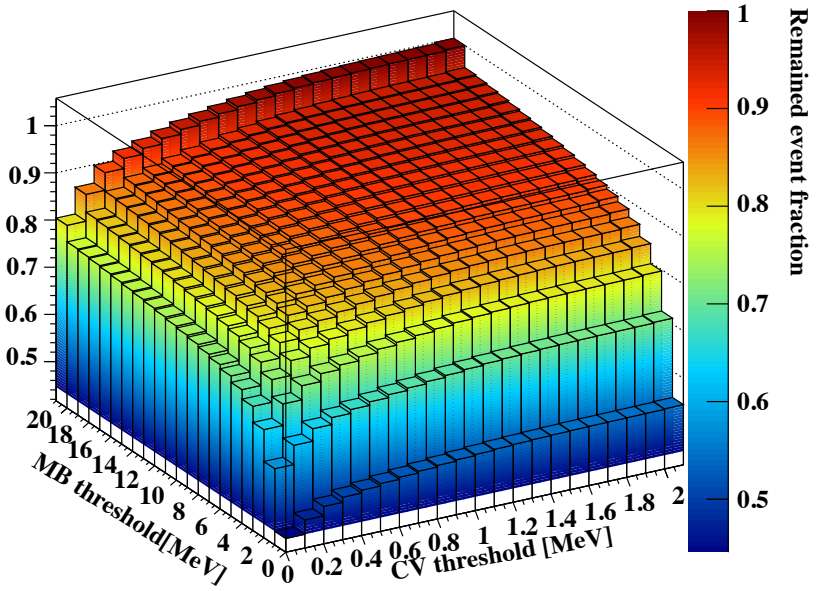

Figure 6.10: $K_L \to \pi^0\nu\overline{\nu}$ backsplash loss due to MB and CV with the accidental overlay. The meanings of axes are the same as in Fig. 6.9.

intensity, the accidental loss will become 1050 % for the design value of the primary proton beam. We had to reduce this effect.

After the engineering run, 200 water tanks were put between the KOTO detector and the concrete shields as shown in Fig. 6.11. In addition, the beam size of the primary protons after the T1 target was made small. Figure 6.12 shows the change of the accidental hit rate of MB outer modules with the same beam power. Since the primary proton beam located in the left side of the figure, the modules on the left side had higher hit rate. The water tanks reduced the accidental hit rate of 62 %, and the beam size adjustment reduced the hit rate of 40 % for the hottest module. We confirmed that the accidental hit rate can be reduced by additional shields between the KOTO detector and the primary beam line. As the estimated hit rate from the K_L beam itself was 1.5×10^4 counts per spill for this beam power, we aspired to the reduction to this level. We plan to add shielding structures further, identify the source of the secondary particles, and make further countermeasures in cooperation with the accelerator group, to solve this problem.

6.3 Comparison with Beam Survey Result

We had measured K_L flux in our beam line in the beam survey experiment in February 2010. In this study, we obtained the consistent result with the previous beam survey. We achieved several improvements from the beam survey. First we introduce the details of the beam survey, and we move to discuss the comparison between these two measurements.

Figure 6.11: Water tanks for the shield. The white tanks with a blue cap are the water tanks. The KOTO detector locates in down-right side of this figure and the primary beam line locates the upside of this figure.

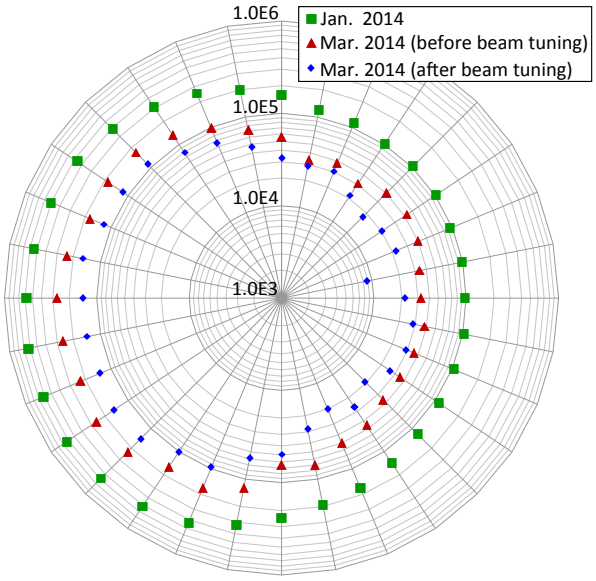

Figure 6.12: Improvement of MB accidental hit rate. The angular coordinate shows the outer modules of MB viewed from the upstream. The radial coordinate shows the hit counts per spill of each module. The energy threshold was 2 MeV. The green squares show the hit rate in January 2014; the engineering run in this research. The red triangles show that in March 2014; after the engineering run. The blue points show that after the beam tuning. The beam power was the same (15 kW) for all the conditions.

Table 6.2: Condition of the two K_L flux measurements

Period	Target			MR Beam Power	Measured Mode
	Material	Thickness	Interaction Length[42]		
2010 Feb.	Pt	60.0 mm	0.658	1 kW, 1.5 kW	$K_L \to \pi^+\pi^-\pi^0$
2013 Jan.	Au	64.8 mm	0.638	15 kW	$K_L \to 3\pi^0$ $K_L \to 2\pi^0$ $K_L \to 2\gamma$

6.3.1 Beam Survey Overview

Conditions of two K_L flux measurements are summarized in Tab. 6.2. The T1 targets were different: 60.0-mm-thick Pt for the beam survey, and 64.8-mm-thick Au for this measurement. Adjusting the length of the targets, we got the same proton loss fractions between them within 2 %. The detector system and the measurement modes were also different. In this measurement, we used the detector system of the KOTO experiment and measured three neutral decay modes. In the beam survey, we built a special detector system for $K_L \to \pi^+\pi^-\pi^0$ measurement[24]. It was composed of an electromagnetic calorimeter and a hodoscope system. In the final state of $\pi^+\pi^-\pi^0$, two photons from the π^0 were detected by the two banks of the calorimeter, and two charged pions were detected with the hodoscope system. Figure 6.13 shows the schematic view of the detectors of the beam survey. With the vertex position of charged tracks, the invariant mass of the two photons was calculated and was compared with the nominal π^0 mass. Then, equations for the transverse momentum balance of the $\pi^+\pi^-\pi^0$ system were solved to derive the absolute momenta of the charged pions. Finally, the invariant mass of $\pi^+\pi^-\pi^0$ was calculated and was compared with the nominal K_L mass in order to identify the $K_L \to \pi^+\pi^-\pi^0$ decay.

6.3.2 Improvement of Systematics

Our resultant K_L flux in this study was $(4.182 \pm 0.017 \pm 0.059) \times 10^7$, while the beam survey result was $(4.19 \pm 0.09^{+0.47}_{-0.44}) \times 10^7$. They were consistent within their errors[3)]. In respect to the systematic uncertainty, we were able to reduce systematic uncertainty from 11 % (beam survey) to 1.4 % (this measurement). The largest systematics in the beam survey came from reproducibility of the invariant mass of $\pi^+\pi^-\pi^0$ of 9 %. We achieved a reduction of the uncertainty by a factor of 8. We established the precise normalization method for the $K_L \to \pi^0\nu\overline{\nu}$ measurement in future.

6.3.3 Improvement of Acceptance

This measurement also improved the acceptance of the K_L compared with the beam survey. As shown in Fig. 6.8, the acceptance of the main $K_L \to \pi^0\nu\overline{\nu}$ has a peak at 2 GeV/c and the high side tail continues over 6 GeV/c. The acceptance of the beam survey, shown in Fig. 6.14, did not have acceptance more than 4 GeV/c and could not measure the high momentum region in spite of sensitivity of $K_L \to \pi^0\nu\overline{\nu}$. In contrast with it, the acceptance of this measurement reached

[3)] We could not identify the 2 % difference between the T1 target due to their error levels.

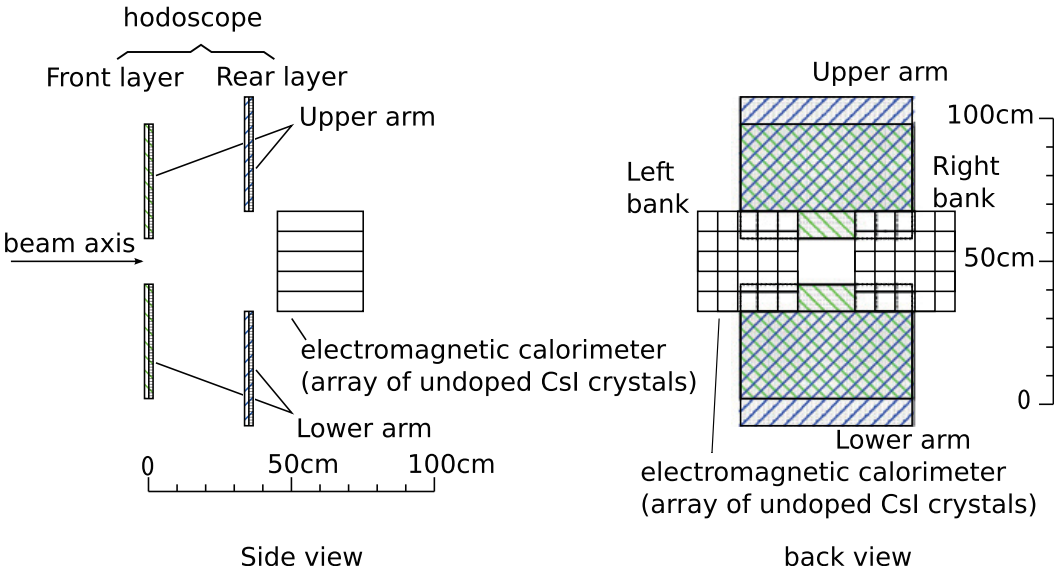

Figure 6.13: Schematic view of the previous K_L flux measurement, performed in the beam survey. Quoted from [24].

7 GeV/c and covered the acceptance of $K_L \to \pi^0\nu\overline{\nu}$. Figure 6.15 shows the acceptances of this measurements in this study. We surveyed wider momentum region in this measurement.

6.4 Rooms for Further Improvements

6.4.1 Interaction between a Charged Pion and the CsI Calorimeter

We mentioned that the CV energy spectrum had a discrepancy in the $K_L \to 2\gamma$ analysis in Sec. 5.7. With the event selection for the $K_L \to 2\gamma$ analysis, the MC simulation could not reproduce the contribution of $Ke3$. It was found that the charged-like component in the CV energy spectrum in the experimental data remained much more than the expectation from the MC simulation. To figure out what caused this discrepancy, we used the $K_L \to \pi^+\pi^-\pi^0$ mode, which also contained charged pions and was able to be reconstructed well. In the reconstruction, we required four clusters in the CsI calorimeter. We also required activities in CV, in order to identify the clusters that were associated with charged pions. Assuming the other two clusters were made by a pair of photons originated from a π^0, we reconstructed the vertex position and the momentum of the π^0 with the same method as the $K_L \to \pi^0\nu\overline{\nu}$ reconstruction. Once determining the vertex position, we calculated the directions of both charged pions by connecting the vertex position and the cluster hit positions in the CsI calorimeter. Assuming the total transverse momentum was zero, finally, we calculated the four-momenta of two charged pions and the initial K_L. The detail reconstruction method is described in Appendix B. Figure 6.16 shows the reconstructed incident energies (relativistic energies) of the charged pions and their deposit energies in the CsI calorimeter. While the reconstructed incident energy spectrum of charged pions was reproduced with the MC simulation, but the energy deposit in the CsI calorimeter made from charged pion interactions was simulated

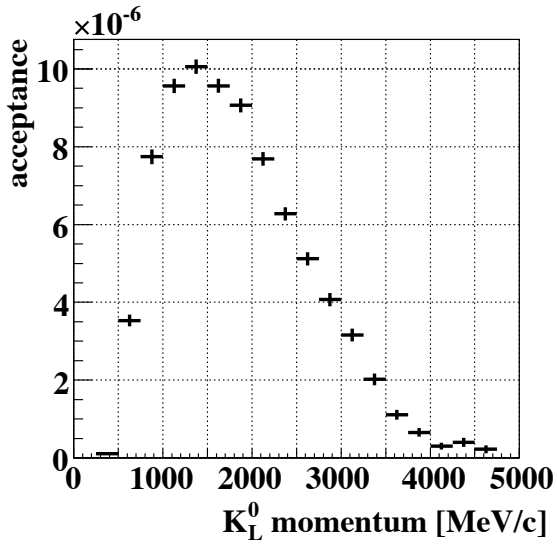

Figure 6.14: Acceptance of the previous $K_L \to \pi^+\pi^-\pi^0$ measurement as a function of the K_L momentum.

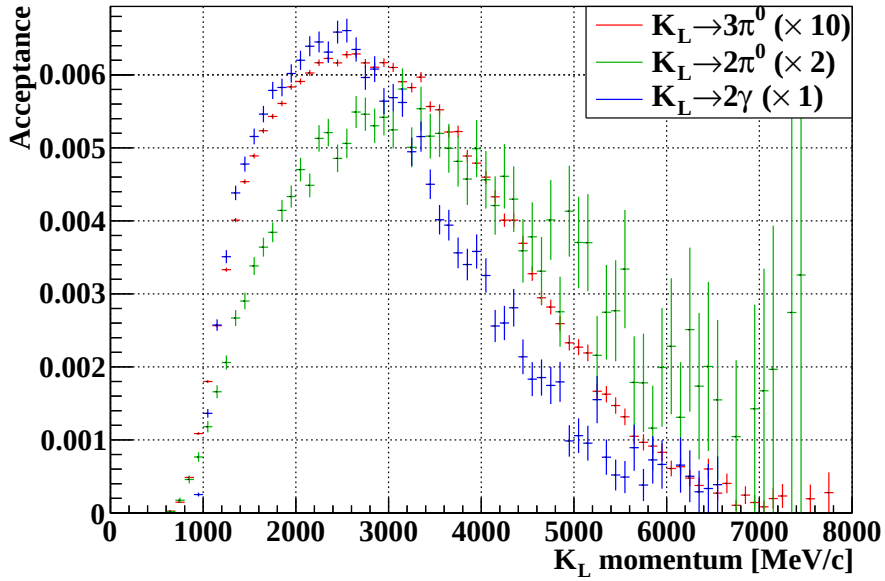

Figure 6.15: Acceptance curves of the normalization modes as a function of the K_L momentum. Red: acceptance of $K_L \to 3\pi^0$ (multiplied by 10); Green: acceptance of $K_L \to 2\pi^0$ (multiplied by 2); Blue: acceptance of $K_L \to 2\gamma$.

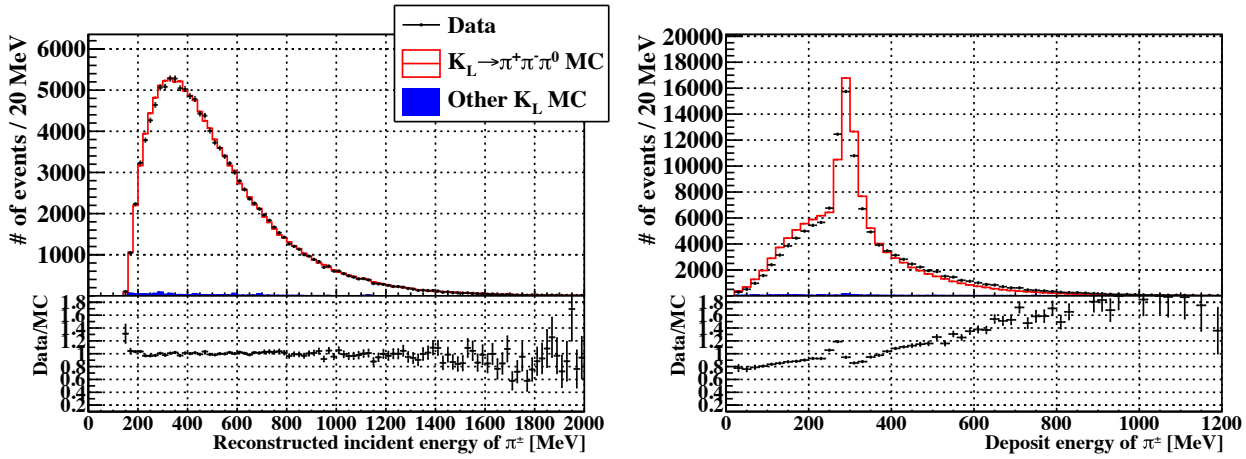

Figure 6.16: (Left) Reconstructed incident energy of charged pion in $K_L \to \pi^+\pi^-\pi^0$. (Right) Deposit energy of charged pion in $K_L \to \pi^+\pi^-\pi^0$. In each figure, the black dots show the experimental data, the red hollow histograms shows the $K_L \to \pi^+\pi^-\pi^0$ MC simulation, and the blue solid histogram shows the other K_L MC simulation. The histogram of the $K_L \to \pi^+\pi^-\pi^0$ is stacked on the other K_L MC histogram. The MC histograms are normalized by the area. The lower graph of each distribution shows the ratio between the experimental data and the MC simulation.

7 % smaller than the experimental data.

We compared the charged pion interaction, with two hadronic interaction models prepared in Geant4 package: the Bertini Cascade (BERT) model[4] and the Binary Cascade (BIC) model. For the energy deposit spectrum, the BIC model had better reproducibility as can be seen in Fig. 6.17. On the other hand, for the probability to generate fifth cluster, the BERT model agreed better with the experimental data, as shown in Fig. 6.18. In these figures, same number of $K_L \to \pi^+\pi^-\pi^0$ were plotted, but the number of fifth clusters in the MC simulation with the BIC model was larger than the BERT model. It meant that the number of clusters made by $K_L \to \pi^+\pi^-\pi^0$ decays in the BIC model was larger than BERT model, and the BERT model had better reproducibility of the number of clusters.

Next we tried to mix the results of the two models. Basically we used the BERT model, and only the energy deposit information was corrected to match the BIC model. The correction was done by using the true incident energy of charged pions and the average deposit energy in the CsI calorimeter. Figure 6.19(a) shows the fraction of the average deposit energy in the true incident energy of charged pions simulated with the BERT model as a function of the true incident energy. In order to obtain this correlation function, we removed the contribution from pions which penetrated the CsI calorimeter to make this correlation function. The correction function we used was:

$$\frac{\text{Corrected } E_{\text{dep}}}{E_{\text{inc}}} = \alpha(E_{\text{inc}}) \left(\frac{E_{\text{dep}}}{E_{\text{inc}}}\right)^2 + (1 - \alpha(E_{\text{inc}})) \frac{E_{\text{dep}}}{E_{\text{inc}}}, \tag{6.5}$$

$$\alpha(E) = \frac{F_{\text{BERT}}(E) - F_{\text{BIC}}(E)}{F_{\text{BERT}}(E)(1 - F_{\text{BERT}}(E))}, \tag{6.6}$$

[4] We used the QGSP_BERT model as the default hadronic interaction model. The BERT model was only used in our energy region.

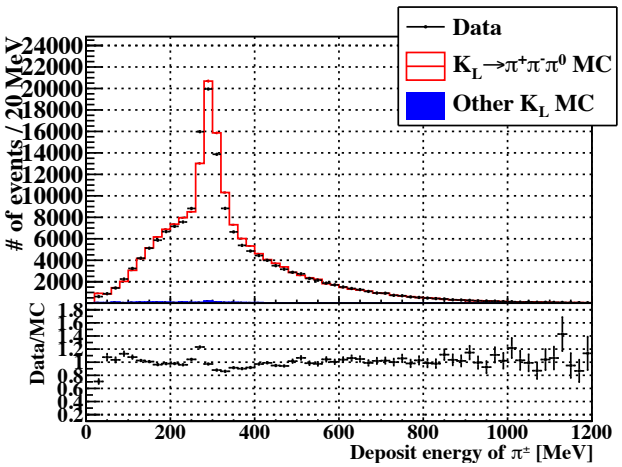

Figure 6.17: Deposit energies of charged pions in $K_L \to \pi^+\pi^-\pi^0$, simulated by the BIC model. The MC histograms are normalized by the BERT result. Extra cluster veto is not applied. The meanings of the plots are the same as in Fig. 6.16.

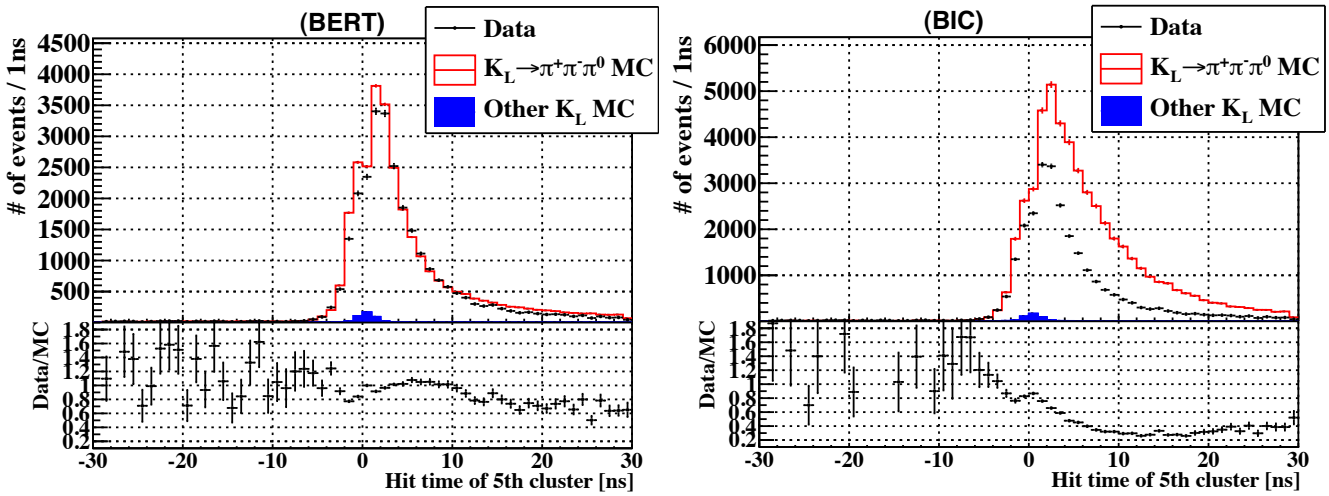

Figure 6.18: Hit timing of the fifth cluster in $K_L \to \pi^+\pi^-\pi^0$ simulated by the BERT (left) model and the BIC (right) model. The MC histograms are normalized by the BERT result. The meanings of the plots are the same as in Fig. 6.16.

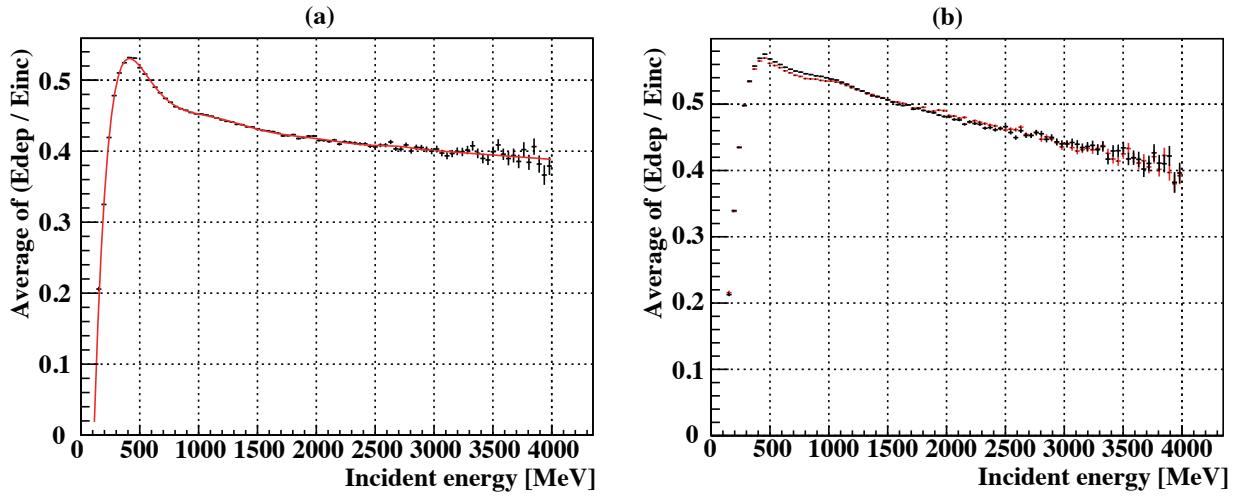

Figure 6.19: (a) Deposit energy (E_{dep}) fraction in the incident energy (E_{inc}) of the charge pions as a function of the incident energy in case of the MC simulation with the BERT model. The red solid curve shows the fit results by a polynomial of degree ten below 3000 MeV and a polynomial of degree two above it, which are described as F_{BERT} in the text. (b) Corrected deposit energy fraction in the incident energy of the charge pions as a function of the incident energy. The black points show the BIC model result and the red points show the corrected BERT result.

where E_{inc} is the true incident energy of charged pions, $F_{\mathrm{model}}(E)$ is the resultant polynomial fit function for each model, and E_{dep} is the simulated deposit energy of charged pions. The resultant plot is shown in Fig. 6.19(b). Figure 6.20 shows the corrected deposit energy spectrum of the charged pions and the CV energy spectrum with all selections except CV veto for the $K_L \to 2\gamma$ analysis. The reproducibility of the deposit energies improved. Here we discussed the phenomenalistic correction method, merging existent physics models, and showed the improvements. In the future, more precise study such as a beam test which measures the interaction between CsI crystals and charged pions is preferable.

Uncertainty Due to Charged Pion Interaction

For the exclusive analysis in the final result, we used sideband data to estimate the background contamination. It was free from the systematic uncertainty of the charged pion interaction. In case of the inclusive analysis, the $Ke3$ contamination, estimated with the MC simulation, should be treated as systematic uncertainty. We considered the $Ke3$ background contamination in the $K_L \to 2\gamma$ analysis here. We derived a scale factor of 1.897 for the $Ke3$ MC simulation to fit the experimental data by using the least square method below 2.5 MeV in the CV energy distribution. Figure 6.21 shows the effect of this scaling. The reproducibility became better. We considered this scale factor was a source of the uncertainty.

We assumed the shape of CV energy spectrum of penetrating charged particles as correct while this scaling; however, the low energy region below the veto threshold was dominated by other decay modes which did not have charged particles in their final states. We should estimate the repro-

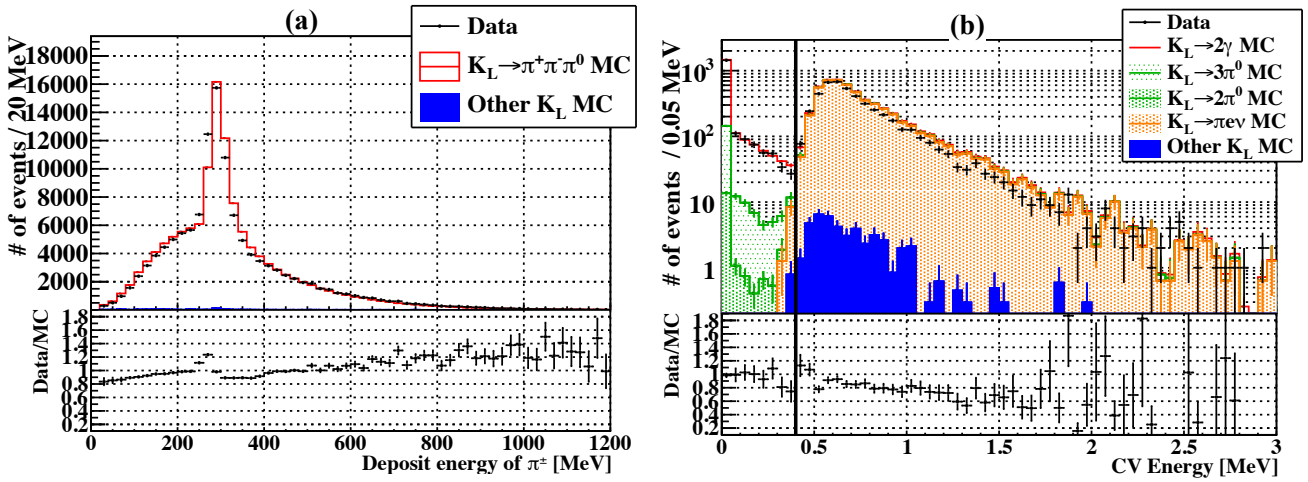

Figure 6.20: Two resultant spectra for the deposit energy correction. (a) Deposit energy spectrum of the charged pions in $K_L \to \pi^+\pi^-\pi^0$. The meanings of the plots are the same as in Fig. 6.16. (b) CV energy deposit spectrum with all selections except CV veto for the $K_L \to 2\gamma$ analysis. The meanings of the plots are the same as in Fig. 5.41.

ducibility of the low energy region below the threshold of the $Ke3$ background to justify this scaling uncertainty. We developed selections to enhance the $Ke3$ decay to estimate the reproducibility of the CV energy spectrum for penetrating charged particles. The selections are listed in Tab. 6.3. Parameters used in the selection were same as the selections in the main analyses but thresholds of some parameters were changed. Photon energy threshold of 500 MeV was set to remove the penetrating muon contamination from the Kμ3; cluster distance was required to be longer than 600 mm to remove $K_L \to 3\pi^0$ contamination. Shape χ^2 selection was also different from the main analyses: smaller Shape χ^2 was required to be less than 5 for an electromagnetic shower selection and larger Shape χ^2 was required to be larger than 5 for a hadronic shower selection. Veto set was same as the main analyses except CV. In this $Ke3$ enhancement, the deposit energy of one or more constitutive modules of CV was required to be larger than 0.4 MeV per module to reduce the $K_L \to 3\pi^0$ contamination. Finally we checked the maximum deposit energy in one plane of CV with requiring the maximum deposit energy in the other plane to be larger than 0.4 MeV. Figure 6.22 shows the spectra. In this case, we scaled the $Ke3$ MC simulation 1.317 times larger to match the number of remaining events of the MC simulation to that of the experimental data. The number of events below 0.4 MeV are listed in Tab. 6.4. The degree of consistency was 10 % between the experimental data and the MC simulation.

As the original $Ke3$ background contamination in the $K_L \to 2\gamma$ analysis was 0.25 %, the systematic uncertainty due to the $Ke3$ background was estimated as:

$$\begin{aligned} \sigma_{Ke3} &= 0.25\ \%\ \text{(background contamination)} \\ &\quad \times\ [38\ \%\ \text{(stat. error of } Ke3\ \text{MC)} \oplus 90\ \%\ \text{(CsI calorimeter)} \oplus 10\ \%\ \text{(CV)}\ ] \\ &= 0.24\ \%, \end{aligned} \tag{6.7}$$

It was small enough to be neglected for this analysis even if we used the inclusive method.

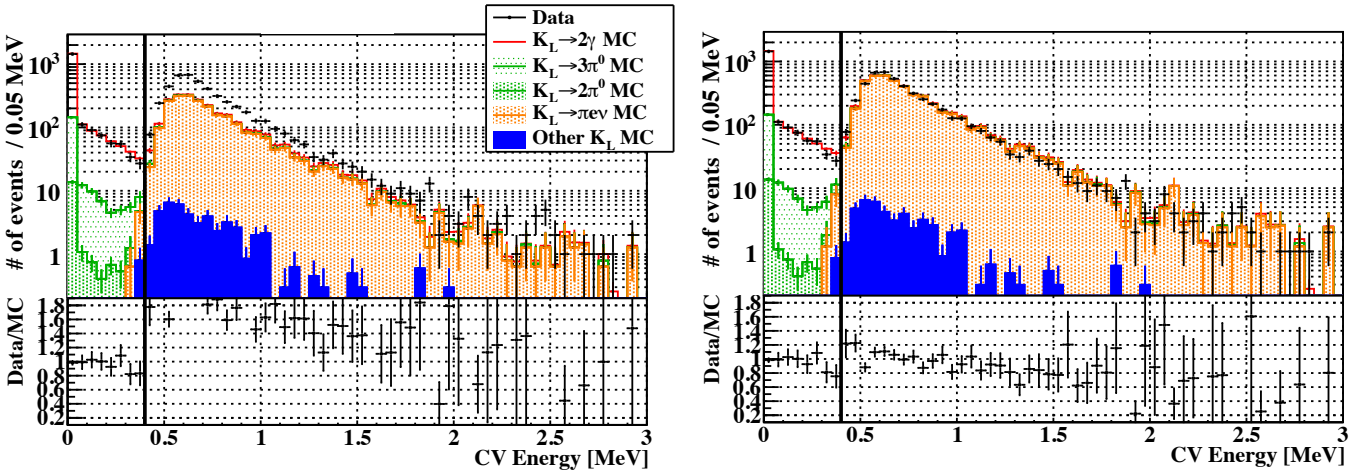

Figure 6.21: CV energy distribution with all selections for the $K_L \to 2\gamma$ decay except for CV Veto. Before the $Ke3$ scaling is shown in the left and after scaling is shown in the right. Except for the $Ke3$ MC simulation, all histograms are same as each other. The meanings of the plots are the same as in Fig. 5.41.

Table 6.3: Kinematic selections for $Ke3$ enhancement

Kinematic Cut	Min.	Max.
Δ vertex time		3 ns
Half Et	350 MeV	
Photon energy	500 MeV	
Innermost photon hit position	120 mm (square)	
Outermost photon hit position		850 mm (radial)
Cluster distance	600 mm	
Smaller Shape χ^2		5
Larger Shape χ^2	5	
Veto	**Threshold**	**Time window**
Extra cluster	-	-10 ns – $+10$ ns
CsI crystal	3–20 MeV	-10 ns – $+10$ ns
$\overline{\text{CV}}$	0.4 MeV	-10 ns – $+10$ ns
MB inner	5 MeV	-26 ns – $+34$ ns

Table 6.4: Number of events below 0.4 MeV in the CV energy spectra

Mode	events
Data	16083
MC total	14471
$Ke3$ MC	13665
$\pi^+\pi^-\pi^0$ MC	535
$3\pi^0$ MC	271

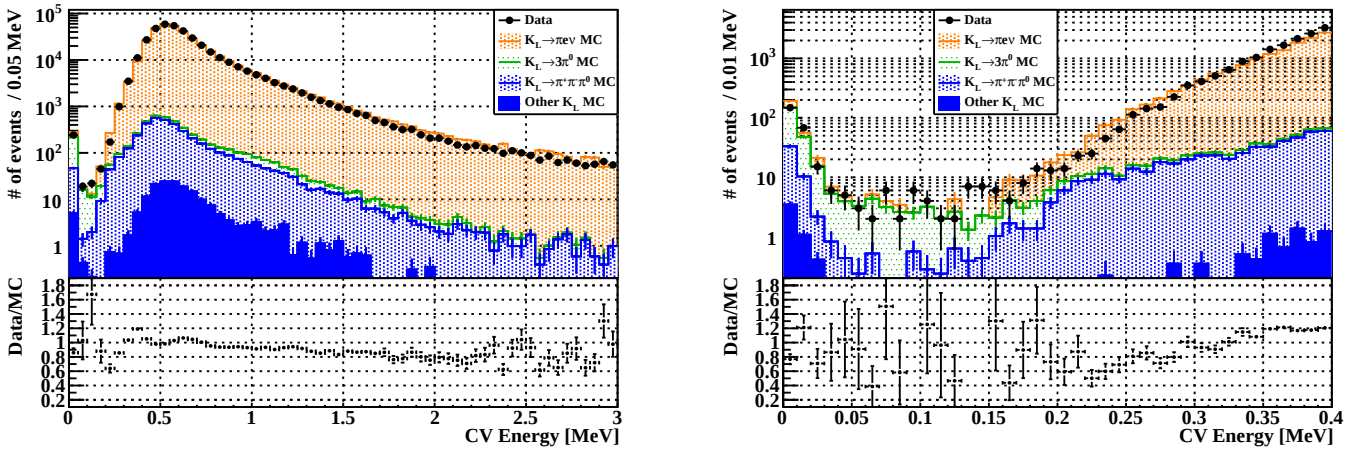

Figure 6.22: CV energy distribution with the $Ke3$ enhancement. These histograms were filled with the maximum deposit energy in one plane of CV with requiring the maximum deposit energy in the other plane to be larger than 0.4 MeV. The figure on the right side is the enlarged view of the low energy region of the left figure. In each figure, the black dots shows the experimental data, the orange histogram show the $Ke3$ MC simulation, the green histogram shows the $K_L \to 3\pi^0$ MC simulation, the blue hatched histogram show $K_L \to \pi^+\pi^-\pi^0$ MC simulation, and the blue solid histogram shows the other MC simulation. The histograms of MC simulation are stacked. The lower graph of each distribution shows the ratio between the experimental data and the MC simulation.

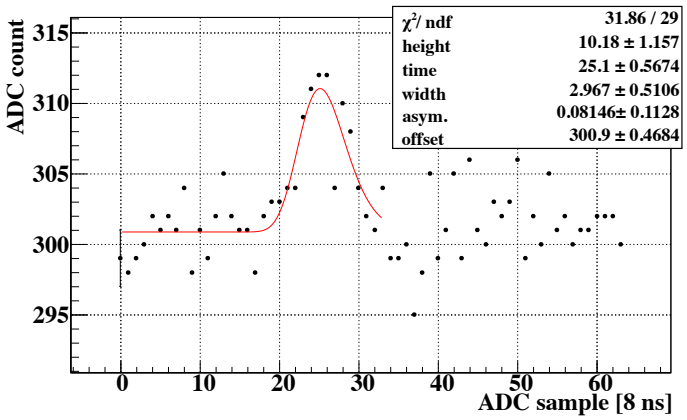

Figure 6.23: Example of a 1 MeV pulse taken by the ADC module. The vertical bar on the first point represents the noise level.

6.4.2 Pulse Shape Analysis

For the $K_L \to \pi^0\nu\overline{\nu}$ analysis, the veto threshold of the CsI calorimeter was set to be 3 MeV at the proposal[21]. We achieved the same threshold in this research by using integrated value of 64 samples as described in Sec. 5.1.1. The typical noise level was 0.4–0.5 MeV in this case. A further improvement is promising. If we use the pulse shape information, we can decrease the noise level at the level of 0.1 MeV and helps us to improve the veto efficiency by setting the veto threshold down. Figure 6.23 shows an example of 1 MeV pulse fitted by an asymmetric gaussian of the form:

$$A \exp\left[-\frac{(t-\mu)^2}{(a(t-\mu)+\sigma)^2}\right] + C, \tag{6.8}$$

where t is the time shown along the horizontal axis, A is the pulse height, μ is the time of pulse peak, σ is the standard deviation of the gaussian distribution, a is an asymmetry parameter, and C is the vertical offset. The fitting returned a pulse height of 10.2 ± 1.2 ADC counts over a noise level of ~ 2 ADC $\text{counts}_{\text{rms}}$. This confirmed that the system was able to resolve signals at the 1 MeV level.

The pulse shape, however, slightly depended on its height as shown in Fig. 6.24. We fitted each pulse shape with Eq. 6.8 and resultant σ, a, and A were filled each other to check these relations. We used small crystals only. As pulse height got higher, the pulse width became wider and the asymmetry slightly became larger. In addition, the shape differed from one crystal to another, and also changed event by event.

A pulse shape analysis is, of course, promising and we will study the detail mechanism of the pulse shape deviation to extract precise information of the energy and timing from the pulse shape.

6.4.3 Cluster Shape Analysis

While we established the methods to extract the energy, hit position, and hit timing from clusters through this measurement, the cluster analysis itself has scopes to continue to improve. If cluster shape reproducibility is established, we will be able to improve the background rejection power because this shape information should be useful to distinguish clusters which are made by two or more photons, $\pi^{\pm}$, and neutron from a genuine one-photon cluster. As already shown in Fig. 5.37, the simulated cluster size was slightly smaller than the experimental data, and Fig. 6.25 shows the energy distribution for crystals having the maximum energy deposit in a cluster and the maximum

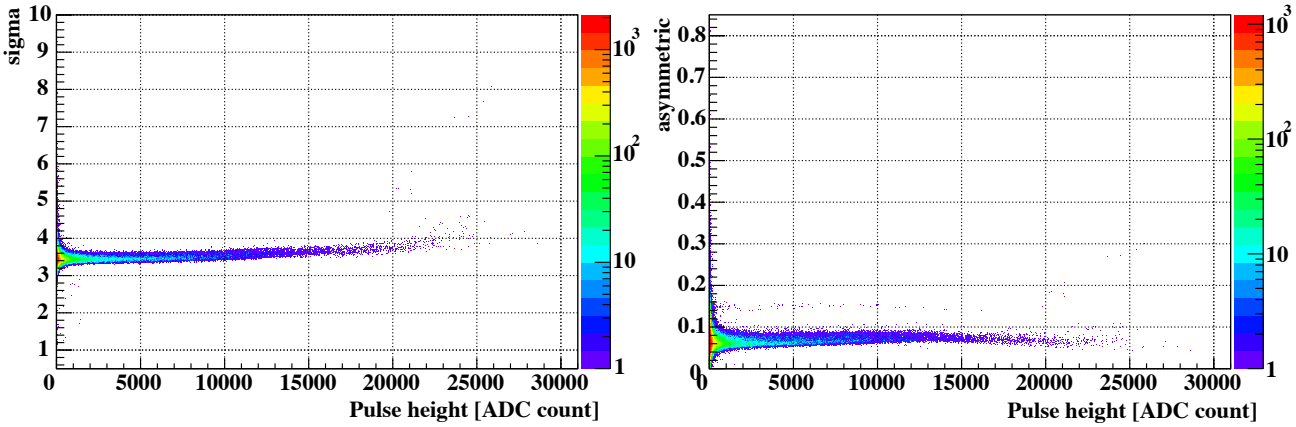

Figure 6.24: Pulse height dependence of the pulse width (σ; left) and pulse asymmetry (a; right) as a function of the pulse height (A).

shape χ^2 among six photon clusters with all selections for the $K_L \to 3\pi^0$. These plots told us that the energy deposit distribution in x-y plane of the experimental data was wider and was less concentrated to the crystals with maximum energy deposit than that of the MC simulation. It might cause the discrepancy of the shape χ^2. Now we have not considered the additional effects such as dead materials between the CsI crystals, cross talk between adjacent crystals, z position deviation of the crystals in our MC simulation. More improvements, by measuring such effects quantitatively and implementing them to the MC simulation, are expected.

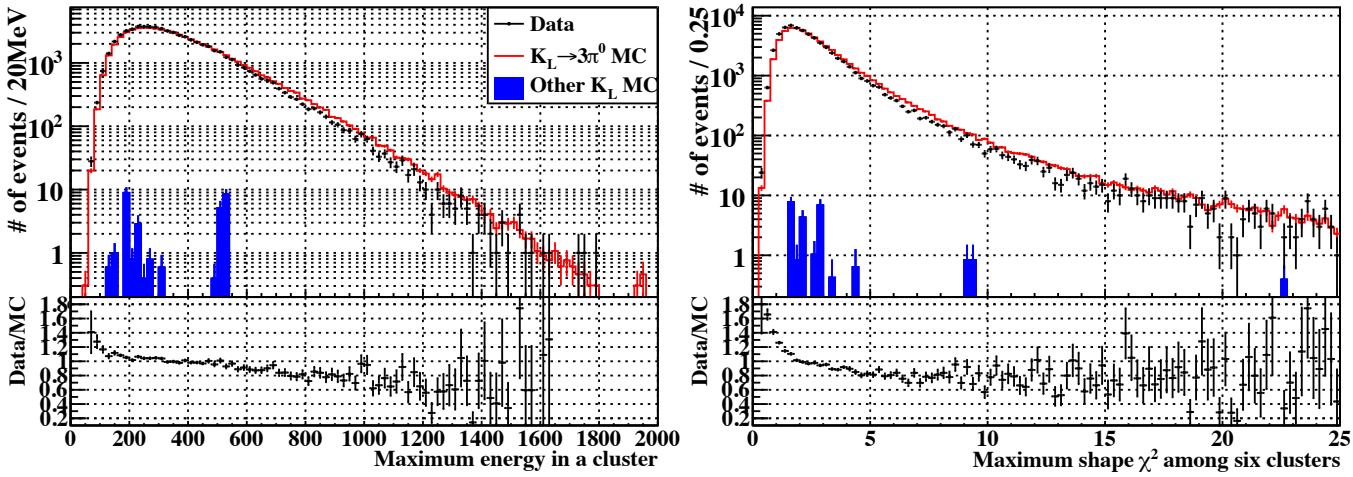

Figure 6.25: Maximum energy deposit of a crystal in a cluster(left) and maximum shape χ^2 among six photons(right). In each figure, the black solid points represent the experimental data, the red hollow histogram is the $K_L \to 3\pi^0$ MC simulation, and the histogram shown in solid blue is the other K_L MC simulation. All MC distributions are normalized by the result of the K_L flux measurement. The histograms of MC simulations are stacked in order. The lower graph of each distribution shows the ratio between the experimental data and the MC simulation. Solid vertical bars in each distribution represent the threshold of each selection.

Chapter 7

Conclusion

Today, the Standard Model of particle physics was successfully constructed. Almost all experimental results have been well explained by the Standard Model. Meanwhile the matter-dominant universe cannot be explained. A key to solve this asymmetry of matter and anti-matter is CP violation in the new physics beyond the Standard Model. The direct CP violating rare decay, $K_L \to \pi^0\nu\overline{\nu}$, is one of the most attractive processes to search experimental evidence of the new physics which breaks CP symmetry in the quark sector. The virtues of this decay, suppressed amplitude and theoretical cleanness, help us to discover the new physics.

The KOTO experiment, at J-PARC, aims at observing the $K_L \to \pi^0\nu\overline{\nu}$ decay. The detector system was renewed to obtain the sensitivity of the Standard Model level. We thus needed to understand the actual detector performance, construct a realistic simulation model, and build an analysis framework to reconstruct objective signals. They were the foundations of the KOTO experiment.

We therefore decided to measure the K_L beam flux prior to physics runs, with the measurements of three neutral decay modes: $K_L \to 3\pi^0$, $K_L \to 2\pi^0$, and $K_L \to 2\gamma$. Using this data, we developed and evaluated the reconstruction method. The good consistency between the experimental data and the simulation was obtained. To achieve the good reproducibility of the simulation, we considered the detailed response of the detectors. Position dependence of the light yield, calibration accuracy, and electrical noise, which caused fluctuations of the energy measurement, were implemented. Accidental activities were also considered to improve the reproducibility.

We got $(4.182 \pm 0.017 \pm 0.059) \times 10^7$ K_L per 2×10^{14} proton on target. The first error was statistical and the second error was systematic error. The three mode results were consistent among them within their statistical errors. The agreement showed that the acceptances of them, estimated with the simulation, were well reproduced. Through this measurement, we successfully established the analysis methods and obtained the realistic MC simulation model based on the detector understandings, which were essential tools of the experiment.

We performed the first physics run in May 2013, after the measurement of this research. We accumulated the experimental data for the analysis of $K_L \to \pi^0\nu\overline{\nu}$. This run aimed at updating the current world record of the branching fraction of $K_L \to \pi^0\nu\overline{\nu}$, and exceeding the Grossman-Nir limit by using the new KOTO detector system. In the analysis, the signal sensitivity and the background contamination are being studied with the analysis framework and the simulation model which were established in this research. New result on the $K_L \to \pi^0\nu\overline{\nu}$ search will come in a year.

Finally, the KOTO experiment will upgrade some detectors to achieve the sensitivity comparable to the Standard Model prediction. Together with improvements in the J-PARC accelerators, the

KOTO experiment will take physics data to obtain the goal of the experiment.

Bibliography

[1] J. Beringer et al.(PDG). *Physical Review D*, 86:010001, 2012.

[2] K. Shiomi. *Measurement of K_L flux at the J-PARC neutral-kaon beam line for the $K_L \to \pi^0\nu\overline{\nu}$ experiment*. PhD thesis, Kyoto University, 1 2012.

[3] J-PARC. http://j-parc.jp/index-e.html, 2013.

[4] Makoto Kobayashi and Toshihide Maskawa. CP-Violation in the Renormalizable Theory of Weak Interaction. *Progress of Theoretical Physics*, 49(2):652–657, 1973.

[5] Lincoln Wolfenstein. Parametrization of the Kobayashi-Maskawa Matrix. *Phys. Rev. Lett.*, 51:1945–1947, Nov 1983.

[6] Joachim Brod et al. Two-loop electroweak corrections for the $K \to \pi\nu\overline{\nu}$ decays. *Phys. Rev. D*, 83:034030, Feb 2011.

[7] Gerhard Buchalla and Gino Isidori. The CP-conserving contribution to $K_L \to \pi^0\nu\overline{\nu}$ in the standard model. *Physics Letters B*, 440(1-2):170 – 178, 1998.

[8] A. J. Buras. CP Violation and Rare Decays of K and B Mesons. arxiv:hep-ph/9905437, 1999.

[9] Monika Blanke. New Physics Signatures in Kaon Decays. volume PoS(KAON13)010. Proceedings of 2013 Kaon Physics International Conference, SISSA, May 2013.

[10] S. Chatrchyan et al. Measurement of the $B_s^0 \to \mu^+\mu^-$ Branching Fraction and Search for $B^0 \to \mu^+\mu^-$ with the CMS Experiment. *Phys. Rev. Lett.*, 111:101804, Sep 2013.

[11] R. Aaij et al. Measurement of the $B_s^0 \to \mu^+\mu^-$ Branching Fraction and Search for $B^0 \to \mu^+\mu^-$ Decays at the LHCb Experiment. *Phys. Rev. Lett.*, 111:101805, Sep 2013.

[12] Yuval Grossman and Yosef Nir. $K_L \to \pi^0\nu\overline{\nu}$ beyond the standard model. *Phys. Lett. B*, 398:163–168, Apr 1997.

[13] Tobias Hurth, Gino Isidori, Jernej F. Kamenik, and Federico Mescia. Constraints on new physics in MFV models: A model-independent analysis of processes. *Nuclear Physics B*, 808(1-2):326 – 346, 2009.

[14] Monika Blanke et al. FCNC Processes in the Littlest Higgs Model with T-Parity: an Update. *Acta Phys. Polon. B*, 41(3):657, 2010.

[15] Monika Blanke et al. Rare K and B Decays in a warped extra dimension with custodial protection. *Journal of High Energy Physics*, 2009:108, 2009.

[16] A. J. Buras et al. Patterns of flavour violation in the presence of a fourth generation of quarks and leptons. *Journal of High Energy Physics*, 2010(9):1–74, 2010.

[17] David M. Straub. New physics correlations in rare decays. arxiv:1012.3893v2, 2011.

[18] Laurence S. Littenberg. CP-violating decay $K_L \to \pi^0\nu\overline{\nu}$. *Phys. Rev. D*, 39(11):3322–3324, Jun 1989.

[19] J. Ahn et al. Experimental study of the decay $K_L^0 \to \pi^0\nu\overline{\nu}$. *Physical Review D*, 81(7), 2010.

[20] Taku Yamanaka for the KOTO collaboration. The J-PARC KOTO experiment. *Prog. Theor. Exp. Phys.*, 2012:02B006, 2012.

[21] J. Comfort et al. Proposal for $K_L \to \pi^0\nu\overline{\nu}$ Experiment at J-Parc, 2006.

[22] Shoji Nagamiya. Introduction to J-PARC. *Progress of Theoretical and Experimental Physics*, 2012(1), 2012.

[23] T. Shimogawa. Design of the neutral K_L^0 beamline for the KOTO experiment. *Nucl. Instr. and Meth. A*, 623(1):585 – 587, 2010.

[24] K. Shiomi et al. Measurement of flux at the J-PARC neutral-kaon beam line. *Nucl. Instr. and Meth. A*, 664(1):264 – 271, 2012.

[25] A. Fasso et al. The physics models of FLUKA: status and recent developments. In *International Conference on Calorimetry in High Energy Physics 2003*, 2003.

[26] A. Fasso et al. A Detector Description and Simulation Tool, Application Software Group, Computing and Networks Division. In *International Conference on Calorimetry in High Energy Physics 1993*, pages 493–502, 1993.

[27] A. Alavi-Harati et al. Measurements of direct CP violation, CPT symmetry, and other parameters in the neutral kaon system. *Phys. Rev. D*, 67:012005, Jan 2003.

[28] J. D. Cockcroft and E. T. S. Walton. Experiments with High Velocity Positive Ions. *Proc. R. Soc. London*, 136(831):619–630, July 1932.

[29] Thomas L. Quarles. *Analysis of Performance and Convergence Issues for Circuit Simulation.* PhD thesis, EECS Department, University of California, Berkeley, 1989.

[30] SUSUMU CO., LTD.. http://www.susumu.co.jp/english/, 2013.

[31] Texas Instruments. http://www.ti.com/, 2013.

[32] Analog Devices. http://www.analog.com/en/index.html, 2013.

[33] Y. Tajima et al. Barrel photon detector of the KEK experiment. *Nucl. Instr. and Meth. A*, 592(3):261 – 272, 2008.

[34] Yosuke Maeda. CHARGED-PARTICLE VETO DETECTOR FOR THE $K_L \to \pi^0\nu\overline{\nu}$ STUDY IN THE J-PARC KOTO EXPERIMENT. In *Proceedings of the PIC 2012*, 2012.

[35] N. Kawasaki. A Gamma and Neutron Counter of Undoped CsI Crystals with WLSFiber Readout for the KOTO Experiment. In *proceedings of "2013 Kaon Physics International Conference"*, 2013.

[36] Yosuke Maeda. Beam Hole Photon Veto For J-PARC KOTO experiment. In *2009 KAON International Conference KAON09*, June 2009.

[37] S. Agostinelli et al. Geant4 - a simulation toolkit. *Nucl. Instr. and Meth. A*, 506(3):250 – 303, 2003.

[38] J. Allison et al. Geant4 developments and applications. *Nuclear Science, IEEE Transactions on*, 53(1):270–278, 2006.

[39] Kazufumi Sato. CsI Calorimeter for KOTO experiment. In *Calorimetry for High Energy Frontiers - CHEF 2013*, 2013.

[40] E. Iwai. *CsI calorimeter fot the J-PARC KOTO experiment.* PhD thesis, Osaka University, 10 2012.

[41] A. Kiyomichi et al. BEAM SPILL CONTROL FOR THE J-PARC SLOW EXTRACTION. In *The 1st International Particle Accelerator Conference, IPAC'10*, 2010.

[42] Atomic Nuclear Properties (PDG). http://pdg.lbl.gov/2013/AtomicNuclearProperties/, 2013.

Appendix A

Veto Counters Calibrations

A.1 Main Barrel

MB was calibrated using cosmic rays. First a timing offset of each channel was calibrated. Once the timing was calibrated, we were able to measure the hit position in each module by using the time difference between the upstream channel and the downstream channel in the module. Next, we determined the calibration constant which converted ADC count to energy.

A.1.1 Timing Calibration

In this paragraph, we defined the timing offset of upstream channel and downstream channel of i-th module as o_{iu} and o_{id}, respectively.

First, we determined the relative timing offset between upstream and downstream channels in each module: $(o_{iu} - o_{id})$. Collecting events in which both channels of upstream and downstream had activities above the half of MIP energy deposit, we got distribution of the time difference between both channels as shown in Fig. A.1. The center of this distribution corresponded to the center hit along the module, and in this case, the time difference between the upstream and downstream channels should be zero to satisfy Eq. 4.11. The both upstream and downstream edge of the distribution were determined by the gaussian and plateau as:

$$A_u \exp\left[-\frac{(t-\mu_u)^2}{2\sigma_u^2}\right] \quad : \text{ for } t \leq \mu_u \text{ of the upstream edge;} \tag{A.1}$$

$$A_u \quad : \text{ for } t > \mu_u \text{ of the upstream edge;} \tag{A.2}$$

$$A_d \quad : \text{ for } t < \mu_d \text{ of the downstream edge;} \tag{A.3}$$

$$A_d \exp\left[-\frac{(t-\mu_d)^2}{2\sigma_d^2}\right] \quad : \text{ for } t \geq \mu_d \text{ of the downstream edge;} \tag{A.4}$$

where t is the time difference shown along the horizontal axis, A_u (A_d) is the height of the edge, μ_u (μ_d) is the mean of the gaussian, and σ_u (σ_d) is the standard deviation of the gaussian. The value of μ was used as the edge position. We thus got $o_u - o_d = (\mu_u - \mu_d)/2$ for each module. After this step, we determined the hit position along the module using timing information of both end channels by using Eq. 4.11.

Second, we determined the timing offset of modules, $(o_{iu} + o_{id})/2$, by the same minimization method as the timing calibration for the CsI calorimeter described in Sec. 5.2.2. We selected tracks

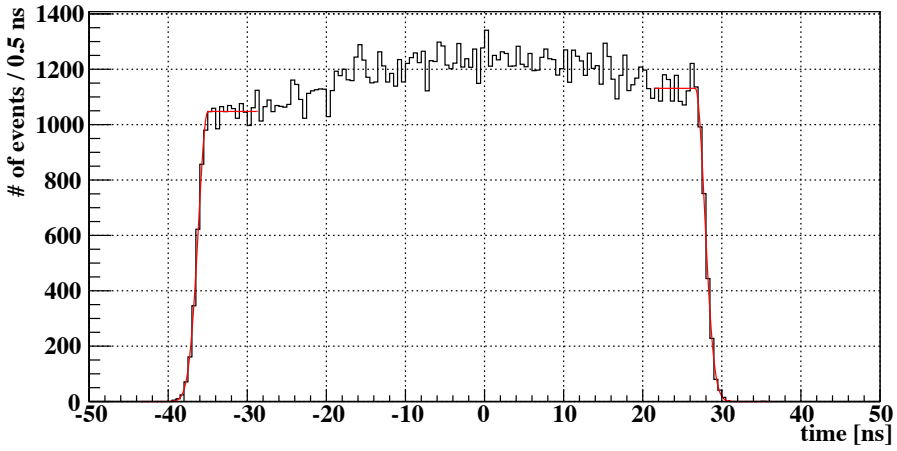

Figure A.1: Time difference between the upstream channel and downstream channel of one MB module with cosmic ray events. The left red line shows the fit result of Eqs. A.1 and A.2, and the right red line shows that of Eqs. A.3 and A.4.

which penetrated multiple modules. Requiring hit positions of all modules to locate at the center within ±200 mm along the modules, we accumulated tracks which flied perpendicular to the z axis at the center of MB. Some examples of such tracks are shown in Fig. A.2. After that we defined the same χ^2 as Eq. 5.13 and minimized the offset $(o_{iu} + o_{id})/2$ for all modules. As we obtained both $(o_{iu} - o_{id})$ and $(o_{iu} + o_{id})$ for all modules, we finally determined the timing offset for each channel as:

$$o_{iu} = \frac{(o_{iu} - o_{id}) + (o_{iu} + o_{id})}{2}, \tag{A.5}$$

$$o_{id} = -\frac{(o_{iu} - o_{id}) - (o_{iu} + o_{id})}{2}. \tag{A.6}$$

A.1.2 Energy Calibration

The energy calibration for the MB was also performed using cosmic rays. To measure the MIP peak values in a unit length, we required cosmic rays to penetrate perpendicular to each module. We used looser track selection criteria than that of the timing calibration as drawn in Fig. A.3, and applied following three corrections to the energy deposit.

- Attenuation correction : to vanish the position dependence along the module using Eq. 4.12,
- Incident angle (θ) correction : to normalize the path length using the angle between the track and z axis,
- Non-diagonal (φ) correction : to normalize the path length using the angle between the track and radial axis.

The deviation due to these corrections was less than 1 % when we limited φ was less than 20°. The MIP peak of one channel is shown in Fig. A.4. It was fitted with a convolution function of gaussian and Landau function. The calibration factor was calculated by assuming the energy deposit in the module to be 15.0 MeV for the inner modules and 30.0 MeV for the outer modules[33].

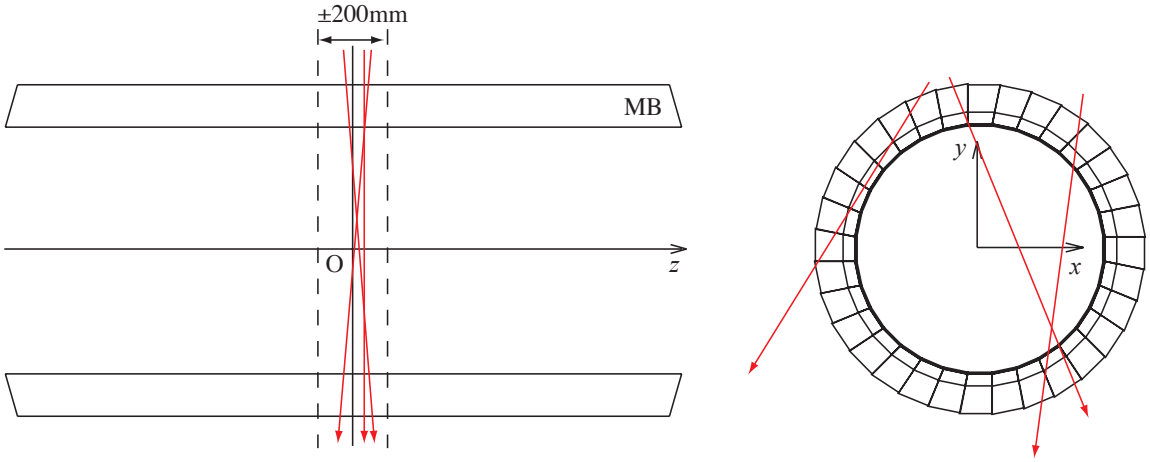

Figure A.2: Cartoon of the cosmic ray track examples used for the MB timing calibration. The left figure is the side view and the right figure is the rear view of the MB. The red arrows represent cosmic ray tracks which are able to be used for the timing calibration between modules.

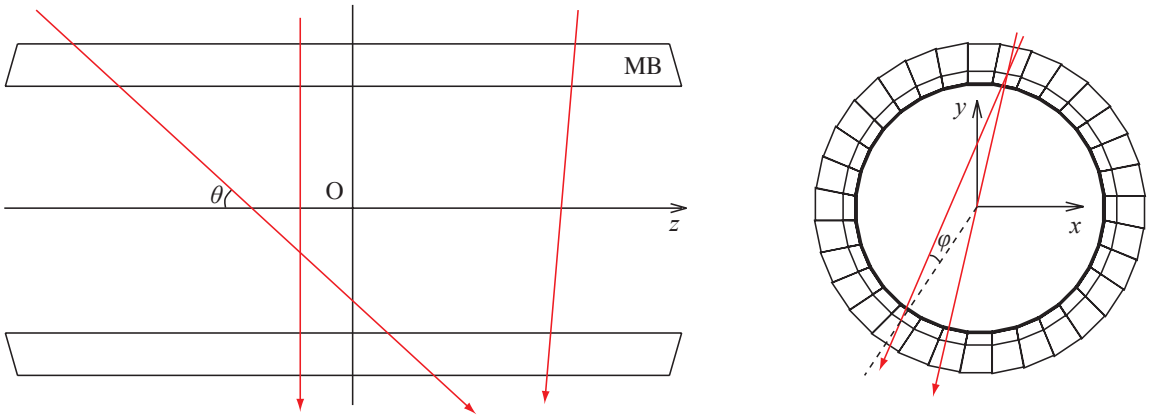

Figure A.3: Cartoon of the cosmic ray track examples used for the MB energy calibration. The left figure is the side view and the right figure is the rear view of the MB. The red arrows represent cosmic ray tracks which are able to be used for the energy calibration.

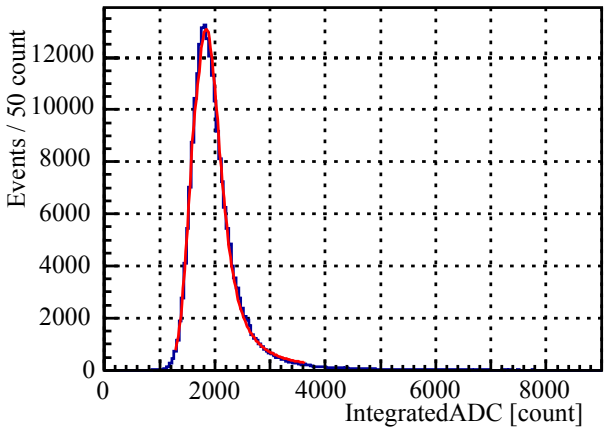

Figure A.4: MIP peak of the MB module fitted with Landau function.

A.2 Charged Veto

In contrast to MB, the calibration of CV was done using beam data in spite of cosmic ray events.

A.2.1 Timing Calibration

The timing offset for each module of CV was calibrated using the same minimization method as in the case of MB. The time difference between pairs of modules were accumulated by using charged particles in the beam instead of cosmic rays. We accumulated the coincidence hits between one of front modules and one of rear modules, and also the CsI calorimeter. To confine the TOF between the front and the rear modules, it was necessary to limit the coincidence quadrant. As drawn in Fig. A.5, the modules were placed with four-fold symmetry, and in each four quadrant, they were placed perpendicularly between the planes. Using data of the beam muon run(Sec. 3.3.3) and requiring the coincidence hits between the same quadrant of the two planes and the behind region of the CsI calorimeter, we were able to accumulate charged tracks parallel to the beam axis in the blue regions shown in Fig. A.5. In this case the x-y hit position was determined as the overlap region between the two modules. In addition, using K_L beam and requiring the coincidence hits between a front module in one quadrant and a rear module in the adjacent quadrant, we selected charged particles which penetrated the red rectangle regions drawn in Fig. A.5. Because all charged particles come from the beam axis, possible directions of a track did not have axial component and the direction were able to be determined by the CV and CsI hit positions. We thus made all pairs of two modules determine the TOF between the two planes. The coincidence pairing for the timing calibration and beam conditions are summarized in Tab. A.1, and cartoons of available events are shown in Fig. A.6. We connected all modules to minimize the timing offsets among the modules.

A.2.2 Energy Calibration

The energy calibration of CV was also performed using the K_L beam. To make clear MIP peak, we used $K_L \to \pi^+\pi^-\pi^0$ enhanced samples. In this time, the event reconstruction was fully same as $K_L \to 2\pi^0$ analysis. We only changed event selection criteria for this enhancement as listed in Tab. A.2. Examples of the resultant energy deposit distributions with the selection are shown in

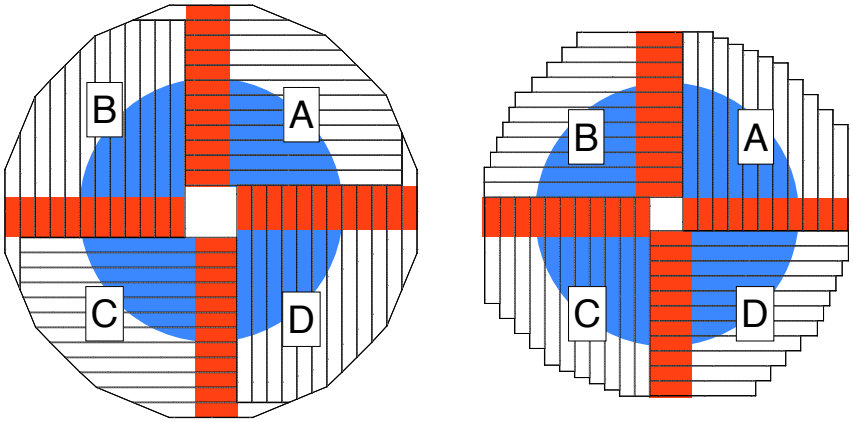

Figure A.5: Cartoon of the CV coincidence region. The rear view of the front plane (left) and the rear plane (right). The colored regions were explained in the main text.

Table A.1: Coincidence pairing for the timing calibration of the CV

Overlap Pattern	Front Quadrant	Rear Quadrant	Beam Condition
Perpendicular	A	A	μ beam
	B	B	
	C	C	
	D	D	
Parallel	A	B	K_L beam
	B	C	
	C	D	
	D	A	

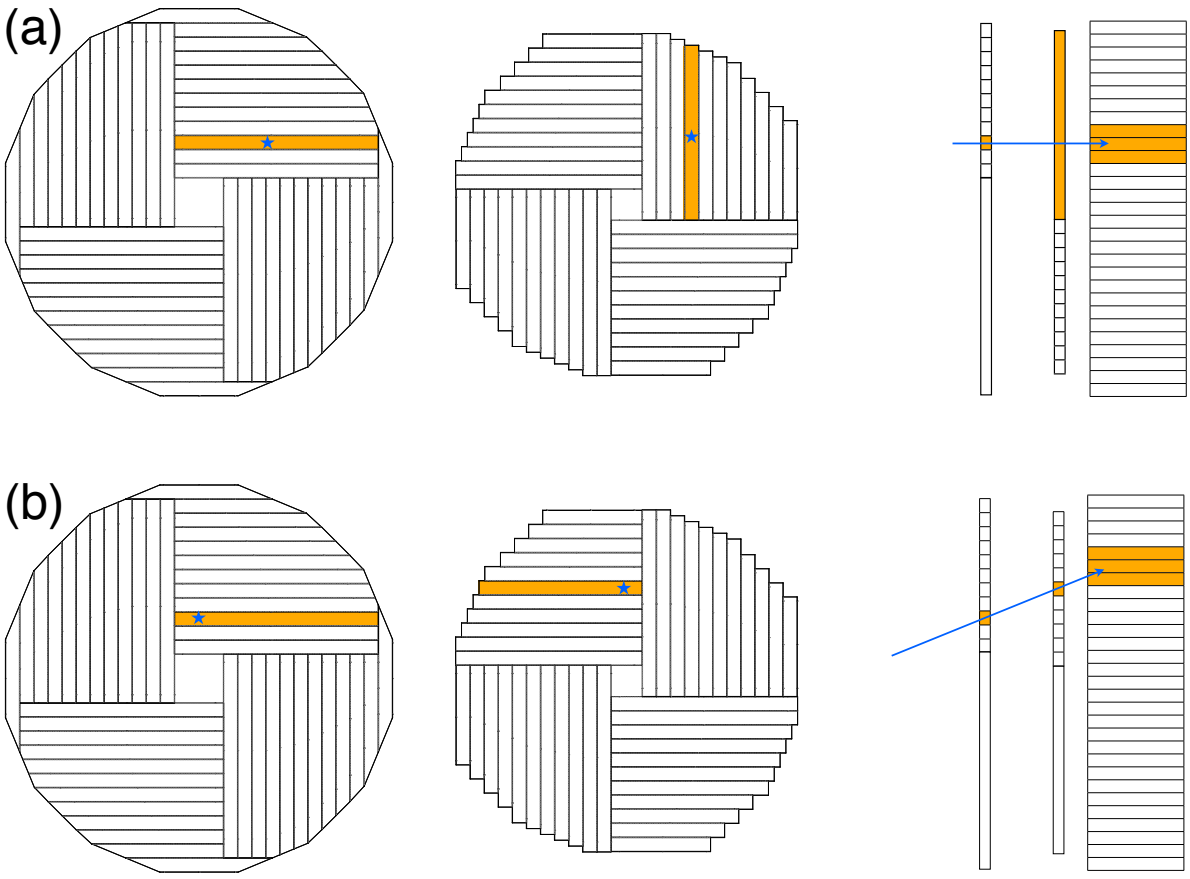

Figure A.6: Cartoon of the coincidence display. (a) Perpendicular coincidence, (b) Parallel coincidence. The left figures are the rear view of the front CV plane, the center figures are the rear view of the rear CV plane, and the right figures show the side view including the CsI calorimeter. The colored modules shown in orange represent hit modules. The positions marked with a star are the hit positions where charged particles penetrated, and the blue arrows in the right figures denote the trajectories of these charged particles.

Table A.2: Event selections for the $K_L \to \pi^+\pi^-\pi^0$ enhancement

Kinematic Cut	Min.	Max.
K_L Mass (w/ $K_L \to 2\pi^0$ assumption)		400 MeV/c^2
Half Et	350 MeV	
Minimam Cluster Energy	300 MeV	
Maximum Cluster Energy	600 MeV	
Veto	Energy Threshold	Time Window
Extra Cluster	-	-10 ns – $+10$ ns
MB Inner	5 MeV	-26 ns – $+34$ ns

Fig. A.7. Clear MIP peaks made of $\pi^+\pi^-\pi^0$ samples existed. We fitted the MIP peak with Landau function and made the calibration factors so as to adjust the peak position of the experimental data to that of the MC simulation. The calibration accuracy evaluated from the fitting error was 1.8 %.

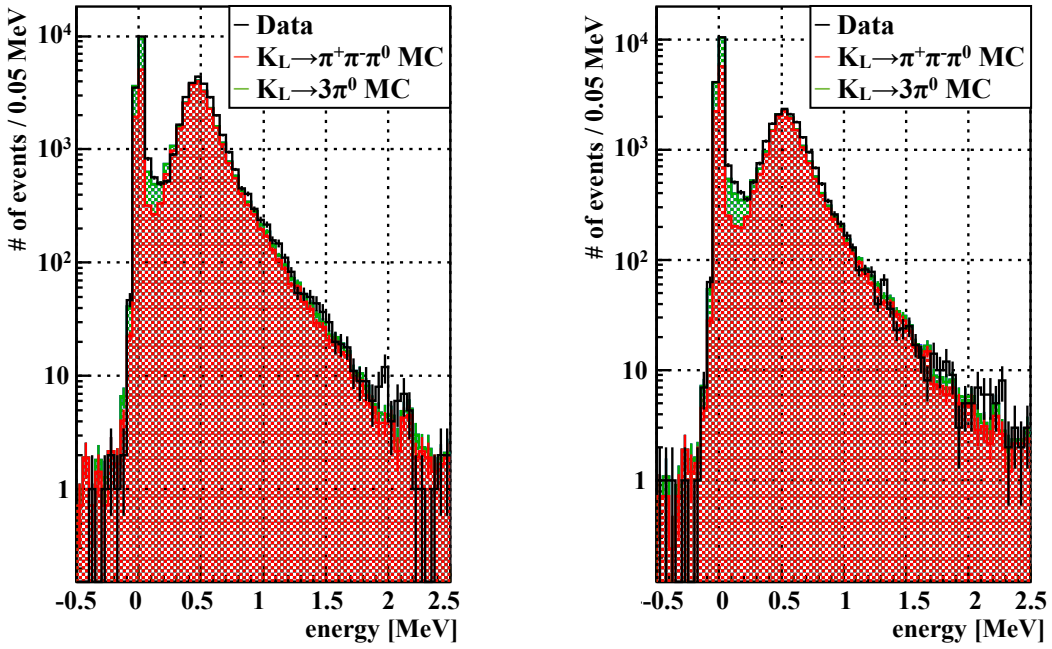

Figure A.7: Two examples of energy distributions of CV modules with the $K_L \to \pi^+\pi^-\pi^0$ enhancement. The innermost module (left) and the adjacent module (right) are shown. The horizontal axes are the energy deposit of each module. The black histograms show the experimental data, the red hatched histograms show the $K_L \to \pi^+\pi^-\pi^0$ MC result, and the green hatched histograms show the $K_L \to 3\pi^0$ MC result. The green hatched histograms are stacked on the red hatched histograms. The MC simulation results were normalized by the number of K_L.

Appendix B

$K_L \to \pi^+\pi^-\pi^0$ reconstruction

B.1 Brief Summary

Here, we introduce the $K_L \to \pi^+\pi^-\pi^0$ reconstruction method. We developed this reconstruction to accumulate pure charged pion samples. A reconstruction flow is shown in Fig. B.1. For $K_L \to \pi^+\pi^-\pi^0$, if two charged pions hit both CV and the CsI calorimeter and two photons from the π^0 also hit the CsI calorimeter, we can reconstruct the vertex and invariant mass of the initial K_L. We used events in which four clusters in the CsI calorimeter. Two of them were charged pions and the other two were photons. Using CV hit information, we distinguished two charged pions and two photons from the four clusters. We assumed π^0 from the two photons and calculated the vertex position with the same method as the main analysis. Once vertex position was determined, we reconstructed two tracks of charged pions by connecting the vertex position to the hit positions on the CsI calorimeter. In addition, we calculated the momenta of both of the charged pions by requiring the momentum balance among them. Finally we reconstructed the initial K_L mass by summing four momenta of the two charged pions and one π^0.

B.2 Discrimination between Charged Pions and Photons

First, we required that there were four or more clusters, whose deposit energy exceeded 20 MeV, in the CsI calorimeter. As is the case of the main analysis, if there were more photon clusters in the time window, we selected four photon clusters whose mutual timings were closest. Clustering method was same as the main analysis. The next step was to discriminate which two clusters were made by charged pions, by using CV hit information.

We required two hits in both front and rear CV planes. Hit was defined that the energy deposit of a module was from 0.2 MeV to 1.5 MeV within ±15-ns-width time window from the average time of the four clusters. To determine the two charged particle tracks, we surveyed overlap positions among the same combinations as the timing calibration (Tab. A.1). The front and rear planes of CV were at right angles to each other in all four quadrant (Fig. A.5). We were thus able to determine the hit position in x-y plane where a charge pion penetrated by requiring the coincidence between a front module and a rear module in a same quadrant. In addition, we were also able to require the adjacent quadrants where the modules were placed in parallel. In such case, we assumed the hit position as follows. The direction perpendicular to the coincident strips was to be at the center of the overlap region and the direction parallel to the modules was at the center of the rear

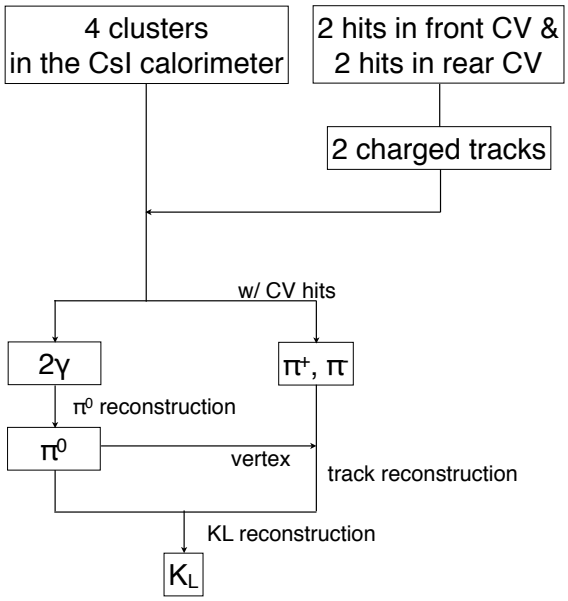

Figure B.1: $K_L \to \pi^+\pi^-\pi^0$ reconstruction flow.

module. We used events in which there were just two combinations between a front module and a rear module. If there were less or more combinations, that event was rejected. After determining the two CV hit positions, we compared the positions of four clusters in the CsI calorimeter and two hits in CV. We identified the nearest cluster for each CV hit as a charged pion. The remained two clusters were assumed to be made by photons.

B.3 Reconstruction

The next step was the reconstruction of each pion. We first reconstructed a vertex and four-momentum of a π^0 from the two photons with the same method as the main analysis described in Sec. 5.3.1. The reconstructed vertex position was assumed as the initial K_L vertex position.

Two charged pion tracks were connected from the vertex to the clusters in the CsI calorimeter. Considering momentum conservation in the plane perpendicular to the beam axis, the following equations hold:

$$p_+ \sin\theta_+ \cos\phi_+ + p_- \sin\theta_- \cos\phi_- + p_{0x} = 0, \quad \text{(B.1)}$$

$$p_+ \sin\theta_+ \sin\phi_+ + p_- \sin\theta_- \sin\phi_- + p_{0y} = 0, \quad \text{(B.2)}$$

where $p_\pm$, $\theta_\pm$, and $\phi_\pm$ are the absolute momenta, the polar angles, and the azimuthal angles of $\pi^\pm$, respectively, and p_{0x} (p_{0y}) is the x (y) component of the π^0 momentum. They are drawn in Fig. B.2. Assigning the values of $\theta_\pm$, $\phi_\pm$, p_{0x}, and p_{0y}, we calculated $p_\pm$. We then assumed these were $\pi^\pm$ and got four-momenta of $\pi^\pm$. Finally, the invariant mass of π^+, π^-, and π^0 was calculated by summing their four-momenta, and the reconstructed K_L mass was obtained.

Applied event selections listed in Tab. B.1, the background contamination was less than 0.5 %. Figure B.3 shows spectra of several parameters of the reconstructed K_L and $\pi^\pm$. The experimental data and the MC simulation were consistent.

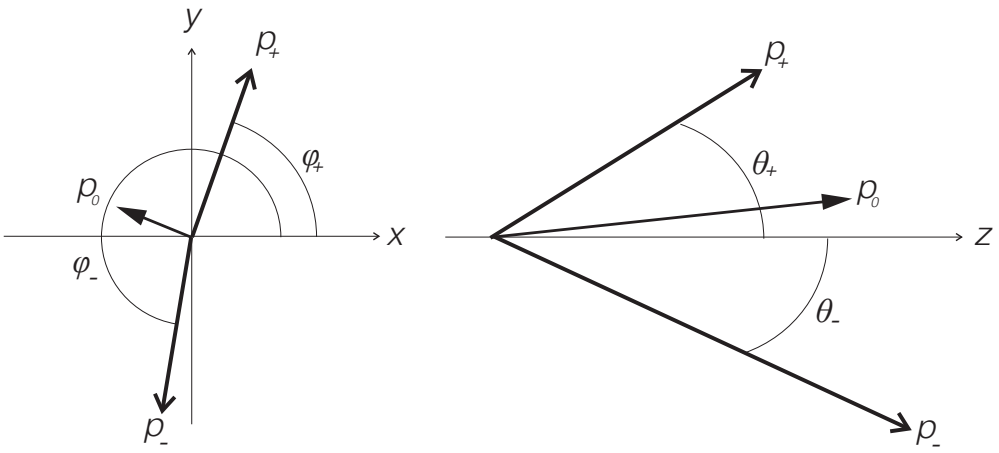

Figure B.2: Notation of the $\pi^{\pm}$ and π^0 momentum parameters. Figure on the left shows the transverse components of the momenta and figure on the right shows the longitudinal components of them.

Table B.1: Event selections for the $K_L \to \pi^+\pi^-\pi^0$ mode

Kinematic Cut	Min.	Max.
Δ Vertex Time		3 ns
Δ K_L Mass	-45 MeV/c^2	45 MeV/c^2
Half Et	350 MeV	
Photon Energy	50 MeV	
Innermost Cluster Hit Position	120 mm (square)	
Outermost Cluster Hit Position		850 mm (radial)
Cluster Distance	150 mm	
Z_{vtx}	2000 mm	5400 mm
Transverse momentum of π		135 MeV/c
Veto	Energy Threshold	Time Window
Extra Cluster	-	-10 ns – $+10$ ns

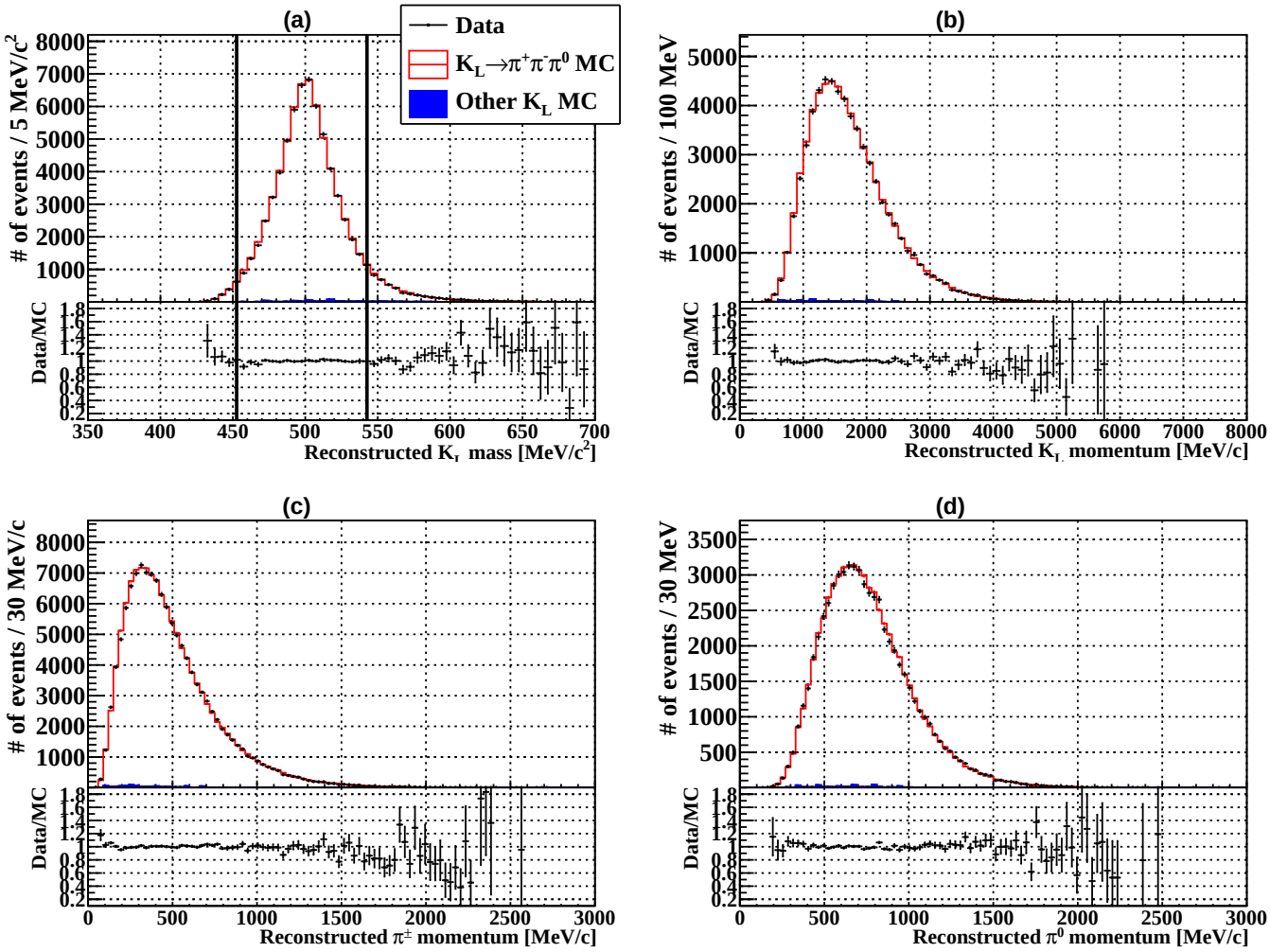

Figure B.3: Four examples of spectra of $K_L \to \pi^+\pi^-\pi^0$ reconstruction with the $K_L \to \pi^+\pi^-\pi^0$ selection. (a) Reconstructed K_L mass, (b) Reconstructed K_L momentum, (c) Reconstructed incident energy of $\pi^\pm$, (d) Larger transverse momentum between reconstructed π^+ and π^-. Black dots show the experimental data. Red hollow histograms show the $K_L \to \pi^+\pi^-\pi^0$ MC simulation, and blue solid histograms show the other K_L decay simulation. Each histogram of the $K_L \to \pi^+\pi^-\pi^0$ MC simulation is stacked on the other K_L decay histogram. The vertical bars in (a) show the thresholds in the event selection (Tab. B.1). The MC simulation results are normalized by the remained number of events with the event selection. Bottom plot of each figure shows the ratio between the experimental data and the MC simulation.

Appendix C

Cosmic Ray Reconstruction with Main Barrel

MB was able to reconstruct cosmic ray tracks with its hit information. It was useful to check the performance of detectors, *e.g.* the energy calibration and the position dependence. A cosmic-ray trajectory was reconstructed by fitting a MB hit pattern with three straight lines in x-y, y-z, and y-t planes.

First we gathered MB modules which had energy deposit of more than 5 MeV and their mutual time were within 24-ns-wide time window. When there were more than three hit modules among all 64 modules, we moved onto the reconstruction. For the fitting, x and y positions were assigned at the center of the modules, and their errors were assumed to be 100 mm by reflecting the module size. z position and hit time (t) were determined with Eqs. 4.11 and 4.10, respectively. Errors of z and t were assumed to be 150 mm and 0.5 ns by considering their resolution, respectively. Figure C.1 shows an example of the event display of a cosmic ray track reconstructed with MB hit information. To collect pure cosmic ray events, all reduced chi-squares of three fit results were required to be less than 2. The following three equations were obtained from the fits:

$$x(y) = \frac{\mathrm{d}x}{\mathrm{d}y}y + x_0, \tag{C.1}$$

$$z(y) = \frac{\mathrm{d}z}{\mathrm{d}y}y + z_0, \tag{C.2}$$

$$t(y) = \frac{\mathrm{d}t}{\mathrm{d}y}y + t_0, \tag{C.3}$$

$$\tag{C.4}$$

where $\mathrm{d}x/\mathrm{d}y$, $\mathrm{d}z/\mathrm{d}y$, $\mathrm{d}t/\mathrm{d}y$, x_0, y_0, and z_0 are fit parameters. Finally, we calculated the full information of the cosmic ray: track position in three-dimensional space, hit timing, and the velocity, as:

$$\text{velocity} = \frac{\mathrm{d}y}{\mathrm{d}t}\sqrt{1 + \left(\frac{\mathrm{d}x}{\mathrm{d}y}\right)^2 + \left(\frac{\mathrm{d}z}{\mathrm{d}y}\right)^2}. \tag{C.5}$$

The resultant cosmic ray velocity, shown in Fig. C.2, was consistent with the light velocity and its resolution was $\sigma/\mu = 5.9$ %. Figure C.3 shows the reconstructed z position distribution with the coincidence with each detector. In this case, $|\mathrm{d}z/\mathrm{d}y|$ was required to be less than 0.03. The

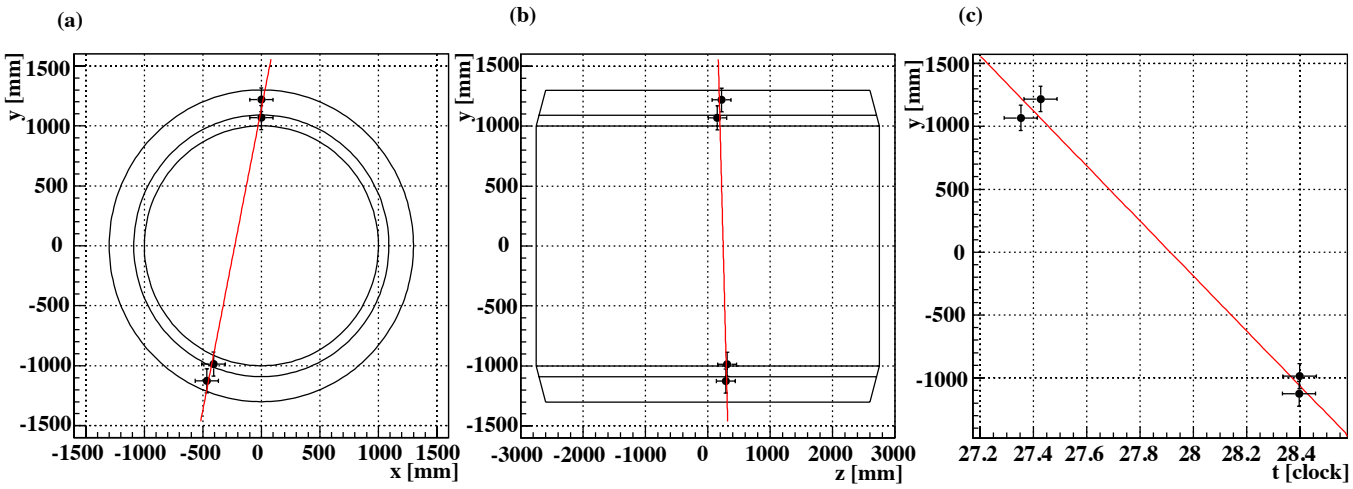

Figure C.1: Cosmic ray track example of MB. (a) x-y plane (rear view). (b) y-z plane (side view). (c) y-t plane, the horizontal axis shows the hit time and the vertical axis shows the y position of the hit module. Each black point shows the hit positions and time for a module.

distribution was consistent with the actual detector position. Obtained position resolution was 56 mm which was evaluated from the width of the reconstructed z position distribution in the $y = 0$ plane with the coincidence between MB modules and rear modules of CV.

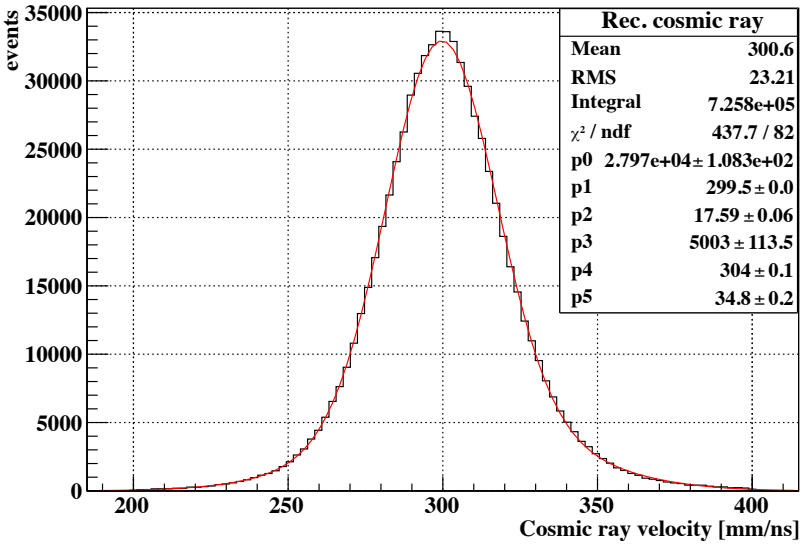

Figure C.2: Reconstructed cosmic ray velocity distribution. The red line shows the fit result with a double gaussian function.

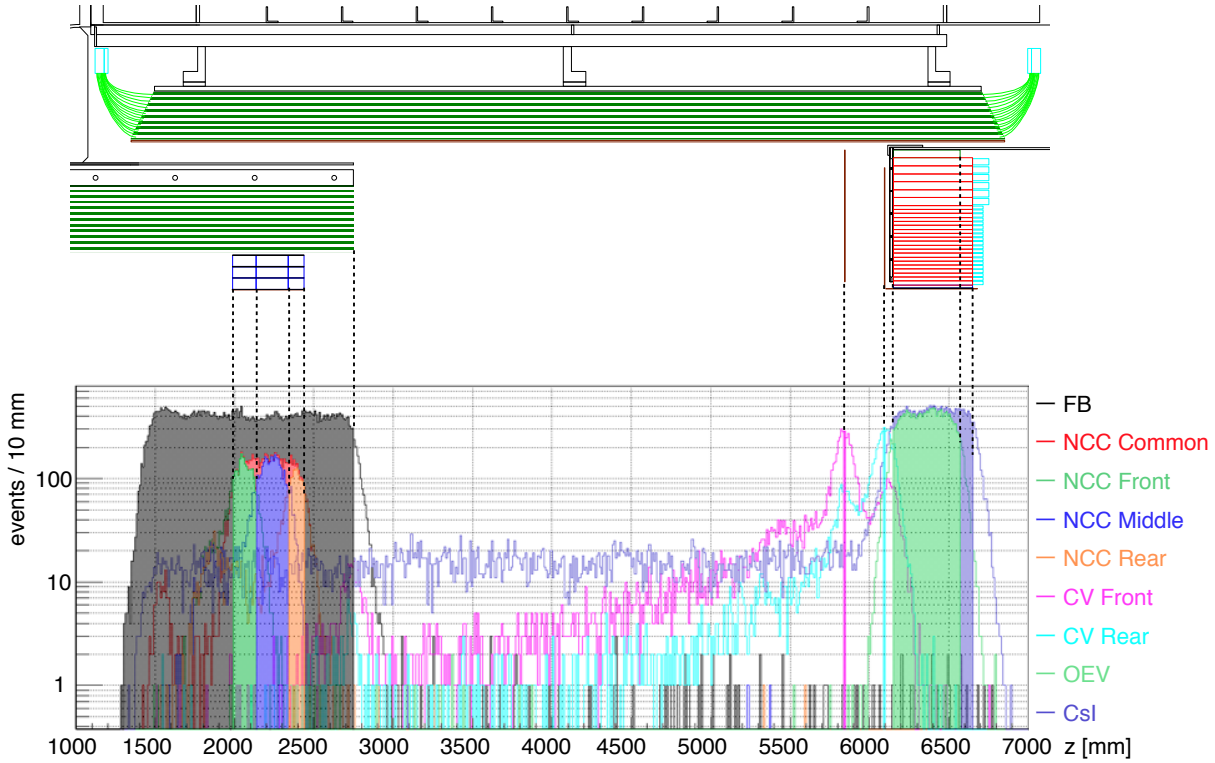

Figure C.3: Cosmic ray position distribution of the coincidence with each detector. Each histogram shows the z position distribution in $y = 0$ plane, when the specified detector had energy deposit, and shaded areas represented the actual detector positions as shown on the top. $|\mathrm{d}z/\mathrm{d}y| < 0.03$ was required.

Appendix D

$K_L \to 3\pi^0$ Calibration Selection Criteria

This chapter listed the detailed selection criteria for the $K_L \to 3\pi^0$ calibration. The overall feature of the $K_L \to 3\pi^0$ is explained in Sec. 5.2.1.

We did not use photons in which a crystal with the largest energy deposit has less than 20 % of the total photon energy or a crystal with the second largest has more than 20 % of the total photon energy, in order to prevent the iteration from diverging. The resultant v_z was required not to deviate from the original v_z more than 200 mm. and the resultant χ^2 calculated during the fitting was required to be less than 5, in order to discard unphysical events. To remove $K_L \to 3\pi^0$ events reconstructed from mis-pairing photons, the paring χ_z^2 should be less than 10 and the difference between the smallest and the second smallest pairing χ_z^2 was required to be larger than 5. The reconstructed K_L mass and π^0 mass were also required to be consistent with their nominal mass within 10 MeV/c^2 and 6 MeV/c^2, respectively. The selection criteria for the $K_L \to 3\pi^0$ calibration is summarized in table D.1.

Table D.1: Selections for the $K_L \to 3\pi^0$ calibration

Selection	Min.	Max.
Max. Energy among the Crystals / Cluster Energy	20 %	
Second Max. Energy among the Crystals / Cluster Energy		20 %
Vertex Change		200 mm
Calibration χ^2		5
Pairing χ_z^2		10
Second Pairing χ_z^2 - First Pairing χ_z^2	5	
ΔK_L mass		10 MeV/c^2
$\Delta\pi^0$ mass		6 MeV/c^2
Z_{vtx}	3000 mm	5000 mm
Cluster Distance	150 mm	
Photon Energy	100 MeV	